Designing of Functional Co-ordination Polymers for diverse Applications

THESIS SUBMITTED FOR THE

DEGREE OF DOCTOR OF PHILOSOPHY (SCIENCE)

JADAVPUR UNIVERSITY

By

MANIK SHIT, M.Sc.

Registration No: SCHEM1215322

Index No.: 153/22/Chem./28

DEPARTMENT OF CHEMISTRY

JADAVPUR UNIVERSITY

K0LKATA-700032

WEST BENGAL, INDIA

2024

Prof. (Dr.) C. Sinha
PhD, FAScT, FESS, FRSC,
Professor & Former Head
Department of Chemistry

JADAVPUR UNIVERSITY
KOLKATA - 700 032, I N D I A
Mobile: +91-7044231277
e-mail: crsjuchem@gmail.com

CERTIFICATE FROM THE SUPERVISOR

This is to certify that the thesis entitled "***Designing of Functional Co-ordination Polymers for diverse Applications***" submitted by ***Mr. Manik Shit***, M.Sc., who got his name registered on ***13.06.2022*** (***Registration No: SCHEM1215322 and Index No.: 153/22/Chem./28***) for the award of Ph.D. (Science) degree of Jadavpur University, is absolutely based upon his own work under the supervision of Dr. Chittaranjan Sinha, Professor, Department of Chemistry, Jadavpur University, Kolkata-700032 and that neither this thesis nor any part of it has been submitted for either any degree / diploma or any other academic award anywhere before.

It is also certified that he has fulfilled all the requirements of the regulations relating to the nature and period of research.

08/07/2024
Professor of Chemistry
Department of Chemistry
Jadavpur University
Kolkata-700 032

Date:

(Prof. Chittaranjan Sinha)
Signature of the Supervisor & date with seal
Department of Chemistry
Jadavpur University
Kolkata -700 032

Declaration of the Scholar

I declare that this written submission suggests my creative approaches in my own words and where other's ideas have been included; I have properly cited with suitable reference from the authentic sources. I also declare that I have adhered to all origins of academic principle and honesty and have not misled or fabricated or falsified any approach/ data/ origin in my submission. I understand such violation of the above will cause for disciplinary action by university and can evoke penal action from the sources which have thus not been properly cited or from whom proper permission has not been taken when needed.

Manik Shit
09/07/24

Date: Manik Shit

DEDICATED TO MY

BELOVED PARENTS

who made all of this possible, with your endless loves, supports, and prayers.

Acknowledgements

"Analytical Chemistry Building

Ground floor, Chittaranjan Sinha Research Lab"

The last five years were like a difficult and long test, which directed me to look over my scientific ability. While taking it, I struggled with myself not to give it up several times. This dissertation would not have been possible without the help of so many people in different way throughout my research carrier.Now I want to acknowledge those person who played a role directly or indirectly for the successful completion of my thesis.

First and foremost,I would like to thank my supervisor, Prof. Chittaranjan Sinha, for taking me into his lab and assigning such a challenging project to me. I also like to express my sincere gratitude to him for the continuous support, encourage and to give me confidence for my research and Ph.D. study. I am grateful for the advice and the training that he provides for me to be prepared for anything in my future endeavors and I am greatly proud of being a member of his group. I could not have imagined having a better advisor and mentor for my Ph.D. study.

I am also extremely thankful to my research advisory committee (RAC) members, Prof. Raju Mondal (Subject Expert, School of Chemical Science, IACS, Kolkata), Prof. Kajal Krishna Rajak (Head, Dept. of Chemistry, JU) and Prof. Chittaranjan Sinha (Supervisor, Dept. of Chemistry, JU, Kolkata) for their valuable suggestions, advises and support during the half-yearly RAC meetings. I am also grateful to Prof. Swapan Kumar Bhattacharya (Former HOD, Department of Chemistry) and all other faculty members of the department of

chemistry for being approachable for any assistance and maintaining such research friendly environment in thedepartment.

I sincerely thank all the collaborators – especially Dr. Kuladip Jana (Division of Molecular Medicine, Bose Institute, Kolkata, India), Dr. Md. Hedayetullah Mir (Department of Chemistry, Aliah University, Kolkata), Dr. Partha Pratim Ray (Department of Physics, Jadavpur University, Kolkata), Prof. Nabin Baran Manik (Department of Physics, Jadavpur University, Kolkata) , Prof. M. Salah El Fallah (Universitat de Barcelona, Martí iFranquès, 1- 11, 08028-Barcelona, Spain), Prof. Sagar Pal (ISM-IIT, Dhanbad, India) for their sincere collaboration.

I also sincerely appreciate the constant encouragement of all the faculty members and non-teaching staffs, especially Mr. Baidyanath Paul, Mr. Atikur Rahaman for their helpful attitude. I am also thankful to the authorities of the Jadavpur University for allowing me to use the necessary infrastructure.

I am also grateful to my M. Sc. project guide Prof. Sudipta Doloi, Department of Chemistry, Inorganic Chemistry Section, vidyasagar University for giving me the important knowledge about research which became very helpful in this journey.

I would also like to thank Narajole Raj college and the authority of this college to allow me to continue my research work at Jadavpur university. I specially thank the department of chemistry, Narajole Raj College where I,m working as a State aided College Teacher and all my colleagues, Prof. Barun kumar mondal, Dr. Sk. Mohammad Aziz, Dr. Soumendu Bisoi and Dr. Bishnupada Satpathi. I would also acknowledge Dr. Anupam Parua (Former Principal), Dr. Ranjit Kumar Khalua (Vice-Principal) and Dr. Basudeb Mandal (Principal) for their support to keep on my doctoral research work. I, also thank to collegue cum friends, Surajit, Sumanta da, Shibu da, Partha da, Suman da for their beautiful company in Narajole Raj College.

This journey would not have been possible without the support of my elder brother cum friends: Dr. Basudeb Dutta (Japan), Dr. Manas Mahapatra (Belgium), Dr. Arnab Samanta (IISER, Kolkata) who have tirelessly helped me from scientific to personal things at everymoment even during dinner, outings to the short trips. Their unconditional friendship have been greatly appreciated.

This journey would not have been possible without the support of my labmates: Dr. Arup Kumar Adak, Dr. Srikanta Jana, Dr. Suvendu Maity, Dr. Kaushik Naskar, Dr. Angeera Chandra, Dr. Suprava Bhunia, Dr. Sukanya Paul, Dr. Mukul Bikash Maity, Dr. Sunanda Dey, Dr. Souvik Pandey, Dr, Rajib Sarker, Mr. Gurupada Bairy, Miss. Sangita Ghosh, Mr. Sambhunath Bera, Mr. Himadri Shekar Chaterjee, Mr. Kumarjit Chowdhury, Mr. Soumya Jyoti Ghosh, Mr. Sabir Ahamed, Mr. Arka Patra, Mr. Koushik Saha and Mr. Sudip Ranjan Jana. I will never forget the beautiful memories and the difficulty that we shared together.

It is a genuine pleasure to express my appreciation to my close friends for their support and encouragement during my research period. I am indebted to my friends Satyajit, Kalipada, Dipankar, Arnab, Mihir da, Subrata, Anik, Kalyan, Avik da for helping me with data analysis of my research work.

I want to express special credit to my friend Somdutta for her support, constant encouragement, motivation and help throughout my work.

Last but not the least, I want to express my heartfelt thanks to some of my very close friends Swapneswar, Dibyendu, Amit, Gopal, Santanu, Ranjit, Biman, Bhabasankar, Laxmikanta, Krishnapada for providing me the company and support through every step of this journey. They were always beside me during the happy and hard moments to push me and motivate me. Without their support this journey would not be smooth and pleasant.

Finally, No thanks can be enough to acknowledge the people who mean a lot to me, my parents, Ma (Bulu Rani) and Baba (Sukumar), for showing faith in me and giving me liberty to choose what I wanted. I salute you all for the selfless love, care, pain and a lots of sacrifice you did to shape my life. They provide me always both the moral as well as emotional support in my life and prayers on my behalf. I would never be able to pay back the love and affection showered upon by my parents.

Also I want to express a heartfelt gratitude to my brothers, sisters, and sister-in-laws for their selfless love, care, support and valuable prayers which contributed a lot for completion of my thesis.

I would like to thank everybody who was important to the successful insight of the thesis, as well as expressing my apology that I could not mention personally one by one.

I am also thankful to CSIR for awarding me JRF fellowship to carry out my research work smoothly.

Finally, I pray the blessings of the almighty to the journey of my research, a search for

Manik Shit
Department of Chemistry
Jadavpur University
Kolkata- 700 032, India.

JADAVPUR UNIVERSITY

KOLKATA-700 032

MARK SHEET

NO.: CW/19052/ 0979

(For Ph.D/M. Phil. Course Work)

Results of the PH.D. COURSE WORK EXAMINATION, 2022

In SCIENCE

Name MANIK SHIT Class Roll No. 202120104020

Examination Roll No. PHDCHEM22220

held in DECEMBER, 2022

Subject Code / Name	Credit Hr.(c_i)	Marks
COMPULSORY UNITS:: CHEM/PHD/CPE-RPE/A/B RESEARCH & PUBLICATION ETHICS,RESEARCH METHODOLOGY & REVIEW WORK	8	57
ELECTIVE UNITS ::	8	74
CHEM/PHD/I-1 :: APPLICATION OF SPECTROSCOPIC STUDIES IN CHEMICAL RESEARCH CHEM/PHD/I-2 :: MATERIALS, CATELYSES & ELECTROCHEMICAL STUDIES CHEM/PHD/I-3 :: METALS IN LIFE & REACTION DYNAMICS CHEM/PHD/I-4 :: SINGLE CRYSTAL X-RAY STR. SUPRAMOLECULAR CHEM.& DFT COMPUTN.		

Total Marks : 131 (out of 200) **Remarks:** P

Prepared by : Checked by :

Date of issue : 28 / 04 / 2023

Controller of Examinations

Preface

[Index No.: 153/22/Chem./28]

The work presented in this thesis entitled **''Designing of Functional Coordination Polymers for diverse Applications''**was initiated in July, 2019 and have been carried out in the Department of Chemistry, Jadavpur University.

The thesis consists of seven chapters which are summarized below.

Chapter1 CoordinationPolymers(CPs) or Metal-Organic Frameworks (MOF) have extensive role in the field of sensing, electrical conductivity, gas absorption, magnetism, water splitting, environmental management, drug delivery and other biological applications. Structural diversity plays important role to exhibit different property with diverse applications. The coordination polymers are synthesized using the different metal nodes with the combination of bridging ligands. Transition metal CPs with N-heterocyclic bridgers and/or aromatic or aliphatic carboxylate (linker) serve as efficient magnetic materials. Many methods (like, slowevaporation, hydrothermal etc.) are followed to synthesize the CPs and characterised by usingdifferent spectroscopic methods (SXRD, TGA, PXRD, IR etc.). Coordination polymers areassembled via C-Cl$\cdots\pi$, $\pi\cdots\pi$, C-H$\cdots\pi$ and H-bonding. The CPs are also used for the selective detection of environmentally important metal ions, anions and small molecules. Extended π-conjugation, structural flexibility, $\pi\cdots\pi$ interaction and metal nodes are the reason for electrical conductivity in the dark/light condition and these materials are used to fabricate the Schottkydiode. The CPs are also used in the field of biology to derive microbiologically potential drugs. A short review and motivation of this research is delineated in the ***Chapter 1***.

Chapter 2 Zn(II)-based 3D CP $\{[Zn_2(tdc)_2(pcih)_2]_n\}$(**1**) ($tdc^{2-}$, 2,5-thiophene dicarboxylate; pich, Pyridine-4-carboxaldehyde isonicotinoyl hydrazine) is structurally characterized by single crystal X-ray crystallography as well as by other spectral data. The material has been used to measure electrical conductivity at dark phase and illumination phase. The anticancer efficiency of **1** has been examined and it shows better impact in inhibiting the proliferation of MDA-MB-231 cells than other cancer cells like HCT-116, HeLa and HepG2.

The ***Chapter 3*** reports $\{[Mn_2(tdc)_2(pcih)_2(EtOH)]_n\}$ (**2**) (pcih, pyridine-4-carboxaldehyde isonicotinoylhydrazone; tdc^{2-}, 2,5-thiophene dicarboxylate), a 3D supramolecular architecture which shows anti-ferromagnetism. It's interesting to note that the **1,** has electrical conductivity in the semiconducting region.

In ***Chapter 4,*** a 3D network, $[Zn(mes)(pcih)(H_2O)_2]_n$,(**1**) is constructed by two bridging molecules, mesaconic acid (H_2mes) and pyridine-4-carboxaldehyde iso-nicotinoylhydrazone (pcih), and shows photoconductivity.

In ***Chapter 5*** a 3D-Coordination Polymer of Mn(II), $[Mn_2(aisp)_3(pcih)_2(solvent)]_n$ (**CP1**) (where pcih = Pyridine-4-carboxaldehyde isonicotinoyl hydrazine and H_2aisp = 5-aminoisophthalic acid) which shows both electrical conductivity and anticancer activity against four cancer cell lines (HeLa, PC3, MDA-MB 231, and A549) is reported. The drug delivery activity of Diclofenac Sodium (DMNa) is observed at pH, 7.4 (blood) while at pH, 1.2 (stomach) it remains silent.

The ***Chapter 6*** also reports Mn(II)-based CP, $[Mn(tdc)(nvp)_2(H_2O)]\cdot(DMF)$ (Mn-CP) (dtc^{2-}, 2,5-thiophenedicarboxlate and nvp, 4-(1-naphthylvinyl)pyridine) which interestingly shows unique pH-dependent emission [λ_{em}= 525 nm (pH = 2.0-4.0) and 450 nm (pH = 5.0-12.0)]. The emission is quenched by Pd^{2+} in aqueous medium in presence of other thirteen cations with reasonably low pH-dependent limits of detection [21.178 ppb (pH= 3), 15.005 ppb (pH = 7.0) and 59.940 ppb (pH = 10.0)].

Chapter 7 represents summary of the Research Work.

List of Abbreviations

CP	Coordination Polymer
MOF	Metal-Organic Framework
PCP	Porous Coordination Polymer
ICP	Intercatenated Coordination Polymer
PCIH	Pyridine-4-carboxaldehyde isonicotinoylhydrazone
TDC	2,5-thiophene dicarboxylic acid
MES	Mesaconic acid
AISP	5-aminoisophthalic acid
NVP	4-(1-naphthylvinyl) pyridine
DMF	N,N′-dimethylformamide
MeOH	Methanol
EtOH	Ethanol
Et_3N	Triethylamine
NaH	Sodium hydride
FESEM	Field Emission Scanning Electron Microscopy
PVA	Polyvinyl Alcohol
TGA	Thermo-gravimetric Analysis
NMR	Nuclear Magnetic Resonance
FT-IR	Fourier transform infra-red spectroscopy
UV-Vis	Ultraviolet–visible
τ	Fluorescence Lifetime
PXRD	Powder X-Ray Diffraction
Φ	Quantum Yield
AIE	Aggregation Induced Emission
PET	Photo-Induced Electron Transfer

ICT	Intramolecular Charge Transfer
FRET	Fluorescence Resonance Energy Transfer
ESIPT	Excited-State Intramolecular Proton Transfer
TCSPC	Time Correlated Single Photon Counting
HEPES	4-(2-Hydroxyethyl)piperazine-1-ethanesulfonic acid
MeOH	Methanol
DMF/dmf	Dimethyl Formamide
H_2O	Water
DMSO/dmso	Dimethyl Sulfoxide
mL	Millilitre
μM	Micro Molar
μL	Micro Litre
nM	Nano Molar
mM	Mili Molar
K_b	Binding Constant
K_a	Association Constant
K_d	Dissociation Constant
K_f	Formation constant
K_{SV}	Stern-Volmer Constant
K_q	Bimolecular Quenching Rate Constant
η	Refractive Index
ΔH^0	Standard Enthalpy Change
ΔS^0	Standard Entropy Change
ΔG^0	Standard Gibbs Free Energy Change
ex	Excitation
em	Emission
λ	Wavelength

HeLa	Human Epithelial Carcinoma Cell
HepG2	Human Hepatocellular Liver Carcinoma Cells
DMEM	Dulbecco's Modified Eagle's Medium
MTT	3-(4,5-di methylthiazol-2-yl)-2,5 diphenyltetrazolium bromide
%T	Percentage of Transmittance
MS	Mass Spectroscopy
NMR	Nuclear Magnetic Resonance
FT-IR	Fourier Transform Infrared
T	Temperature
h	Hours
mg	Milligram
Et_3N	Triethylamine
f	Oscillator Strength
°	Degree
Å	Angstrom
eV	Electron Volt

Contents

Chapter 3

Page

Exploration of Variable Temperature Magnetism and Electrical Property of a Pyridyl-isonicotinoyl Hydrazone Bridged 3D Mn-MOF with ThiopheneDicarboxylato Link

Chapter 4 Page

Strategy for the improvement of electrical conductivity of a 3D Zn(II)-coordination polymer doubly bridging by mesaconato and pyridyl-isonicotinoyl hydrazide Schottky diode device

Chapter 5 Page

Mn (II) 3D coordination framework with mixed 5-aminoisophthalatoand Pyridyl-isonicotinoylHydrazone Bridges: Structure, Electrical Conductivity, Anti-cancer Activity and Drug delivery

Chapter 1

Introduction: A Literature Survey

"Where the world ceases to be the scene of our personal hopes and wishes, where we face it as free beings admiring, asking and observing, there we enter the realm of Art and Science. If what is seen is seen and experienced is portrayed in the language of logic, we are engaged in science. If it is communicated through forms whose connections are not accessible to the conscious mind but are recognized intuitively as meaningful, then we are

*engaged in art"- **Albert Einstein***

*"If you want to live a happy life, tie it to a goal, not to people or objects." — **Albert Einstein***

The exploration of metal ligand coordination chemistry offers a wide spread opportunities towards diverse, fascinating and aesthetic structural architecture and potential applications. The structural diversities of the coordination compounds depend on the nature of metal centre and coordinating ligands. Multidentate and bridging ligands coordinated to metal centre(s) can generate multidimensional structures synonymous to coordination polymer (CP). The structural varieties of these polymeric coordination compounds can be named as Metal-Organic Frameworks (MOFs).[1-3] Porous Coordination Polymers (PCPs), Metal-Organic Coordination Networks (MOCNs),[4] Metal Organic Layers (MOLs),[5] Metal Organic Polyhedra (MOPs),[6] Metal Organic Nanolayers (MONs)[7] and Metal Organic Sponges (MOSs).[8] Among all these coordination diversities, the current dissertation focuses on the synthesis and structural characterisation of new coordination polymers (CPs) and metal organic frameworks (MOFs)[9-10] and exploration of their different application. The structural varieties of synthesized compounds have been achieved through the judicious selection of secondary building units (SBUs) and organic bridging ligands.[11] The structure directly affects the surface area and hence the surface properties. The large surface area of such hybrid materials has been employed for the wide spectrum of potential applications in gas sorption and separation, catalysis, electrical conductivity, electronic devices, drug action and drug delivery and sensing of ions / molecules.[12-16]

1.1 Coordination Polymers

The Coordination Compounds are the backbone of modern inorganic and bio–inorganic chemistry, chemical and pharmaceutical industry, drug delivery, renewable energy sources and environmental remediation etc. A compound in which the cation (metal ion) bounds to a number of atoms, molecules, or ions called ligands is called a coordination complex**.** The importance of the field received attention after winning the Nobel Prize in 1913 by German scientist Alfred Werner. Numerous scientific advances in the field of coordination chemistry have been made possible by the investigation and experimentation of many scientists. Metal ions and ligands are the integral parts of the coordination compounds. Using a ligand consisting of more than one donating centres can bind more than one coordination site about the metal ion to form a chelate complex or can bind more than one metal ions to form dimer/trimer or polymer (**Figure 1.1**).[17, 18]

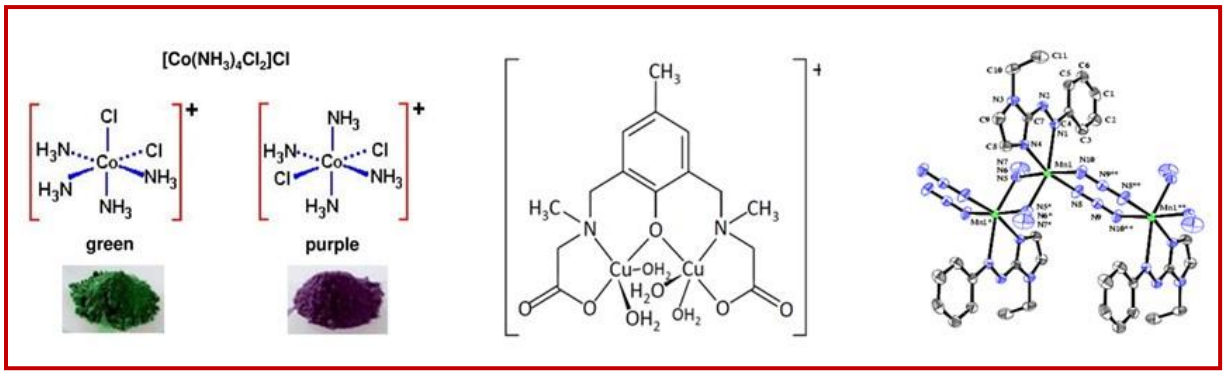

Figure 1. 1 Coordination compound, a phenolato-bridging dimer and azido bridged polymer

Prof. J.C. Bailar first introduced the term coordination polymer. A coordination polymer (CP) is an inorganic or organometallic polymer containing metal cation centers or metal clusters as knots and ligands are the bridging agents to connect the adjacent metal ions. Generally, a coordination polymer is a coordination compound with repeating coordination entities extending in one, two, or three dimensions. According to IUPAC, its definition is "A coordination compound continuously extending in 1 (1D), 2 (2D) or 3 dimensions (3D) through coordination bonds." Presence of permanent cavities in the coordination polymers are recognised as Porous Coordination Polymers (PCPs) or MOFs (metal-organic frameworks) or MOCNs (metal-organic coordination networks).[19, 20] They are characterized in terms of their dimension – one dimensional or chain like (1D); two dimensional or plane like (2D); three dimensional (3D) (**Figure 1.2**)**.** A summary of the organic linkers reported in the literatures is listed in **Figure 1.3**. The metal organic frameworks (MOFs) are porous crystalline structures with large surface area and high porosity.[21,22] The structure of MOF is constituted by inorganic secondary building units (SBUs) and organic linker molecules/ions between them.[23,24]

The SBUs are generally metal ions/metal clusters while organic linkers are ionic or neutral organic molecules with O and N donor centres in general. By combining different SBUs with different linkers, it is possible to obtain various different structures with different properties.[25-27] In general, the porous structure of MOFs makes them a great candidate for gas storage, adsorption and separation, drugs and drug delivery, photoconductivity, electrical conductivity, carbon capture and conversion, H_2-generation, waste water treatment and environmental remediation, heterogeneous catalysis, sensing of ions/molecules.[28-32]

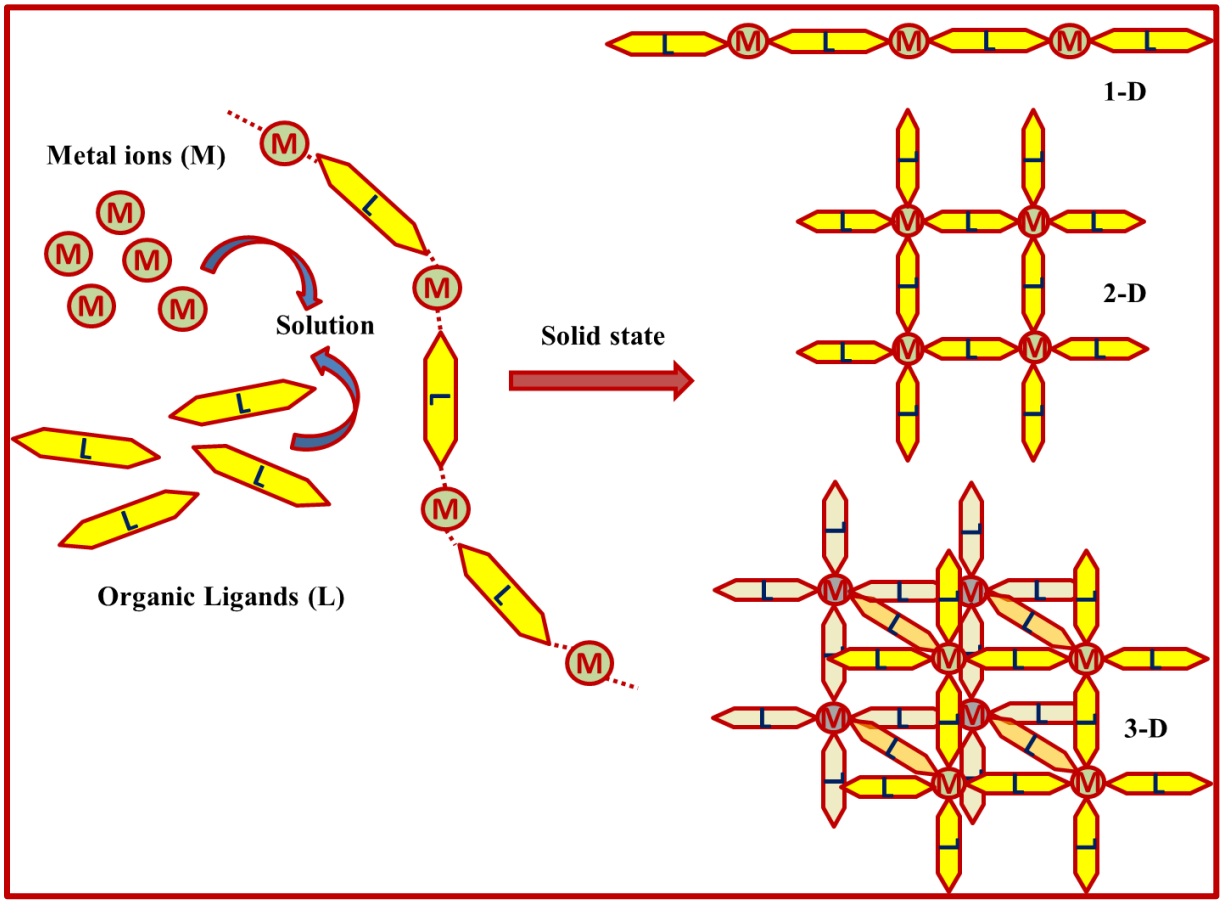

Figure 1.2 Design of different dimensional MOFs/CPs formation (1D, 2D and 3D) from the same primary building units (PBUs).[32]

It is a prospective precursor for the development of new materials due to its high surface area and good physical and chemical characteristics. While the majority of MOFs those have been reported in the literature are non-conducting, crystalline ordered forms of inorganic-organic hybrid materials, they contain single metals or metal clusters that are extended through the coordination of ligands, such as neutral or anionic linkers, with repeating coordination entities that extend through a variety of covalent and non-covalent interactions in one, two, and three (1D, 2D, and 3D)-dimensional arrangements[21,22].

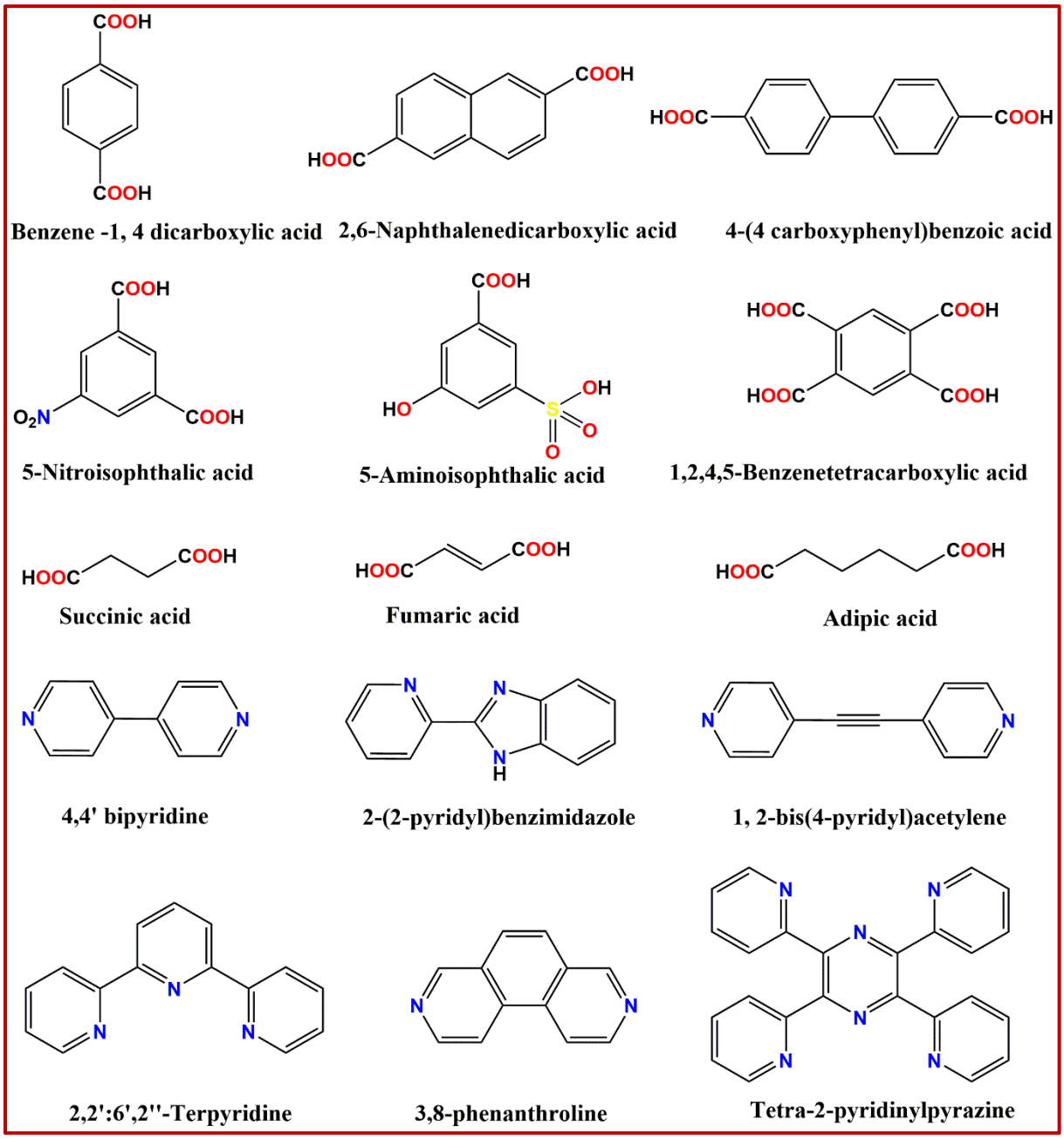

Figure 1.3 Representative examples of organic ligands used in the synthesis of CPs/MOFs.

Initially, research on the adaptability of CPs revealed that differences in the functionality and topology of the newly developed CPs could be achieved by altering the metal atoms or even the size of the organic linkers.[34-37] Carboxylate linkers as well as the nitrogen linker group 4,4/ bipyridine (BIPY) are often utilized to make CPs and study the coordination chemistry of their derivatives.[38]

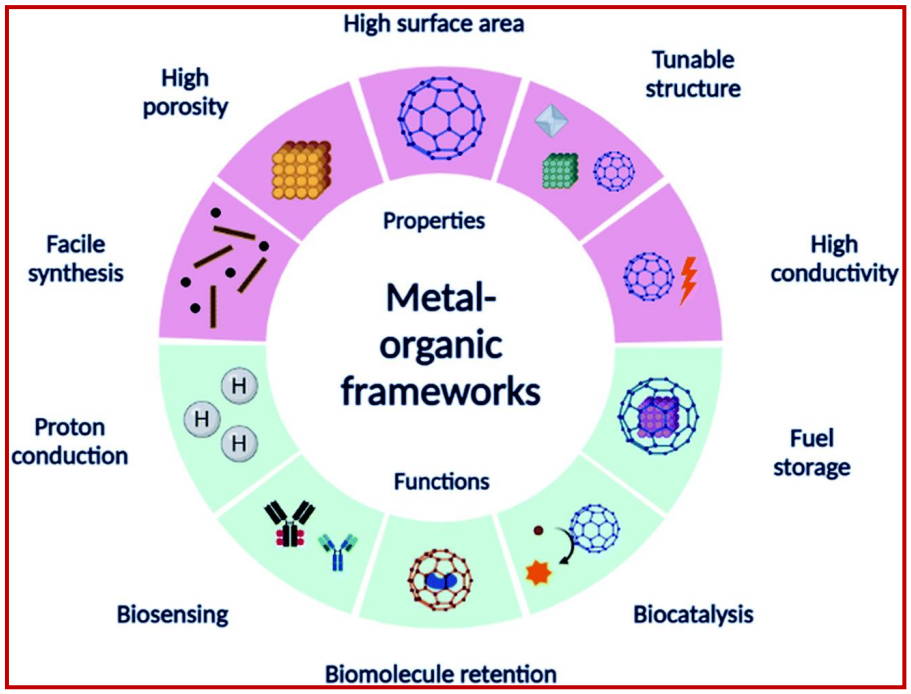

Figure 1.4 Various properties and applications of MOFs.[33]

The term "reticular chemistry" was introduced by Prof. Omar M. Yaghi and colleagues from University of California, Berkeley, USA to describe the comprehension of molecular chemistry and its precision in forming and breaking connections inside a solid-state framework structure. Following the first report of MOF-5 ($Zn_4O(BDC)_3$, where BDC^{2-} = 1,4-benzodicarboxylate) by Yaghi et al. in 1995, a novel polymer with a large surface area for sorption similar to carbon tubes was developed. Since then, MOFs have been the most talked-about subject in material chemistry, and for the previous few decades, they have grown in significance (**Figure 1.4**).[39-41].

In the initial phase, scientists aim to regulate and enhance multiple structural elements such as (i) the sizable pore aperture, (ii) the elevated surface area, and (iii) the potent metal-based adsorption characteristic in metal-organic frameworks (MOFs) or porous coordination polymers (PCPs) for gas storage.[42-43]

Prof. Susumu Kitagawa (1998), Kyoto University, Japan categorized PCPs according to their generation in term of stability, porosity, flexibility and guest capturing ability. The PCPs are divided into four generations (**Figure 1.5**) first, second, third and fourth generation.[44-45] The generation of MOFs are classified in view of the structural flexibility and cavity specificity.

The 1st generation MOFs has only nonpermanent porosity and collapsed on releasing of guest. The structure is rigid and stability depends on the guest or known as guest specific MOF. The second-generation MOFs are discovered to be rigid and stable and do not breakdown on removing the guest molecules from the framework. The cavity is porous and flexible. The pores have sizeable flexibility. Second-generation materials can be separated from third-generation materials by their dynamic and flexible nature, which allows them to reversibly remove guest molecules from the framework. The fourth generation MOFs can withstand post-processing (modifiable places include (1) metal/cluster sites, (2) organic linkers, and (3) empty space based on asymmetry feature and hierarchical character.[46-49]

1.2 Historical Progress of CPs/MOFs

The most common The Coordination Polymers (CPs) show a number of beneficial qualities.[50] Early inorganic CPs (i-CPs) included cyanide complexes, Prussian blue, and Hofmann clathrates.[51] Following i-CPs, three key advances made in recent decades have had a measurable impact on the direction of research trends (**Figure 1.6**). The first step was the identification of organic ligand-bridged structures. The addition of organic ligands to CPs transformed the chemistry into one that is modular and designable, yielding a chemical library. To characterize these structures, single crystal X-ray analysis was required. This chemistry started with copper ions. The first organic ligand-bridged CPs (o-CPs) described by X-ray were made from the d^{10} metal ion Cu^{+} and adiponitrile $(CH_2)_4(CN)_2$).[52] Several decades later, further comparable constructions were reported. Square grid (1986),[53] diamond (1989),[54] and honeycomb (1992)[55] networks of copper ions were created, followed by networks including other d^{10} metal ions (Cd^{2+}, Ag^{+}, and Zn^{2+}) in the mid-1990s.[56]

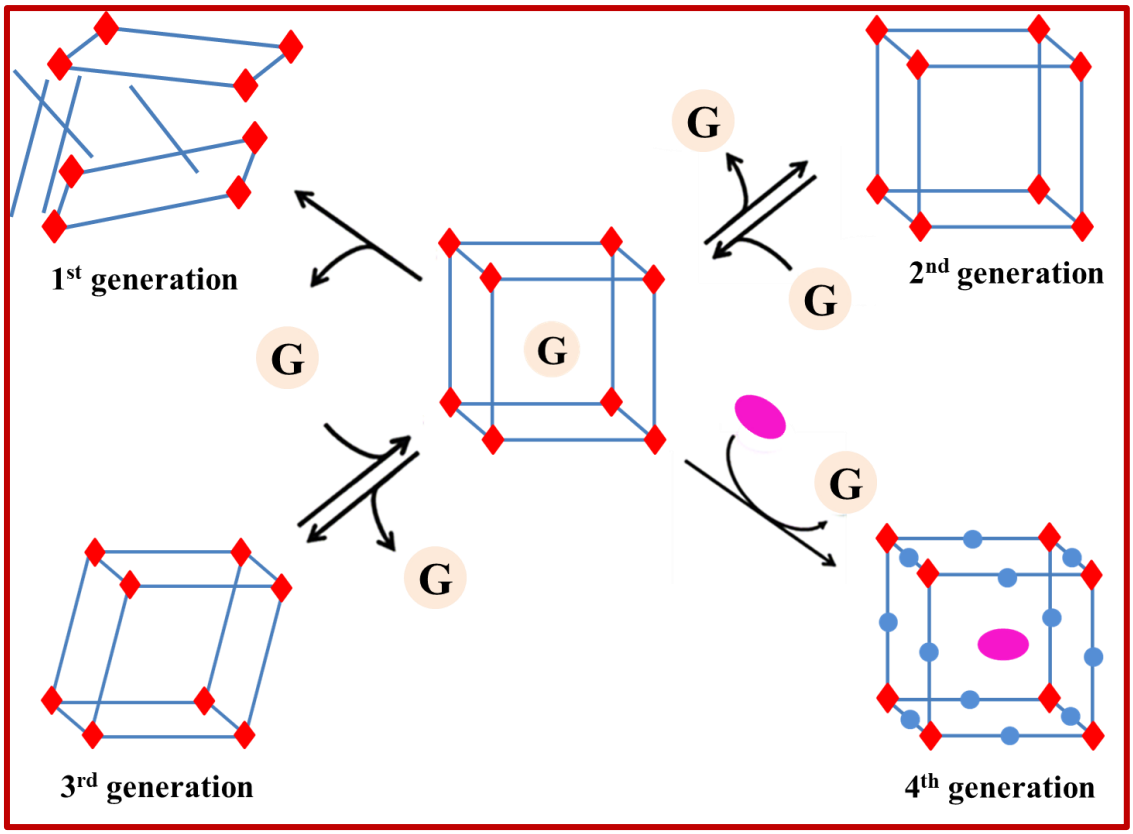

Figure 1.5 Classification of MOFs: 1st generation MOFs to 4th generation MOFs. [57] **(G = Guest)**

There have been four major advances in the development of o-CPs:[57] the construction of o-CPs and determination of their X-ray structure (first generation (1G)), permanent porosity by gas adsorption (second generation (2G)), soft crystal, such as crystal-to-crystal transformation upon chemical/physical stimuli (third generation (3G)), and liquid and glassy states of o-CPs and metal-organic frameworks (MOFs) derived from crystalline states (fourth generation (4G)).

The second significant advancement is the synthesis of o-CPs with robust and permanent porosities via gas adsorption, which opened up a new avenue for porous materials chemistry.[58]The discovery of porous o-CPs resulted in useful porous materials that follow design principles. Since then, a considerable number of these porous crystals have been created, and they are now known as metal-organic frameworks (MOFs) or porous coordination polymers (PCPs) (**Figure 1.7**).

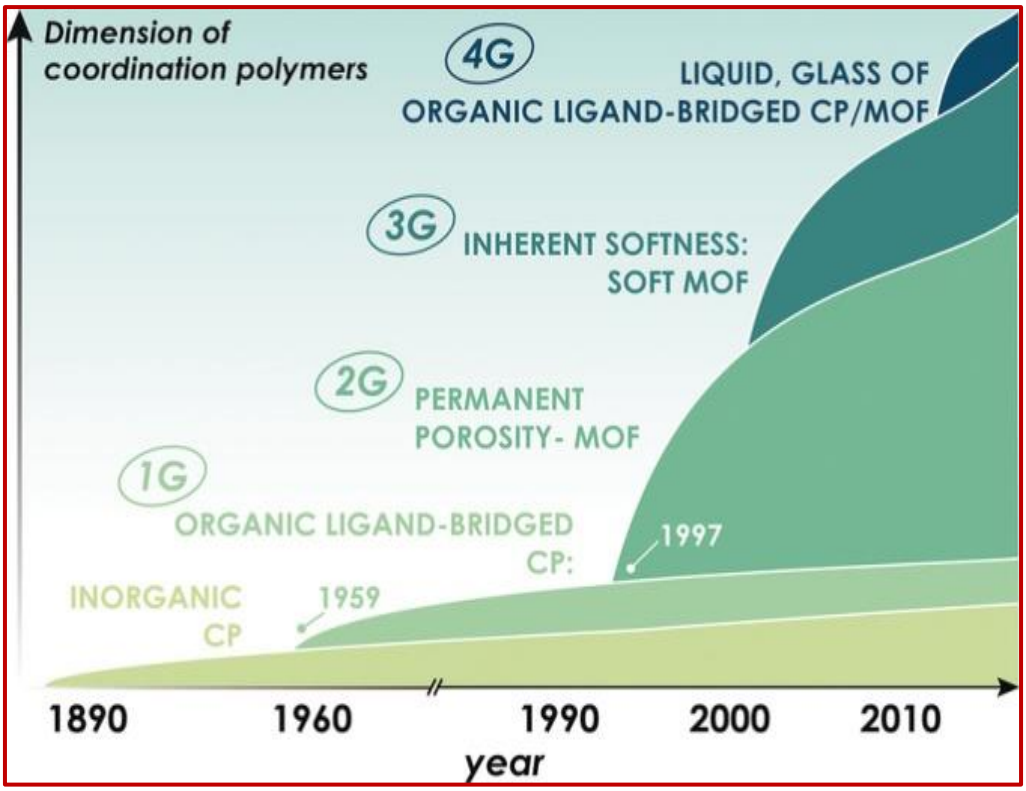

Figure 1.6 Coordination polymers (CPs) progress chronologically.

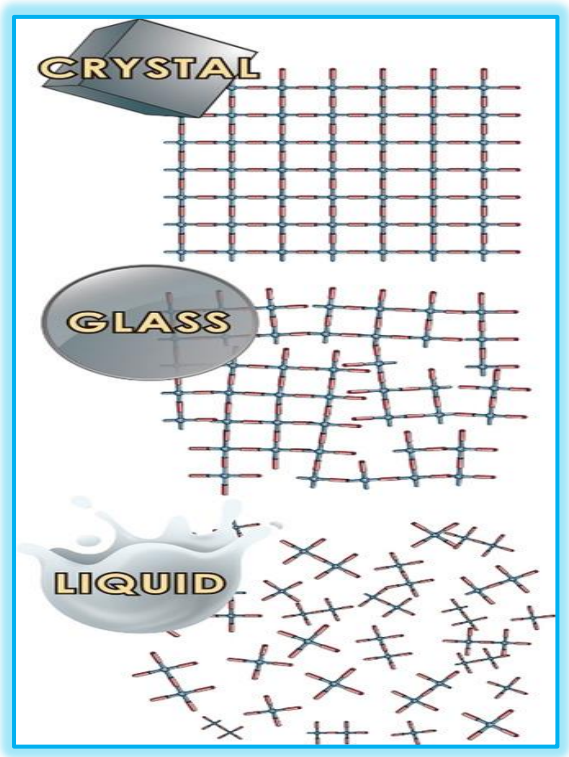

Figure 1.7 Schematic architectures of crystal, glass, and liquid states of o-CPs as a snapshot.

Metal ions are represented by blue cores and red bars, while organic ligands bridge them. According to current knowledge, we propose that (i) glassy states have middle-range order, indicating metal-ligand connectivity to form networks, (ii) X-ray absorption studies show that the first coordination spheres of metal ions in three phases are nearly identical, and (iii) liquid states have more fragmented (but not entirely) metal-ligand networks.[57]

The final step was to demonstrate intrinsic flexibility and dynamic characteristics in MOF structures.[58] This encompasses the complete modification of crystal structure and local molecular motion in crystals, which is caused by chemical stimuli (gas sorption and substrate inclusion) or physical stimuli (temperature, pressure, light, and electric fields).[59] These structures are distinguishable from other traditional porous solids by their flexibility/dynamics and bi-stability with porosity. Examples include Graphenes, CNTs, zeolites, phosphates, and mesoporous silica. The dynamics of coordination bonds and the multi-stability of phases in o-CPs are important not only for crystal-to-crystal transformations, but also for crystal-to-liquid/glass transformations, which are the focus of this chapter. (**Figure 1.7**)

A fourth development is currently underway in relation to the melting and vitrification of crystals from a range of o-CPs, including MOFs. Thus, crystallography has helped to develop the chemistry of o-CPs. However, the three primary material families (polymers, metals, and ceramics) exhibit both crystalline and non-crystalline forms. They contain liquids and glasses, and both states are critical for discovering new properties and developing materials. The liquid or glassy phases of o-CPs, on the other hand, have received less attention due to the difficulties of both their synthesis and characterization. The appearance and management of liquid/glassy phases of o-CPs opens up new research possibilities in this sector.

1.3 Crystal Engineering

The term "Crystal Engineering" was initially developed by R. Pepinsky in 1955, but Gerald Schmidt was the one who applied it to the photodimerization of cinnamic acids.[60] Crystal engineering has been defined by G. R. Desiraju in 1989 which is the understanding of intermolecular interactions in the context of crystal packing and the utilization of such understanding in the design of new solids with desired physical and chemical properties.[61]

Furthermore, chemistry and molecular crystallography have been connected through the use of crystal engineering. The ability to manipulate the connections of molecules into a solid crystalline structure is known as crystallographic ability in chemistry.[62]Crystal engineering was

initially only based on organic systems, but starting in the late 1990s, a wide range of organic-inorganic hybrid compounds were investigated in different structural architectures and topologies.[63-64] Recently, D. T. McGrath et. al Investigated the crystal engineering of the pillared paddlewheel metal–organic framework $Zn_2(NH_2BDC)_2DABCO$ (**Figure 1.8**).

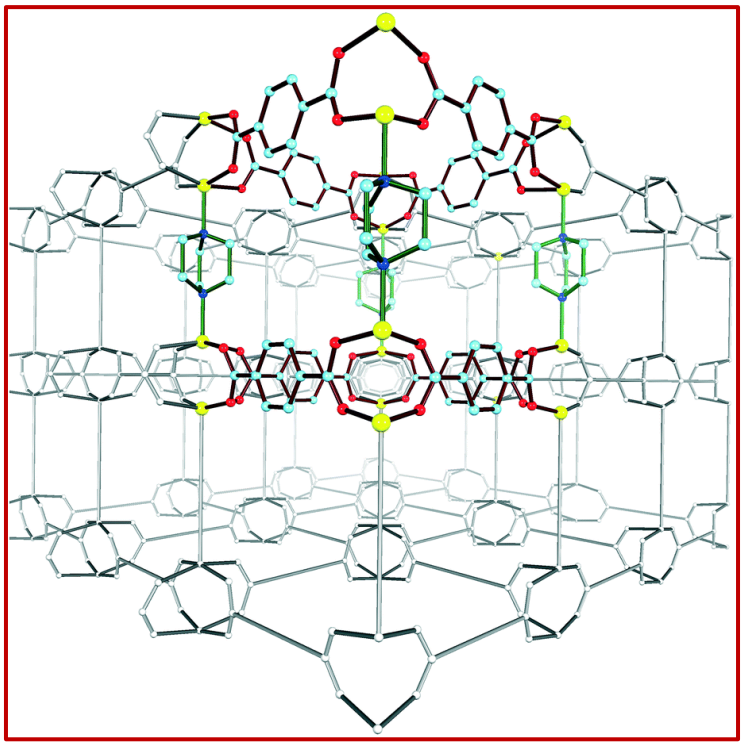

Figure 1.8 The crystal structure of $Zn_2(NH_2BDC)_2DABCO$ shows how pairs of zinc cations interact via BDC units (dark red bonds) to produce a paddlewheel $Zn_2(COOR)_4$ sheet. The overall pillared paddlewheel MOF is formed by connecting these sheets by a DABCO pillar (dark green bonds). Zinc (yellow), oxygen (red), carbon (light blue) and nitrogen (dark blue). Amino groups have been removed for clarity.[64]

The design approach of crystal engineering makes it easier to bring together pharmacological science,[65] molecular biology, and material science under a single structure. The fundamental concept of crystal engineering is the association of such supramolecular synthons as organic molecules (linkers) and inorganic cations (metal ions as knots) into a solid-state by non-covalent and self-assembly.[66] When weak intermolecular forces like hydrogen bonds and $\pi\cdots\pi$ interactions are involved in the construction of metal-organic building blocks, it is known as

inorganic crystal engineering. In contrast, organic crystal engineering primarily deals with these forces.[67]

In contrast to organic crystal engineering, inorganic crystal engineering has become the most used potent technology in scientific research. It accomplishes this by applying weak intermolecular forces like hydrogen bonds. In addition to hydrogen bonding, investigations on crystal engineering have explored weak intermolecular forces of the aromatic π-system, such as π…π and C–H···π interactions. The functions of supramolecular halogen···halogen, S···S interactions have not been well studied, although their significance continues to increase regularly. Three-dimensional crystals have been rationally designed beyond constructive approaches, although the predictions over such 3D crystal structures are still fascinating.[68-70]

The subject is contributed significantly to the emergence of a number of highly important internationally scientific publications, including *Dalton Transaction*, *CrysEngComm*, *New Journal of Chemistry* (The Royal Society of Chemistry) ;*Crystal Growth and Design*, *Inorganic Chemistry*, *ACS Applied Polymer Materials, ACS Applied Bio Materials* (The American Chemical Society); *Applied Organometallic Chemistry* (Wiley); *Journal of the Indian Chemical Society* (Elsevier), *J. Chem. Sci.* (Springer), *Indian J Chemistry A (NISCAIR),*and *Journal of Coordination Chemistry* (Taylor & Francis). A few new open access journals, small Crystals from MDPI and IUCrJ from the International Union of Crystallography, have been established to represent the significance of this contemporary field.

1.4 Applications of CPs/MOFs

Environmentalists and analytical chemists are becoming more and more involved in the remediation of global challenges related to pollution, degradation, and climate change, as a part of Sustainable Development Goals (SDGs). The most pressing issue in recent years is the segregation of pollutants hazardous inorganic (such as heavy metal ions, radioactive species, oxyanions, and oils) and organic (such as oils, dyes, pesticides, and pharmaceutical products), biomedical and removal of them from the environmental sources.

Because of their huge surface area and tuneable porosity, coordination polymers/metal-organic frameworks (CPs/MOFs) have gained recognition in this sector as a highly valued class of material within the families of porous materials (e.g., zeolites, activated carbons, porous silica, mesoporous clay materials, etc.).[71] The last 20 years have seen a vigorous exploitation of CP/MOF materials due to their unique features in a variety of application fields, including gas

storage and separation, sensing, electrical conductivity, photochromism, heterogeneous catalysis, electrochemical studies, etc.[72] **(Figure 1.9)**.

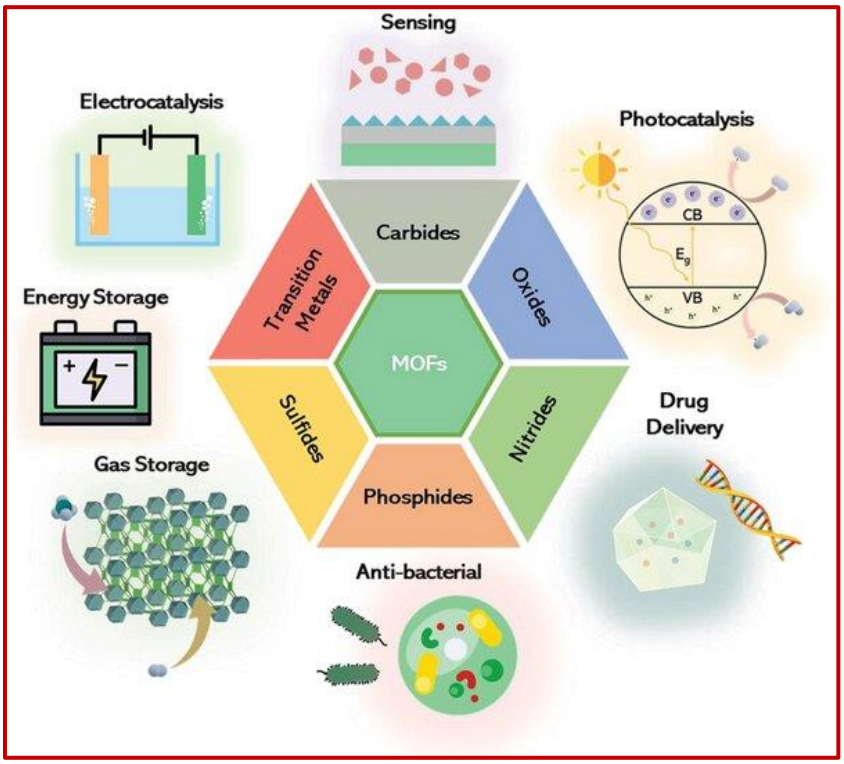

Figure 1.9 Families of metal-based derivatives produced from MOFs and their possible uses.[73]

Despite being widely used in different fields, the MOFs have not yet received much attention in the areas of electrical conductivity and photochromic applications. In order to address the worldwide energy problem, electro-conductive MOFs or PCPs have been granted new opportunities to enhance device performance as an energy storage application.[74] Over the past five years, novel methods for exhibiting both high electrical conductivity and porosity have demonstrated the extensive expansion of electro-conductive MOFs (**Figure 1.9**).[75]

1.4.1 Electrical Conductivity Related Terms

A diode is an electrical device with two terminal electronic components that only allows current to flow in one direction. One side has low resistance while the other has higher resistance, which prevents the current from flowing. The term "hot carrier semiconducting diode" refers to a Schottky diode. A Schottky diode is often formed when a metal and semiconductor are combined, creating the barrier. In this instance, the cathode in the n-type diode is metal, and the anode is p-type semiconductor.

1.4.2 Diode and Schottky Barrier

Here we have performed Schottky diode applications by applying electrical voltage. Schottky diode is an electronic device which permits current to flow in one direction while opposes the current in the opposite direction with a high resistance.[76]

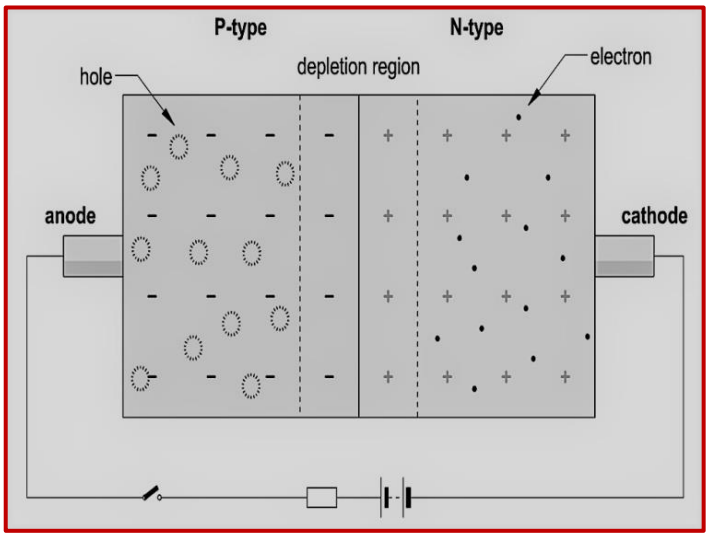

Figure 1.10 Schottky barriers and work function for semiconductors.[80]

Schottky diode is a kind of semiconductor which is known as hot carrier diode and it has a low forward bias voltage. This lower bias voltage drop offers improved efficiency and switching speed of the system In general, Schottky diode is made by generating a Schottky barrier between semiconductor and metal. In Schottky diode, cathode acts as n-type semiconductor and the metallic part behaves as anode material of the diode (**Figure 1.10**).[77-79] Metal and semiconductor have different work functions which emerges the electrostatic barrier in a schottky diode. For n type, electron transfer occur semiconductor to metal and reached

equilibrium between the Fermi levels and forms a depletion region, when the work function of metal ((ϕ_m) exceeds the work function of the semiconductor **((ϕ_s).**[81-82.]

The diffusion potential V_{do} as

$$V_{do} = \phi_m - \phi_s \quad (1)$$

For n-type semiconductor, when $\phi_m > \phi_s$, and the bands are bent upwards; the electrons have to overcome the electrostatic barrier to transfer semiconductor into metal. For p-type semiconductor, the band-bending due to no barrier to the holes motion, and an 'ohmic' contact formation taking place. When $\phi_m < \phi_s$, downwards bending of band provides an ohmic contact for a n-type semiconductor whereas, a rectifying contact is formed for a p-type semiconductor.[83]

1.4.3 Advantages of Schottky Diode

Low turn on voltage: Turn on voltage in between the 0.2 to 0.45 volts is good for Schottky diode.

Fast recovery time: Because of the quick recovery period, a tiny amount of stored charge is used for the high-speed switching application.

Low junction capacitance: Capacitance level is very low if the contact area is very small.

1.4.4 Applications

Schottky diode is used in the application of radio frequency and radio detector due to their low capacitance, high switching speed and high frequency capability. Most powerful application appears in the rectifiers, because of low forward voltage drop and high current density. So, low power was used in the Schottky diode than the general p-n junction. Schottky barrier acts as circuits in the two power supplies.

Solar cell applications: In the solar cell low voltage drop Schottky diode is used, because voltage drop in the solar cell is not expected. Ability of the solar cell is reduced due to this voltage drops.

Clamp diode: Actually, clamp diode is a Schottky diode and it is used in the transistor circuit in controlling the speed of the process during the switching process.

1.4.5 Diode Parameters

Ideality Factor (η): Ideal behavior of the Schottky diode is measured by ideality factor. Current in the low voltage region is measured by this factor and it is directly proportional to the dV/dlnI.

Series Resistance (Rs): Total amount of resistance value in a series of Schottky diode is known as series resistance and current flows through the all resistors.

Barrier Height (φ): Schottky barrier height (SBH) is an important characteristic at the metal semiconductor (MS) interface. Schottky barrier height represents the rectifying barrier to electrical conduction through the MS. The Schottky barrier height of a metal/n-type semiconductor is the difference between the metal fermi level and the semiconductor's conduction band minimum. The Schottky barrier height is the difference between the metal fermi level and the semiconductor's valance band maximum in the case of p-type.

1.4.6 Charge transport parameter

Mobility (μ): Mobility is defined as the how fast carriers transfer charge through the metal or semiconductor. Mobility of the semiconductor depends on the electron, hole concentration, impurity concentration (like, donor and acceptor concentration), electric field and temperature.

Transit time (τ): Time required for a carrier to travel from the cathode to anode or vice versa is called the transit time. This time related to the total time of free carries as well as time required for the trapped carrier in the traps.

Diffusion Length (D): The current flow through the metal semiconductor junction is dependent on the majority carriers. Among the exciting mechanism, diffusion of the carriers from the semiconductor to metal is an important mechanism. According to the diffusion theory, diffusion length is a length of depletion layer where driving force is distributed.

1.4.7 Magnetism

The interaction of elementary particle spin motion with an applied external magnetic field gives rise to magnetism. When electron spins align in various directions, a magnetic moment is created. Paramagnetic compounds are those that interact to an applied magnetic field.[84]The paramagnetic materials can be classified as ferromagnetic or antiferromagnetic based on the amount of magnetically active ions they contain. An external magnetic field has a significant attraction on ferromagnetic materials. In the same direction as the applied magnetic field, the electron spins align (**Figure 1. 11**).

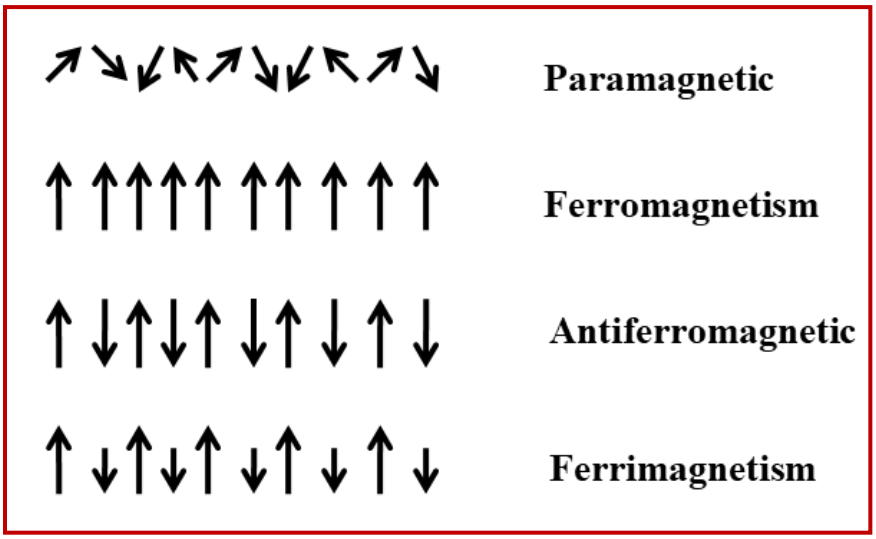

Figure 1. 11 Schematic illustration of various type of magnetism.[85]

We see a phenomenon known as hysteresis as a result of this feature long after the external magnetic field has been removed.[86] Permanent magnetization is possible for ferromagnetic materials. Magnetite Fe_3O_4 is the most prevalent example of a ferromagnetic material. Paramagnetic materials exhibit typical ferromagnetism all the way up to the Curie point (**Figure 1.12**).

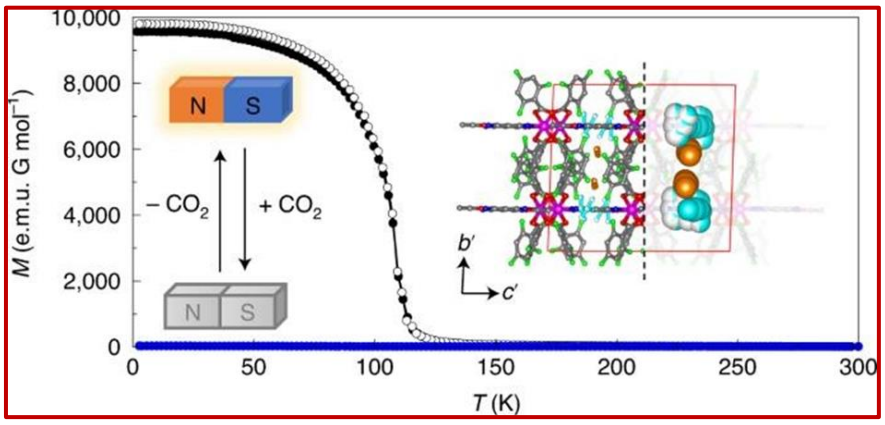

Figure 1.12 CO_2-induced transitions between paramagnetism and ferrimagnetism of a MOF material.[87]

The attraction of an external magnetic field is weak for paramagnetic materials. In paramagnetic materials containing metal ions whose spins are coupled up in the presence of an

external magnetic field, antiferromagnetism is also observed. Because of their diverse dimensional structural design and tuneable properties, coordination polymers and metal-organic frameworks are among the most significant magnetic materials for use in everyday life from a magnetic perspective.

1.4.8 Sensor Application

The use The development and reproduction of all living systems are governed by cations and anions, which have a role in the origin of civilization and continuation of life itself. A metal ion, non-biodegradable in nature, actively participates in the food chain and plays a potent pollutant in the ecological system. As a result, each metal has a certain safe zone limit. International organizations such as the World Health Organization (WHO) and the Environmental Protection Agency (EPA) assess the maximum contamination level of certain metals in different types of drinking water. The standard guidelines for heavy metals are recommended by the EPA and WHO (**Table 1.1**).[88-91]

Table 1.1 Threshold limit of biologically important/toxic metals in human body

Metal	WHO ppm	EPA ppm	Metal	WHO ppm	EPA ppm	Metal	WHO ppm	EPA ppm
Mn	0.4	-	Pd	$4x10^{-7}$	-	Hg	0.001	0.002
Zn	3	5	As	0.010	0.010	Al	0.9	-
Cr	0.05	-	Fe	1.0	-	Cu	2	1.3
Ni	0.07	0.04	Pb	0.010	0.015	Cd	0.003	-
V	0.05	-	Co	0.02	-	Mo	10-50	-

1.4.11 Advantages of Fluorescence Technique in Quantitative Analysis

Different analytical methods like volumetric, spectrophotometric, gravimetric and electrochemical techniques are used for quantitative analysis of ions and elements in the analytical field. Voltammetry,[92] ICPMS (inductively coupled plasma mass spectrometry),[96]

ICP-AES (inductively coupled plasma-atomic emission spectrometry),[94,95] AAS (flame or graphite furnace atomic absorption spectroscopy),[93] thin chitosan films,[98] flame atomic absorption spectroscopy (FAAS),[97] etc. methods are used for detection of ion/molecules.[99,100] In addition to this, fluorescence and UV-Visible spectroscopy are used to recognize the important analytes along with the cell imaging of analyte in biological system important of this technique is its low-level detection limit. low-level detection limit. Fluorescence technique is important for researcher in the biochemical and chemical science field due to their sensitivity, selective detection, quick response, operational simplicity, cost-effectiveness, and high temporal resolution and easy to signal detection.

1.4.12 Fluorescence sensing mechanism

The BCG Three basic requirements are receptor, transducer and signal processing unit for the ideal fluorescence sensing device; (i) receptor has strong binding affinity towards the target analytes and bind to the analytes selectively, (ii) Interference of local environment is neglected by the fluorescence signal and (iii) under this experimental process sample should be stable. Generally, 'Turn on' and 'Turn off' type fluorescence mechanism are observed. 'Turn on' process is mainly three types: (a) wavelength shift, (b) normal turn on and (c) ratio-metric turn on.

1.4.12.1 Paramagnetic fluorescence quenching

Another The term "paramagnetic quenching" refers to the addition of paramagnetic metal ions to fluorophore materials that facilitate forbidden inter-system crossover (ISC) quickly. The fluorophore is excited to the S1 state, and when paramagnetic metal ions are present, they travel from S1 to T1 via the ISC before being deactivated by a non-radiative mechanism. (**Figure 1.13**).[101]

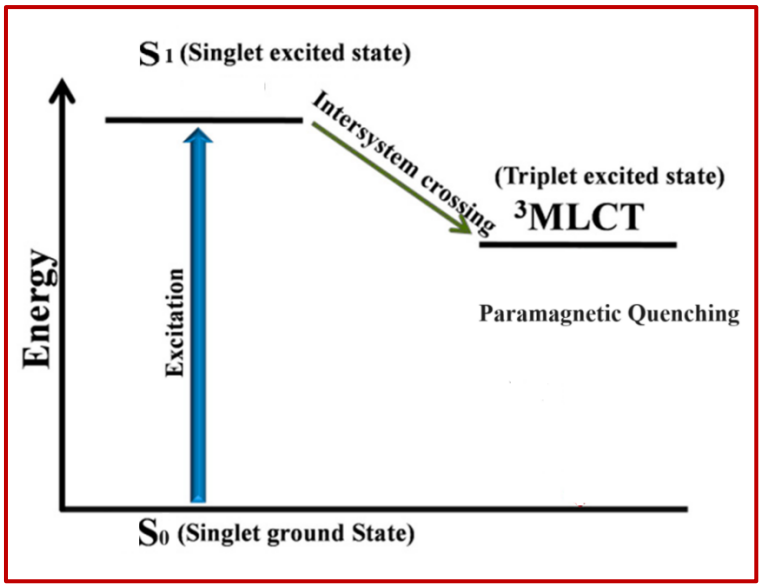

Figure 1.13 Schematic diagram shows binding of a paramagnetic ion (eg.Mn^{2+}) with fluorophore.

1.4.12.2 Photo-induced electron transfer (PET)

Typically, the PET involves the donation of electrons to the excited fluorophore's HOMO from the donor centers of N, O, S, and P. When the metal ions engage with the donor atoms and fluorescence turns on, the PET process is inhibited.

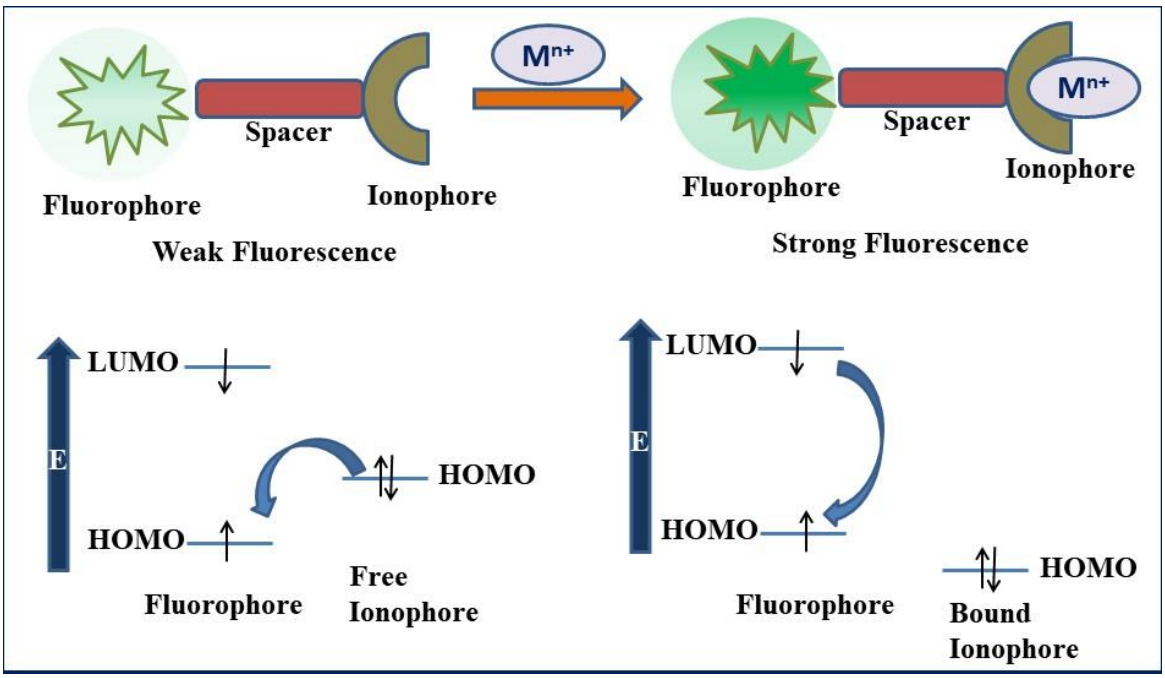

Figure 1.14 Schematic diagram for PET mechanisms.

Additionally, the polarity of the solvent affects the PET process. The polar solvent facilitates easier electron transport. The photo-induced electron transfer (PET) inhibition mechanism is the process by which the fluorescence sensor operates. The addition of metal ions inhibits PET and activates emission (**Figure 1.14**).[102]

1.4.12.3 Intra and intermolecular charge transfer (ICT)

The presence of light excitation increases intra- and intermolecular charge transfer from the electron donor center to the acceptor. Fluorophore and acceptor are directly coupled, generating an electron-rich system and electron-deficient terminals, without the need for a spacer (**Figure 1.15**).[103]

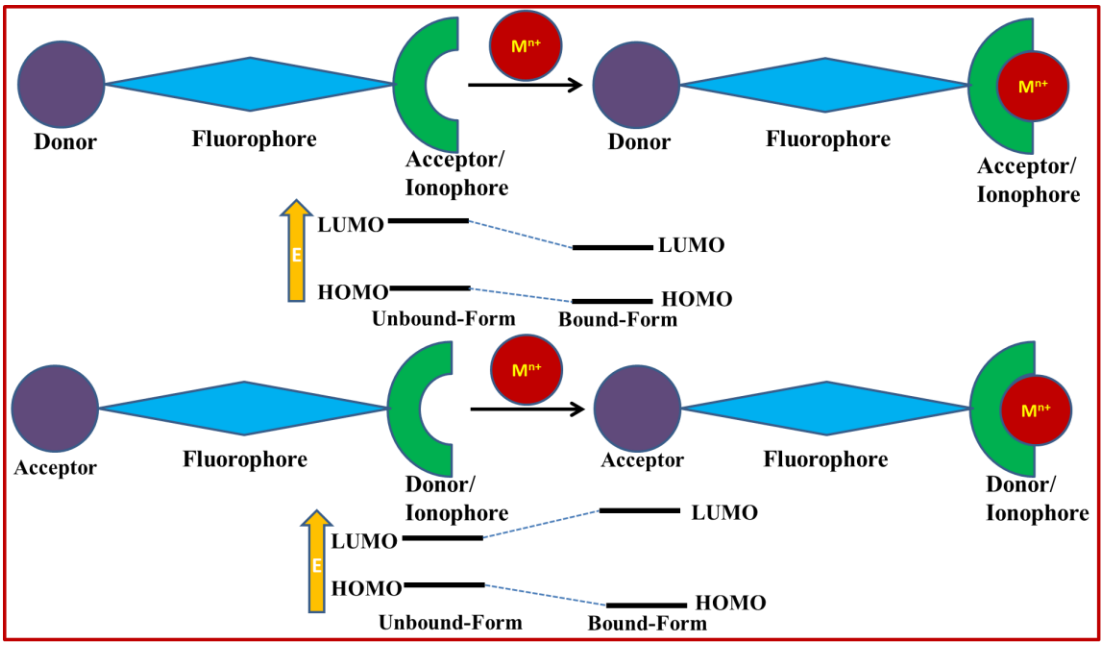

Figure 1.15 Schematic diagram of ICT mechanism.

1.4.12.4 Chelation enhanced fluorescence (CHEF) and Chelation enhanced quenching (CHEQ)

A metal ion binds with the receptor in a fluorescent probe, emission intensity is enhanced or quenched. Chelation enhanced fluorescence (CHEF) exhibits the red shift of emission band and blue shift was shown due to the chelation enhanced quenching (CHEQ). Forbidden intersystem crossing (ISC) was faster upon addition of the paramagnetic metal ions in the fluorophore and quenching process occurs. Upon excitation, the fluorophore moves from S1

state and presence of the paramagnetic metal ions goes S1 to T1 through the ISC and subsequently deactivated by non-radiative process (**Figure 1.16**).[104]

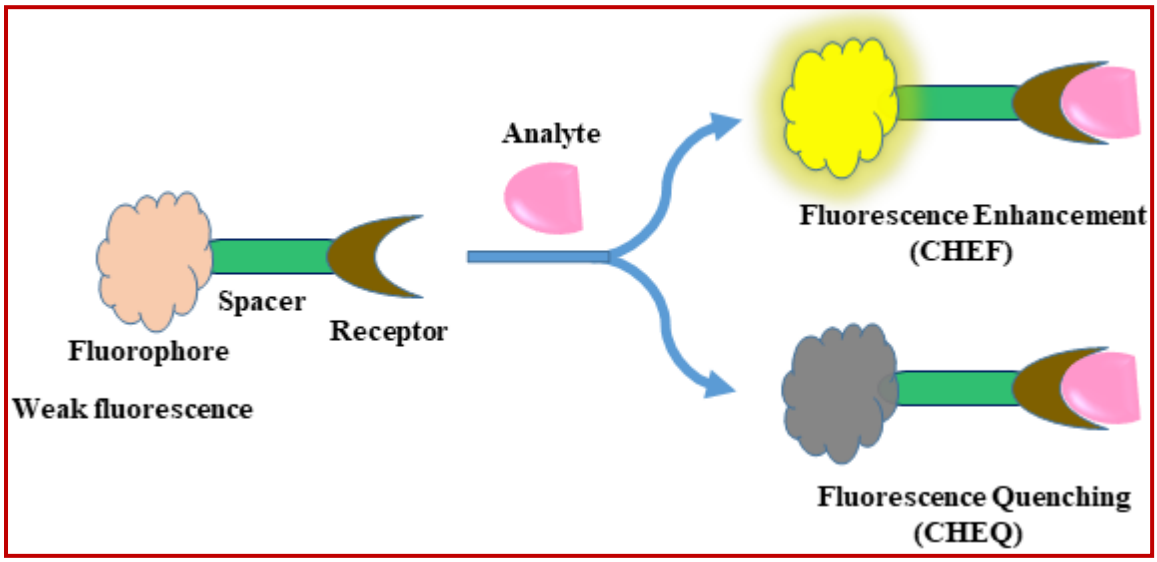

Figure 1.16 Schematic diagram of CHEF processes.

1.4.12.5 Excited-state intramolecular proton transfer (ESIPT)

ESIPT process is the process where the excited molecules relax their energy through the proton transfer in the excited state. Hydroxyl/amino group acts as a proton donor and acceptor group is containing nitrogen or oxygen atoms who are engaged by the intramolecular H-bonding mainly. During ESIPT process the excited molecule has less probability of the photochemical reaction and increase the photo stability of the molecule with a large specious stokes shift (**Figure 1.17**).[105]

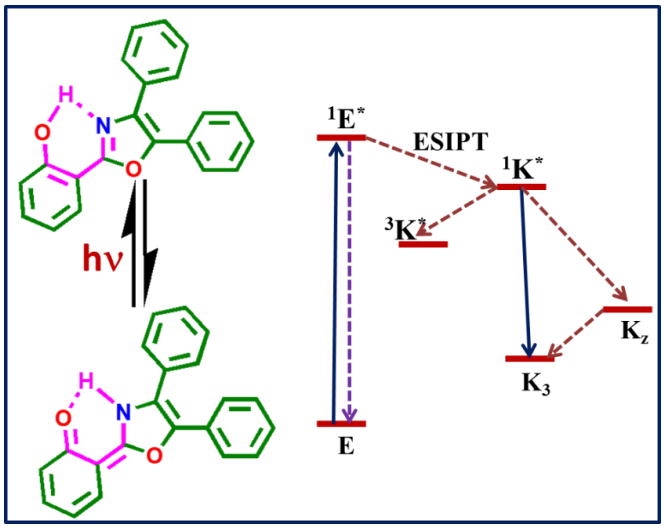

Figure 1.17 Schematic diagrams shows ESIP processes.

This process can be described as E*(S1) → K*(S1), and it involves a four-state photochemical pathway where the ground state is represented as enol (E) form, which, upon photoexcitation, undergoes tautomerization to keto (K) form. The pathway also passes through intramolecular hydrogen bonding with a five- or six-membered cyclic transition state. With the use of the reverse protons transfer (RPT) mechanism, it then quickly returns to its original enol form. Nonetheless, a comparable pathway from the excited keto (K*) form to the ground state keto (K) form is followed by radiative decay and the non-radiative ESIPT process. However, ESIPT moves more quickly than radiative decay. With a few exceptions, the keto tautomer (K) causes the ESIPT chromophores to glow since they are highly sensitive to their environment. The ESIPT process is inhibited by the solvents that donate hydrogen bonds and are polar.

1.4.12.6 Cation sensor

Out of naturally occurring elements about 1/3 (27 elements) are involved in the origination, sustenance and death of living cells. Metal ions are fundamental to life; some of the cations appear in bulk amount (Na, K, Mg, Ca) and some other present in trace amount (Cr, V, Mn, Co, Fe, Cu, Ni, Zn, Mo, Al, Si, Se, Sn). Any change in balance of concentration of the ions shows huge impact on the metabolic, electrical charge balance, neural signaling and muscular activities, osmotic pressure, photosynthesis, redox processes, DNA stability and activity, DNA transcription etc. Thus, they are essential in right concentration for the maintenance of life. Therefore, their quantitative measurement is of first truck information to the sustainability in the environment.

1.4.12.7 Pd^{2+} sensors

Pd is primarily utilized in catalysis for the synthesis of a wide range of important organic compounds, medicines, and polymers. Besides, it is used in the making of jewellery, watch making, electrical contact and surgery equipment etc. In the organic and organometallic complexes; it is used in different type of coupling reaction like Heck reaction, Suzuki coupling, Wacker oxidation process etc. Because of this, sensing of Pd is important in the field of fluorescence field. In 2015, S. Sanda et al. synthesized a Zn(II)-constructed coordination polymer for the sensing of Pd^{2+} ion.[106] Here, the CP exhibits blue emission and in presence of Pd^{2+} the emission is quenched. M. H. Mir et al. synthesized a 1D CP, $[Cd(4\text{-nvp})_2(5\text{-ssa})]$, (4-nvp = 4-(1-Naphthylvinyl)pyridine and 5-ssa = 5-Sulfosalicylic acid).[107]This 1D CP is selectively sensing of Pd^{2+} in aqueous medium. In the presence of the Pd^{2+} emission intensity

of the CP is decreased due to the incorporation of Pd^{2+} in the CP network. A. K. Adak et al. characterized Rhodamine-Appended Benzophenone Probe for the detection of Pd^{2+} by changing 'blue' colour of the probe to 'pink' emission in the UV-chamber.[108]Emission intensity of the probe is increased in presence of Pd^{2+} with a detection limit (LOD) 34 nM. B. Dutta et al. synthesized the $[Zn(cit)(4\text{-nvp})]_n$ coordination polymer for the sensing of Pd^{2+} in water, where 4-nvp = 4-(1-Naphthylvinyl)pyridine and H_2cit = citraconic acid. It exhibits the machano-chromism in the detection of Pd^{2+} ion.[109]

1.5 Biological Activity

Discoveries of new anticancer therapeutics have inspired researchers to use investigate metal-organic frameworks (MOFs),[110-111] which are a promising new class of for antibacterial and oncological treatments.[112] Manganese and zinc MOFs have attracted a lot of interest among them because of their special physicochemical characteristics, which include high porosity, adjustable surface chemistry, and the capacity to successfully encapsulate and transport medically active molecules. (**Figure 1.18**)

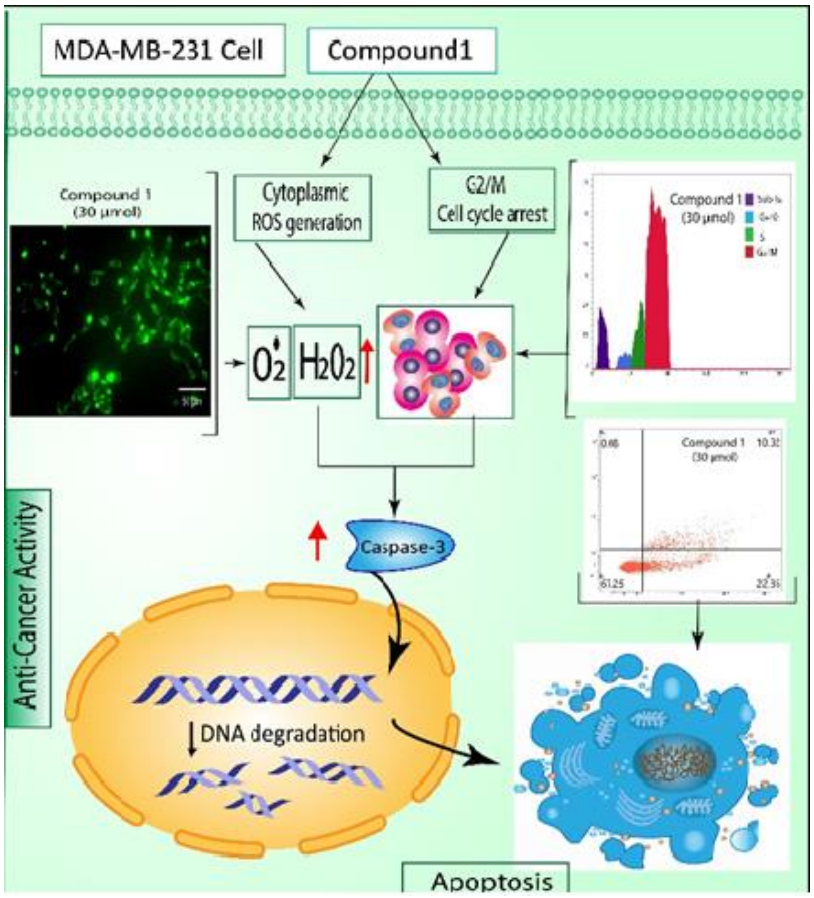

Figure 1.18 Schematic diagrams shows various biological activity.

Extensive variety of cancer cell lines were used in the study including MDA-MB-231 (triple-negative breast cancer), MCF-7 (estrogen receptor-positive breast cancer), PC-3 (prostate cancer), HeLa (cervical cancer), and A549 (lung cancer), to confirm the anticancer qualities of Mn-MOF and Zn-MOF.[113-116] These cell lines were selected in order to provide a comprehensive assessment of the MOFs' effectiveness across a range of cancer types, owing to their unique genetic and phenotypic features. Furthermore, normal cell lines were used to evaluate the MOFs' selectivity and cytotoxicity towards non-cancerous cells for good comparisons. These cell lines were NKE (normal kidney epithelial cells) and WI-38 (normal human lung fibroblasts).

The MTT assay (3-(4, 5-dimethylthiazolyl-2)-2, 5-diphenyltetrazolium bromide), a colorimetric test that evaluates cell metabolic activity as a sign of cell viability, proliferation, and cytotoxicity, was used in the first stage of experimental analysis.[117-118] The half-maximal inhibitory concentration (IC_{50}) values for the MOFs across the chosen cancer cell lines were made easier to determine the quantity of cancer drugs. Determination of the IC_{50} values was essential in order to determine the MOFs' effective dosages that inhibit 50% of cell viability.

Different other experiments were designed such as V-FITC apoptosis studies, ROS analysis and CASPASE-3 activation experiments to explain the plausible mechanism of action of the drug on cancer cells. Ongoing discussion explores the importance and research gap of the use of MOF in tackling many issues of the life and society. This is encouraged to select our problem to be investigated.

1.6 Aim and Scope of the Dissertation

Above discussion reveals the social importance and scientific background of the studies on the CPs/MOFs. Design and synthesis of the material also a part of intricate chemical research and also exploration of their versatile application towards Sustainable Development Goals (SDGs) which is an inbuilt objective of the material research. We have gone through literature in depth and have found the research gap that belongs to the design of energy saving material and also biomaterial to control microbial diseases and cancer. In this thesis we have chosen transition metal ions, Mn(II) (d^5) and Zn(II) (d^{10}) those have symmetric d-electronic configuration.[119] This research focuses on the synthesis, spectroscopic and structural characterisation and applications of Mn(d^5) and Zn(d^{10})-based CPs/MOFs using bridging ligands such as 2,5-thiophene dicarboxylic acid, Pyridine-4-carboxaldehyde isonicotinoyl hydrazine, Mesaconic

acid, 5-aminoisophthalic acid and 4-(1-Naphthylvinyl)pyridine (**Figure 1.19**). These ligands will bridge metal ions to form CPs/MOFs. The materials are synthesised by layering technique and have been characterised by all possible spectroscopic techniques and are discussed in subsequent chapters (**Chapters 2-6**).

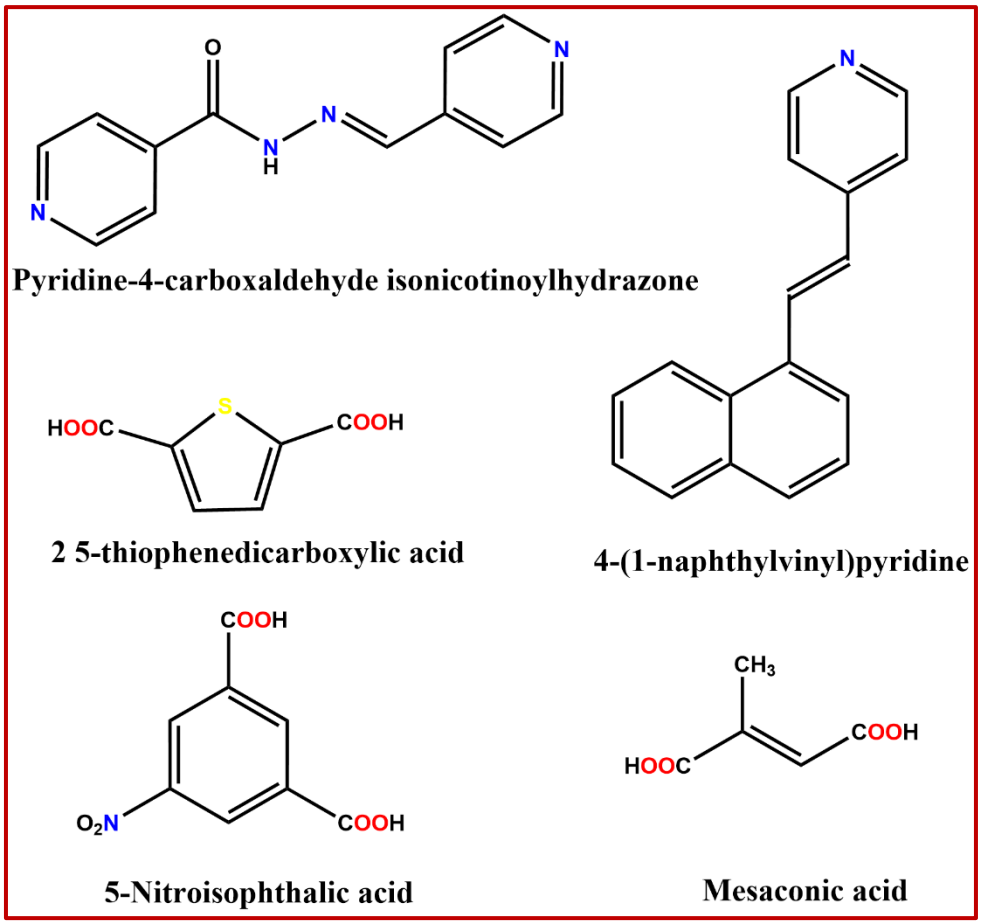

Figure 1.19 Representative examples of bridging ligands used in the synthesis of CPs/MOFs.

1.7 Physical Measurements

(i) ***FT-IR spectra***: Infrared (IR) spectrum (400–4000 cm^{-1}) was recorded using a Perkin Elmer SPECTRUM II LITA FT-IR spectrometer.

(ii) ***UV-vis spectra***: The UV-Vis absorbance spectral studies were carried out on a PerkinElmer Lambda 25 spectrophotometer using a 1 cm path length quartz cuvette in the wavelength range of 190-900 nm.

(iii) ***Single crystal X-ray diffractometer (SCXRD):*** Single Crystal X-ray diffractometer made by Bruker and model SMART APEX III outfitted with graphite-monochromatic MoKα radiation (λ = 0.71073 Å) was utilised to collect data on a single crystal of compound.

(iv) ***Powder X-Ray Diffraction (PXRD):*** Powder X-ray diffraction (PXRD) measurements were performed at room temperature with a PANalytical diffractometer equipped with a Cu micro focal tube (λ = 1.54178 Å) at 40 kV and 40 mA.

(v) ***Thermogravimetric analysis (TGA):*** Thermo gravimetric analysis (TGA) was carried out on a PerkinElmer Pyris Diamond TG/DTA thermal analyser under nitrogen atmosphere (flow rate: 50 cm^3 min^{-1}) at the temperature range of 30−800 °C with a heating rate of 2 °C/min.

(vi) ***Fluorescence spectra***: Steady-state fluorescence measurements were performed with a PTI QM-40 spectrofluorometer by using a fluorescence free quartz cuvette of 1 cm path length.

(vii) ***Lifetimes measurements****:* Fluorescence lifetimes were determined from time-resolved intensity decay by the method of time correlated single photon counting (TCSPC) measurements using a picosecond diode laser (IBH Nanoled-07) in an IBH fluorocube apparatus. The fluorescence decay data were collected on a Hamamatsu MCP photomultiplier (R3809) and examined by the IBH DAS6 software.

(viii) ***Field emission scanning electron microscopy (FESEM) analysis****:* The surface morphology of compound was observed via a scanning electron microscopy (FESEM: FEI QUANTA FEG 250).

(ix) ***Cell imaging***: Cell imaging studies have been performed under fluorescence microscope. Bright field and fluorescence images of the CHO and KB cells were taken using a fluorescence microscope (Olympus, model IX-81) with an objective lens of 40x, 20x magnification.

(x) ***pH study:*** The pH of the solutions was recorded using a Systronics digital pH meter(Model 335, India) with the pH range 2–12. The pH meter was calibrated using standard buffer solutions (Acros Organics) of pH 4.0, 7.0 and 10.0.

(xi) ***DFT Computational Study:*** Optimization of the gas phase geometry of the compound was carried out using Density Functional Theory (DFT) calculation of Gaussian Program Package 09.

(xii) ***Fluorescence Microscope:*** The coverslips carrying the stained cells were then mounted onto slides, and nuclear morphology was observed under a fluorescence microscope (Leica).

(xiii) ***BD FACS:*** Data were acquired using the BD FACS Verse flow cytometer (BD Biosciences, San Jose, CA).

1.8 References

(1) Kitagawa, S. Metal–organic frameworks (MOFs). *Chem. Soc. Rev.* **2014,** *43*, 5415-5418.

(2) Furukawa, H.; Cordova, K. E.; O'Keeffe, M. and Yaghi, O. M. The chemistry and applications of metal-organic frameworks. *Science.* **2013**, *341*, 1230444.

(3) Li, H.; Eddaoudi, M.; O'Keeffe, M. and Yaghi, O. M. Design and synthesis of an exceptionally stable and highly porous metal-organic framework. *Nature*. **1999**, *402*, 276-279.

(4) Dmitriev, A.; Spillmann, H.; Lin, N.; Barth, J. V. and Kern, K. Modular assembly of two-dimensional metal–organic coordination networks at a metal surface. *Angew. Chem. Int. Ed.* **2003**, *42*, 2670-2673.

(5) Cao, L.; Lin, Z.; Peng, F.; Wang, W.; Huang, R.; Wang, C.; Yan, J.; Liang, J.; Zhang, Z.; Zhang, T. and Long, L. Self-supporting metal–organic layers as single-site solid catalysts. *Angew. Chem. Int. Ed.* **2016**, *55*, 4962-4966.

(6) Perry Iv, J. J.; Perman, J. A. and Zaworotko, M. J. Design and synthesis of metal–organic frameworks using metal–organic polyhedra as supermolecular building blocks. *Chem. Soc. Rev.* **2009**, *38*, 1400-1417.

(7) Sakamoto, R.; Fukui, N.; Maeda, H.; Toyoda, R.; Takaishi, S.; Tanabe, T.; Komeda, J.; Amo-Ochoa, P.; Zamora, F. and Nishihara, H. Layered metal-organic frameworks and metal-organic nanosheets as functional materials. *Coord. Chem. Rev.* **2022**, *472*, 214787.

(8) Du, Q.; Peng, J.; Wu, P. and He, H. Metal-organic framework based crystalline sponge method for structure analysis. *TrAC. Trends Anal. Chem.* **2018**, *102*, 290-310.

(9) Mendes, F. R and Paz, A. F. Transforming metal–organic frameworks into functional materials. *Inorg. Chem. Front*. **2015**, *2*, 495-509.

(10) Kitagawa, S.; Kitaura, R. and Noro, S.I. Functional porous coordination polymers. *Angew. Chem. Int. Ed.* **2004**, *43*, 2334-2375.

(11) Chen, L. and Hong, M.C. eds. Design and construction of coordination polymers. John Wiley &Sons., 2009.

(12) Alhamami, M.; Doan, H. and Cheng, C. H. A review on breathing behaviors of metal-organic-frameworks (MOFs) for gas adsorption. *Materials*. **2014**, *7*, 3198-3250.

(13) Zhu, L.; Liu, X. Q.; Jiang, H. L. and Sun, L. B. Metal–organic frameworks for heterogeneous basic catalysis. *Chem. Rev.* **2017**, *117*, 8129-8176.

(14) Li, C.; Zhang, L.; Chen, J.; Li, X.; Sun, J.; Zhu, J.; Wang, X. and Fu, Y. Recent development and applications of electrical conductive MOFs. *Nanoscale*. **2021**, *13*, 485-509.

(15) Stavila, V.; Talin, A. A. and Allendorf, M. D. MOF-based electronic and opto-electronic devices. *Chem. Soc. Rev.* **2014**, *43*, 5994-6010.

(16) Liu, Y.; Xie, X. Y.; Cheng, C.; Shao, Z. S. and Wang, H.S. Strategies to fabricate metal–organic framework (MOF)-based luminescent sensing platforms. *J. Mater. Chem. C*. **2019**, *7*, 10743-10763.

(17) Zhang, L. P.; Ma, J. F.; Yang, J.; Liu, Y. Y. and Wei, G. H. 1D, 2D, and 3D metal−organic frameworks based on bis (imidazole) ligands and polycarboxylates: syntheses, structures, and photoluminescent properties. *Cryst. Growth. Des.* **2009**, *9*, 4660-4673.

(18) Uemura, K. and Takamori, A. Recent studies on the magnetic properties of paramagnetic metals linked by diamagnetic second metals. *Coord. Chem. Rev.* **2022**, *471*, 214736.

(19) Umemura, A.; Diring, S.; Furukawa, S.; Uehara, H.; Tsuruoka, T. and Kitagawa, S. Morphology design of porous coordination polymer crystals by coordination modulation. *J. Phys. Org. Chem.* **2011**, *133*, 15506-15513.

(20) Eddaoudi, M.; Moler, D. B.; Li, H. L.; Chen, B. L.; Reineke, T. M.; O'Keeffe, M.; Yaghi, O. M. Modular Chemistry: SecondaryBuildingUnits as a Basis forthe Design of Highly Porous and Robust Metal−Organic Carboxylate Frameworks. *Acc. Chem. Res.* **2001**, *34*, 319–330.

(21) Biradha, K.; Ramanan, A.; Vittal, J. J. Coordination polymers versus metal-organic frameworks. *Cryst. Growth Des.* **2009**, *9*, 2969-2970.

(22) Bailar jr, J. C. Coordination Chemistry. *Prep, Inorg. React*. **1964**, *1*, 1–27.

(23) Ha, J.; Lee, J. H. and Moon, H. R. Alterations to secondary building units of metal–organic frameworks for the development of new functions. *Inorg. Chem. Front*. **2020**, *7*, 12-27.

(24) Halder, P.; Prerna and Singh, J. K. Building unit extractor for metal–organic frameworks. *J. Chem. Inf. Model*. **2021**, *61*, 5827-5840.

(25) Eddaoudi, M.; Moler, D. B.; Li, H.; Chen, B.; Reineke, T. M.; O'keeffe, M. and Yaghi, O.M. Modular chemistry: secondary building units as a basis for the design of highly porous and robust metal− organic carboxylate frameworks. *Acc. Chem. Res*. **2001**, *34*, 319-330.

(26) Qin, J. S.; Yuan, S.; Wang, Q.; Alsalme, A. and Zhou, H. C. Mixed-linker strategy for the construction of multifunctional metal–organic frameworks. *J. Mater. Chem. A.* **2017**, 5, 4280-4291.

(27) Haldar, R. and Maji, T. K. Metal–organic frameworks (MOFs) based on mixed linker systems: structural diversities towards functional materials. *CrystEngComm.* **2013**, *15*, 9276-9295.

(28) Sun, L.; Campbell, M. G.; Dincă, M. Electrically Conductive Porous Metal-Organic Frameworks. *Angew. Chem., Int. Ed.* **2016**, *55*, 3566.

(29) Danaci, D.; Bui, M.; Mac Dowell, N.; Petit. C. Exploring the limits of adsorption-based CO_2 capture using MOFs with PVSA - from molecular design to process economics. *Mol. Syst. Des. Eng.* **2020**, *5*, 212-231.

(30) Wang, S.; Wang, Q.; Feng, X.; Wang, B. and Yang, L. Explosives in the cage: metal–organic frameworks for high-energy materials sensing and desensitization. *Adv. Mater.* **2017**, *29*, 1701898.

(31) Zhang, L.; Zou, C.; Zhao, M.; Jiang, K.; Lin, R.; He, Y.; Wu, C.-D.; Cui, Y.; Chen, B.; Qian. G. Doubly Interpenetrated Metal-Organic Framework for Highly Selective C_2H_2/CH_4 and C_2H_2/CO_2 Separation at Room Temperature. *Cryst. Growth Des*. **2016**, *16*, 7194–7197.

(32) He, H.; Collins, D.; Dai, F.; Zhao, X.; Zhang, G.; Ma, H. and Sun, D. Construction of metal− organic frameworks with 1D chain, 2D grid, and 3D porous framework based

on a flexible imidazole ligand and rigid benzenedicarboxylates. *Cryst. Growth. Des.* **2010,** *10*, 895-902.

(33) Burtch, N.C.; Heinen, J.; Bennett, T. D.; Dubbeldam, D. and Allendorf, M. D. Mechanical properties in metal–organic frameworks: emerging opportunities and challenges for device functionality and technological applications. *Adv. Mater.* **2018**, *30*, 1704124.

(34) Li, H.; Eddaoudi, M.; O'Keeffe, M.; Yaghi, O. M. Design and synthesis of an exceptionally stable and highly porous metal-organic framework. *Nature*. **1999**, *402*,276.

(35) Kitagawa, S.; Matsuda, R. Chemistry of coordination space of porous coordination polymers. *Coord. Chem. Rev***. 2007**, *251*,2490.

(36) Kitagawa, S. and Uemura, K. Dynamic porous properties of coordination polymers inspired by hydrogen bonds. *Chem. Soc. Rev*. **2005**, *34*,109.

(37) Ghosh, S. K.; Zhang, J. P.; Kitagawa, S. Reversible topochemical transformation of a soft crystal of a coordination polymer. *Angew. Chem., Int. Ed*. **2007**, *46*, 7965.

(38) Cheng, X.; Guo, L.; Wang, H.; Gu, J.; Yang, Y.; Kirillova, M.V. and Kirillov, A. M. Coordination Polymers from Biphenyl-Dicarboxylate Linkers: Synthesis, Structural Diversity, Interpenetration, and Catalytic Properties. *Inorg. Chem.* **2022**, *61*, 12577-12590.

(39) Kaur, H.; Devi, N.; Siwal, S. S.; Alsanie, W. F.; Thakur, M. K. and Thakur, V. K. Metal–organic framework-based materials for wastewater treatment: superior adsorbent materials for the removal of hazardous pollutants. *ACS omega*. **2023**, *8*, 9004-9030.

(40) Seo, J.; Matsuda, R.; Sakamoto, H.; Bonneau, C.; Kitagawa, S. A Pillared-Layer Coordination Polymer with a Rotatable Pillar Acting as a Molecular Gate for Guest Molecules. *J. Am. Chem. Soc*. **2009**, *131*, 12792.

(41) Masoomi, M. Y.; Morsali, A.; Dhakshinamoorthy, A. and Garcia, H. Mixed-metal MOFs: unique opportunities in metal–organic framework (MOF) functionality and design. *Angew. Chem.* **2019**, *131*, 15330-15347.

(42) García, E. J.; Bahamon, D. and Vega, L. F. Systematic search of suitable metal–organic frameworks for thermal energy-storage applications with low global warming potential refrigerants. *ACS Sustain Chem Eng*. **2021**, *9*, 3157-3171.

(43) Chen. Z, Kirlikovali. KO, Li. P, Farha. OK. Reticular chemistry for highly porous metal–organic frameworks: The chemistry and applications. *Acc. Chem. Res.* **2022**, 3, 4579-91.

(44) Jiang, H. L. and Xu, Q. Porous metal–organic frameworks as platforms for functional applications. *Chem.Comm.* **2011**, 47, 3351-3370.

(45) Pepinsky, R. Crystal Engineering-New Conceptin Crystallography, *Phys. Rev.* **1955**, *100*, 971.

(46) Schmidt, G. M. Photodimerization in the solid state. *Pure Appl. Chem.* **1971**, *27*,647.

(47) Batten, S. R.; Champness, N. R.; Chen, X. M.; Garcia-Martinez, J.; Kitagawa, S.; Öhrström, L.; O'Keeffe, M.; Suh, M. P.; Reedijk, J.; *Pure Appl. Chem.* **2013**, *85*, 1715-1724.

(48) Ma, N. and Horike, S. Metal–organic network-forming glasses. *Chem. Rev.* **2022**, *122*, 4163-4203.

(49) Kinoshita, Y.; Matsubara, I.; Higuchi, T. and Saito, Y. *Bull. Chem. Soc. Jpn.* **1959**, *32*, 1221-1226.

(50) Ding, M.; Cai, X. and Jiang, H. L. Improving MOF stability: approaches and applications. *Chem. Sci.* **2019**, *10*, 10209-10230.

(51) Hoskins, B.F. and Robson, R. Infinite polymeric frameworks consisting of three dimensionally linked rod-like segments. *J. Am. Chem. Soc.* **1989**, *111*, 5962-5964.

(52) Kitagawa, S.; Munakata, M. and Tanimura, T. Synthesis of the novel infinite-sheet and-chain copper (I) complex polymers {[Cu ($C_4H_4N_2$)3/2 (CH_3CN)](PF_6). cntdot. 0.5 C_3H_6O}. infin. and {[$Cu_2(C_8H_{12}N_2)_3$](ClO_4)$_2$}. infin. and their x-ray crystal structures. *Inorg. Chem.* **1992**, *31*, 1714-1717.

(53) Yaghi, O.M. and Li, H., Hydrothermal synthesis of a metal-organic framework containing large rectangular channels. *J. Am. Chem. Soc.* **1995**, *117*, 10401-10402.

(54) Kitagawa, S. Future porous materials. *Acc. Chem. Res.* **2017**, *50*, 514-516.

(55) Li, H.; Eddaoudi, M.; Groy, T. L. and Yaghi, O. M. Establishing microporosity in open metal− organic frameworks: gas sorption isotherms for Zn (BDC)(BDC= 1, 4-benzenedicarboxylate). *J. Am. Chem. Soc.* **1998**, *120*, 8571-8572.

(56) Horike, S.; Shimomura, S. and Kitagawa, S. Soft porous crystals. *Nat. chem.* **2009**, *1*, 695-704.

(57) Horike, S.; Nagarkar, S. S.; Ogawa, T. and Kitagawa, S. A new dimension for coordination polymers and metal–organic frameworks: towards functional glasses and liquids. *Angew. Chem. Int. Ed.* **2020**, *59*, 6652-6664.

(58) Desiraju, G. R. Crystal Engineering: The design of Organic Solids, Elsevier, Amsterdam, The Netherlands, 1989.

(59) Desiraju, G. R. Crystal Engineering: From Molecule to Crystal. *J. Am. Chem. Soc.* **2013**, *135*, 9952.

(60) Nangia, A. Supramolecular chemistry and crystal engineering. *J. Chem. Sci*. **2010**, *122*, 295-310.

(61) (a) G. R. Desiraju, Crystal Engineering. The Design of Organic Solids; Elsevier: Amsterdam, **1989**.

(62) Desiraju, G. R.; Vittal, J. J.; Ramanan, A. Crystal Engineering: A Text Book, World Scientific: Singapore, **2011**.

(63) Corpinot, M.K. and Bucar, D. K. A practical guide to the design of molecular crystals. *Cryst. Growth Des*. **2018**, *19*, 1426-1453.

(64) McGrath, D. T. Downing, V.A. and Katz, M. J. Investigating the crystal engineering of the pillared paddlewheel metal–organic framework $Zn_2(NH_2BDC)_2DABCO$. *CrystEngComm.* **2018**, *20*, 6082-6087.

(65) Lin, N. and Liu, X. Y. Correlation between hierarchical structure of crystal networks and macroscopic performance of mesoscopic soft materials and engineering principles. *Chem. Soc. Rev*. **2015**, *44*, 7881-7915.

(66) Steed, J. W.; Atwood, J. L., Supramolecular Chemistry. Wiley: Chichester,2000.

(67) Schmeck, Harold M. Jr. "Chemistry and Physics Nobels Hail Discoveries on Life and Superconductors; Three Share Prize for Synthesis of Vital Enzymes". New York Times, 1987.

(68) Corpinot, M. K. and Bucar, D. K. A practical guide to the design of molecular crystals. *Cryst. Growth. Des.* **2018**, *19*, 1426-1453.

(69) Greer, J.; Erickson, J. W.; Baldwin, J. J. and Varney, M. D. Application of the three-dimensional structures of protein target molecules in structure-based drug design. *J. Med. Chem.***1994**, *37*, 1035-1054.

(70) Lin, N. and Liu, X. Y. Correlation between hierarchical structure of crystal networks and macroscopic performance of mesoscopic soft materials and engineering principles. *Chem. Soc. Rev.* **2015**, *44*, 7881-7915.

(71) Kaur, H.; Devi, N.; Siwal, S. S.; Alsanie, W. F.; Thakur, M. K. and Thakur, V. K. Metal–organic framework-based materials for wastewater treatment: superior adsorbent materials for the removal of hazardous pollutants. *ACS omega*. **2023**, *8*, 9004-9030.

(72) Ma, Z.; Guan, B.; Guo, J.; Wu, X.; Chen, Y.; Zhang, J.; Jiang, X.; Bao, S.; Chen, L.; Shu, K. and Dang, H. State of the art and prospectives of heterogeneous photocatalysts based on metal–organic frameworks (MOFs): design, modification strategies, and their applications and mechanisms in photodegradation, water splitting, and CO 2 reduction. *Catal. Sci. Techno.* **2023**, *13*, 4285-4347.

(73) Dutta, B.; Das, D.; Datta , J.; Chandra, A.; Jana, S.; Sinha, C.; Ray , P. P.; Mir, M. H. Synthesis of a Zn(II)-based 1D zigzag coordination polymer for the fabrication of optoelectronic devices with remarkably high photosensitivity. *Inorg. Chem. Front.* **2019**, *6*, 1245-1252.

(74) Koralkar, N.; Mehta, S.; Upadhyay, A.; Patel, G. and Deshmukh, K. MOF-Based nanoarchitectonics for Lithium-ion batteries: a Comprehensive Review. *J. Inorg. Organomet. Polym. Mater.* **2024**, *34*, 903-929.

(75) Dutta, B.; Dey, A.; Maity, S.; Sinha, C.; Ray, P. P. and Mir, M. H. Supramolecular Assembly of a Zn (II)-Based 1D Coordination Polymer through Hydrogen Bonding and

π··· π Interactions: Crystal Structure and Device Applications. *ACS omega*. **2018**, *3*, 12060-12067.

(76) Xu, G.; Nie, P.; Dou, H.; Ding, B.; Li, L. and Zhang, X. Exploring metal organic frameworks for energy storage in batteries and supercapacitors. *Mater. Today*. **2017**, *20*, 191-209.

(77) Dutta, B.; Dey, A.; Sinha, C.; Ray, P. P.; Mir, M. H. Photochemical Structural Transformation of a Linear 1D Coordination Polymer Impacts the Electrical Conductivity. *Inorg. Chem.***2018**, *57*,8029−8032.

(78) Naskar, K.; Maity, S.; Jana, S.; Dutta, B.; Tanaka, S.; Mallick, D.; Akitsu, T.; Sinha, C. Arylazoimidazole Coordinated and Naphthalene-Dicarboxylato Bridged Polymers of Co(II) and Photochromic Zn(II) Complexes. *Cryst. Growth. Des*. **2018**, *18*, 2986–2997.

(79) Dutta, B.; Jana, R.; Sinha, C.; Ray, P. P.; Mir, M. H. Synthesis of a Cd(II) based 1D coordination polymer by in situ ligand generation and fabrication of a photosensitive electronic device. *Inorg. Chem. Front.***2018**, *5*,1998-2005.

(80) Mönch, W. Metal-semiconductor contacts: electronic properties. *Surf. Sci*. **1994**,*299*, 928-944.

(81) Gomes, W. P. and Cardon, F. Electron energy levels in semiconductor electrochemistry. *Prog. Surf. Sci*.**1982**, *12*, 155-215.

(82) Sahoo, T. and Kale, P. Work function-based metal–oxide–semiconductor hydrogen sensor and its functionality: A review. *Adv. Mater. Interfaces*. **2021**, 8, 2100649.

(83) Halder, S.; Dey, A.; Bhattacharjee, A.; Ortega-Castro, J.; Frontera, A.; Ray, P. P. and Roy, P. A Cd (II)-based MOF as a photosensitive Schottky diode: experimental and theoretical studies. *Dalton Trans.* **2017**, *46*, 11239-11249.

(84) Wang, W.; Yan, L. Q.; Cong, J. Z.; Zhao, Y. L.; Wang, F.; Shen, S. P.; Zou, T.; Zhang, D.; Wang, S. G.; Han, X. F. and Sun, Y. Magnetoelectric coupling in the paramagnetic state of a metal-organic framework. *ScI. Rep.* **2013**, *3*, 2024.

(85) Thorarinsdottir, A. E. and Harris, T. D. Metal–organic framework magnets. *Chem. Rev.* **2020**, *120*, 8716-8789.

(86) Park, J. G.; Collins, B. A.; Darago, L. E.; Runčevski, T.; Ziebel, M. E.; Aubrey, M. L.; Jiang, H. Z.; Velasquez, E.; Green, M. A.; Goodpaster, J. D. and Long, J. R.; Magnetic ordering through itinerant ferromagnetism in a metal–organic framework. *Nat. chem.* **2021**, *13*, 594-598.

(87) Zhang, J.; Kosaka, W.; Kitagawa, Y.; Miyasaka, H. A metal–organic framework that exhibits CO_2-induced transitions between paramagnetism and ferrimagnetism. *Nature.* **2021**, *13*, 191–199.

(88) Sorenson, J. R. J.; Campbell, I. R.; Tepper, L. B. and Lingg, R. D. Aluminum in the Environment and Human Health, Environ. *Health Perspect*. **1974**, *8*, 3–95.

(89) Baral, M.; Sahoo, S. K. and Kanungo, B. K. Tripodal amine catechol ligands: A fascinating class of chelators for aluminium(III), *J. Inorg. Biochem*. **2008**, *102*, 1581–1588.

(90) Gupta, V. K.; Jain, A. K. and Maheshwari, G. Aluminum(III) selective potentiometric sensor based on morin in poly(vinyl chloride) matrix, *Talanta*, **2007**, *72*, 1469–1473.

(91) Berg, C. M. G. Chemical Speciation of Iron in Seawater by Cathodic Stripping Voltammetry with Dihydroxynaphthalene, *Anal. Chem*. **2006**, *78*, 156–163.

(92) Cerchiaro, G.; Manieri, T. M. and Bertuchi, F. R. Analytical methods for copper, zinc and iron quantification in mammalian cells, *Metallomics*. **2013**, *5*, 1336-1345.

(93) Pomazal, K.; Prohaska, C.; Steffan, I.; Reich, G. and Huber, J. F. K. Determination of Cu, Fe, Mn, and Zn in blood fractions by SEC-HPLC-ICP-AES coupling, *Analyst.* **1999**, *124*, 657–663.

(94) Vanloot, P.; Coulomb, B.; Brach-Papa, C.; Sergent, M. and Boudenne, J. L. Multivariate optimization of solid-phase extraction applied to iron determination in finished waters, *Chemosphere*. **2007**, *69*, 1351–1360.

(95) Ammann, A. A. Inductively coupled plasma mass spectrometry (ICP MS): a versatile tool, *J. Mass Spectrom*. **2007**, *42*, 419-427.

(96) Shamspur, T.; Sheikhshoaie, I. and Mashhadizadeh, M. H. Flame atomic absorption spectroscopy (FAAS) determination of iron(III) after preconcentration on to modified analcime zeolite with 5-((4-nitrophenylazo)-N-(2′,4′-

dimethoxyphenyl))salicylaldimine by column method, J. Anal. At. *Spectrom*. **2005**, *20*, 476–478.

(97) McIlwee, H. A.; Schauer, C. L.; Praig, V. G.; Boukherroub, R. and Szunerits, S. Thin chitosan films as a platform for SPR sensing of ferric ions, *Analyst.* **2008**, *133*, 673–677.

(98) Mehta, V. N.; Kailasa, S. K.; Wu, H.-F. Sensitive and Selective Colorimetric Sensing of Fe^{3+} Ion by Using P-Amino Salicylic Acid Dithiocarbamate Functionalized Gold Nanoparticles. *New J. Chem*. **2014**, *38*, 1503–1511.

(99) Yin, Z.-Z.; Li, Y.; Jiang, L.-P.; Rana, R. K.; Zhu, J.-J. Synthesis and Electrocatalytic Activity of Haemin-Functionalised Iron (II, III) Oxide Nanoparticles. *Anal. Chim. Acta*.**2013**, *781*, 48–53

(100) Chang, J. H.; Choe, Y. M.; Sin, Y. G. A Significant Fluorescence Quenching of Anthryl amino benzo crown Ethers by Paramagnetic Metal Cations. *Bull. Korean Chem. Soc*.**2001**, *22*, 527–530.

(101) Xu, Z.; Xiao, Y.; Qian, X.; Cui, J.; Cui, D. Ratiometric and Selective Fluorescent Sensor for CuII Based on Internal Charge Transfer (ICT). *Org. Lett*.**2005**, *7*, 889–892.

(102) Serin, J. M.; Brousmiche, D. W.; Fréchet, J. M. J. A FRET-Based Ultraviolet to Near-Infrared Frequency Converter. *J. Am. Chem. Soc*.**2002**, *124*, 11848–11849.

(103) Zhao, J.; Ji, S.; Chen, Y.; Guo, H.; Yang, P. Excited State Intramolecular Proton Transfer (ESIPT): From Principal Photophysics to the Development of New Chromophores and Applications in Fluorescent Molecular Probes and Luminescent Materials. *Phys. Chem. Chem. Phys*.**2012**, *14*, 8803–8817.

(104) Sanda, S.; Parshamoni, S.; Biswas, S. and Konar, S., Highly selective detection of palladium and picric acid by a luminescent MOF: a dual functional fluorescent sensor. *Chem. Comm*.**2015**, *51*, 6576-6579.

(105) Adak, A. K.; Purkait, R.; Manna, S. K.; Ghosh, B. C.; Pathak, S. and Sinha, C. Fluorescence sensing and intracellular imaging of Pd^{2+} ions by a novel coumarinyl-rhodamine Schiff base. *New J. Chem*. **2019**, *43*, 3899-3906.

(106) Mir, M. H.; Bera, S.; Khan, S.; Maity, S.; Sinha, C. and Dutta, B.; Sunlight assisted SCSC dimerization of a 1D coordination polymer impacts the selectivity of Pd (II) sensing in water. *Chem. Comm*. **2021**, *57*; 6197-6200.

(107) Dutta, B.; Debsharma, K.; Dey, S.;Naaz, S.; Sinha, C. and Mir, M. H. Designing of Interdigitated Coordination Polymer for Fluorogenic Sensing of Pd (II) in Water with Reversible NonphaseMechanochromism. *Adv. Mater. Interfaces*. **2022**, *9*, 2201120.

(108) Dey, S., Purkait, R.; Pal, K.; Jana, K. and Sinha, C. Aggregation-induced emission-active hydrazide-based probe: selective sensing of Al^{3+}, HF^{2-}, and nitro explosives. *ACS omega*. **2019**, *4*, 8451-8464.

(109) Paul, S.; Dey, S.; Pal, K.; Maity, S.; Jana, K. and Sinha, C. A Fluorogenic Triphenyl-Amine- Naphthyl- Hydrazide Probe Selective for Cu^{2+} and Cysteine Detection via an ON- OFF- ON Logic path with Real Applications. *ChemistrySelect*. **2020**, *5*, 15233-15242.

(110) Fatima, S.F.;Sabouni, R.; Garg, R. and Gomaa, H. Recent advances in Metal-Organic Frameworks as nanocarriers for triggered release of anticancer drugs: Brief history, biomedical applications, challenges and future perspective. *Colloids Surf. B.* **2023**, 113266.

(111) Li, S.; Tan, L. and Meng, X. Nanoscale metal- organic frameworks: synthesis, biocompatibility, imaging applications, and thermal and dynamic therapy of tumors. *Adv. Funct. Mater*. **2020**,*30*, 1908924.

(112) Wen, T.; Quan, G.; Niu, B.; Zhou, Y.; Zhao, Y.; Lu, C.; Pan, X. and Wu, C. Versatile nanoscale metal–organic frameworks (nMOFs): An emerging 3D nanoplatform for drug delivery and therapeutic applications. *Small*. **2021**, *17*, 2005064.

(113) Kulmány, Á.E., Frank, É., Kovács, D., Kirisits, K., Krupitza, G., Neuperger, P., Alföldi, R., Puskás, L.G., Szebeni, G.J. and Zupkó, I., 2021. Antiproliferative and antimetastatic characterization of an exo-heterocyclic androstane derivative against human breast cancer cell lines. *Biomed. Pharmacother*. **2021**, *140*, 111728.

(114) Nesaragi, A.R.;Algethami, J.S.; Alsaiari, M.;Alsareii, S.A.;Mathada, B.S.;Ningaiah, S.; Sasidhar, B.S.;Harraz, F.A. and Patil, S.A. A comprehensive overview of coumarinyl-triazole hybrids as anticancer agents. *J. Mol. Struct*. **2024**, 137478.

(115) Zhou, R.; Xu, L.; Ye, M.; Liao, M.; Du, H. and Chen, H. Formononetin inhibits migration and invasion of MDA-MB-231 and 4T1 breast cancer cells by suppressing MMP-2 and MMP-9 through PI3K/AKT signaling pathways. *Horm Metab Res*. **2014**,*46*, 753-760.

(116) Rai, Y.; Pathak, R.; Kumari, N.; Sah, D.K.; Pandey, S.; Kalra, N.; Soni, R.; Dwarakanath, B.S. and Bhatt, A.N. Mitochondrial biogenesis and metabolic hyperactivation limits the application of MTT assay in the estimation of radiation induced growth inhibition. *Sci. Rep.* **2018**, *8*, 1531.

(117) Ganot, N.;Meker, S.;Reytman, L.; Tzubery, A. and Tshuva, E.Y. Anticancer metal complexes: synthesis and cytotoxicity evaluation by the MTT assay. *J Vis Exp*. **2013**, 81, 50767.

(118) Karim, S.; Halder, S.; Mukherjee, S.; Debnath, U.; Misra, A.K.; Jana, K. and Das, D. Glutathione Depleting a Chemoselective Novel Pro-oxidant Nano Metal–Organic Framework Induced G2/M Arrest and ROS-Mediated Apoptotic Cell Death in a Human Triple-Negative Breast Cancer Cell Line. *ACS Appl. Mater. Interfaces*. **2023**, *15*, 26442-26456.

(119) Hiraoka, S.; Harano, K.; Shiro, M.; Ozawa, Y.; Yasuda, N.; Toriumi, K. and Shionoya, M. Isostructural Coordination Capsules for a Series of 10 Different d^5–d^{10} Transition-Metal Ions. *Angew. Chem. Int. Ed.* **2006**, *45*, 6488-6491.

Chapter 2

Pyridyl-isonicotinoyl Hydrazone Bridged Zn(II) coordination framework with Thiophenedicarboxylatolink: Structure, Biological activity and Electrical Conductivity

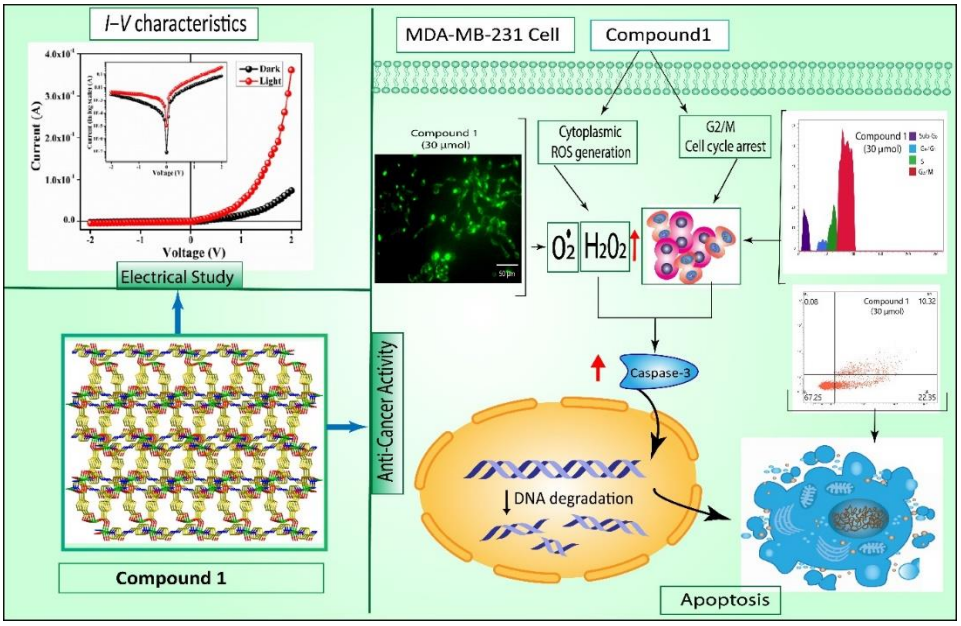

Abstract:

Multidimensional performance of functional materials is the main attraction of current scientific research. Highly stable and crystalline coordination polymers have been served as one of the active members in the group of multifunctional materials. Toaccomplish, a3-dimensional(3D) coordination framework, {[Zn_2(**tdc**)$_2$(**pcih**)$_2$]$_n$}(**1**) (**tdc**$^{2-}$, 2,5-thiophene dicarboxylate; **pich**, Pyridine-4-carboxaldehyde isonicotinoyl hydrazine)is designed and has been structurally characterised by single crystal X-ray crystallography and also by other spectral data. One of the carboxylate groups of **tdc**$^{2-}$chelatesto Zn(II) while other -COO acts as bridging-O to neighbouring Zn(II) centres; the **pcih** serves as pyridyl-N bridging motif to adjacentZn(II) centres and thus a 2D network is build up. It is then self-assembled *via* H-bonding (2.050 Å) and π···π interactions (3.964 Å) to generate 3D robust geometry. Using absorption spectral data of **1** the Tauc'splot determines the optical band gap,3.74 eVwhichimplies probable semiconducting ability of the material.Metal-semiconductor (MS) junction device was fabricatedto measure *I-V* characteristics and determine the electrical conductivity,2.21 × 10^{-5} S $cm^{-1}$and series resistance (R_s), 807 Ωat dark phase those have improved significantly to 6.36 × 10^{-5} S cm^{-1} and 460 Ωrespectively under illumination condition. In addition,isoniazid, parent amine of **pcih**, and Zn (II) have medicinal and biological importance; that is why,the anticancer efficiency of the compound **1**has been examined and it shows better impact in inhibiting the proliferation of MDA-MB-231 cells (IC_{50}: 19.43 ±1.36 µM) than other cancer cells (IC_{50}: 24.43 ± 2.02 µM (HeLa), 26.06 ± 3.48 µM (HCT-116), 44.28 ± 3.04 µM (HepG2)). Therefore,thesynthesized material has significant contribution in the case of two stimulating field, efficient electronic device construction and biological activity, for the sustainability of modern civilization, which resembles to 'to hook two birds in one stone!'.

2.1 Introduction

A considerable success has been made in the field of Coordination Polymers/Metal Organic Frameworks (CPs/MOFs) towards the application in various fields of science, engineering, technology, health etc. in the last three decades (**Chapter 1**).[1-3]To convey sustainable feature in this field, intensive research design and material adaptation are required because of their high porosity, large surface area, and flexible surface chemistry, adorable surface activity etc. These materials have been used in separation, storage, catalysis, drug transport, sensing of ions/small molecules etc.[4-12] Recent strategy has been focused onthe challenging program of integrating different functions in one system of CPs/MOFs towards the design of the multifunctional materials for achieving Sustainable Development Goals (SDGs) especially for the designing of energy saving materials[13,14] and biologically efficient drugs.[15]

Zinc based Coordination Polymers or Metal Organic Frameworks (Zn-CPs/Zn-MOFs) have attracted much attention due to their versatile application in the field of high electrical conductivity,[16] CO_2 capture-and-reduction to C-fuels and activation for the chemical transformation to useful organics,[17]heterogeneous catalyses,[18]sensing for toxic ions and explosives atultratrace level,[19] gas sorption and separation,[20] drug delivery[21,22]etc. Metallo-organic polymers are designed by exploiting appropriate organic spacers with functional groups those are accomplished of bridging metal or metal clusters for architecting the crystalline materials for useful in material science.Research on metal-organic frameworks (c-MOFs) are of high priority. Although Zn-CPs/Zn-MOFs have received considerable attention in the chemical science and material engineering but their application to the electrical conduction and energy saving fields has been focused only recently.[13,23]

Thedevice fabricated by using CPs/MOFs shows, in many cases,stimulationby light irradiation and enhancement of electrical conductivity; which will truly helpful to utilize therenewable energy sources for real application.[24-28]Towards the objective of **"**Global Science for Global Wellbeing"one of thepriority areas is the gesture of 'laboratory-to-land' application;design principle is focused for multifunctional hybrid materials with potential use in the environmental monitoring and the improvement of Human Development Index**.**[29-32]The CPs or MOFsare the organic-inorganichybrid materials and are capable to generate variation in voltage in MS (metal semiconductor)junction;[13, 23-32]these are useful in transistors, diodes,

DIAC (diode for alternating current), photocell etc. The composition and structure of the materials directly affect the electrical conductivity and charge transmission.

Zinc is one of the important bioactive metal and is constituent of more than 300 metalloenzymes.[33] Zn-based co-ordination compounds are utilized in various biological and medicinal fields. Anti-microbacterial, anticancer and cell imaging application are developingarea of Zn(II)-co-ordination compounds.[34,35]This has encouraged us to explore medicinal activity of newly designed Zn-CPs/MOFs.[36,37]

In this work, Pyridine-4-carboxaldehyde isonicotinoylhydrazine (**pich**) and 2,5-thiophen dicarboxylic acid (**H_2tdc**) are used to construct mixed bridging 2D coordination polymer of Zn(II), {[Zn_2(**tdc**)$_2$(**pcih**)$_2$]$_n$} (**1**) and the Single Crystal X-ray Diffraction measurement has been used to determinethe structure. Because of antimicrobial and anti-tuberculotic activity of isoniazid and biological importance of Zn(II), the anticancer activity of the compound **1** is examined which shows considerable cytotoxicity against MDA-MB 231, HCT-116, HeLa, HepG2 cell lines (cancer cells), and has been compared with WI-38 (normal lung fibroblast cell line).Anti-proliferative activity of the compound **1** is correlated with standard drug Etoposide.Highest anticancer efficiency is observed for MDA-MB-231 (IC_{50}:19.43 ±1.36 μM) cell line. The Tauc's plot suggests semiconducting (3.74 eV) nature of the material and the electrical characterization reveals the considerable improvement (~ 3-times) of electrical conductivity upon irradiation (6.36×10^{-5} S cm^{-1}) compared to dark phase conductance (dark phase, 2.21×10^{-5} S cm^{-1}) and thus the network can be potentially useful in the fabrication of optoelectronic devices. Hence, multidimensional applicability towards photo-responsive electronic devicemanufacturing and anticancer drug activity exploration of the compound **1**makes it as a potential member of multifunctional materials for the next generation in view of technological aspect in energy crisis and human health.

2.2 Experimental Section

2.2.1 Materials and General Methods

Isoniazid (INZ), 4-Pyridine Carboxaldehyde and 2, 5-thiophene dicarboxylic acid (**H_2tdc**) were purchased from TCI Chemicals (India) Pvt. Ltd. High purity Zinc (II) nitrate hexahydrate was purchased from Sigma Aldrich Co. DCFDA (# D6883) was purchased from Sigma-Aldrich (India). Fetal bovine serum (#16000044) was obtained from Gibco, USA and

MEM sodium pyruvate, MEM non-essential amino acids L-glutamine and Gentamicin, were procured from Hi-Media, India. All other chemicals including solvents were of AR grade. All the above chemicals were used without further purification.

Infrared (IR) spectrum (cm^{-1}) was recorded using a Perkin Elmer SPECTRUM II LITA FT-IR spectrometer. Elemental analysis (carbon, hydrogen, and nitrogen) of the compound was performed using a PerkinElmer 240C elemental analyzer. Thermo gravimetric analysis (TGA) was carried out on a PerkinElmer Pyris Diamond TG/DTA thermal analyser under nitrogen atmosphere (flow rate: 50 cm^3 min^{-1}) at the temperature range of 30−800 °C with a heating rate of 2 °C/min. Powder X-ray diffraction (PXRD) measurements were performed at room temperature with a PANalytical diffractometer equipped with a Cu micro focal tube (λ = 1.54178 Å) at 40 kV and 40 mA.UV−vis spectra were collected using a PerkinElmer Lambda 25 spectrophotometer.

Single Crystal X-ray diffractometer made by Bruker and model SMART APEX III outfitted with graphite-monochromatic MoKα radiation (λ = 0.71073 Å) was utilised to collect data on a single crystal of **1** (0.05 x 0.09 x 0.16 mm^3). The SHELX-97 package was used to solve the structure.Non-hydrogen atoms were refined using anisotropic thermal parameters. The composition of unit cell parameters and crystal-orientation matrices of $C_{18}H_{12}N_4O_5SZn$, were estimated by least-squares refinement of all hkl-range reflections $-11 < h < 11$, $-23 < k < 23$, $-16 < l < 16$. All of the hydrogen atoms were constrained to ride on their parent atoms in their geometrically perfect positions.

2.2.2 Synthesis of {$[Zn_2(tdc)_2(pcih)_2]_n$}, (1)

The ^1H NMR and Pyridine-4-carboxaldehyde isonicotinoylhydrazine (**pcih)** solution(0.045 g, 0.2 mmol) in methanol (2 mL) was gradually and expertly covered onto an aqueous solution (2 mL) of $Zn(NO_3)_2{\cdot}6H_2O$ (0.060 g, 0.2 mmol) using DMF and MeOH buffer (2 mL, 1:1 v/v) followed by layering of **H_2tdc** (0.035 g, 0.2 mmol) neutralized with Et_3N (0.042 g, 0.4 mmol) in EtOH (2 mL). After 7 days, block-shaped yellow colouredcrystals of $[Zn_2(\mathbf{tdc})_2(\mathbf{pcih})_2]_n$ (**1**) **(Scheme 2.1)** were obtained (0.201 g, yield 70%).

Preliminary characterisation was carried out by the elemental analysis (%) calcd for $C_{18}H_{12}N_4O_5SZn$: C, 46.90; H, 2.70; N, 12.20; found: C, 46.82; H, 2.62; N, 12.13; FTIR (cm^{-1}): 1556, $\nu_{as}(COO^-)$; 1352, $\nu_{sys}(COO^-)$**(Figure 2.1); t**hermogravimetry**;** and PXRDdata**.**

Structure has been confirmed by the Single Crystal Diffraction measurements (CCDC Number: 2194333)

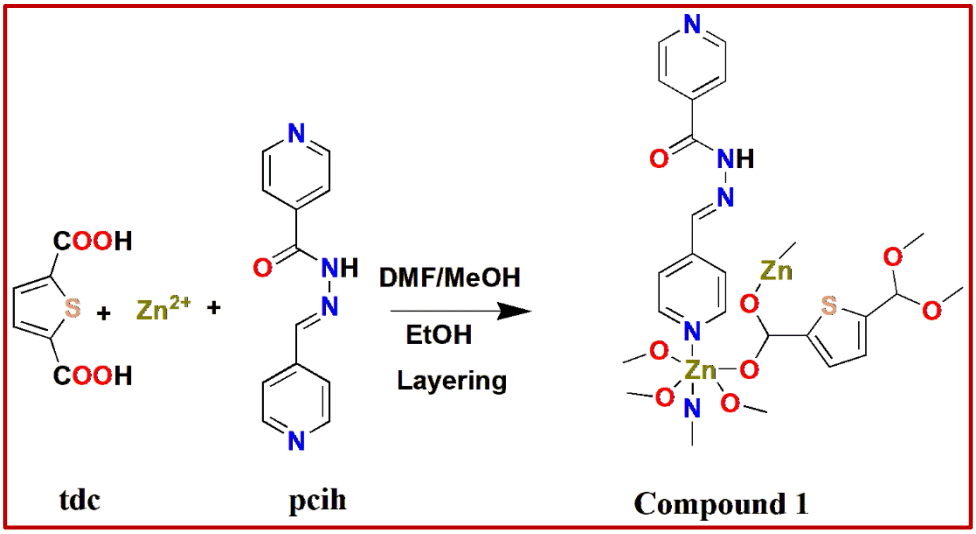

Scheme 2.1 Synthetic route of compound **1.**

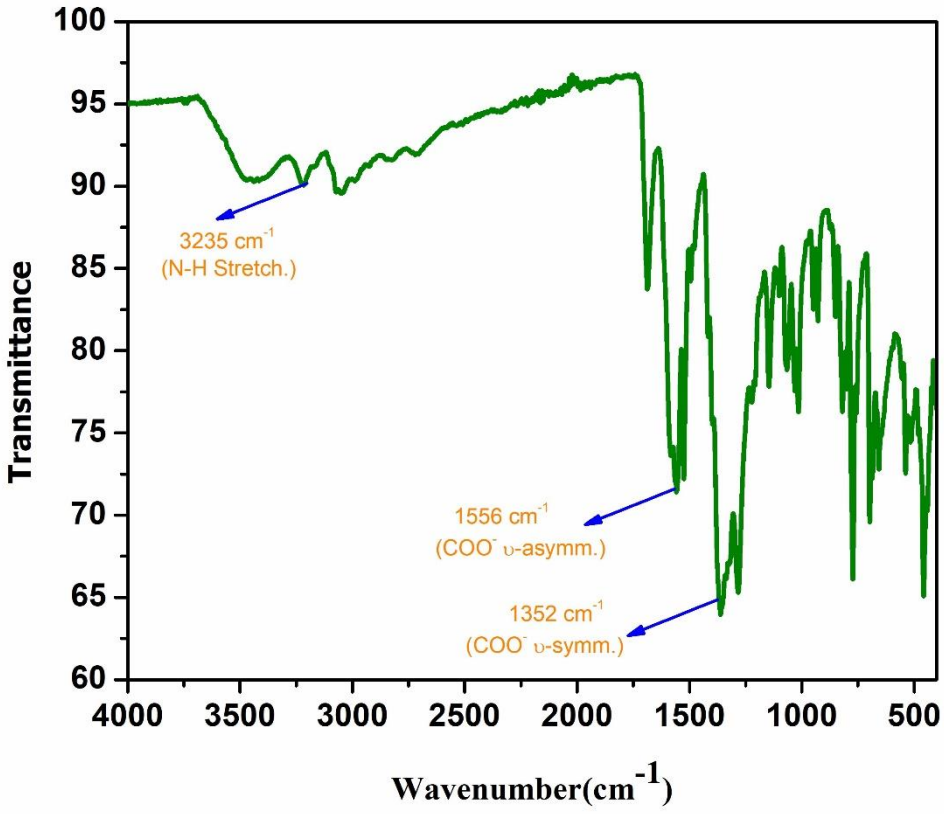

Figure 2.1 Synthetic route of compound **1.**

2.3 Results and Discussion

2.3.1 Crystal Structure of $\{[Zn_2(tdc)_2(pcih)_2]_n\}$ (1)

In this article, The compound **1**crystallizes in the Monoclinic crystal system, $P2_1/n$ space group and D_{calcd}=1.482g/cm^3 having Z = 4 in Crystallographic Data, **Tables 2.1.** The bond parameters are added in **Table 2.2**. The geometrical arrangement surrounding the central metal, Zn(II), is distorted octahedral with ZnO_4N_2 coordination unit.This is formed by the simultaneous coordination of **pcih** and **tdc**$^{2-}$. The **tdc**$^{2-}$ is coordinated (**Figure 2.2a**) through chelating and bridging pattern and has constituted 2D framework (**Figure 2.3**).

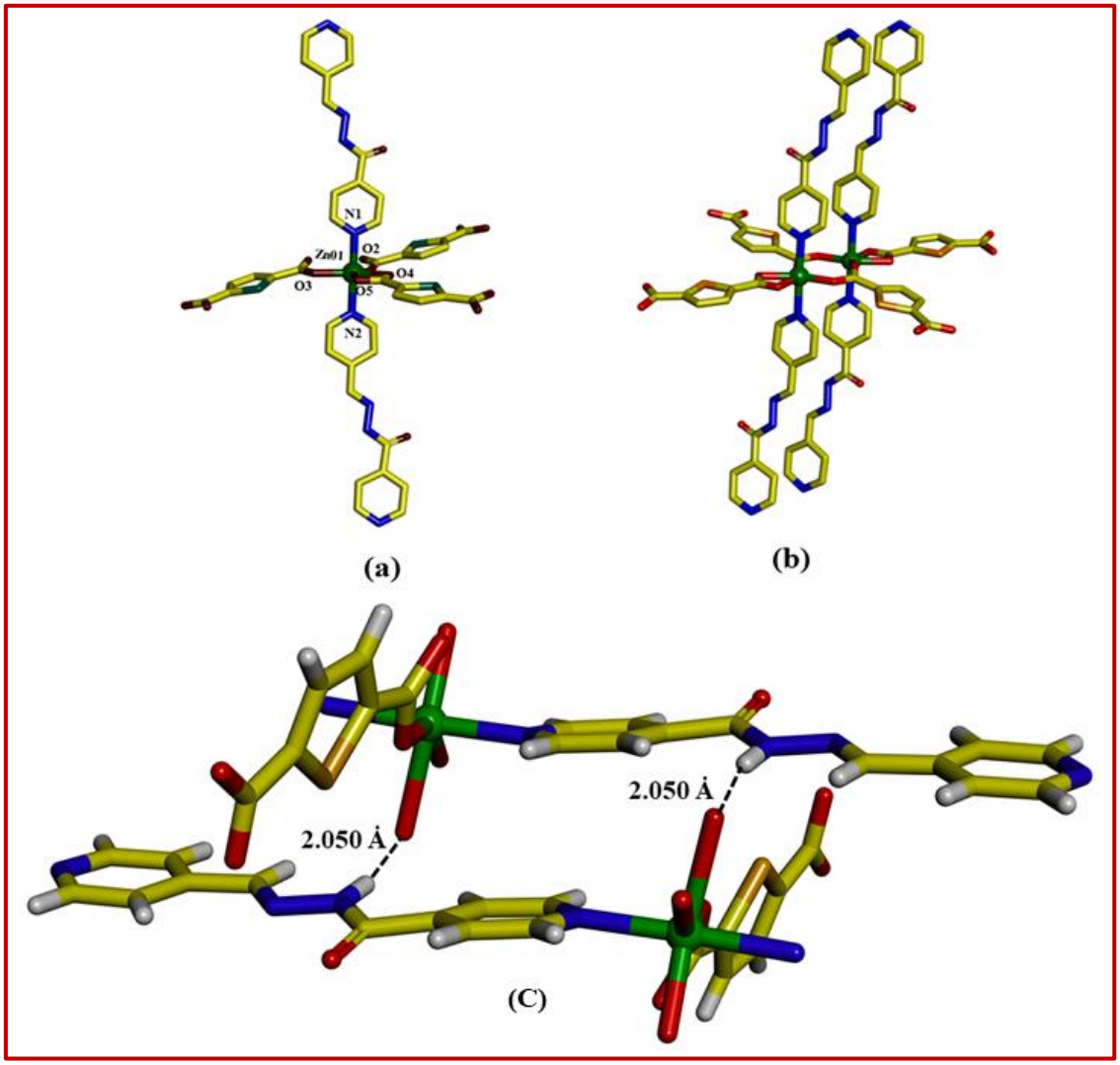

Figure 2.2 (a) Perspective view of the repeating asymmetric unit of 1,(b)Acetato bridged coordination cycle, and (c) Inter-layer H-bonding motif.

Two Zn1 metal centres are mono-dentate bridged through one of the carboxylate groups (-COO) of **tdc**$^{2-}$ to generate an 8-membered metallacycle (**Figure 2.2b**) and the pyridyl-N (**pcih**) coordinates tofulfil the six-coordination number as demanded for the distorted octahedral geometry.The Zn-O bond (Zn1-O2, 2.051; Zn1-O3, 2.027; Zn1-O4, 2.113; Zn1-O5, 2.415 Å) and Zn-N bond (Zn1-N1, 2.155; Zn1-N2, 2.194 Å) distances are comparable with reported results.[36,37]The synthon of the 2D network is assembled *via* non covalent interactions (**Figure 2.4, Figure 2.2c**) to generate 3D molecular architecture; major contribution comes from π···πinteractions (3.964 Å, **Figure 2.4(a,b))** between pyridyl rings of **pcih** ligand.

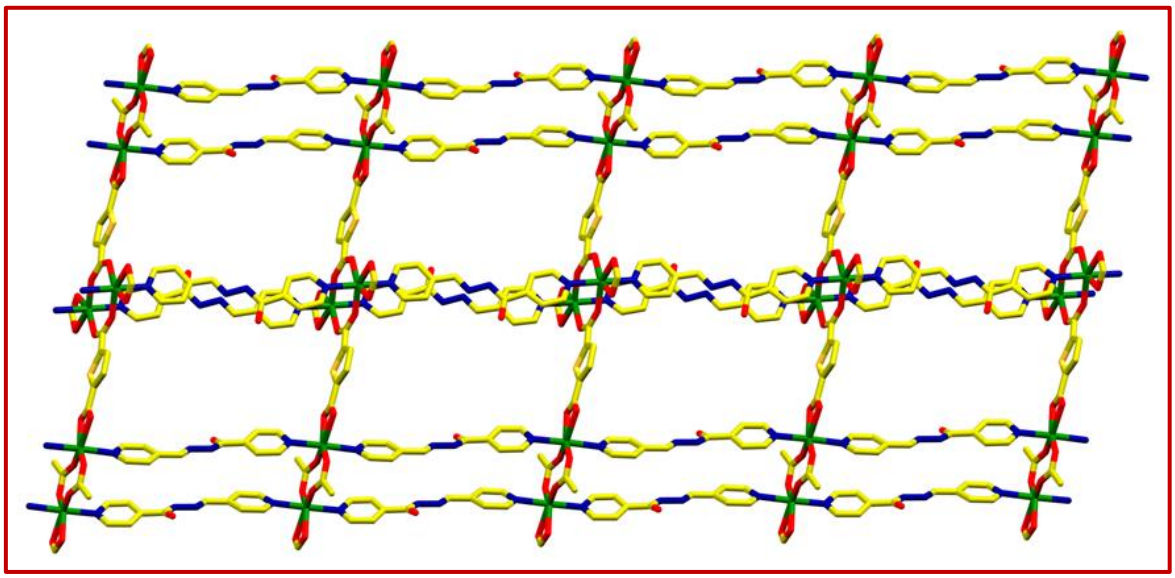

Figure 2.3 2D rectangular network of **1**.

The analysis was performed using the program *topcryst.com*[38]. The RCSR three-letter codes[39]were used to designate the network topologies. The nets, those are absent in the RCSR, are designated with the TOPOS NDn nomenclature[40], where N is a sequence of coordination numbers of all non-equivalent nodes of the net, D is periodicity of the net (D=M, C, L, T for 0-,1-,2-,3-periodic nets), and n is the number of the net in the set of all non-isomorphic nets with the given ND sequence. To calculate the underlying nets, we used algorithms[40],[41]. The TTD collection[42] was used to determine the topological type of the crystal structure. The topology of the as-synthesized compound **1** (**Figure 2.4c)** belongs to the point symbol {4^12.6^3} for extended point symbol, [4.4.4.4.4.4.4.4.4.4.4.6(4).6(4).6(4)];three-digit

topology ispcu, 6/4/c1; and the 6-c netfor a unimodal system shows interpenetrated lattice arrangement**.**

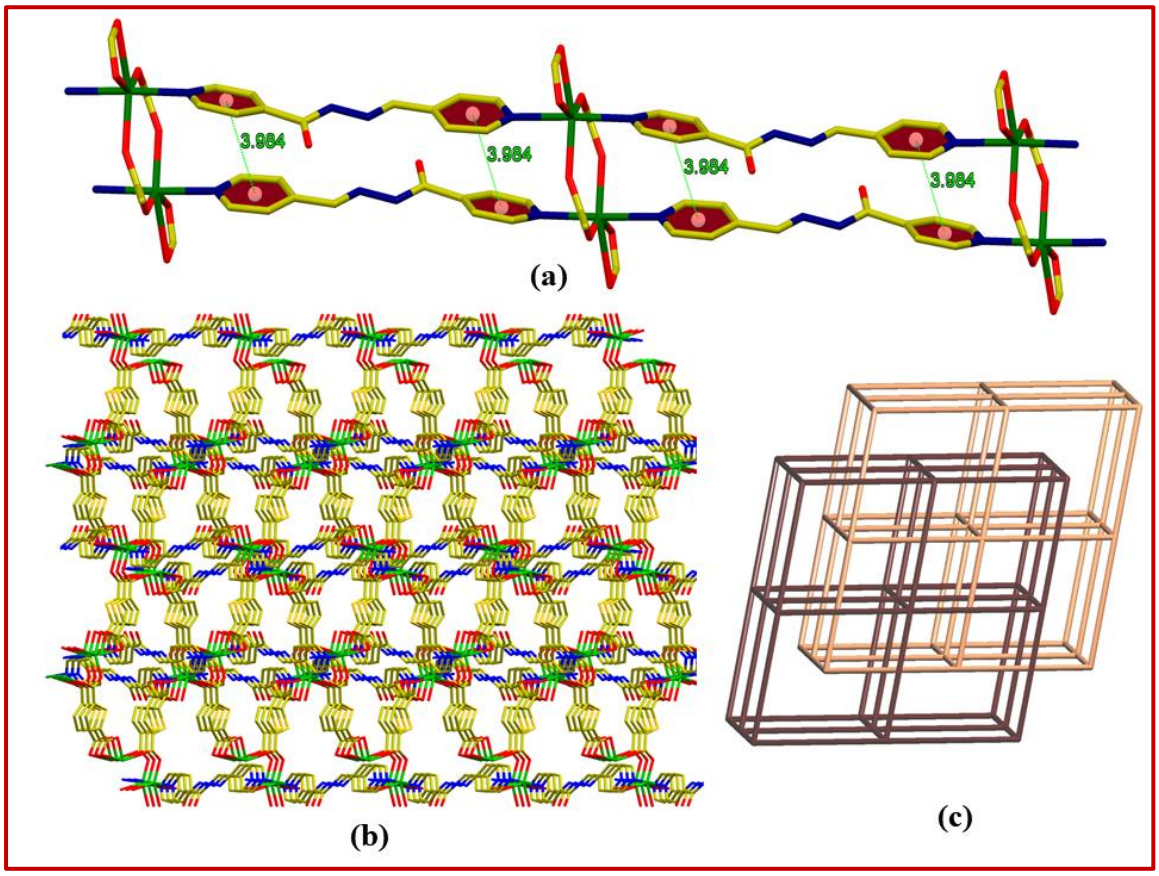

Figure 2.4 (a) The π···π interactions of pyridyl rings (3.964 Å) in **1**; **(b)** 3D supramolecular assembly of **1** through the coordination (**pcih** and **tdc**$^{2-}$); **(c)** Topological structure of compound **1.**

Table 2.1 Crystal data and refinement parameters for compound1.

Complex	**1**
CCDC No.	2194333
empirical formula	$C_{18}H_{12}N_4O_5SZn$
formula weight	461.77

crystal system	Monoclinic
space group	P21/n
a(Å)	9.0144(7)
b(Å)	18.1794(13)
c(Å)	12.6308(9)
β(°)	91.939(2)
V(Å^3)	2068.7(3)
T(K)	273(2)
Z	4
D_{calcd}(Mg/m^3)	1.483
μ(mm^{-1})	1.324
λ(Å)	0.71073
θ range (°)	2.52-27.06
total reflections	3612
unique reflections	3242
refine parameters	262
R_1[a] [$I > 2\sigma(I)$]	0.0471
wR_2[b]	0.1508
goodness-of-fit	0.993

[a]$R_1=\Sigma||F_o|-|Fc||/\Sigma|F_o|$, [b]$wR_2=[\Sigma w(F_o^2-Fc^2)^2/\Sigma w(F_o^2)^2]/2$, $w=1/[\sigma^2(F_o^2)+(0.1000P)^2+0.3347P]$, where $P=(F_o^2+2Fc^2)/3$

Table 2.2 Selected Bond Length and Bond angle of 1

Bond-Length	Å	Bond Angle	Degree (°)
Zn(1) - O(3)	2.026(2)	O(3) - Zn(1) - N(1)	92.07(11)
Zn(1) - N(1)	2.158(3)	O(3) - Zn(1) - N(2)a	87.71(11)
Zn(1) - $N(2)_a$	2.196(3)	O(3) - Zn(1) - O(4)c	147.34(10)
Zn(1) - $O(4)_c$	2.111(3)	N(1) - Zn(1) - O(4)c	91.22(11)
Zn(1) - $O(5)_C$	2.155(3)	N(1) - Zn(1) - O(5)c	97.25(11)
Zn(1) - O(2)e	2.047(3)	O(3) - Zn(1) - O(5)c	89.93(9)
O(3) - Zn(1) - O(2)e	119.31(11)	N(1) - Zn(1) - N(2)a	177.90(10)
N(1) - Zn(1) - O(4)c	91.24(10)	N(1) - Zn(1) - O(5)c	97.28(9)
N(1) - Zn(1) - O(2)e	89.47(10)	N(2)a - Zn(1) - O(4)c	90.07(11)
N(2)a - Zn(1) - O(5)c	84.81(9)	N(2)a - Zn(1) - O(2)e	88.82(10)
O(4)c - Zn(1) - O(5)c	57.43(9)	O(4)c - Zn(1) - O(2)e	93.21(11)
O(5)c - Zn(1) - O(2)e	149.82(10)	C(14) - S(1) - C(17)	91.37(17)
C(13) - O(2) - Zn(1)e	156.8(2)	Zn(1) - O(3) - C(13)	119.9(2)
C(18) - O(4) - Zn(1)d	97.0(2)	C(18) - O(5) - Zn(1)d	83.1(2)
Zn(1) - N(1) - C(1)	118.7(2)	Zn(1) - N(1) - C(5)	124.4(2)
C(1) - N(1) - C(5)	116.3(3)	C(9) - N(2) - C(11)	117.0(3)
C(9) - N(2) - Zn(1)b	122.4(3)	C(11) - N(2) - Zn(1)b	120.4(2)
N(4) - N(3) - C(6)	118.2(3)	N(3) - N(4) - C(7)	115.7(3)

a = -1+x,y,1+z , b = 1+x,y,-1+z , c= 1/2-x,-1/2+y,3/2-z ,d= 1/2-x,1/2+y,3/2-z , e= -x,1-y,1-z

Thermogravimetric analysis (TGA) of compound **1**in the range of 30-800 °C at a rate of 10°C min^{-1} in a N_2 atmosphere shows good stability up to 210°C (**Figure 2.5**), after which the compound undergoes thermal decomposition. The final residue is ZnO (Cal. 17.62%; Exptl. 17.89%). The crystallinity of the finely grounded sample was checked by using powder X-ray diffraction (PXRD) at room temperature and compared to a simulated spectrum. Almost all of the major peaks in the PXRD pattern of the as-synthesized compound **1 (Figure 2.6)** matched with that of simulated from single crystal data, indicating phase clarity and bulk material uniformity.

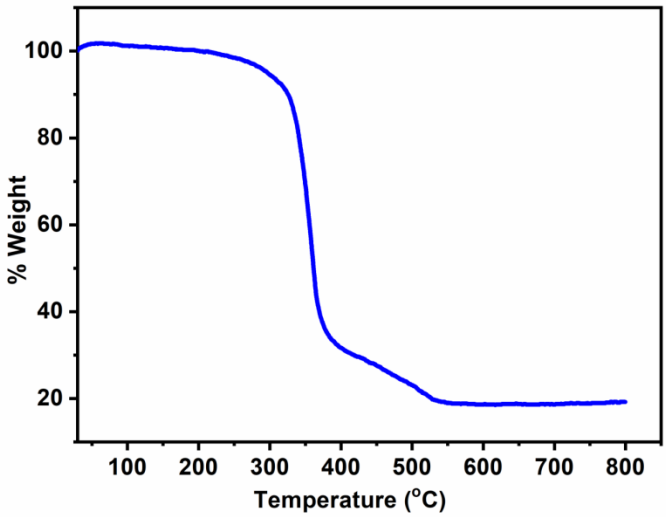

Figure 2.5 TGA plot of compound**1.**

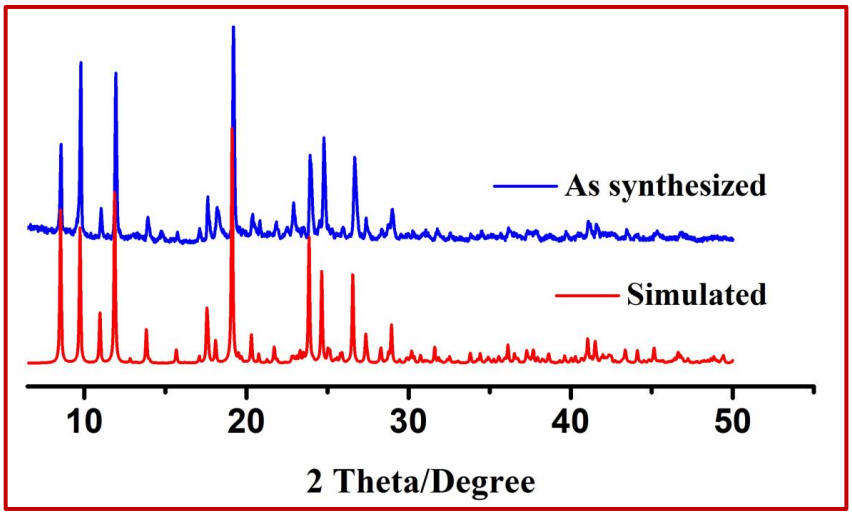

Figure 2.6 PXRD plot of compound **1.**

The SEM (scanning electron microscopy) and EDX (energy-dispersive X-ray) analysis are helpful to examine for any fouling, either dissociation/association or impurity, of the sample.[43]For these reasons the SEM and EDX analyses of compound **1** were performed. Thecrystal of **1**was dipped into the solution of pH = 7.4 and in DMSO for few minutes separately and then the SEM images were collected (**Figure 2.7 (a-c)**).

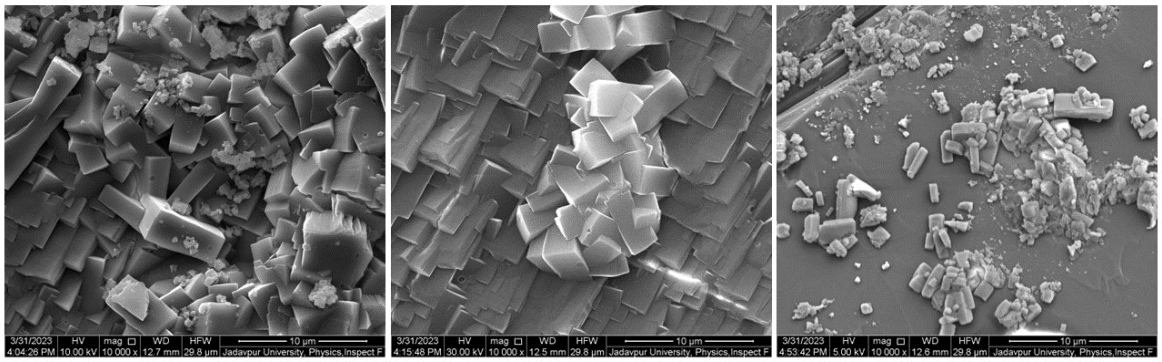

(a) **(b)** **(c)**

Figure 2.7 (a-c). The SEM images of (**a**) original compound **1; (b)** Compound **1** collected from the solution at pH 7.4; (**c**) collected the compound **1** dipped in DMSO.

The EDX of original compound **1** and after dipping into the solution of pH 7.4 and DMSO were also recorded to confirm the stability of the chemical composition and structure of **1**; the presence of different elements in the compound (**Figure 2.8 (a-c)**) proves the structural identity.

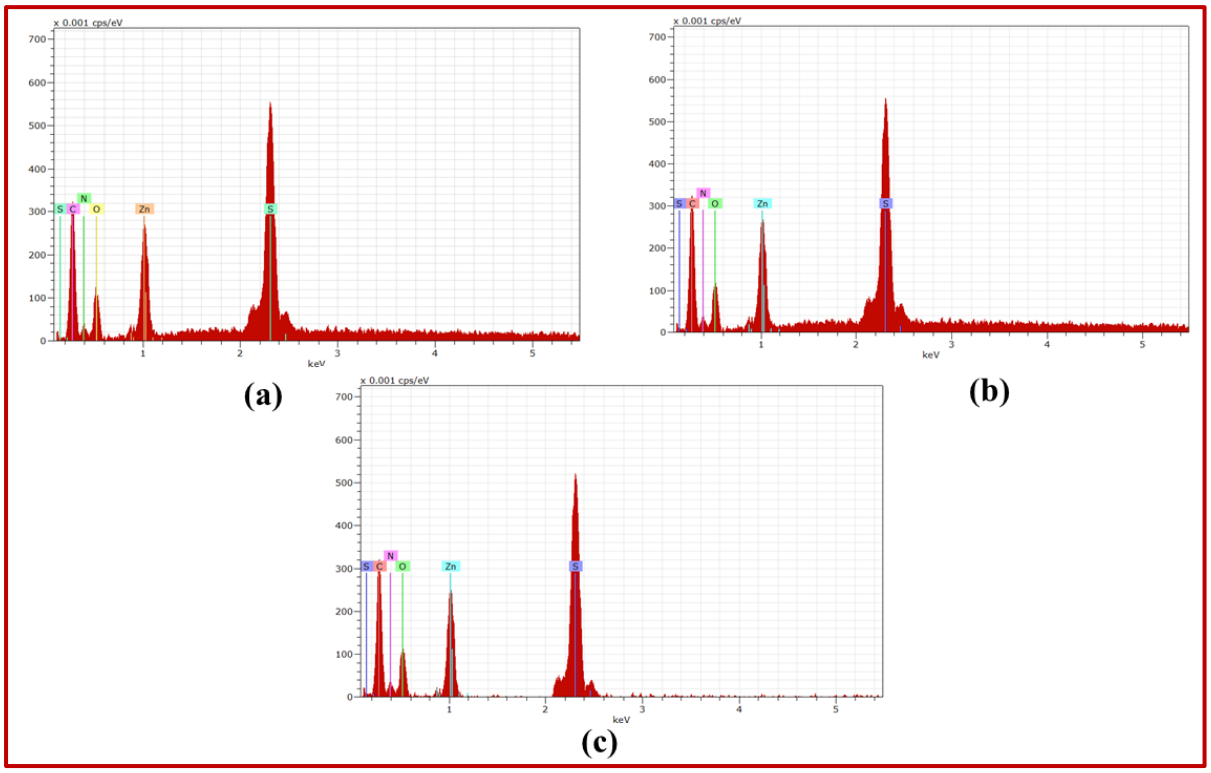

Figure 2.8 (a-c). The EDX of (**a**) original compound **1; (b)** compound **1** collected from the solution of pH 7.4; (**c**) collected the compound **1** dipped in DMSO(Elements need to be enlarged)

The stability has been confirmed form the EDX mapping (**Figure 2.9**)

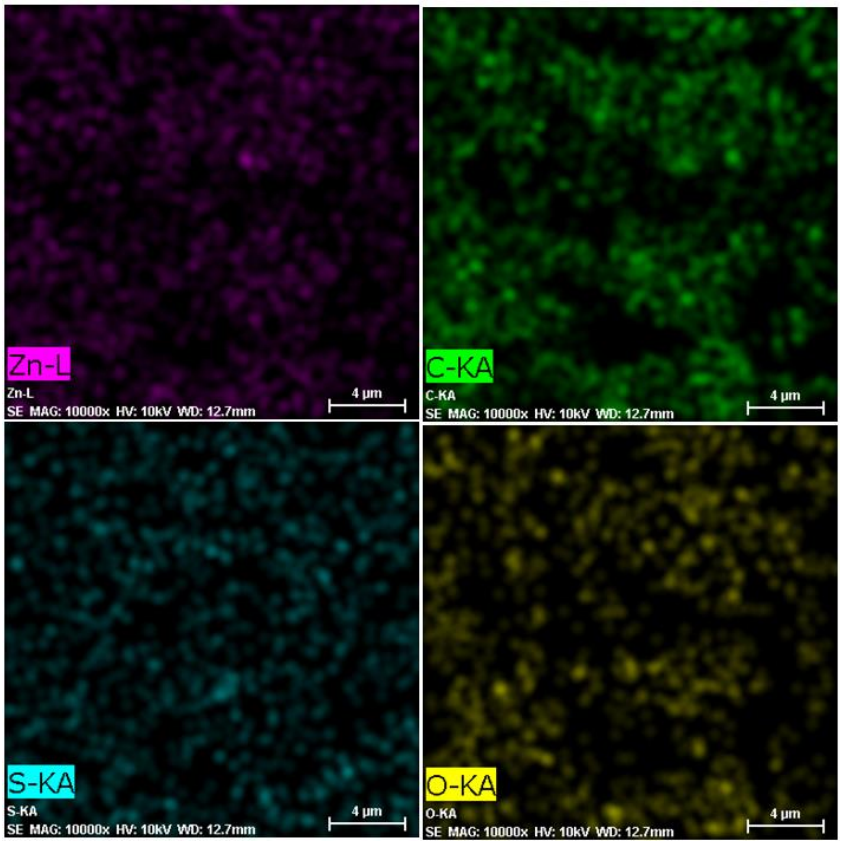

Figure 2.9 The homogeneous distribution of elements (C, O, S, and Zn) within the compound **1** was confirmed form the EDX mapping.

The Powder X-ray Diffraction (PXRD) pattern of original **1**and compound collected from different conditions (**Figure 2.10,** pH 7.4 and DMSO) exhibit that the peak positions and intensities are remained unchanged; which have confirmed the bulk phase consistency of material during different applications.

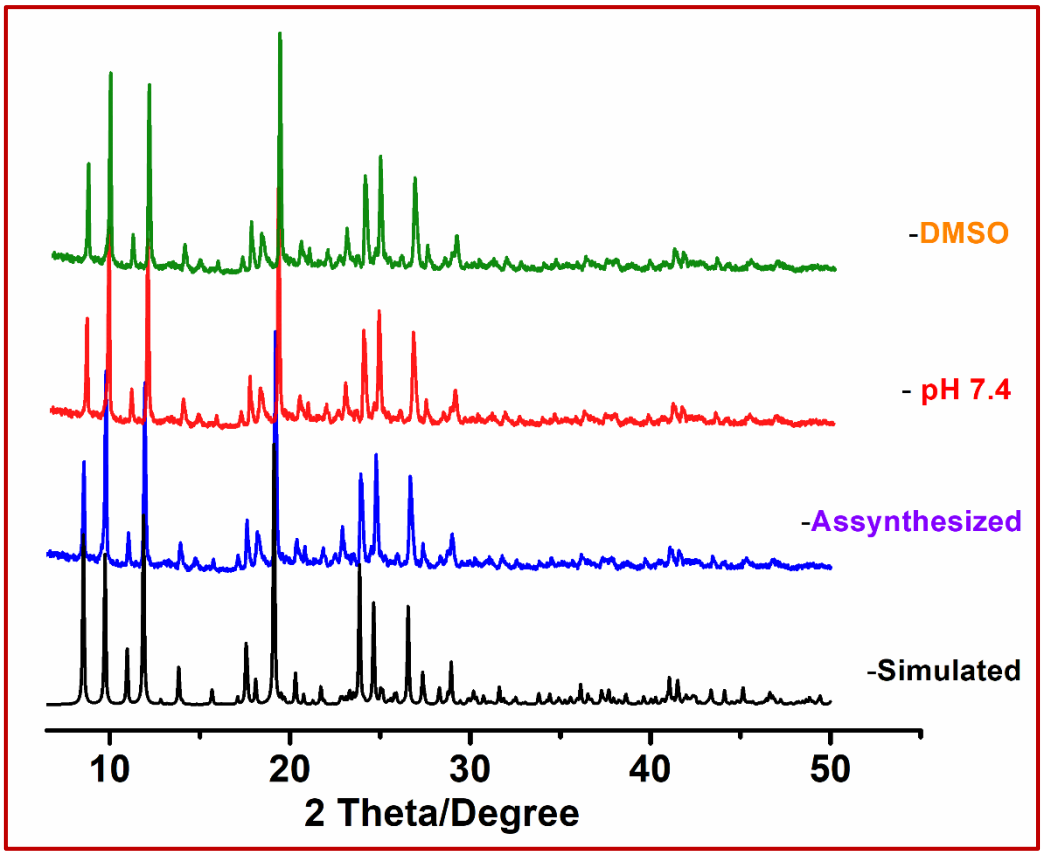

Figure 2.10 Powder X-ray Diffraction spectra of (**a**) compound **1; (b)** Compound **1** collected from the solution of pH 7.4; (**c**) The compound **1** collected after dipped in DMSO.

2.3.2 DFT Computational Study

Optimization of the gas phase geometry of the Zn-CP was carried out using Density Functional Theory (DFT) calculation of Gaussian Program Package 09.[44-47]All calculations were performed using SCXRD coordinates and B3LYP method. LanL2DZ basis set were employed for all elements including Zn.Different electronic transitions were theoretically determined using the time-dependent density functional theory (TDDFT) formalism calculation.[47]Vibrational frequency calculations were performed to ensure that the DFT-optimized geometries represent the local minima and only positive eigenvalues.

Optimization of the asymmetric unit of compound **1** was performed using the coordinates of the Single Crystal X-Ray Diffraction data. The energy difference between HOMO (-7.06 eV)

and LUMO (-2.99 eV) is 4.07 eV(**Figure 2.11**) (experimental band gap is 3.74 eV, **Figure 2.12**). The geometrical factor may be the reason for the deviation from experimental data; in DFT, the single individual molecular synthon is considered while in the experiment the compound **1** has been grown on multiple metal-semiconductor (MS) junction devices to fabricate ITO/synthesized compound **1**/Al. For coordination polymer with d^{10} system, the band edges depend on the electronic state of the geometrical framework.

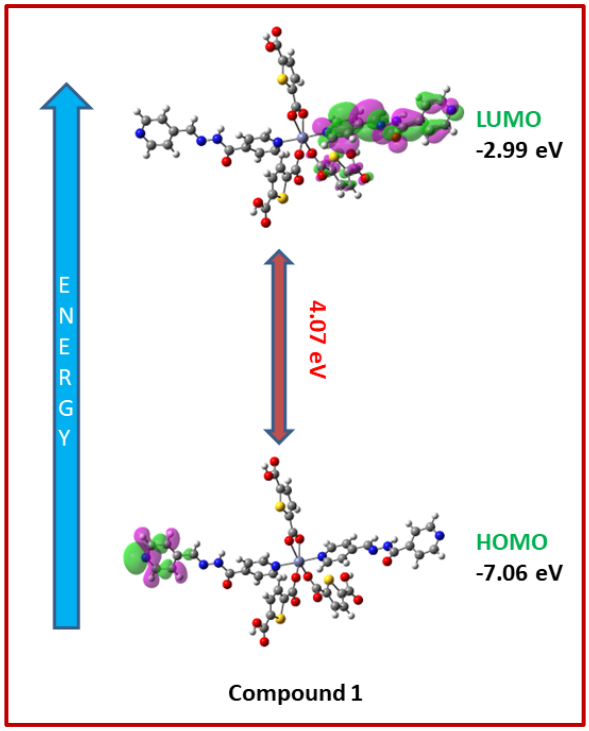

Figure 2.11 HOMO-LUMO gap of compound **1** from DFT computation of the crystal structure data of **1.**

Some selected FMOs along with their respective energies are listed in the Supplementary Material (**Table 2.3**).

Table 2. 3 Some selected MOs of the **Zn-CPs** along with their energy.

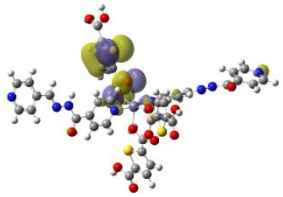 **HOMO-5** **(-7.43 eV)**	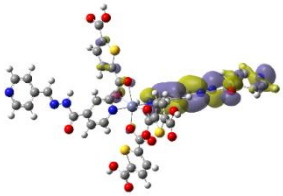 **HOMO-4** **(-7.36 eV)**	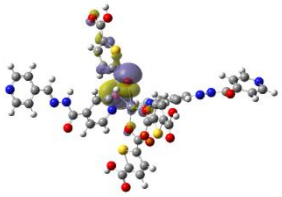 **HOMO-3** **(-7.28 eV)**
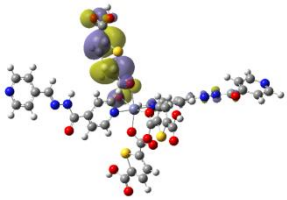 **HOMO-2** **(-7.22 eV)**	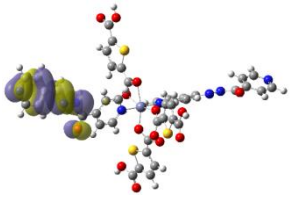 **HOMO-1** **(-7.11 eV)**	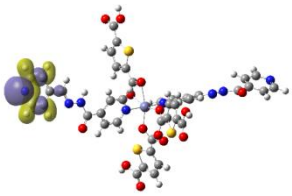 **HOMO** **(-7.06 eV)**
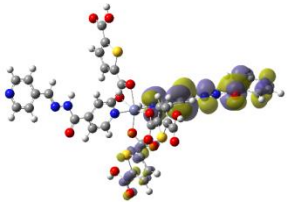 **LUMO** **(-2.99 eV)**	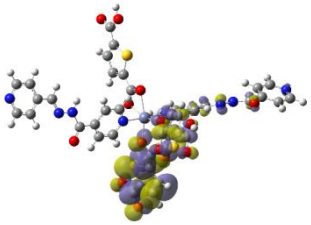 **LUMO+1** **(-2.95 eV)**	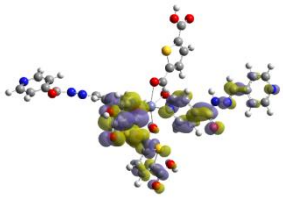 **LUMO+2** **(-2.88 eV)**
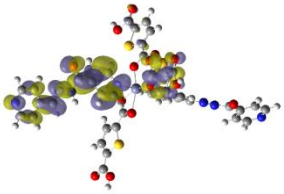 **LUMO+3** **(-2.85 eV)**	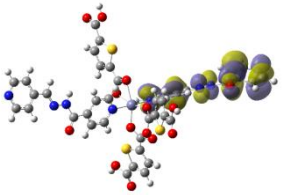 **LUMO+4** **(-2.62 eV)**	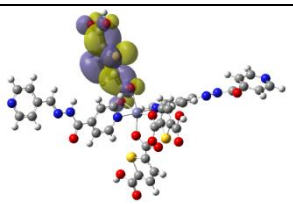 **LUMO+5** **(-2.17 eV)**

2.3.3 Optical and Electrical Characterization

The solid-state thin film UV-Vis absorption spectrum (Inset of **Figure 2.13**) of the compound **1** has been used to calculate the optical band gap, 3.74 eV following the Tauc's equation[48-50] (**Equation 1**).[51](**Figure 2.13**).

$$(\alpha h\nu) = A(h\nu - E_g)^n \quad (1)$$

Whereα, E_g, h, and νstand for absorption coefficient, band gap, Planck's constant, and frequency of light. The exponent 'n' is the electron transition processes dependent constant. 'A' is a constant which is considered as **1** for the ideal case. To calculate the direct optical bandgap the value of the exponent 'n' in the above equation has been considered as n = ½.[52]By extrapolating the linear region of the plot $(\alpha h\nu)^2$ *vs.*$h\nu$ (**Figure 2.13**) to α = 0 absorptions, the values of optical direct band gap (E_g) have been calculated as 3.74 eV for synthesized compound **1**.

The $I-V$ characteristic of **1** was further analyzed by thermionic emission theory. Cheung's method was also employed to extract important diode parameters.[51]In this regard, the obtained $I-V$ curve was analyzed quantitatively by considering the following standard equations (**Equations 2, 3**).[53,54]

$$I = I_0 exp\left(\frac{qV}{\eta KT}\right)\left[1 - exp\left(\frac{-qV}{\eta kT}\right)\right] \quad (2)$$

$$I_0 = AA^*T^2 exp\left(\frac{-q\emptyset_B}{kT}\right) \quad (3)$$

where, I_0, k, T, V, A, η, and A* stand saturation current, electronic charge, Boltzmann constant, temperature in Kelvin, forward bias voltage, effective diode area, ideality factor, and effective Richardson constant, respectively. The effective diode area was estimated as 7.065×10^{-2} cm^2 and the effective Richardson constant was considered as 32 AK^{-2} cm^{-2} for all the devices.

The series resistance, ideality factor and barrier potential height was also determined by using **Equations 4** to **6**, which was extracted from Cheung's idea,[53,54]

$$\frac{dV}{dln(I)} = \left(\frac{\eta kT}{q}\right) + IR_S \quad (4)$$

$$H(I) = V - \left(\frac{\eta kT}{q}\right) ln\left(\frac{I_S}{AA^*T^2}\right) \quad (5)$$

$$H(I) = IR_S + \eta\emptyset_B \quad (6)$$

From the saturated values of capacitance at the higher frequency regime (**Figure 2.14**) the dielectric permittivity of the complex was calculated using the **Equation 7**:[55]

$$\varepsilon_r = \frac{1}{\epsilon_0} \cdot \frac{C.D}{A} \quad (7)$$

Where *C* is the capacitance (at saturation), *D* is the thickness of the film which was considered as ~1 μm and *A* is the effective area. Using the above formula, the relative dielectric constant of the material was estimated as 4.86×10^{-1} for compound **1**.

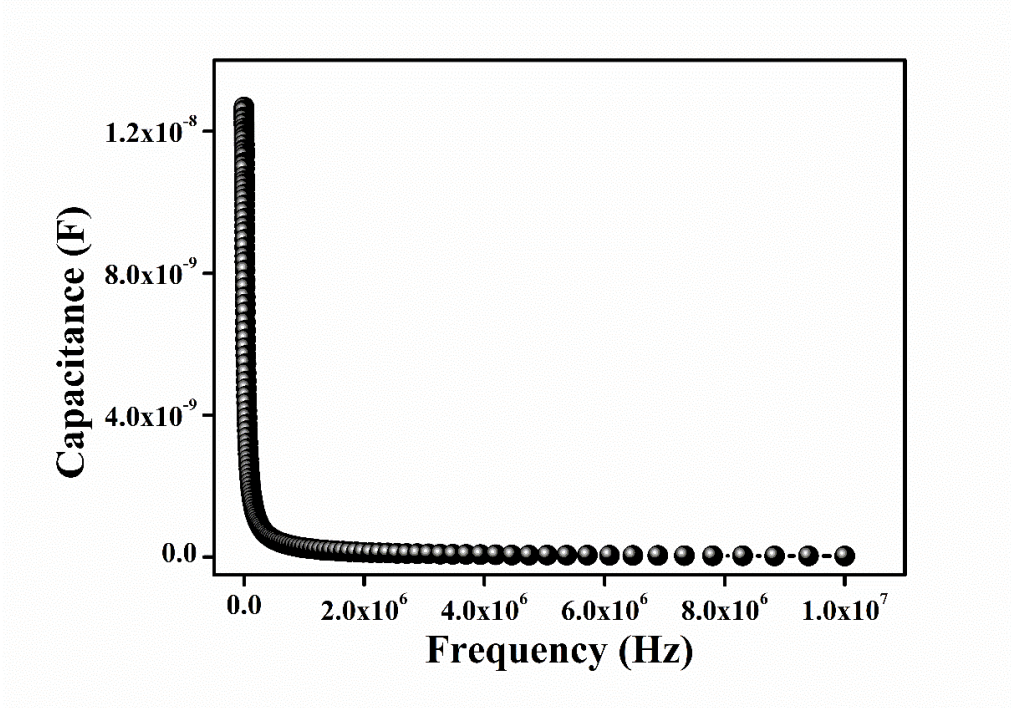

Figure 2.14 Capacitance vs. Frequency graph of compound **1**.

2.3.4 Device Fabrication

In this study, multiple metal-semiconductor (MS) junction devices were fabricated in ITO/synthesized compound **1**/Al sandwich structure to perform the electrical study. In this regard, well dispersion of the synthesized compound was made in N,N-dimethyl formamide (DMF) by mixing and sonicated the right proportion (18 mg/ml) of the complex in a vial. This freshly prepared stable dispersion of the compound was deposited on the top of the ITO-coated glass substrate by spinning firstly at 600 rpm for 5 min and thereafter at 900 rpm for another 5 min with the help of SCU 2700 spin coating unit. Afterward, the as-deposited thin film was dried in a vacuum oven at 80 °C for several minutes to evaporate the solvent part fully. Here we used gold as the metal electrode, which was deposited using a Vacuum Coating Unit on the active layer of the devices by maintaining the effective area as 7.065×10^{-2} cm^{-2} with shadow masks. Using Sourcemeter made by Keithley (model no: 2401), the current-voltage (*I-V*) characteristics of the devices were measured to analyze the electrical properties. All the device fabrication and measurements were carried out at room temperature and under ambient conditions.

The electrical property of metal (Al)–semiconductor (compound **1**) (MS) junction thin-film device (Supplementary Material)[39]is estimated from the current-voltage (*I-V*) plot (**Figure 2.13**) at room temperature (26 °C) at dark and in presence of light (Intensity, ~100 $mWcm^{-2}$) at applied bias voltage sequentially within the limit of ±2 V. The electrical conductivity of **1** at dark is 2.21×10^{-5} S cm^{-1} and is increased to 6.36×10^{-5} S cm^{-1} on light irradiation. The enhancement of electrical conductivity during the light phase may be attributed to the "hopping transport" process which signifies the charge transfer in the molecules *via*intramolecular charge transition process.

The *I-V* characteristics of **1** represent nonlinear rectifying behaviour at dark and light phase conditions (**Figure 2.13**). The curves describe the formation of the Schottky barrier diode (SBD) at the Al/compound **1** interface. The rectification ratios (I_{on}/I_{off}) at ±2 V are 26.27(dark) and 80.85 (light) of **1**, also support photoconductivity enhancement. Upon light irradiation, the *I-V* characteristics curve of **1** demonstrates an increase of current at the highest applied bias for this experiment. The ratio of current (highest applied bias) between dark and

light has been considered as photo-responsive factor and is calculated as 4.88 (~ 5). This was also supported by thermionic emission theory (Cheung's method) to determine some important diode parameters. [56-58]

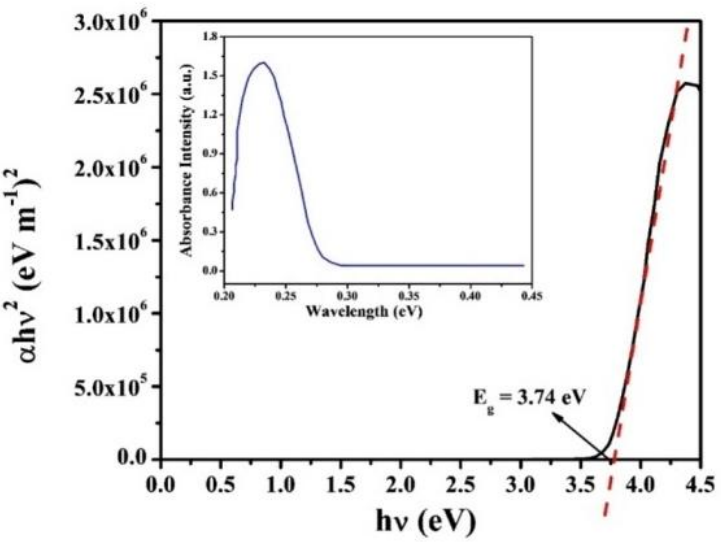

Figure 2.12 Optical direct band gap (***E*$_g$**) and UV-Vis absorption spectra (inset) for compound **1** by Tauc's plot.

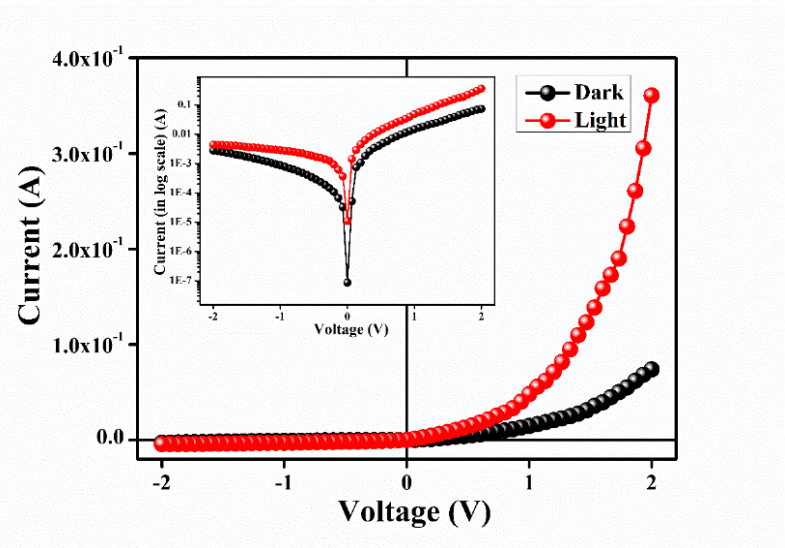

Figure 2.13 *I*−*V* characteristics curve for **1** under dark and photo illumination conditions.

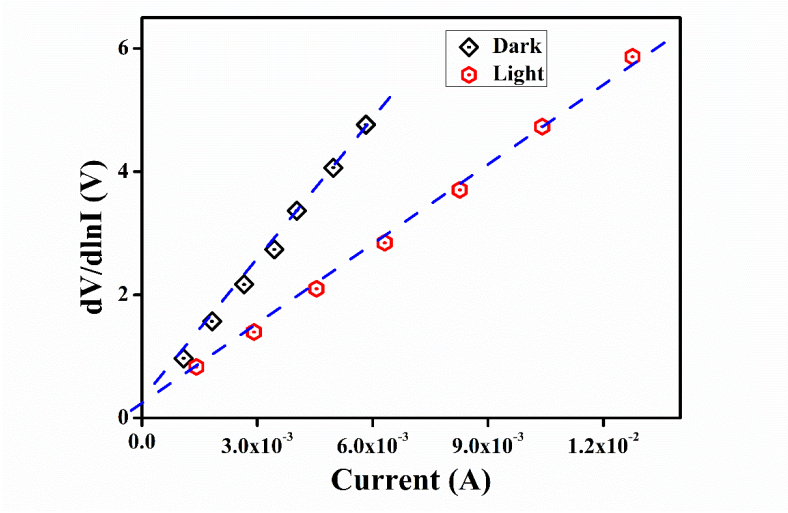

Figure 2.14 *dV/dlnIvs.I* graph of**1** under dark and photo illumination conditions.

The ideality factor (***η***) of **1**at light phase (2.08) is less than that of dark phase (2.93) which are calculated from the intercept of the *dV/dlnIvs.I* plot (**Figure 2.14**); the series resistance (***R*S**) of the device also supports this conjecture (**Table 2.4**). The calculated value of ***η*** deviates considerably from the ideal value (~1). These deviations symbolizeinhomogeneitiesat the interface state of Schottky barrier.[48,49] It is noteworthy that***η***(ideality factor) of **1**approach closer to ideal value, and shows in photo-irradiated conditions. This represents less charge carrier recombination probability at the interface and the formation of better homogeneity at the barrier of Schottky junctions.[59,60,62]As a result of light irradiation, **1** has improved barrier homogeneity, resulting in a reduced amount of carrier recombination at the junction.

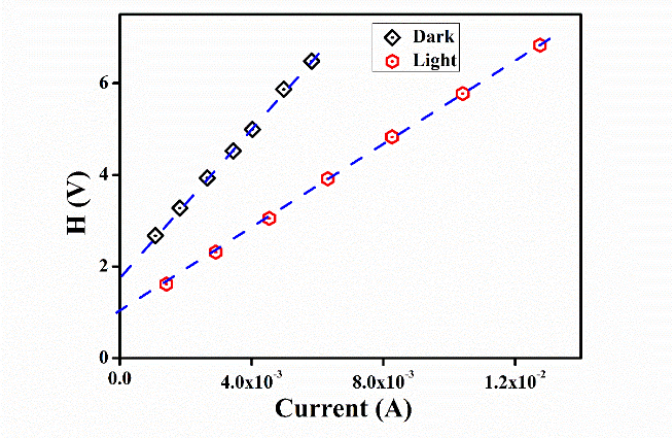

Figure 2.15 *H vs.I*curves for **1**in dark and light.

The barrier height ($\emptyset_B$) estimated from the intercept of *Hvs.I* plots (**Figure 2.15**), 0.61 (dark) and 0.47 (light),also reflect the enhancement of the photoconductivity effect. The reason for this declining of $\emptyset_B$ at light irradiation condition is probably the formation of photoinduced charge transporters and their gathering in the vicinity of the conduction band. The slope of this plot was also used to determine the series resistance (R_S) of the device (**Table 2.4**) that substantiates the proposal.

The plots of ln(I) *vs.* ln(V) of **1** under dark and photo-illumination conditions (**Figure 2.16**) show two different slopes - Regions I and II. The slope is ~1 for Region I and indicates that *I-V* relation follows the Ohmic rule. In Region II, $I \propto V^2$ relation is followed (**Figure 2.16**) which signifies the trap-free space charge limited current (SCLC) regime.[48,61]The spreading of the injected carriers follows the SCLC protocol when the background carriers are less than the injected carriers.

Table 2.4 Schottky device parameters of **1.**

Condition	**Rectification ratios (I_{on}/I_{off})**	**Conductivity (S. cm^{-1})**	**Photosensitivity**	**Ideality factor (η)**	**Barrier height ($\emptyset_B$) (eV)**	**Series Resistance (R_S)**	
						From *dV/dlnI* (Ω)	**From *H* (Ω)**
Dark	26.27	2.21×10^{-5}	4.88	2.93	0.61	801.49	807.18
Light	80.85	6.36×10^{-5}		2.08	0.47	456.70	460.82

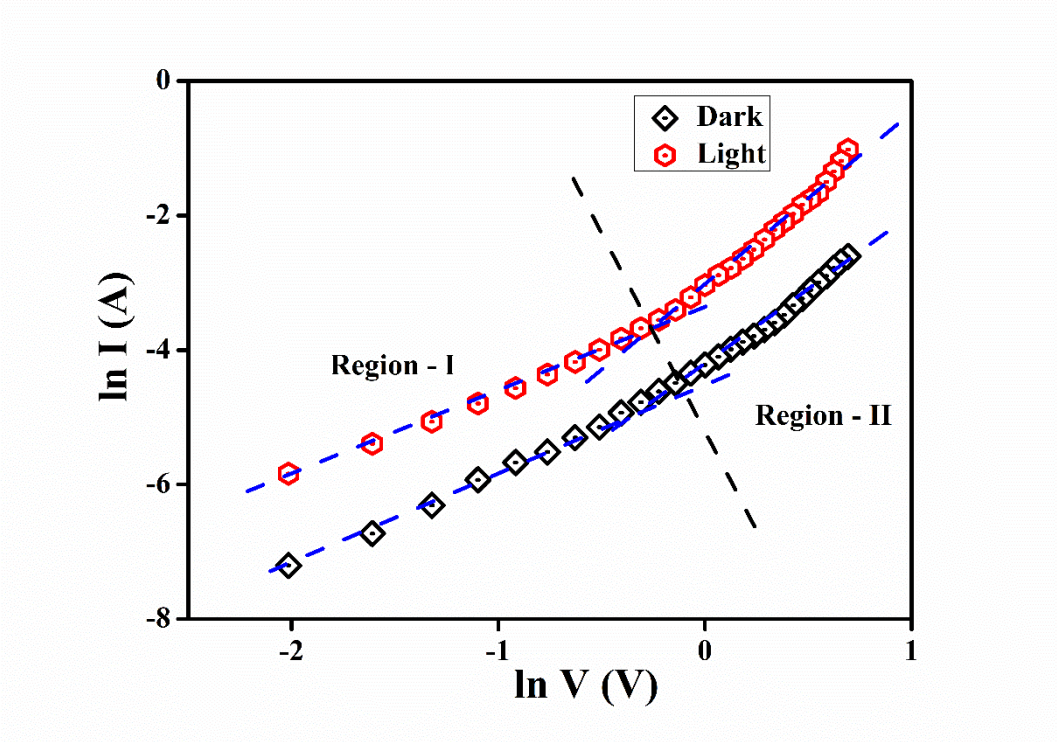

Figure 2.16 *ln I vs. ln V* curves for **1**under dark and irradiation conditions.

TheSCLC theory has been adopted to estimate the performance of the device and the effective carrier mobility from the higher voltage section of the I*vs.*V^2 plot (**Figure 2.17**) obeys the Mott-Gurney **Equation 8**.[39,44-47]

$$I = \frac{9\mu_{eff}\varepsilon_0\varepsilon_r A}{8}\left(\frac{V^2}{d^3}\right) \qquad \textbf{(8)}$$

where, ε_0, ε_r, μ_{eff} and*I*denote the permittivity of free space, the relative dielectric constant of the synthesized material,effectivemobilityand current, respectively.

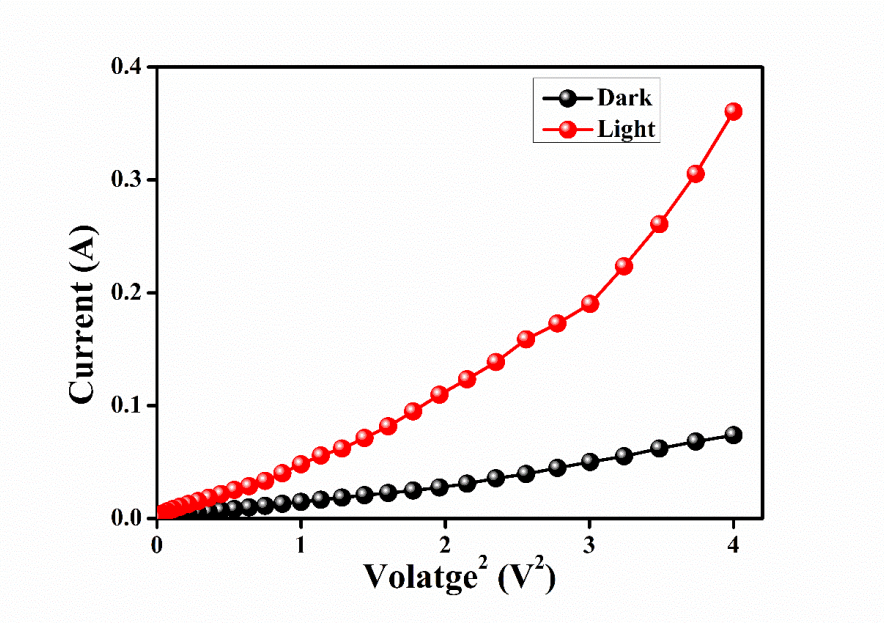

Figure 2.17 *I vs.* V^2 curves for **1** under dark and irradiation condition.

The relative dielectric constant, 0.486, was obtained from the capacitance *vs.* frequency plot at constant bias potential (**Figure 2.17**)[48] for **1** .The assessed transit time ($\boldsymbol{\tau}$) and diffusion length ($\boldsymbol{L_D}$) to analyse charge transport across the junction also support the charge mobilisation conjecture. The slope of SCLC region (Region-II) in logarithmic representation of forward *I-V* curve (**Figure 2.16**) was used to evaluate the $\boldsymbol{\tau}$from (**Equation 9**).[48]

$$\boldsymbol{\tau = \frac{9\varepsilon_0\varepsilon_r A}{8d}\left(\frac{V}{I}\right)} \qquad \textbf{(9)}$$

$$\boldsymbol{\mu_{eff} = \frac{qD}{kT}} \qquad \textbf{(10)}$$

$$\boldsymbol{L_D = \sqrt{2D\tau}} \qquad \textbf{(11)}$$

Here, *D* = the diffusion coefficient.Dwas determined from Einstein–Smoluchowski equation (**Equation 10**).[48]Diffusion length ($\boldsymbol{L_D}$) (**Equation11**) of charge carrier plays an influential role in device performance when a MS junction is formed.All the calculated parameters support the improved charge transport properties of the material after light irradiation (**Table 2.5**). The higher mobility implies a higher transport rate under irradiation.On the other hand, photo-irradiation increased the number of charge carriers.

As the L_D increases under illumination, the charge carriers may travel a longerpath before being recombined.This represents the ultimate increase in current. The improved photo-irradiation performance of **1** indicates improved charge transfer kinetics, which encourages its use in semiconductor devices.

Table 2.5 Charge conducting parameters of **1**.

Condition	ε_r	μ_{eff} **($m^2V^{-1}s^{-1}$)**	τ **(sec)**	$\mu_{eff}\tau$	D	L_D **(m)**
Dark	3.66×10^{-1}	6.26×10^{-4}	5.02×10^{-10}	3.14×10^{-13}	1.62×10^{-5}	1.27×10^{-7}
Light		4.07×10^{-3}	20.2×10^{-10}	8.22×10^{-13}	1.05×10^{-4}	2.06×10^{-7}

The efficiency of current fabricated semiconductor device has been compared with the results of reported data (**Table 2.6**) and shows the superiority of current work.

Table 2.6 Comparison table of electrical parameters of **1** with other reported results

Material	Rectification ratios (Ion/Ioff)	Ideality factor (η)	Barrier height (eV) ($\emptyset_B$)	Series resistance (Ω) (R_S)	Ref.
ZnCdS	29	2.22	-	17300	**63**
$[Cd(4bpd)(SCN)_2]_n$	46.55	5.52	0.36	-	**64**
$C_{40}H_{34}Cu_2N_6O_{18}$	8.46	2.78	0.47	-	**65**
$[Cd_4L_2(NCO)_6]_n$	12.44	3.47	0.526	5310	**66**
Zn-AA metallogel	49.63	2.16	0.45	3790	**67**
Zn@TAmetallogel	37.06	3.78	0.47	3751	**68**
1	80.85	2.08	0.47	456.70	Present work

From the **Table 2.6** it is clear that the ideal factor of **1** is more ideal (~1) i.e. ideality factor is more near to **1** than the other reported Zn-based polymer made semiconductor devices. Moreover, the series resistance is much lower for **1** compared to other devices. This proves that the performance of our fabricated device is quite better than the reported Zn-based polymer made semiconductor devices.

2.4 Biological Study

2.4.1 Cell culture and maintenance

For this current study different cancer cell lines namely- HeLa (cervical cancer cell line), MDA-MB-231 (triple-negative breast cancer (TNBC)) and HCT-116 (colon cancer) and WI-38 (human normal lung fibroblast) were obtained from NCCS, Pune. These cell lines were sustained in a T25 flask with DMEM, supplemented with 10% Fetal bovine serum, sodium pyruvate (1 mM), non-essential amino acids, L-glutamine (2 mM), penicillin (100 units/L), streptomycin (100 mg/L), and gentamycin (50 mg/L) in a 37°C humidified incubator containing 5% CO_2.

2.4.2 MTT cell proliferation assay

Effect of compound **1** on the cell proliferation of above-mentioned active cells had been carried out by the MTT assay experiment.[69,70,71] Multiplates of 96-wells were used for seeding at a density of 1 $\times 10^4$ cells/well and exposed to different concentration (1 -100 μM) of compound **1** for 48 h. Further in this current study Etoposide was used as a standard control considering its tremendous anti-proliferative activity.The wells were allowed for incubation followed by the addition of the MTT solution (0.5 mg/ml) and further incubated under humidified condition containing 5% CO_2 at 37°C. The wells were allowed to stay for 4 h followed by dissolution in DMSO (100 μL) per well and the absorbance was measured at 570 nm using microplate reader. Cell viability was expressed as a percentage of the control experimental setup.

2.4.3 Trypan blue exclusion assay

Trypan blue exclusion assay was performed and the number of viable cells present in the cell suspension was determined. One such experiment was briefly described. MDA-MB-231 cells were exposed to experimental solution of **1** and after treatment, the cells were resuspended within 1 x PBS buffer and mixed with trypan bluesolution (0.4%) in 1:1 dilutionfor the duration of 10 min and counted with hemo-cytometer.[72]

2.4.4 Cell cycle profiling assay by propidium iodide staining

The MDA-MB 231 cells were seeded in each petri dish for 24 h and then were treated with different concentration of the compound **1** (10µM, 20 µM, and 30 µM) for the time period of 48 h. Post treatment, cells were fixed by 75% ethanol for 24hat −20 °C.After centrifugation, the cells pellets were re-suspended in 1×PBS buffer and RNaseA (20 µM) was treated for 2 h at 37°C. Finally, propidium iodide (PI) was added and incubated at room temperature for 20 min and were analyzed using BD FACS Verse flow cytometer and analysed using BD FACS DIVA software.[73]

2.4.5 Annexin V-FITC/PI staining for apoptosis assay

Flow cytometric analysis was performed to study the initiation of apoptosis using the Annexin V-FITC apoptosis detection kit (BD Bioscience).[72,73]The MDA-MB 231 cells were seeded in a 6 well plate and post-treatment control and compound **1** (10 µM, 20 µM, and 30 µM) treated cells were harvested with 1X Trypsin and washed in ice cold 1xPBS followed by re-suspended in 1X binding buffer (100µL). Finally, cells were incubated with 4 µL of annexin V-FITC and 4 µL of PI for 15 min at room temperature in dark before acquiring data using BD FACS Verse flow cytometer. Annexin V/FITC positive cells were regarded as apoptotic cells analysed using Cell Quest Software (BD Biosciences).

2.4.6 Cellular ROS measurement

The intercellular ROS (reactive oxygen species) production due to catalytic influence of compound **1** treatment had been measured by DCFDA method.[74] The MDA-MB 231 cells were seeded in a 6 well plate and treated with test compound **1** (10 µM, 20 µM, and 30 µM)

for 48 h time period. Post-treatment media were discarded and incubated with 10 µM H_2DCFDA for 30 min at 37°C. For fluorescent imaging, H_2DCFDA incubated cells were washed, resuspended in 1xPBS and directly imaged under fluorescent microscope (Leica). For flowcytometric analysis cells were then trypsinized, washed with 1x PBS buffer and collected in centrifuge tubes. DCF fluorescence was then measured using BD FACS Verse flow cytometer.

2.4.7 Caspase 3/7 activation assay

To estimate the changes in caspase 3 protease activity, MDA-MB 231 cells were treated with the compound **1** and colorimetric assay using caspase 3/7 assay kit (abcam) was completed.[72]After treating with the desired concentration of compound **1** (10, 20, and 30 µM) cell lysates were prepared from MDA-MB 231 cells, with RIPA buffer method using aliquot of protein (150 µg) per step. DTT (10 mM) and DEVD-p-NA substrate (200 µM) were added according to manufacturer's decorum and incubated at 37°C for 2 h. Finally, absorbance was recorded at 400 nm in microplate reader and the graph was plotted.

2.4.8 Apoptotic Nuclear Morphology Study by DAPI Staining

Upon addition of compound **1** a morphological change to MDA-MB 231 cells had been examined by DAPI (4′, 6-diamidino-2-phenylindole) staining.[75]The MDA-MB 231 cells were sowed in 6-well plates containing coverslips and preserved with respective quantities for 48 h. Post treatment cells were washed with 1x PBS and DAPI staining was done under fluorescence microscope (Leica).

2.4.9 Detection of Mitochondrial Membrane Potential by JC1 staining

The changes in mitochondrial membrane permeability were determined by JC1 (Molecular probes). Briefly, MDA-MB 231 cells were treated with test compound **1** (10 µg/ml, 20 µg/ml, and 30 µg/ml) for the indicated period, harvested, washed twice in 1×PBS, resuspended in PBS supplemented with JC-1 dye (3µM final concentration), incubated for 15 min in the dark at 370 C and flow cytometric analysis was immediately performed using a FACS-Verse instrument (BD) or images were captured with a fluorescent microscope (Leica).

2.4.10 Cytotoxicity studies of compound1against cancer cell lines

The cytotoxic ability of compound **1** has been assessed using different cell lines and out of them four cell lines - MDA-MB 231 (human breast adenocarcinoma), HCT-116 (colon Cancer cell), HeLa (cervical cancer), HepG2 (liver cancer cells) have responded satisfactorily and the results had been compared with the effect of WI-38 (normal lung fibroblast cell line). Etoposide has been used as a standard control (**Figure 2.18**) to compare the ability of new drug. The MTT assay shows the drug efficacy of compound **1** in inhibiting the proliferation of MDA-MB-231 (IC_{50}:19.43 ±1.36 µM) is highest compared to other cancer cells (IC_{50}:24.43 ± 2.02 µM (HeLa), 26.06 ± 3.48 µM (HCT-116), 44.28 ± 3.04 µM (HepG2). The trypan blue assay was done using MDA-MB 231 and WI-38 cell (normal) line and the results had shown the dose-dependent increase in intensity.Thisobservation indicates that the significant higher cytotoxic ability of compound **1** in MDA-MB-231 cells, as compared to normal cells WI-38 (**Figure 2.18d**). To support the findings, the phase contrast microscopic imaging of compound **1** treated with MBA-MB 231 cells was performed which had shownthe concentration-dependent increase in the level of morphological change to induce cell death of MDA-MB 231 cells compared to control setup.

2.4.11 The cell cycle progression by inducing G2/M arrest

FACS (Fluorescence activated cell sorting)analysis using PI (propidium iodide) was performed to measure the effects of **1** on cell cycle distribution profile of MDA-MB 231 cells and their anti-proliferative mechanism. Interestingly flow cytometric data clearly show a significant level of increase in the G2/M phase cell proportion upon addition of **1** which is accompanied by a significant decrement in G1 phase cell population. A dose dependent increase in induction of G2/M arrest at a concentration of 10 µM, 20 µM, and 30 µM of **1**showed by 20.12%, 36.2% and 55.24 % of cell population respectively (**Figure 2.19b**).

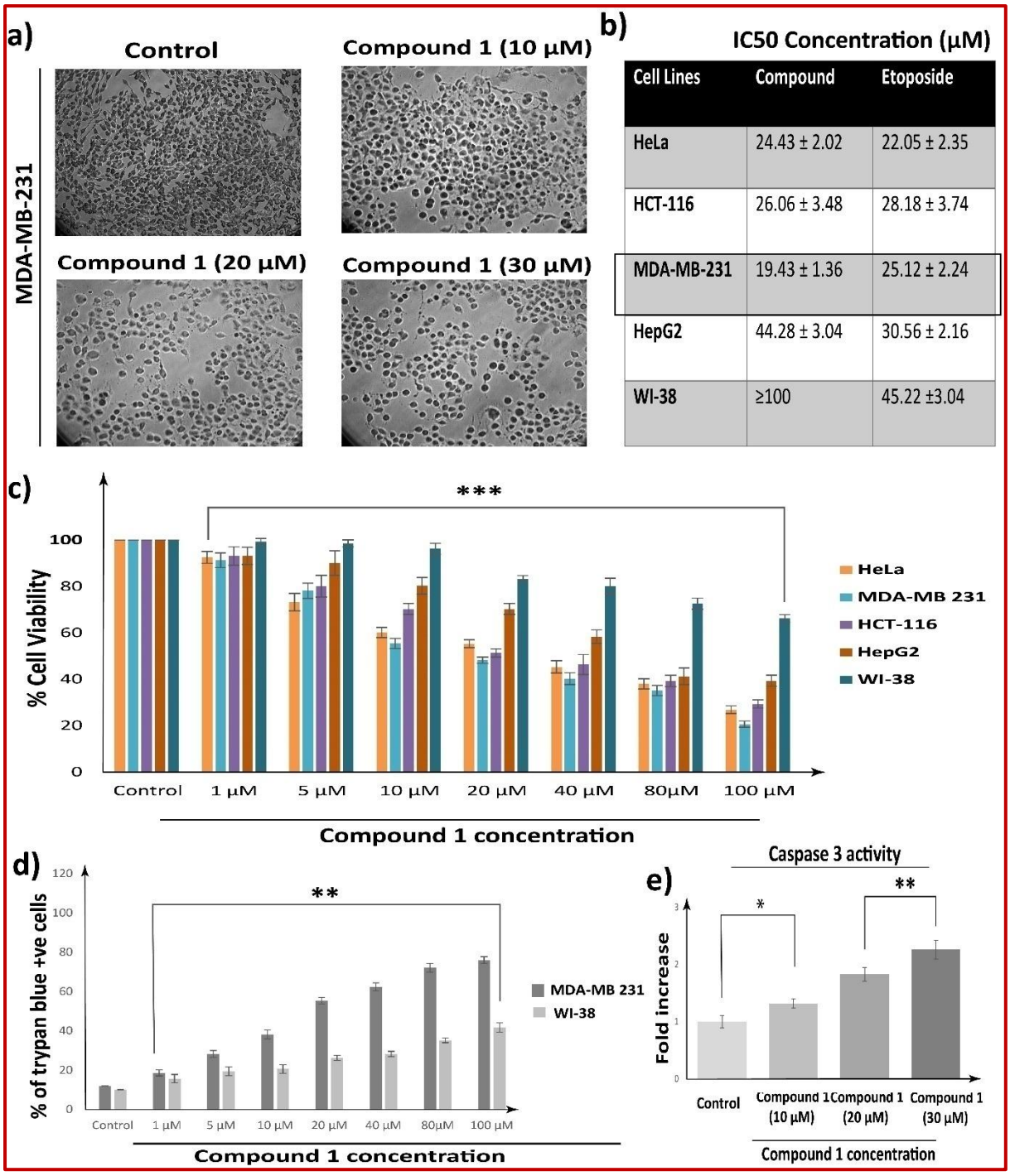

Figure 2.18 Photomicrographs (**a**) show the dose-dependent anti-proliferative effect ofSK06A in MDA-MB 231. (**b, c**) Cytotoxic activity (IC_{50}) of **1** using the MTT assay,(**d**) Trypan blue assay. Cell line includes HeLa, MDA-MB 231, HCT-116, HepG2 (cancer cells), and WI-38 cells (normal cell line),(**e**) Estimation of the changes in caspase 3 protease activity.

2.4.12 Apoptotic cell death and involves activation of caspase 3

Further flow cytometric data from Annexin V-FITC/PI FACS assay showed an increased number of apoptotic cell population with increase in the concentration of compound **1**. Upon treatment of **1** for 48h the annexin V-FITC^{+}/PI^{-} (early apoptotic) and annexin V-FITC^{+}/PI^{+} (late apoptotic) cell population have been increased to 7.80%, 12.01% and 32.67% respectively in comparison to 0.01% in control setup.

To further reinstate our finding, thecaspase-3/7 activity assay was performed treating compound **1.** The results (**Figure 2.18e)** designate thedose dependent increase in caspase 3 activity at a concentration of 10,20 and 30 µMof**1**and it is observed that 1.32-times, 1.82-times and 2.26-times increase in caspase 3 activity, respectively when compared with control set up. This observation specificallyrecommends that the compound **1** mediates death of MDA-MB 231 cells which is due to apoptosis induction, persuaded by increase caspase 3.

2.4.13 DNA damage and induction of intracellular ROS accumulation

The H_2DCFDA (2′,7′-dichlorodihydrofluorescein diacetate) fluorescence assay and ROS generation were measured using fluorescence microscopic and flow-cytometric analysis for establishing the apoptotic cell death mechanism that was induced by the compound **1** due to intracellular ROS accumulation. A dose dependent increase in the level of green fluorescent intensity as compared to control untreated cells with **1** treated cell indicates the intracellular ROS accumulation even at a concentration 10 µM. Nonetheless, MDA-MB 231 cells pre-treated with 10 mM N-Acetyl-Cysteine (NAC), a potent and widely accepted inhibitor of ROS, has decreased compound **1** induced ROS generation in comparison to compound **1** treatment alone, at a concentration of 20 µM (**Figure 2.20a**). Moreover, flow cytometric data also show

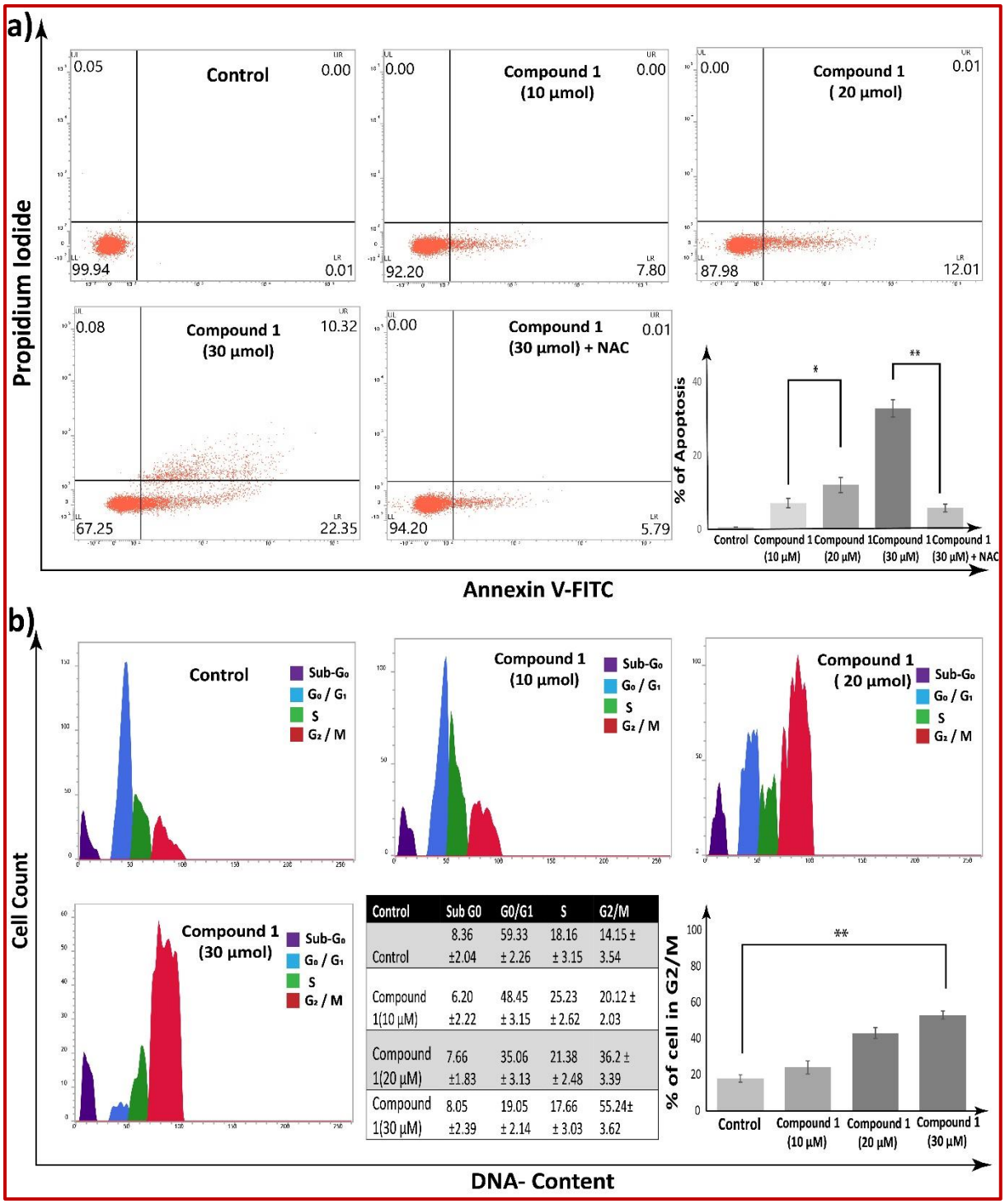

Control	Sub G0	G0/G1	S	G2/M
Control	8.36 ±2.04	59.33 ± 2.26	18.16 ± 3.15	14.15 ± 3.54
Compound 1(10 µM)	6.20 ±2.22	48.45 ± 3.15	25.23 ± 2.62	20.12 ± 2.03
Compound 1(20 µM)	7.66 ±1.83	35.06 ± 3.13	21.38 ± 2.48	36.2 ± 3.39
Compound 1(30 µM)	8.05 ±2.39	19.05 ± 2.14	17.66 ± 3.03	55.24± 3.62

Figure 2.19 (**a**)Quantification of apoptosis Induction *via* flow cytometric analysis of control and compound **1** treated cells that were stained with annexin V-FITC/PI.(**b**)Cell cycle profiling assay by propidium iodide staining using BD FACS Verse flow cytometer.

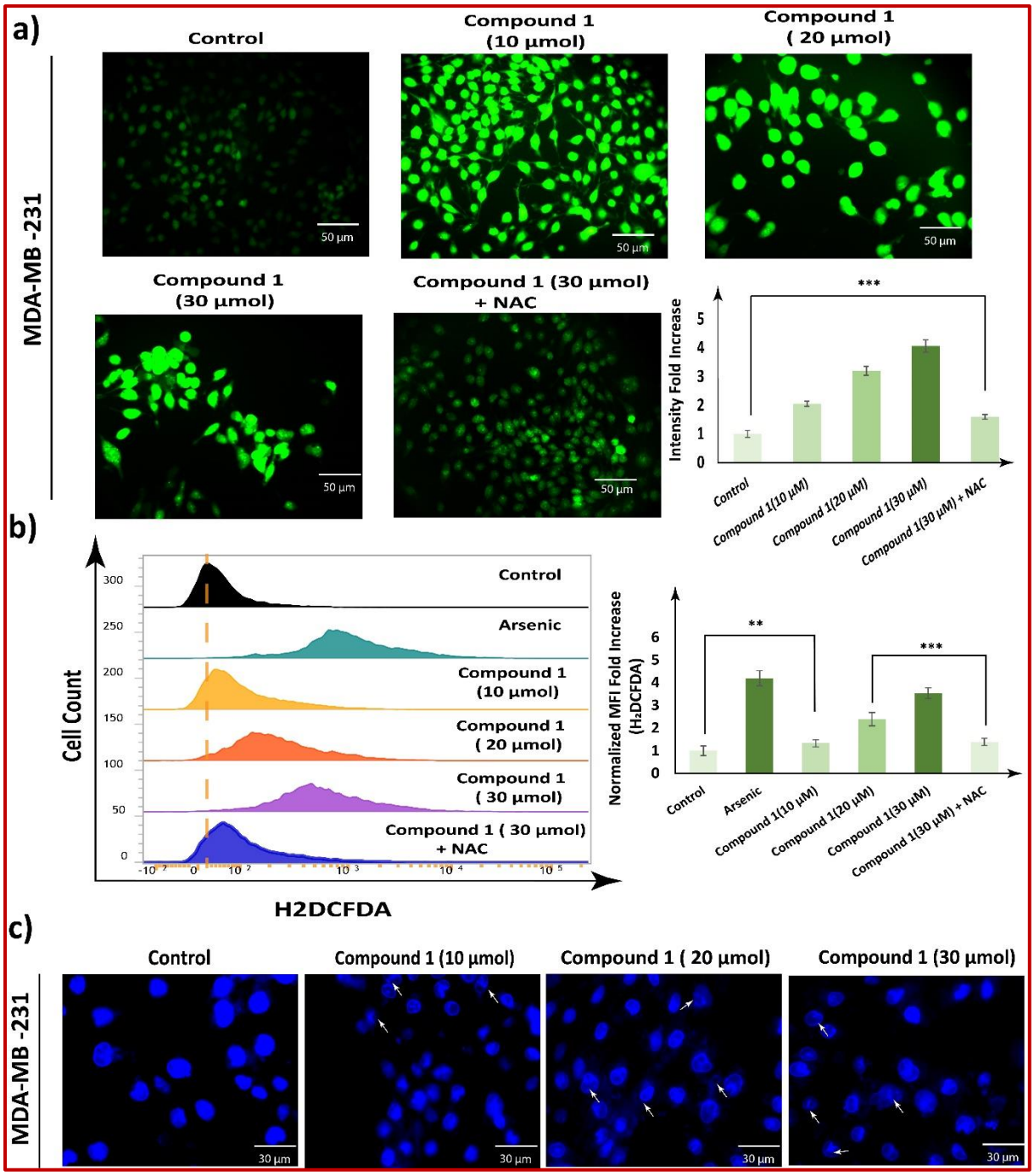

Figure 2.20 Fluorescence Microscopic (**a**) and flowcytometric (**b**) analysis to estimate the intercellular reactive oxygen species (ROS) production due to compound **1**treatment using DCFDA method. Apoptotic Nuclear Morphology Study by DAPI Staining (**c**) for the detection of compound **1** mediated DNA damage.

dose dependent growth in the level of mean fluorescent intensity (MFI) in compound **1** treated cells (**Figure 2.20b**). Further, DAPI staining also showed dose dependent increase in polynuclear fragmentation and nucleus shrinking in MDA-MB 231 cells in response to compound **1** treatment. In comparison no polynuclear fragmentation or nucleus shrinking was observed in control set (**Figure 2.20c**). Therefore, the observation clearly indicates that intracellular compound **1** mediated DNA fragmentation and ROS accumulation is involved in compound **1** mediated apoptotic cell death.

2.4.14 Compound 1-induced mitochondrial membrane potential disruption

In order to examine the potential disruption of mitochondrial membrane potential (MMP) following treatment with compound **1** in MDA-MB 231 cells, additional analysis was conducted. MMP was measured by JC1 staining using both fluorescence microscopic and flow-cytometric methods. Dose-dependent increase in green fluorescence intensity or decrease in the red/green fluorescence intensity ratio in response to Compound **1** treatment after 24h was observed (**Figure 2.21(a,b)**). Further, flow cytometric analysis showed a dose-dependent increase in green fluorescence intensity upon exposure to Compound **1** (**Figure 2.21(c, d)**). On treatment with Compound **1**an increase in JC-1 green fluorescence intensity in 43.06%, 85.23%, and 91.06% of the cellular population at a concentration of 10, 20, and 30 µg/ml, respectively, in comparison to 4.35% in the control cell population after 24h (**Figure 2.21(c, d)**) is observed. Disruption in the MMP of the MDA-MB 231 cells in response to Compound **1**could play a central role in Compound **1**induced apoptotic cell death in MDA-MB-231 cells.

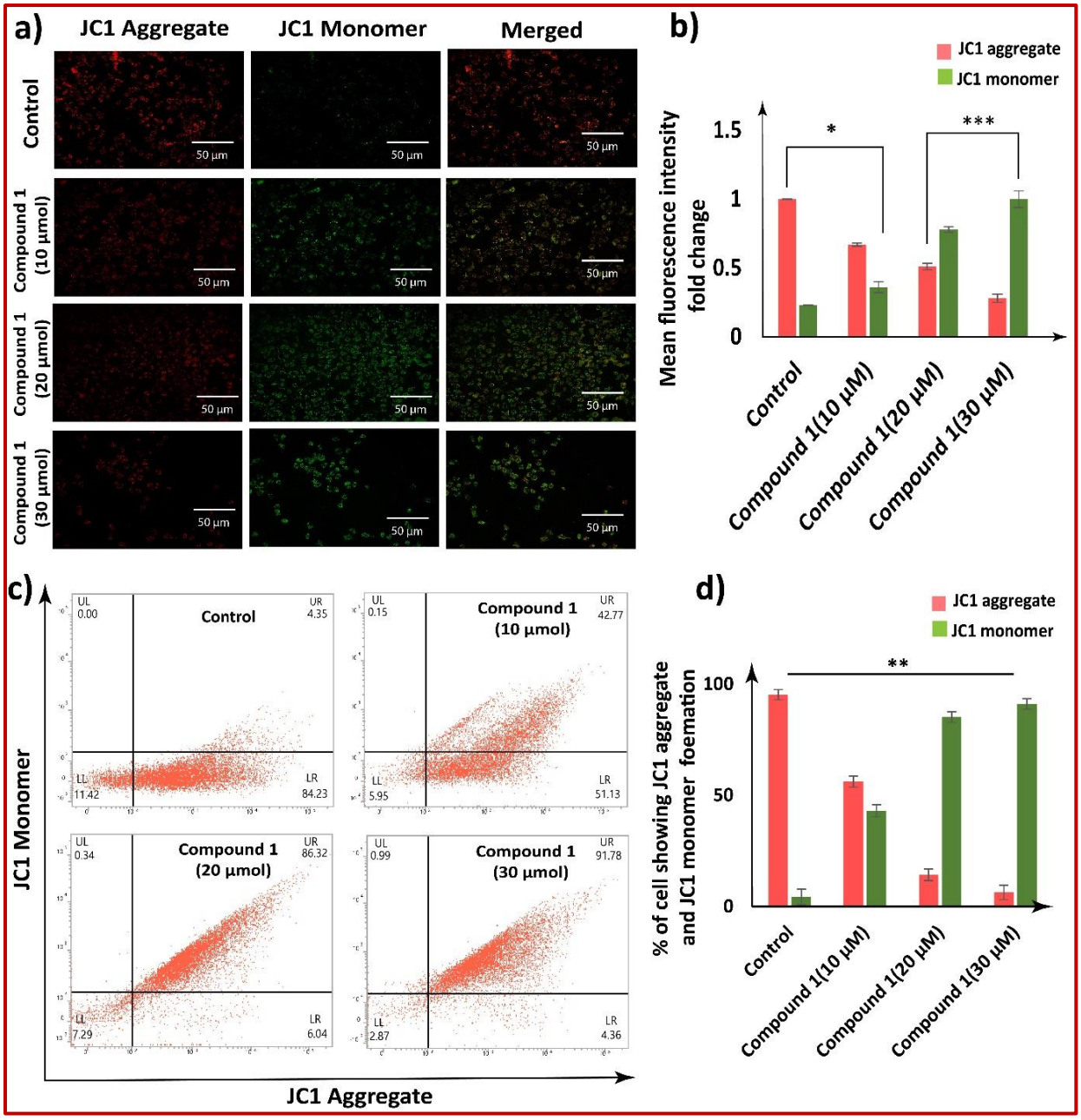

Figure 2.21 Fluorescence Microscopic (**a** and **b**) and flowcytometric (**c** and **d**) analysis to estimate the mitochondrial membrane potential disruption due to compound **1**treatment using JC1.

2.5 Conclusion

A 3D Zn(II)-coordination framework consisting of two bridging motifs – 2,5-thiophene dicarboxylate; Pyridine-4-carboxaldehyde isonicotinoyl hydrazinehas been used to design Schottky Diode barrier (band gap 3.74 eV) and shows high electrical conductivity (2.21×10^{-5} S cm^{-1}) which has been improved upon light irradiation (6.36×10^{-5} S cm^{-1}). The material shows promising anticancer activity against MDA-MB-231 cancer cells. Detail plausible mechanisms of both photo conductivity and efficient anticancer activity have been studied. Therefore, we expect a break though in the research of Zn(II)-based coordination polymer to instigate multifunctional applications to aid the Sustainable Development Goals.

2.6 References

(1) Zhou, H. –C. ‘‘Joe’’ and Kitagawa, S. Metal–Organic Frameworks (MOFs), *Chem. Soc. Rev.* **2014**, *43*, 5415 – 5418.

(2) Kaskel (Ed), S. The Chemistry of Metal-Organic Frameworks: Synthesis, Characterization, and Applications, Vols. 1 & 2, Wiley-VCH Verlag GmbH & Co KGaA, Weinheim, Germany, 2016.

(3) Miller, S. E.; Teplensky, M. H.; Moghadam, P. Z. and Fairen-Jimenez, D. Metal-organic frameworks as biosensors for luminescence-based detection and imaging. *Interface Focus*. **2016**, *6*, 20160027.

(4) Shi, Y. X.; Chen, H. H.; Zhang, W. H.; Day, G. S.; Lang, J. P. and Zhou, H. C. Photoinduced nonlinear contraction behaviour in metal–organic frameworks. *Chem. Eur. J.* **2019**, *25*, 8543-8549.

(5) Li, N. Y.; Liu, D.; Abrahams, B. F. and Lang, J. P. Covalent switching, involving divinylbenzene ligands within 3D coordination polymers, indicated by changes in fluorescence. *ChemComm.* **2018**, *54*, 5831-5834.

(6) Shi, Y. X.; Li, W. X.; Zhang, W. H. and Lang, J. P. Guest-induced switchable breathing behavior in a flexible metal–organic framework with pronounced negative gas pressure. *Inorg. Chem.* **2018**, *57*, 8627-8633.

(7) Shi, Y. X.; Li, W. X.; Chen, H. H.; Young, D. J.; Zhang, W. H. and Lang, J. P. A crystalline zinc (II) complex showing hollow hexagonal tubular morphology evolution, selective dye absorption and unique response to UV irradiation. *Chem. Comm.* **2017**, *53*, 5515-5518.

(8) Liu, D.; Ren, Z. G.; Li, H. X.; Lang, J. P.; Li, N. Y. and Abrahams, B. F. Single- Crystal- to- Single- Crystal Transformations of Two Three- Dimensional Coordination Polymers through Regioselective [2+ 2] Photodimerization Reactions. *Angew. Chem., Int. Ed.* **2010**, *49*, 4767-4770.

(9) Shi, Y. X.; Zhang, W. H.; Abrahams, B. F.; Braunstein, P. and Lang, J. P. Fabrication of photoactuators: Macroscopic photomechanical responses of metal–organic frameworks to irradiation by UV light. *Angew. Chem., Int. Ed.* **2019**, *58*, 9453-9458.

(10) Yang, F.; Xu, G.; Dou, Y.; Wang, B.; Zhang, H.; Wu, H.; Zhou, W.; Li, J. R. and Chen, B. A flexible metal–organic framework with a high density of sulfonic acid sites for proton conduction. *Nat. Energy*. **2017**, *2*, 877-883.

(11) Wang, B.; Lv, X. L.; Feng, D.; Xie, L. H.; Zhang, J.; Li, M.; Xie, Y.; Li, J. R. and Zhou, H. C. Highly stable Zr (IV)-based metal–organic frameworks for the detection and removal of antibiotics and organic explosives in water. *J. Am. Chem. Soc*. **2016**, *138*, 6204-6216.

(12) Lv, X. L.; Wang, K.; Wang, B.; Su, J.; Zou, X.; Xie, Y.; Li, J. R. and Zhou, H. C. A base-resistant metalloporphyrin metal–organic framework for C–H bond halogenation. *J. Am. Chem. Soc.* **2017**, *139*, 211-217.

(13) Qiu, T.; Liang, Z.; Guo, W.; Tabassum, H.; Gao, S. and Zou, R. Metal–Organic Framework-Based Materials for Energy Conversion and Storage. *ACS Energy Lett.* **2020**, *5*, 520–532.

(14) Sima, J. Y.; Li, H. X.; Young, D. J.; Braunstein, P. and Lang, J. P. Reversible dielectric switching behavior of a 1D coordination polymer induced by photo and thermal irradiation. *Chem. Comm.* **2019**, *55*, 3532-3535.

(15) Horcajada, P.; Serre, C.; Vallet-Regí, M.; Sebban, M.; Taulelle, F.; Férey, G. Metal–Organic Frameworks as Efficient Materials for Drug Delivery. *Angew Chem., Int. Ed.* **2006**, *45*, 5974-5978.

(16) Jihye, P.; Allison, C. H.; Zhehao, H.; Gan, C.; AndreyYakovenko, A.; Xiaodong, Z.; Zhenan B. High Thermopower in a Zn-Based 3D Semiconductive Metal− Organic Framework. *J. Am. Chem. Soc.* **2020**, *142*, 20531-20535.

(17) Patel, P.; Parmar, B.; Kureshy, R. I.; Noor-ul, H. K. and Suresh, E. Amine-functionalized Zn (II) MOF as an efficient multifunctional catalyst for CO_2 utilization and sulfoxidation reaction. *Dalton Trans.***2018**, *47*, 8041-8051.

(18) Zhu, L.; Liu, X. Q.; Jiang, H. L. and Sun, L. B. Metal–organic frameworks for heterogeneous basic catalysis. *Chem. Rev.* **2017**,*117*, 8129-8176.

(19) Yao, R. X.; Cui, X.; Jia, X. X.; Zhang, F. Q. and Zhang, X. M. A luminescent zinc (II) metal–organic framework (MOF) with conjugated π-electron ligand for high iodine capture and nitro-explosive detection. *Inorg. Chem.***2 016**, *55*, 9270-9275.

(20) Wu, D.; Liu, J.; Jin, J.; Cheng, J.; Wang, M.; Yang, G. and Wang, Y. Y. New doubly interpenetrated MOF with [Zn_4O] clusters and its doped isomorphic MOF: sensing, dye, and gas adsorption capacity.*Cryst. Growth Des.* **2019**, *19*, 6774-6783.

(21) Sun, Y.; Zheng, L.; Yang, Y.; Qian, X.; Fu, T.; Li, X.; Yang, Z.; Yan, H.; Cui, C. and Tan,W.Metal–Organic Framework Nanocarriers for Drug Delivery in Biomedical Applications, *NanomicroLett*.**2020**,*12*, 103.

(22) Mallakpour, S.; Nikkhoo, E. and Hussain, C. M. Application of MOF materials as drug delivery systems for cancer therapy and dermal treatment, *Coord. Chem. Rev.* **2022**, *451*, 214262.

(23) Wang, H.; Zhu, Q. -L.; Zou, and Xu, Q.Metal-Organic Frameworks for Energy Applications, *Chem.* **2017**, *2*, 52-80.

(24) Liu, X.; Kozlowska, M.; Okkali, T.; Wagner, D.; Higashino, T.; Brenner-Weiß, G.; Marschner, S. M.; Fu, Z.; Zhang, Q.; Imahori, H.; Br-se, S.;Wenzel, W.; Wçll, C. and Heinke, L. Photoconductivity in Metal–Organic Framework (MOF) Thin Films, *Angew. Chem. Int. Ed.* **2019**, *58*, 9590 –9595.

(25) Chandra, A.; Das, M.; Pal, K.; Jana, S.; Dutta, B.; Ray, P. P. and Sinha, C. Three-dimensional-coordination polymer of Zn (II)-carboxylate: Structural elucidation, photoelectrical conductivity, and biological activity. *ACS omega*.**2019**, *4*, 17649-17661.

(26) Sthel, M. S.; Tostes, J. G. and Tavares, J. R. Current energy crisis and its economic and environmental consequences: Intense human cooperation. 2013.

(27) Hayashi, K.; Matsuishi, S.; Kamiya, T.; Hirano, M. and Hosono, H. Light-induced conversion of an insulating refractory oxide into a persistent electronic conductor. *Nature*. **2002**,*419*, 462-465.

(28) Jiang, H.; Hershtig, G.; Richter, S.andJelinek, R. Light-induced conductivity in a solution-processed film of polydiacetylene and perylenediimide. *J. Phys. Chem. Lett.***2016**, *7*, 1628-1631.

(29) Cojocariu, C. and Rochon, P. Light-induced motions in azobenzene-containing polymers. *Pure Appl. Chem.* **2004**, *76*, 1479-1497.

(30) Qazi, A.;Hussain, F.; Rahim, N. A.; Hardaker, G.; Alghazzawi, D.; Shaban, K.;Haruna, K. Towards sustainable energy: a systematic review of renewable energy sources, technologies, and public opinions. *IEEE Access*. **2019**, *7*, 63837-63851.

(31) Gandini, A.;Lacerda, T. M.; Carvalho, A. J.andTrovatti, E. Progress of polymers from renewable resources: furans, vegetable oils, and polysaccharides. *Chem. Rev.***2016**, *116*, 1637-1669.

(32) Wang, C.; Liu, D. and Lin, W. Metal–organic frameworks as a tunable platform for designing functional molecular materials. *J. Am. Chem. Soc.* **2013**, *135*, 13222-13234.

(33) H. A. O. Hill.; A. Galdes, Zinc metalloenzymes, in Inorganic Biochemistry, Vol. 3 (H. A. O. Hill (Ed.)), RSC Publishing, 1983.

(34) Pellei, M.; Bello, F. D.; Porchia, M. and Santini, C. Zinc coordination complexes as anticancer agents, *Coord. Chem. Rev.* **2021**, *445*, 214088.

(35) Porchia, M.; Pelei, M.; Bello, F. D. and Santini,C. Zinc Complexes with Nitrogen Donor Ligands as Anticancer Agents, *Molecules.* **2020**, *25*, 5814.

(36) Dutta, B.; Hazra, A.; Datta, S.; Sinha, C.; Banerjee, P. and Mir, M.H. In Situ Trans–Cis Isomerization of Naphthylvinylpyridine Ligand in a Zinc (II) Coordination Polymer: Liquid and Vapor Phase Sensing of Mutagenic Pollutants and Nitroexplosives. *ACS Appl. Poly. Mater.***2 022**, *4*, 2841-2850.

(37) Chandra, A.; Dutta, B.; Pal, K.; Jana, K. and Sinha , C. Designing of an Adipic acid bridged Zn (II) coordination polymer: Synthesis and biological study, *J. Mol. Str.* **2021**, *1243*, 130923.

(38) Blatov V. A.; Shevchenko A. P.; Proserpio D. M. Applied topological analysis of crystal structures with the program package ToposPro, *Cryst. Growth Des.***2014**, *14*, 3576–3586.

(39) O'Keeffe M.; Peskov M. A.; Ramsden S. J.; Yaghi O. M. The reticular chemistry structure resource (RCSR) database of, and symbols for, crystal nets. *Acc. Chem. Res.* **2008**, *41*, 1782-1789.

(40) Alexandrov E. V.; Blatov V. A.; Kochetkov A. V.; Proserpio D.M. Underlying nets in three-periodic coordination polymers: topology, taxonomy and prediction from a computer-aided analysis of the Cambridge Structural Database. *CrystEngComm*. **2011**, *13*, 3947-3958.

(41) Blatov V. A.; Shevchenko A. P. Simplify to understand: how to elucidate crystal structures. *Struct. Chem.***2021**.

(42) Alexandrov E. V.; Shevchenko A. P.; Blatov V. A. Topological Databases: Why Do We Need Them for Design of Coordination Polymers? *Cryst. Growth Des.***2019**, *19*, 2604-2614.

(43) Fay, F.; Linossier, I.; Langlois, V.; Haras, D.; Vallee-Rehel, K.,SEM and EDX analysis: Two powerful techniques for the study of antifouling paints, *Prog. Org. Coatings*. **2005**, *54*, 216.

(44) Frisch, M. J.; Trucks, G. W.; Schlegel, H. B.;Scuseria, G. E.;Robb, M. A.;Cheeseman, J. R.;Scalmani, G.;Barone, V.;Mennucci, B.;Petersson, G. A.;Nakatsuji, H.;Caricato, M.;Li, X.;Hratchian, H. P.;Izmaylov, A. F.;Bloino, J.;Zheng, G.; Sonnenberg, J. L.; Hada, M.; Ehara, M.; Toyota, K.;Fukuda, R.;Hasegawa, J.; Ishida, M.; Nakajima, T.; Honda, Y.; Kitao, O.; Nakai, H.; Vreven, T.; Montgomery Jr., J. A.; Peralta, J. E.; Ogliaro, F.; Bearpark, M.; Heyd, J. J.; Brothers, E.; Kudin, K. N.; Staroverov, V. N.; Kobayashi, R.; Normand, J.;Raghavachari, K.; Rendell, A.; Burant, J. C.; Iyengar, S. S.; Tomasi, J.; Cossi, M.; Rega, N.; Millam, J. M.; Klene, M.; Knox, J. E.; Cross, J.

B.;Bakken, V.;Adamo, C.; Jaramillo, J.; Gomperts, R.; Stratmann, R. E.; Yazyev, O.; Austin, A. J.; Cammi, R.; Pomelli, C.; Ochterski, J. W.; Martin, R. L.; Morokuma, K.; Zakrzewski, V. G.; Voth, G. A.; Salvador, P.; Dannenberg, J. J.; Dapprich, S.; Daniels, A. D.; Farkas, O.; Foresman, J. B.; Ortiz, J. V.; Cioslowski, J. ; Fox, D. J.; Gaussian 09, Revision D.01, Gaussian Inc., Wallingford, CT, 2009.

(45) Becke, A. D. Density- functional thermochemistry. III. The role of exact exchange, *J. Chem. Phys.* **1993**, *98*, 5648-5652.

(46) Hay, P.J.;Wadt, W.R. Ab initio effective core potentials for molecular calculations. Potentials for K to Au including the outermost core orbitals. *J. Chem. Phys*. **1985**,*82*, 299-310.

(47) O'Boyle, N. M.; Tenderholt, A. L.; Langner, K. M.Cclib: a library for package- independent computational chemistry algorithms. *J. Comput. Chem.* **2008**, *29*, 839-845.

(48) Dey, A.; Middya, S.; Jana, R.; Das, M.; Datta, J.; Layek, A. and Ray, P.P. Light induced charge transport property analysis of nanostructured ZnS based Schottky diode. *J. Mater. Sci.: Mater. Electron*. **2016**, *27*, 6325-6335.

(49) Bairy, G.; Dey, A.; Dutta, B.; Ray, P.P. and Sinha, C. 2D Cd (II)-MOF of Pyridyl-Imidazoquinazoline: Structure, Luminescence, and Selective Detection of TNP and Fabrication of Semiconducting Devices. *Cryst. Growth Des*. **2022**, *22*, 3138-3147.

(50) Dutta, B. and Halder, S. Fabrication of Schottky Barrier Diodes Utilizing Schiff Base Compounds and Metal Complexes with Schiff Base Ligands. *ChemistrySelect*. **2023**, *8*, 202301586.

(51) Dey, A.;Middya, S.;Jana, R.; Das, M.; Datta, J.;LayekA.; Ray, P. P.Light induced charge transport property analysis of nanostructured ZnS based Schottky diode. *J. Mater. Sci.: Mater. Electron.* **2016**, *27*, 6325-6335.

(52) Rhoderick, E. H. Metal Semiconductors Contacts, Oxford University Press, Oxford. 1978.

(53) Cheung, S.K.; Cheung, N.W. Extraction of Schottky diode parameters from forward current- voltage characteristics. *Appl. Phys. Lett*. **1986**, *49*, 85-87.

(54) Dey, A.; Layek, A.; Roychowdhury, A.; Das, M.;Datta, J.; Middya, S.; Das D.; Ray, P. P.; Investigation of charge transport properties in less defective nanostructured ZnO based Schottky diode. *RSC Adv.***2015**, *5*, 36560-36567.

(55) Dey, A.; Ray, S. K. Analysis of Photoresponse and Charge Transport Properties of Hydrothermally Synthesized ZnSe Nanoparticle Based Schottky Device.*Int. J. Adv. Sci. Eng.* **2020**,*6*,1-6.

(56) Rhoderick,E.H.Metal Semiconductors Contacts, Oxford University Press, Oxford. 1978.

(57) Cheung, S. K. and Cheung, N. W. Extraction of Schottky diode parameters from forward current- voltage characteristics. *Appl. Phys. Lett.***1986**, 49, 85-87.

(58) Dey, A.; Layek, A.; Roy Chowdhury, A.; Das, M.; Datta, J.; Middya, S.; Das, D. and Ray, P.P. Investigation of charge transport properties in less defective nanostructured ZnO based Schottky diode. *RSC Adv*. **2015,** *5*, 36560-36567.

(59) Gupta, R. K. and Yakuphanoglu, F. Photoconductive Schottky diode based on Al/p-Si/SnS2/Ag for optical sensor applications. *Sol. Energy*. **2012**, 86, 1539-1545.

(60) Miao, X.; Tongay, S.; Petterson, M.K.; Berke, K.; Rinzler, A.G.; Appleton, B.R. and Hebard, A. F. High efficiency graphene solar cells by chemical doping. *Nano Lett*. **2012**, 12, 2745-2750.

(61) Blom, P. W.; De Jong, M. J. M. and Van Munster, M.G. Electric-field and temperature dependence of the hole mobility in poly (p-phenylenevinylene). *Phys. Rev. B*. **1997**, 55, R656.

(62) Naskar, K.; Sil, S.; Sahu, N.; Dutta, B.; Slawin, A. M. Z.; Ray, P. P. and Sinha, C. Enhancement of electrical conductivity due to structural distortion from linear to nonlinear dicarboxylato-bridged Zn (II) 1D-coordination polymers. *Cryst. Growth. Des*.**2019**, *19*, 2632-2641.

(63) Das, M.; Datta, J.; Jana, R.; Sil, S.; Halder, S.; Ray, P.P. Synthesis of rGO–Zn 0.8 Cd 0.2 S via in situ reduction of GO for the realization of a Schottky diode with low barrier height and highly enhanced photoresponsivity. *New J. Chem*.**2017**, *41*, 5476-5486.

(64) Halder, S.; Dey, A.; Bhattacharjee, A.; Ortega-Castro, J.; Frontera, A.; Ray, P.P.; Roy, P. A Cd (II)-based MOF as a photosensitive Schottky diode: experimental and theoretical studies. *Dalton Trans*.**2017**, *46*, 11239-11249.

(65) Hossain, A.; Dey, A.; Seth, S.K.; Ray, P.P.; Ballester, P., Pritchard, R.G., Ortega-Castro, J.; Frontera, A. Mukhopadhyay, S. Enhanced Photosensitive schottky diode behavior of pyrazine over 2-aminopyrimidine ligand in Copper (II)-phthalate MOFs: Experimental and theoretical rationalization. *ACS omega*.**2018**, *3* ,9160-9171.

(66) Ghorai, P.; Dey, A.; Brandao, P.; Ortega-Castro, J.; Bauza, A.; Frontera, A.; Ray, P.P.; Saha, A. The development of a promising photosensitive Schottky barrier diode using a novel Cd (II) based coordination polymer. *Dalton Trans*.**2017**, *46*, 13531-13543.

(67) Karmakar, K.; Dey, A.; Dhibar, S.; Sahu, R.; Bhattacharjee, S.; Karmakar, P.; Chatterjee, P.; Mondal, A.; Saha, B. A novel supramolecular Zn (II)-metallogel: an efficient microelectronic semiconducting device application. *RSC Adv.***2023**, *13*, 2561-2569.

(68) Majumdar, S.; Dey, A.; Sahu, R.; Lepcha, G.; Dey, A.; Ray, P.P.; Dey, B.; An aromatic acid based supramolecular Zn (II)-metallogel for fabricating light-sensitive metal-semiconductor junction type Schottky diode with satisfactory rectification ratios. *Mater. Res. Bull*. **2023**, *157*,112003.

(69) Twentyman, P. R. and Luscombe, M. A study of some variables in a tetrazolium dye (MTT) based assay for cell growth and chemosensitivity. *Br J Cancer.***1987**, *198756*, 279–285.

(70) Mosmann, T. Rapid colorimetric assay for cellular growth and survival: application to proliferation and cytotoxicity assays. *J. Immunol. Methods*.**1963**, *55-63*, 198365.

(71) Strober, W.; Trypan blue exclusion test of cell viability. CurrProtoc Immunol.2001, Appendix 3, Appendix3B.

(72) Miller, E.; Apoptosis measurement by annexin v staining. *Methods Mol. Med*.**2004**, 88, 191–202.

(73) Dutta, A.; Dhara, D.; Parida, P. K.; Si, A.; Yesuvadian, R.; Jana, K. and Misra, A. K. C-Glycosylated cinnamoylfuran derivatives as novel anti-cancer agents. *RSC advances*.**2017**, *7*, 28853-28864.

(74) Eruslanov, E. and Kusmartsev, S. Identification of ROS using oxidized DCFDA and flow-cytometry. *Methods mol. biol*. **2010**, *594*, 57-72.

(75) Vemuri, S. K.; Halder, S.; Banala, R. R.; Rachamalla, H. K.; Devraj, V. M.; Mallarpu, C. S.; Neerudu, U. K.; Bodlapati, R.; Mukherjee, S.; Venkata, S. G. P.; Venkata, G. R. A.; Thakkumalai, M. and Jana, K. Modulatory Effects of Biosynthesized Gold Nanoparticles Conjugated with Curcumin and Paclitaxel on Tumorigenesis and Metastatic Pathways-In Vitro and In Vivo Studies. *Int J Mol Sci*.**2022**, *23*, 2150.

Chapter 3

Exploration of Variable Temperature Magnetism and Electrical Property of a Pyridyl-isonicotinoyl Hydrazone Bridged 3D Mn-MOF with ThiopheneDicarboxylato Link

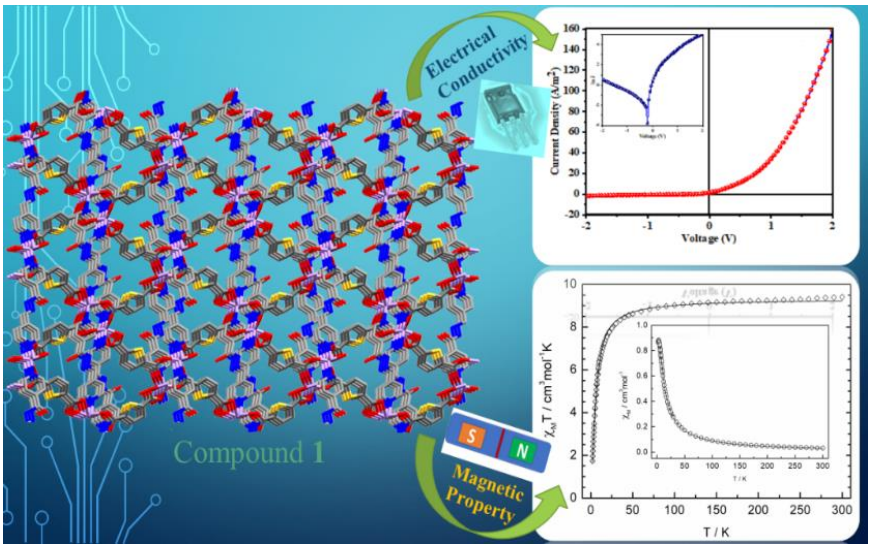

Abstract:

In this current trend of technology dependent civilization multifunctional applicability of coordination polymers (CPs) are highly stimulating. In search of such chemical compounds, a Mn(II) coordinated MOF has been designed. The structure determination of $\{[Mn_2(tdc)_2(pcih)_2(EtOH)]_n\}$ (**1**)(**H_2tdc**=2,5-thiophene dicarboxylic acid, **pcih**=Pyridine-4-carboxaldehyde isonicotinoylhydrazone) has revealed the formation of 3D supramolecular architecture *via* the combined nearly perpendicular bridging of **pcih** and **tdc^{2-}** ligands. Variable Temperature Magnetic measurement of **1** shows weak anti-ferromagnetism ($\chi_M T$, 9.41cm^3Kmol^{-1}at 300 K) with two as good as "isolated" Mn (II) ions (S=5/2 with g ~ 2.07). Magnetic exchange is considered through carboxylato bridged nine/ten atoms inclusive two spanned Mn(II) centres at 4.114 Å. Interestingly, the 3D assembly of **1** exhibits electrical conductivity in the semiconducting region (band gap, 3.72 eV; barrier height, 0.65 eV; series resistance, 0.03Ω). Schottky barrier diode feature is recorded at threshold potential 0.19 V and follows non-Ohmic relation ($I\alpha V^2$) and the conductivity is 3.42× 10^{-5}S m^{-1}. The Galvano-static charge-discharge (GCD) experiment measures the moderate specific capacitance of 1F/g at 2mV/s scan rate.

3.1 Introduction

Magnetic property is unique characteristics of transition metal containing compounds. Transition metal ions have unpaired electrons at any of its redox state and individual electron has both spin and orbital components of magnetic moment. Ions of multi-electrons (d^n, f^n; n>1) show inter-electronic interactions and constitute different states of varying spin and orbital multiplicities those are influenced by the symmetry of their environments. Thus, electronic configuration is dependent on intrinsic ion characteristics, number of adjoining magnetic centres and extrinsic factors such as structure, stereochemistry, and dimensionality,etc.[1] The coordination of π-conjugated ligands with such metal ions provides an opportunity to the unpaired electron(s) for extensive delocalization and the magnetic properties may vary substantially. In recent years, Coordination Polymers (CPs)/Metal−Organic Frameworks (MOFs)[2-6] with magnetically unsaturated centres either from transition metal ions as integral components or captivated with magnetic oxide nanoparticles in the pores of the MOF may constitute a highly challenging material.The

combination of large surface area, high porosity, excellent thermal and chemical stability, sensitivity towards external stimuli (mechanical, thermal, optical etc.)[7-17] and wide conjugation through magnetic centres has originated exploration of many advanced material applications.[18-24]Enzyme immobilized/encapsulated magnetic–MOF offers an interesting device for application in bio sensor such as very accurate and fast blood glucose analysis; cell line analysis of H_2O_2, N_2H_4 etc.[18, 19] Magnetic-NPs in MOF are superior performer than individual components towards hydrogenation catalysis[20], drug delivery[21]and useful in sustainable development through pollution management.[22,23]. In addition to magnetic properties the electrical conductivity of unpaired electron(s) in the material is important towards the perspective of energy sustainability. Most of the MOFs are insulators and the electrical conductivity of these materials are only in recent focus.[24] The CPs or MOFs have their mixed electronic nature and have been useful to generate variation in potential or voltage in metal-semiconductor (CPs or MOFs) junctions.[25-28]Various semiconducting devices such as transistors, diodes, a diode for alternating current(DIAC), photocell, etc. have been fabricated using such hybrid materials. In this field of electrical conductivity, charge transportation is the common criterion, which has been directly dependent on structural parameters.It is well known that there are straight relationships among structure, property, and applications.In this research, Mn^{2+}, a highest spin state 3d transition metal ion (d^5, spin free state), is bridged *via* 2,5-thiophene dicarboxylato (**tdc**$^{2-}$) and a Schiff base, Pyridine-4-carboxaldehyde isonicotinoyl hydrazine(**pcih**) ligands to constitute a 3D supramolecular robust architecture. The spectroscopic studies determine the structure and has been confirmed by single crystal X-Ray diffraction measurements. Temperature dependent magnetic properties and electrical conductivity at ambient condition are reported in this work.

3.2 Experimental Section

3.2.1 Materials and General Methods

Isoniazid (INZ), Isoniazid (INZ), 4-Pyridine Carboxaldehyde, 2,5-thiophene dicarboxylic acid (H_2tdc), and $N_2H_4.H_2O$ were purchased from TCI Chemicals (India) Pvt. Ltd. High purity Manganese (II) Chloride tetrahydrate was purchased from Sigma-Aldrich Co. All other chemicals including solvents were of AR grade and were used without further purification. Pyridine-4-carboxaldehyde isonicotinoyl hydrazine Schiff base was prepared following published procedure.[29]

Infrared (IR) spectrum was recorded using a Perkin Elmer SPECTRUM II LITA FT-IR spectrometer. Elemental analysis (carbon, hydrogen, and nitrogen) of the compound was performed using a PerkinElmer 240C elemental analyzer. Thermogravimetric analysis (TGA) was carried out on a PerkinElmer Pyris Diamond TG/DTA thermal analyzer under a nitrogen atmosphere (flow rate: 50 cm^3 min^{-1}) at the temperature range of 30−800 °C with a heating rate of 20 °C/min. Powder X-ray diffraction (PXRD) patterns in different states of the sample were recorded on a Bruker D8 Discover instrument using Cu−Kα radiation. UV−vis spectra were collected using a PerkinElmer Lambda 25 spectrophotometer.

3.2.2 Synthesis of {[Mn_2(tdc)$_2$(pcih)$_2$(EtOH)]$_n$}, (1)

A solution of **pcih**(0.045 g, 0.2 mmol) in MeOH (2 mL) was slowly and carefully layered onto an aqueous solution (2 mL) of $MnCl_2$, $4H_2O$ (0.039 g, 0.2 mmol) using buffer solution of DMF and MeOH (2 mL, 1:1 v/v) followed by layering of **tdc^{2-}** (0.035 g, 0.2 mmol) neutralized with Et_3N (0.042 g, 0.4 mmol) in EtOH (2 mL). The yellow, needle-shaped crystals of {[Mn_2(tdc)$_2$(pcih)$_2$(EtOH)] $_n$}, (**1**) **(Scheme 3.1)** were obtained after 7 days (0.201 g, yield 70%). Elemental analysis (%) calcd for $C_{20}H_{18}MnN_4O_6S$: C, 48.30; H, 3.65; N, 11.26; found: C,48.23; H,3.71, N, 11.41.IR (cm^{-1}): 1590 $\nu_{as}(COO^-)$, 1322 $\nu_{sys}(COO^-)$ (**Figure 3.1**).

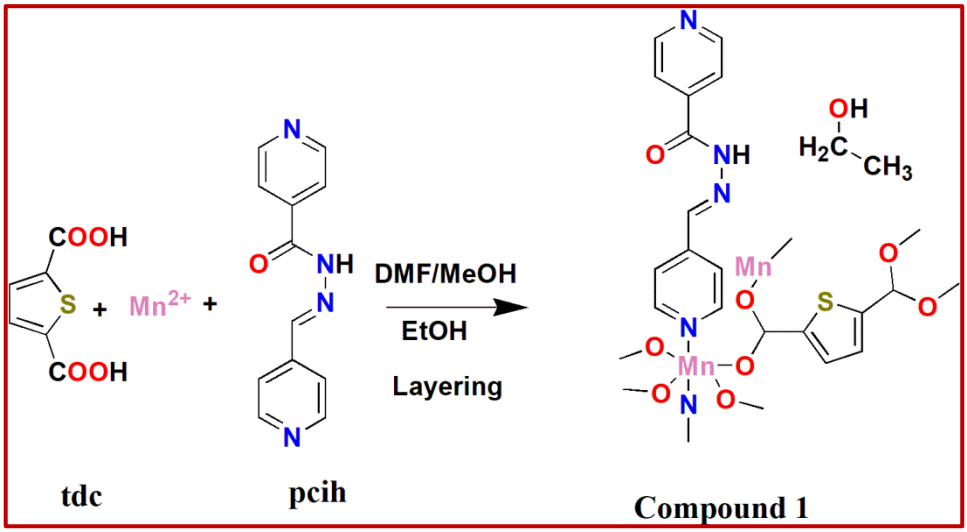

Scheme 3.1 Synthetic route of Compound **1.**

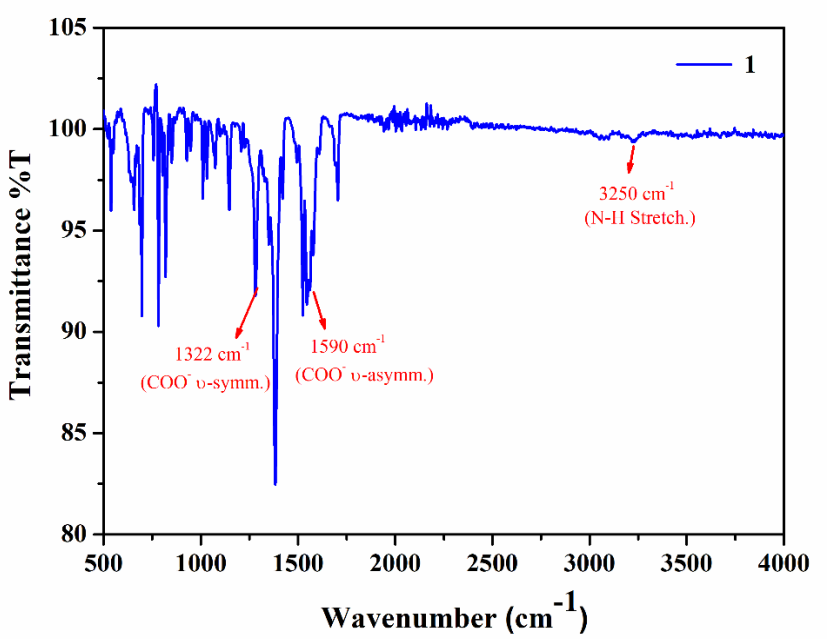

Figure 3.1 IR spectroscopy of Compound 1.

3.2.3 General X-ray Crystallography

A suitable shaped single crystal of compound **1** (0.160 × 0.090 × 0.050 mm^3) was used for Single Crystal X-ray diffraction (SCXRD) data collection using a Bruker SMART APEX III diffractometer equipped with graphite-monochromatic MoKα radiation (λ = 0.71073 Å). The structure was solved using the SHELX-97 package.[30]Non-hydrogen atoms of the diffracted compound were refined with anisotropic thermal parameters. The unit cell parameters and crystal-orientation matrices of the compound of composition, $C_{20}H_{18}MnN_4O_6S$, were determined by least-squares refinement of all reflections within the hkl range $-11 \leq h \leq 11$, $-23 \leq k \leq 23$, $-16 \leq l \leq 16$. All the hydrogen atoms were placed in their geometrically perfect positions and constrained to ride on their parent atoms. The crystallographic data for compound **1** are summarized in **Table 3.1**. The selected bond lengths and bond angles around the coordination atmosphere of the metal ion are also given in **Table 3.2.**

Table 3.1 Crystal data and refinement parameters for compound **1**.

CCDC No.	2160260
Formula	C_{20} H_{18}Mn N_4 O_6 S(**1**)
Fw	497.38

Crystsyst	Monoclinic
space group	P 21/n
a (Å)	9.0058(11)
b (Å)	18.490(2)
c (Å)	12.6980(15)
α(deg)	90
β(deg)	93.032(3)
γ (deg)	90
V (Å^3)	2111.5(4)
Z	4
D_{calcd}(g/cm^3)	1.565
μ(mm^{-1})	0.770
λ(Å)	0.71073
GOF on F^2	0.996
total reflections	4703
unique reflections	3849
refine parameters	292
final *R* indices [$I > 2\sigma(I)$]^{a,b}	$R1$ = 0.0529 $wR2$ = 0.1599

$^{a}R1 = \Sigma||F_o| - |F_c||/ \Sigma|F_o|$, $^{b}wR2 = [\Sigma w(F_o^2 - F_c^2)^2/\Sigma w(F_o^2)^2]^{1/2}$

Table 3.2 Selected bond lengths and bond angles in **1.**

Mn (1) - O (1)	2.098(3)	O (1)-Mn (1)-O (2)d	121.46(11)
Mn (1) - N (4)	2.267(4)	O (1)-Mn (1)-O (3)f	147.55(10)
Mn (1) - N (3)a	2.304(3)	O (1)-Mn (1)-O (4)f	97.28(11)
Mn (1) - O (2)d	2.124(2)	N (4)-Mn (1)-N (3)a	177.04(12)

Mn (1) - O (3)f	2.380(3)	N (4)-Mn (1)-O (2)d	91.15(11)
Mn (1) - O (4)f	2.209(3)	N (4)-Mn (1)-O (3)f	97.81(11)
S (1) - C (14)	1.723(4)	N (4)-Mn (1)-O (4)f	91.31(11)
S (1) - C (17)	1.719(3)	N (3)a-Mn (1)-O (2)d	87.07(11)
O (1) - C (13)	1.255(5)	N (3)a-Mn (1)-O (3)f	84.57(10)
O (3) - C (18)	1.251(4)	N (3)a-Mn (1)-O (4)f	91.46(11)
O (4) – C (18)	1.263(5)	O (2)d -Mn (1)-O (3)f	90.30(9)
O (1)-Mn (1)-N (4)	88.74(12)	O (2)d -Mn (1)-O (4)f	147.22(2)
O (1)-Mn (1)-N (3)a	90.17(11)	O (3)f -Mn (1)-O (4)f	57.00(9)
C (14)-S (1)-C (17)	91.17(18)	N (1)-N (2)-C (4)	117.9(3)
Mn (1)-O (1)-C (13)	159.8(3)	C (9)-N (3)-C (12)	117.0 (3)
C (13)-O (2)-Mn (1)d	116.3(2)	C (9)-N (3)-Mn (1)	120.1(3)
C (18)-O (3)-Mn (1)e	86.8(2)	C (12)-N (3)-Mn (1)	122.6(3)
C (18)-O (4)-Mn (1)e	94.3(2)	Mn (1)-N (4)-C (1)	118.1(3)
N (1)-N (2)-C (7)	116.1(3)	Mn (1)-N (4)-C (6)	124.4(3)

Symmetry code: a = -1+x, y,1+z , b = 1+x, y, -1z , c = 1/2-x,1/2+y,5/2-z ,d = -x,1-y,2-z ,e = -1/2+x,3/2-y,-1/2+z ,f = 1/2+x,3/2-y,1/2+z

3.2.4 Device Fabrication and Optical Measurements

An ITO-coated glass substrate was cleaned prior to device fabrication utilising an ultrasonic bath in Extran MA 02, distilled water, ethanol, and acetone, and finally in IPA for 15 min. The substrate was then dried at 90 ˚C for 1hour. The crushed crystals of compound **1**(15 mg) were taken in a vial and dispersed in 1 ml DMF. A thin film of the synthesized material was obtained by spin coating this solution at 1000 rpm for 60 sec. This process was repeated once again to get full coverage of the film on the ITO glass substrate. Then the substrate was put on a preheated hot plate at 95 °C for 15 min to evaporate the solvent part completely. Finally, aluminium (Al) electrodes were created on the film using proper masking to get a 3 × 3 mm^2 effective area of the device. The current-voltage (*I-V*) measurements were carried out by using a Keithley 2400 source meter in the range of -2 V to +2 V.

The material's optical properties were investigated using a SHIMADZU UV-1900 spectrophotometer. The absorption spectra in the 250–600 nm wavelength region was obtained using a well-dispersed compound **1** in a DMF solution.

3.2.5 Magnetic measurements

Magnetic measurements were carried out in the Servei de Magnetoquímica of Universitat de Barcelona on polycrystalline samples with a Quantum Design SQUID MPMS-XL magnetometer working in the 2-300 K range. The magnetic field was 0.3 T from 300 K to 2 K and 0.02 T from 30 K to 2 K. The diamagnetic corrections were evaluated from Pascal's constants.

3.2.6 Electrochemical Measurement

UV−vis spectra were collected using a PerkinElmer Lambda 25 spectrophotometer. The electrochemical activities of the as-prepared Mn(II) based material was carried out using three-electrode systems employing Ag/AgCl (filled with saturated KCl) as a reference electrode, Pt wire as a counter electrode, and fabricated glassy carbon as a working electrode. To prepare the working electrode a glossy carbon rod was used and drop casted the active material on one of the top surfaces of the carbon rod. A viscous slurry of the active material was prepared by adding 85 wt% synthesized material, 10 wt% graphite powder, and 5 wt% PVDF in N-Methyl-2-pyrrolidone (**NMP**) solution. Then the slurry was drop casted on one of the top surfaces of the carbon rod and dried in vacuum at 325K for 4 h. All the electrochemical measurements were done in 1M Na_2SO_4 electrolyte. The CV measurement was taken at various scan rates (100, 80, 60, 40, 20, 10, 5, and 2 mV/s) in a potential range -0.2V to 0.4V. Full range (-2.0 to +2.0 V) scan was initially performed and selected the working potential range.

3.3 Results and Discussion

3.3.1 Crystal Structure of {$[Mn_2(tdc)_2(pcih)_2(EtOH)]_n$} (1)

The compound **1** crystallizes in the monoclinic crystal system, space group P 21/n and D_{calcd}(g/cm^3) =1.565 having Z value 4. The Crystallographic Data are given in **Tables 3.1**. The bond parameters are summarised in **Table 3.2**. The structure reveals distorted octahedral with MnO_4N_2 coordination sphere (**Figure 3.1a**). This molecular unit is generated through the

combined coordination of **pcih** and **tdc**$^{2-}$. The **tdc**$^{2-}$ anion is coordinated with two different manners (**Figure 3.1a)** one **tdc**$^{2-}$ is chelated through carboxylato-oxygen, and other one is in bridging (μ_2-O) fashion to adjacent Mn(II) centres. Number of bridging atoms in the 1D chain of Mn(μ-**tdc**) Mn may be nine or ten and the bridge length is 4.114 Å. Second ligand, **pcih** coordinates through pyridyl-N at the end of the ligands to two Mn(II) centres and the average length of 13-members in the bridge is 12.19 Å. In the bridging of **tdc**$^{2-}$ two metal (Mn01) centres generate a puckered 8-membered metallo-macrocycle **(Figure 3.1(b)).** The **pcih-N** linking to two Mn(II) centres constitute another 1D sheet network to -Mn(μ-**tdc**)Mn- chain and develops a 2D polymer (**Figure 3.1(c)**). The coordination network and solvent molecules are self-assembled to construct 3D molecular architecture.

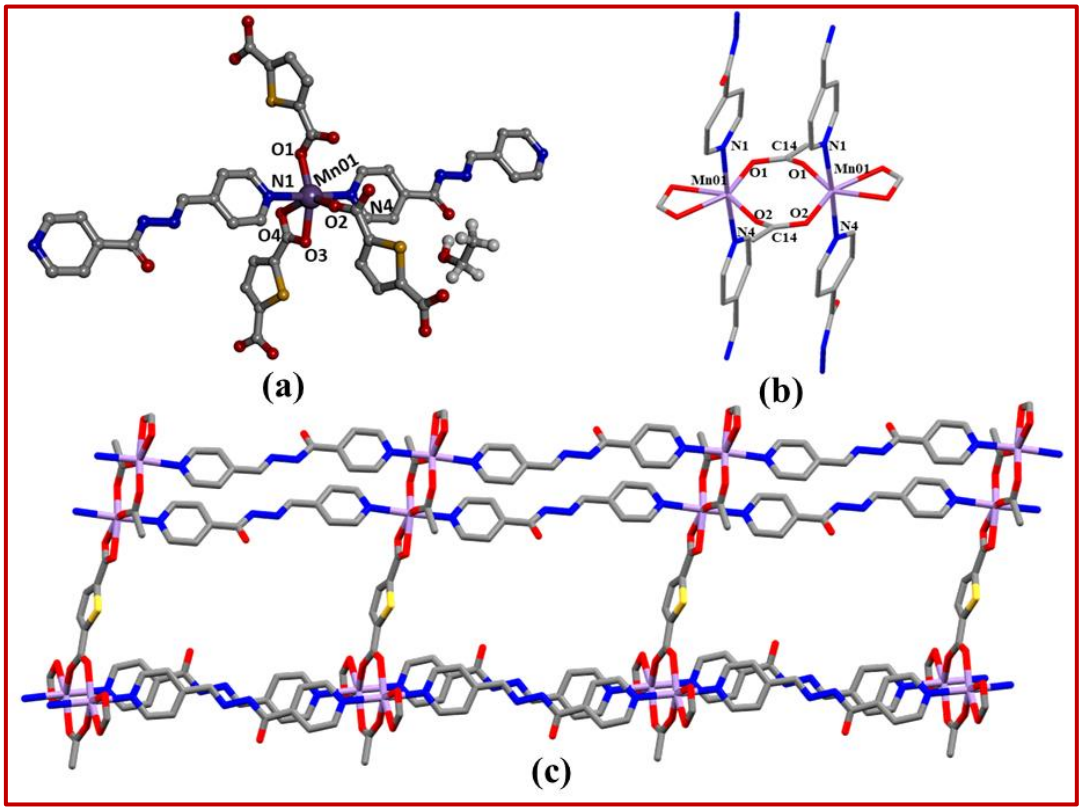

Figure 3.1 (a). Perspective view of the repeating monomeric unit of **1; (b)** To make 8-membered puckered ring; **(c)** A 2D rectangular network has formed though the respiting co-ordination of **pcih** and **tdc**$^{2-}$.

Within this molecular construction there are a number of potential secondary interactions such as, H-bonding with ethanolic-OH and O-atom of isoniazid moiety (H6···O5=2.242Å) and

weak C-H···π interactions (3.621Å) (**Figure 3.2(a)**). Other H-bonding interactions are H(5)....O(3) =2.50 Å and H(12)....O(2) = 2.47 Å(**Figure 3.2(a)**) those make a super-robust architecture. The weak π···πinteractions are there within the pyridyl rings of **pcih** (3.917Å) **(Figure 3.2(b)).** However, the overall molecular construction has exhibited a pillar layered 3D assembly **(Figure 3.3(a))**.

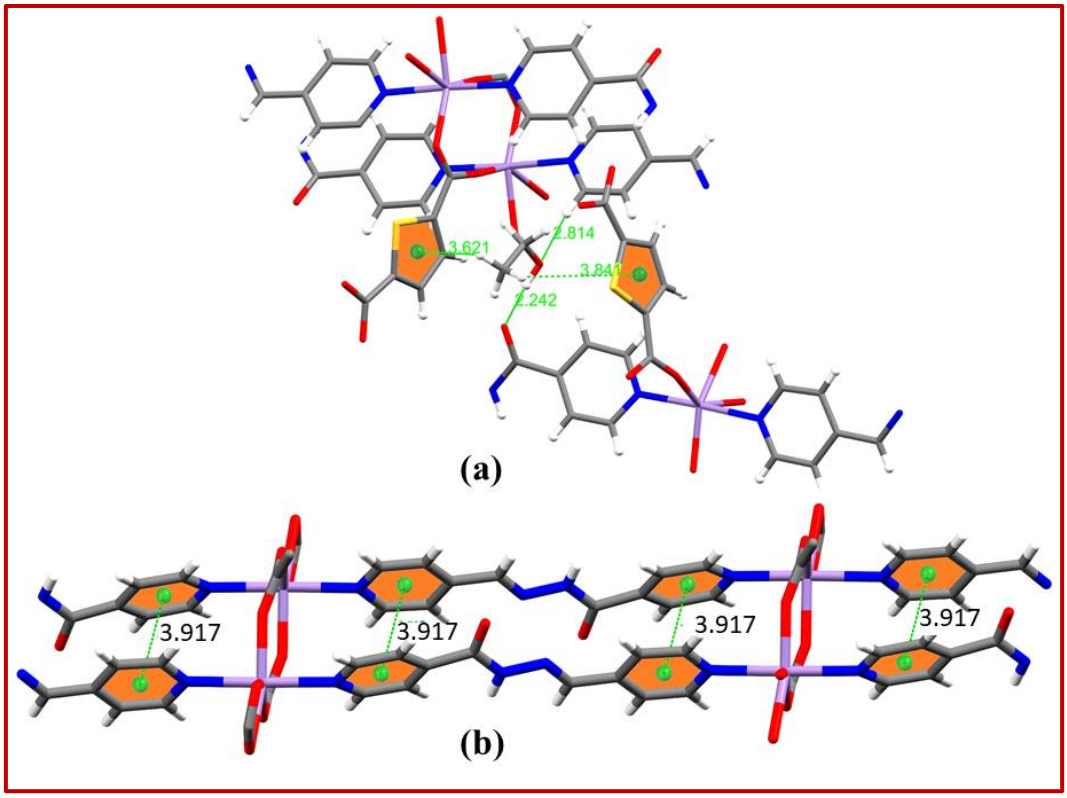

Figure 3.2 (a). C-H···π and H-bonding interactions with CH_3CH_2OH (Å); **(b)** π···π interactions of pyridyl rings (Å);

The topology of the as-synthesized Compound **1** is presented in (**Figure 3.3(b)**) with the point symbol {4^12.6^3} for extended point symbol: [4.4.4.4.4.4.4.4.4.4.4.6(4).6(4).6(4)] the Vertex symbol [4.4.4.4.4.4.4.4.4.4.4.*.*.*] and the 6-c net for a uninodal net that shows interpenetrated lattice arrangement**.**

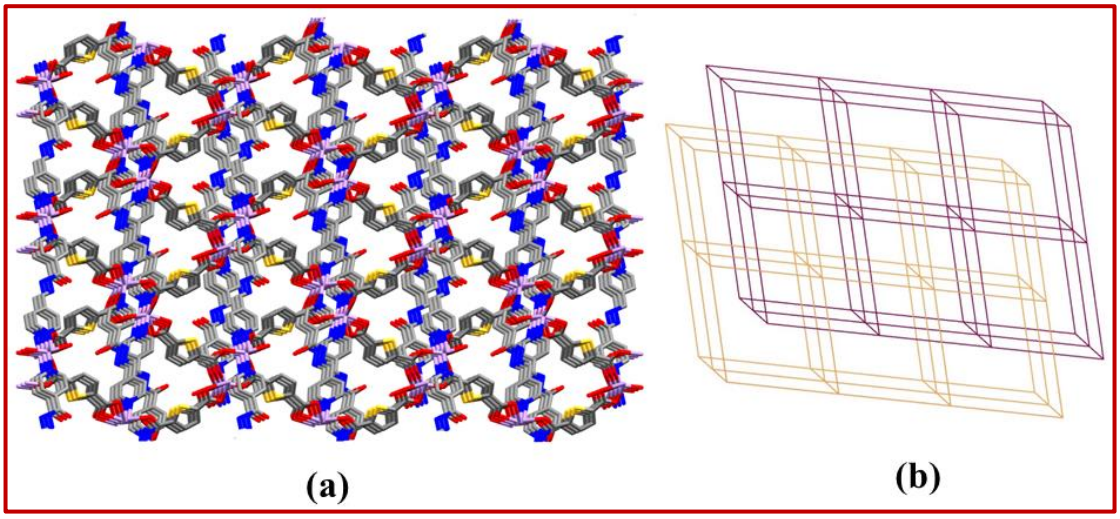

Figure 3.3 **(a)** 3D supramolecular assembly of **1** through the coordination bonding (of **pcih** and **tdc**$^{2-}$) and secondary interactions (solvent molecules are abolished for clarity). (**b**) Topological framework structure of compound **1**.

3.3.2 Hirshfeld surface analysis

The Hirshfeld surfaces is carried out using the crystal explorer program.[31]In **(Figure 3.4)**, the Hirshfeld surfaces (HS) of the heteroleptic compound **1** is given in the form of dnorm, shape index and curvature, respectively, where $d_{norm}$is a standardized contact distance, and the color depth of HS is to highlight the close contact degree of adjacent atoms on the surface, the darker the color, the stronger the interaction between adjacent atoms, and vice versa.

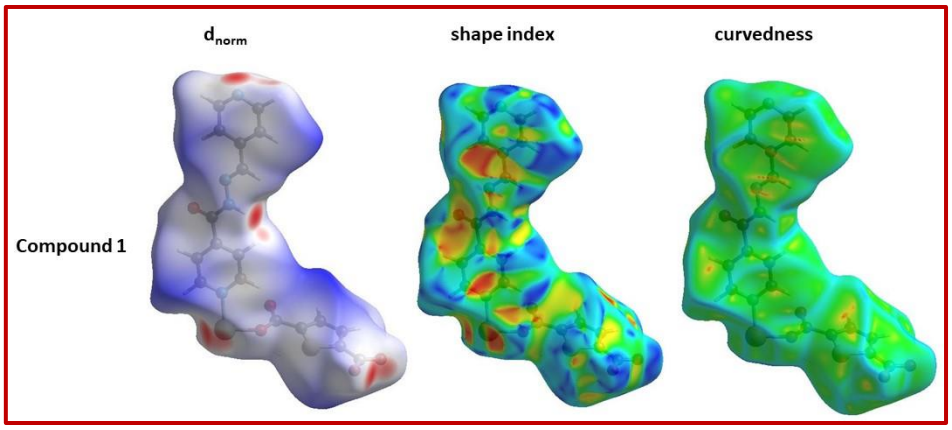

Figure 3.4 Hirshfeld surface analysis map of the compound **1**

Through Hirshfeld surface and related 2D fingerprint plot,[32-34] the type and population of corresponding interatomic close contact was readily clarified for the compound **1**. As shown in **(Figure 3.5)**, the gray part represents the whole fingerprint area, and the blue part represents the short-range interaction between different molecules or atoms. For any intermolecular atomic pair, the close contact enables to be marked readily on both the surface and the 2D fingerprint plot.[35] We can clearly see that in the whole fingerprint area, the H-H, O-H and C-H of the compound **1** account for 24.9%, 22.5% and 19.7% respectively.

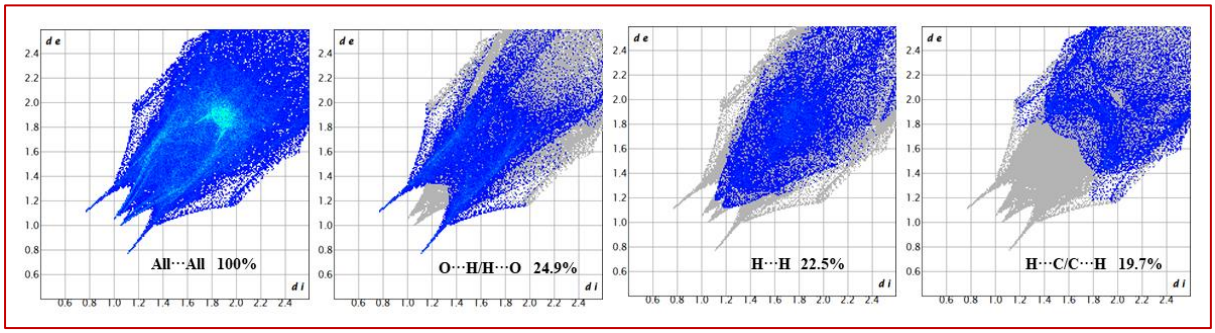

Figure 3.5 Various 2D fingerprints of the compound **1**.

3.3.3 Phase purity and Thermal Stability

Powder X-ray diffraction (PXRD) of the finely ground sample has been carried out at room temperature to check the crystallinity and has been compared with simulated spectrum. Almost all the major peaks of the PXRD pattern of the as-synthesized compound (**Figure 3.6**) match well with those simulated from single-crystal data indicating phase clarity and uniformity of the bulk material.

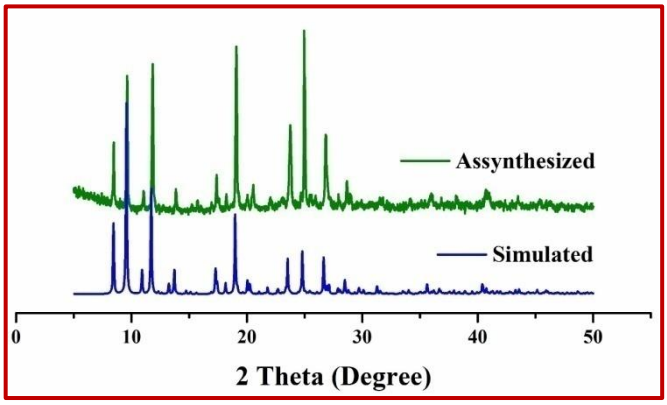

Figure 3.6 PXRD plot of compound **1**.

Thermogravimetric analysis (TGA) of 1in the temperature range of 30−800 °C at a rate of 20 °C min^{-1} under a N_2 atmosphere shows fair stability up to 370 °C (**Figure 3.7**) and after that the compound undergoes thermal decomposition.The final residue corresponds to MnO (cal. 14.26%) which assumed to experimental residue(15.74%).

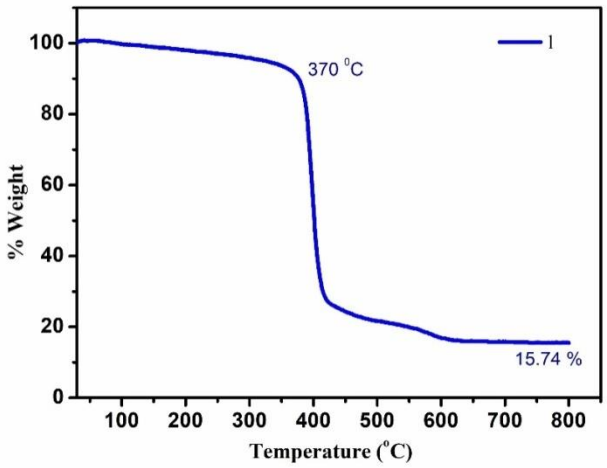

Figure 3.7 TGA plot of Compound **1**.

3.3.4 Magnetic Properties

The crystallinity of the finely grounded sample was checked by using powder X-ray diffraction (PXRD) at room temperature and compared to a simulated spectrum. The overall magnetic behavior of compound **1** corresponds to weak anti-ferromagnetically coupled system (**Figure 3.8**).

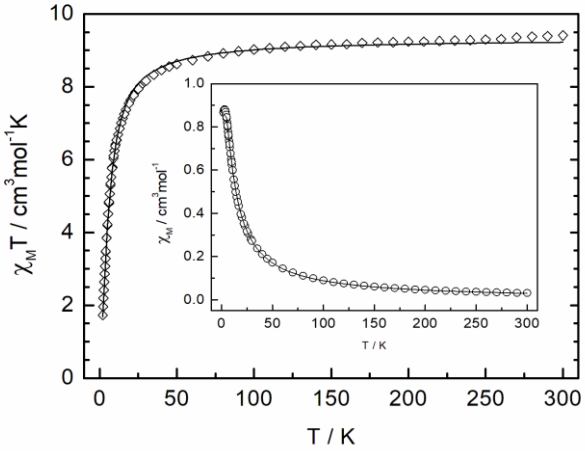

Figure 3.8 Plot of $\chi_M T$ and χ_M vs T for **1**. Solid line represents the best-fit calculation.

At room temperature, $\chi_M T$ shows a value of 9.41cm^{3}Kmol^{-1} which is as expected for two "isolated" Mn (II) ions (S=5/2 with g ~ 2.07). When the sample iscooled, the $\chi_M T$ value remains constant, and below approximately 40K decreases quickly to 1.73cm^{3}Kmol^{-1}at very low temperatures (2K). The$\chi_M$value increases continuously on cooling from 0.031 cm^{3}mol^{-1} to reach a maximum value of 0.882 cm^{3}mol^{-1}at 3 K and then small decrement is observed (0.867 cm^{3}mol^{-1} at 2K) (**Figure 3.8**).

The structure of **1** consists of hexa-coordinated MnO_4N_2 sphere where Mn(II) ionsarelinked by the **pcih** and **tdc^{2-}**ligands, to give a 3Dnetwork (**Figure 3.3(a)**). In order to interpret the magnetic properties, we assume that the exchange pathways parameters *J* between two neighboring Mn(II) ions in **1**is effective only throughthe double carboxylate group (RCO_2^-) of the ligand **tdc^{2-}** since the distance does not exceed to 4.114 Å (**Figure 3.9**).

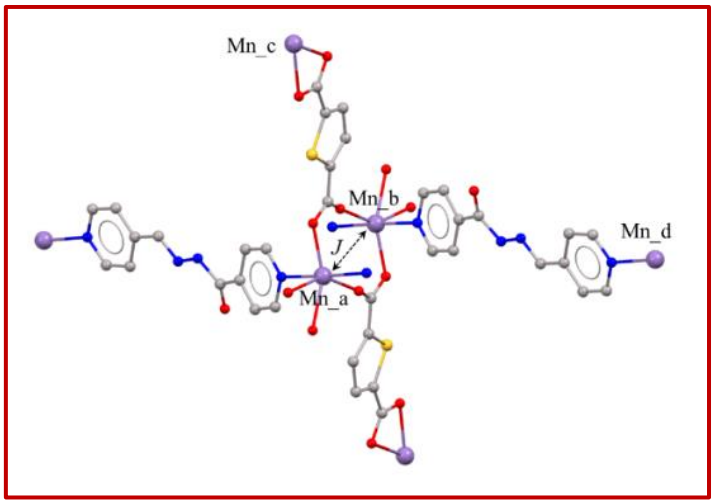

Figure 3.9 Fragment structure of **1** showing different linkage of manganese centers and the magnetic interaction pathway *J*considered to analyze the magnetic data. The main Mn(II)···Mn(II) distances(Å) are Mn_a···Mn_b = 4.114 Å, Mn_a···Mn_c = 10.059Å,Mn_b···Mn_c = 10.555 Å and Mn_b···Mn_d = 15.951 Å.

Any more magnetic contribution across the **pcih** or **tdc^{2-}** ligands has been discarded due to the large distances between manganese atoms (15.951,10.059 and 10.555 Å). This assumption reduces the system to a dinuclear unit effectively to a magnetically isolated arrangement.Thus, the experimental magnetic data have been fitted using the **Equation 1** which is derived from the isotropic Heisenberg Hamiltonian H= -JS_1S_2, considering, $S_{Mn(II)}$ = 5/2 and assuming that the two paramagnetic metal ions have the same g value **1**.The best-fit parameters for reproducing satisfactorily the experimental data, as shown in (**Figure 3.8) ,**are

J=−0.80±0.005 cm^{-1}, and g= 2.06±0.002 with R = 4.1×10^{-5}($R = \sum_i(\chi T_{icalc}-\chi T_{iexp})^2/(\chi T_{iexp})^2$), indicating a very weak coupling, as may be expected from the *syn-anti* coordination mode of the carboxylate ligand bridge.

$$\chi_M = \frac{Ng^2\mu_B^2}{k_BT}\frac{2e^x+10e^{3x}+8e^{6x}+60e^{10x}+110e^{15x}}{1+3e^x+5e^{3x}+7e^{6x}+9e^{10x}+11e^{15x}} \quad \text{With } x = J/k_BT \qquad (1)$$

($N$is Avogadro's number; $\mu_B$is the Bohr magneton and k_B is the Boltzmann constant).

The very weak antiferromagnetic interaction was confirmed by magnetization measurements at 2 K up to an external field of 5.5 T. At the higher field, the magnetization in M/Nμ_B units indicates a two isolated quasi-saturated S = 5/2 system for the compound (**Figure 3.10**). Comparison of the overall shape of the experimental plot with the Brillouin one (solid plot) for a fully two isolated ions with S = 5/2 system and g = 2 indicating slower magnetization, which is consistent with the presence of week antiferromagnetic interaction.

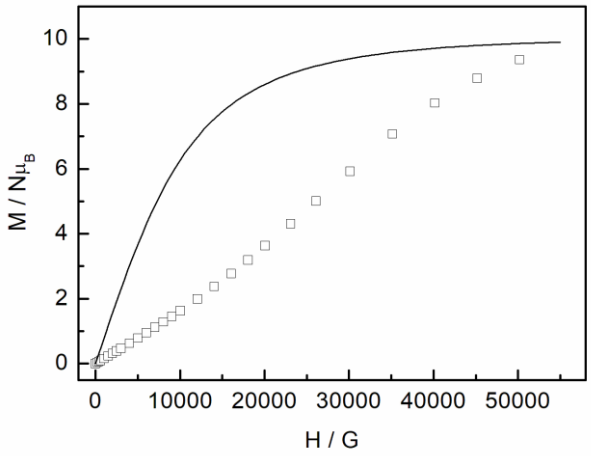

Figure 3.10 Plot of the reduced magnetization at 2 K for compound **1**, solid line represents the M/Nμ_B simulation for two isolated ions S = 5/2 system at 2 K with g = 2.00.

3.4 Electrical Measurements

3.4.1 Optical characterization

The optical bandgap (3.72 eV) of **1**was estimated using Tauc's equation (**Equation 2**)[36]employing the absorption spectra (inset, **Figure 3.11**), indicating that the material is semiconducting.

$(\alpha h\nu) = A(h\nu - E_g)^n$ **(2)**

(his Planck's constant;ν is the frequency of light; α is the absorption coefficient; E_g is the sample bandgap and the exponent n is the electron transition process constant, which is assumedto be 1/2. A is the constant that has been considered as **1** in the ideal scenario.)

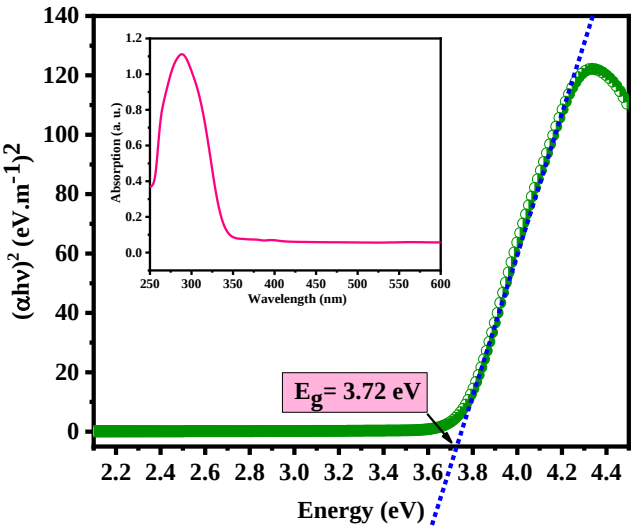

Figure 3.11 Tauc's plot to determine the band gap of the **1**and the UV-Vis absorption spectrum (inset); the extrapolation of the linear region of the $(\alpha h\nu)^2$ versus hν plot to α = 0 is used to calculate the band gap.

3.4.2 Electrical characterization

The measurement of band gap (3.72 eV) encourages us to check the Schottky diode natureof the metal-semiconductor (MS) junctions and the significant current growth is usual at low supply voltage. An electrode structure, ITO/**1**/Al, was fabricated and studied to realize the Schottky device. The current density–voltage (*J*–*V*) characteristic of the sampleshows a non-linear behaviour with a rectification ratio of 61.75 in 1V (**Figure 3.12(a)**). A linear increase in rectification ratio has been observed (**Figure 3.12(b)**) and the experimental conductivity is 3.42×10^{-5} $S.m^{-1}$.Thehighcovalency in Metal-O(carboxylato)may not favour through bond charge transportation and hence the conductivity may be granted through spacechargetransportation*via* non-covalent H-bonding interactions in 2D hydrogen-bonded sheets. Mn(II) (d^5) possesses a stable electron configuration and may play the key role in developing the moderate conductivity.

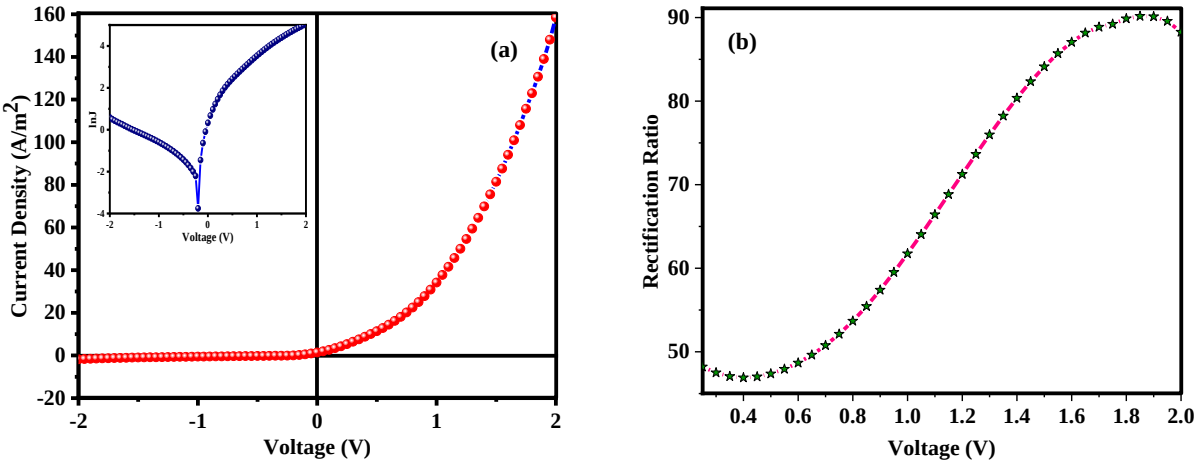

Figure 3.12 (**a**).*J-V* characterization of the **1** based Schottky device, (**b**) Rectifying behaviour of the device

The thermionic emission (TE) theory has been used (**Equation 3**)[37]for better understanding the mechanism of charge transportation.

$$J = J_0\left[exp\left(\frac{qV}{mkT}\right) - 1\right] \qquad J_0 = A^*T^2 exp\left(-\frac{q\Phi_b}{kT}\right) \tag{3}$$

(J is the forward current; J_0 is the reverse saturation current; V is the applied bias voltage; q is the electronic charge; k is the Boltzmann constant; T is the absolute temperature and m is the ideality factor,A^* is the Richardson constant given by 1.20 × 10^6 A K^{-2} m^{-2}, and $\phi_b$is the Schottky barrier height.)

The plot of lnJ vs. V (inset, **Figure 3.12(a)**) provides the value oftheideality factor and barrier height of the Schottkydevice (**Table 3.3**).Cheung's Equation **(Equation 4)**[38]has been used to estimate the series resistance (R_s), ideality factor, and barrier height from the forward bias *J–V* characteristics [38]:

$$\frac{dV}{d(lnJ)} = JR_S + \frac{mkT}{q} \tag{4}$$

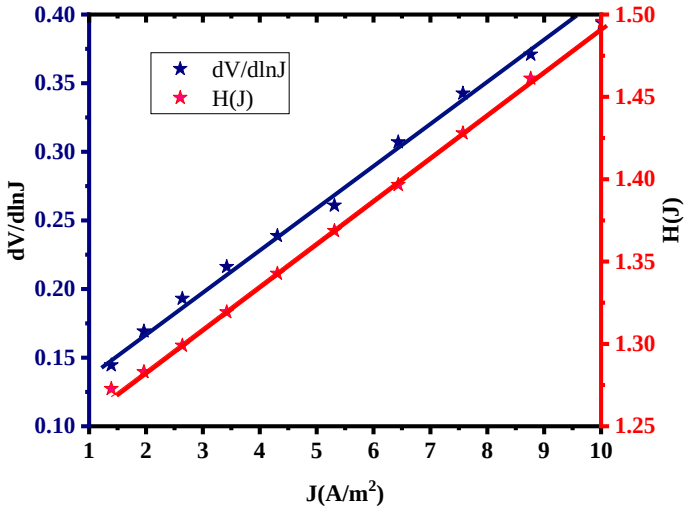

Figure 3.13 *dV/dlnI vs. J (A)*and *H (I) vs.I* curves for**1** based device in absence of light

The intercept of *dV/dlnJ* vs. *J* plot (**Figure 3.13**) calculates the idealityfactor (m) for the fabricated device whereas the slope of this plot gives the value of R_S of the devices.The calculated value of m from this method has been matched well with data estimated from the InJ-V plot **(**inset, **Figure 3.12(b))** and has been used to calculateϕ_b(barrier height) and $R_s$may be estimated by another equation of Cheung (**Equation 5**):

$$H(I) = V - \frac{mkT}{q} ln\left(\frac{I}{AA^*T^2}\right)$$

$$= m\phi_b + R_S I \qquad (5)$$

The intercept of the *H (J) vs. J* curve (**Figure 3.13**) evaluates the value of the potential barrier height (ϕ_b) of the device. The value of $R_S$obtained from the slope of this plot also comparable to former data. The value of m has diverged from the ideal value due to Schottky barrier height in-homogeneities, a high chance of electron and hole recombination in the depletion zone, charge trapping, series resistance at the junction, and the presence of interface states[39]. The experimental value of m (barrier height) obtained from two different methods (0.65 eV and 0.60 eV) does not differ much. The series resistance (R_s) obtained from both plots (**Figure 3.13**) shows asimilar resultwhich signifies its **1** applicability in the field of electronics devices.

Table 3.3 Schottky Device Parameters for the Composite (1) Based Thin Film Device

Condition	Conductivity (S. m^{-1})	Ideality factor (m)		Series Resistance from (R_s, Ω)		Barrier Height from (ϕ_b, eV)	
		lnJ-V plot	dV/dlnJ - J	dV/dlnJ -*J*	H(J)-J	lnJ-V plot	H(J)-J
Dark	3.42×10^{-5}	4.44	4.20	0.03	0.026	0.65	0.60

Further, the forward J-V curve was examined to gain a better understanding of the carrier transport mechanism through the metal semiconductor contact, and the product of the mobility and dielectric constant, threshold voltage, and charge carrier trapping energy were calculated using space charge limited current (SCLC) theory.

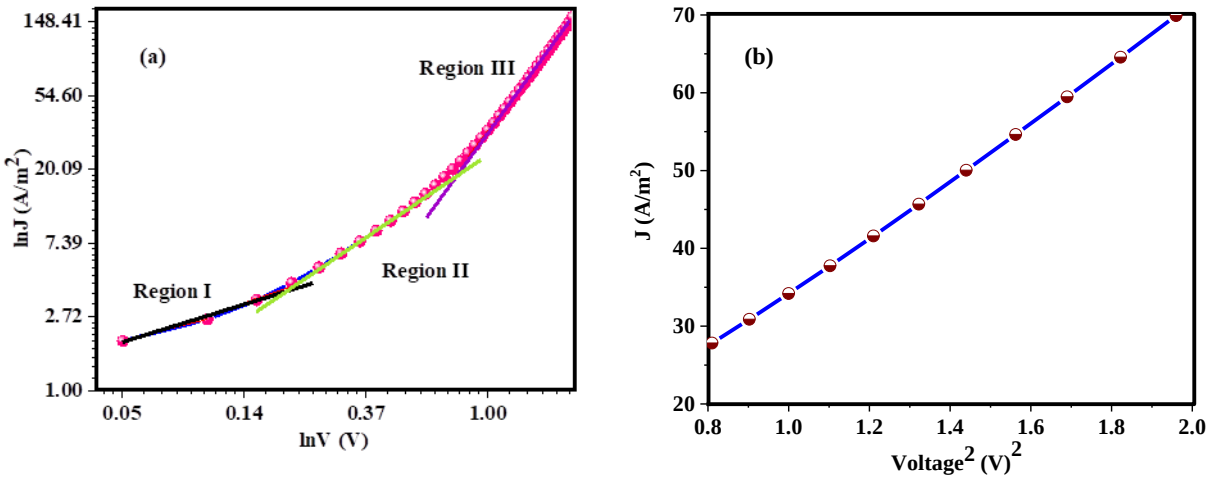

Figure 3.14 (**a**) lnJ vs. lnV curve, (**b**) V^2 (Voltage^2) vs. J (A/m^2) of CP**1** based Schottky device

The lnJ vs. lnV graph (**Figure 3.14(a)**) clearly shows three distinct regions with various slopes. The Region-I follows an Ohmic pattern (I α V)and the current is mainly contributed by the generated electrons of the film, instead of the injected free carriers[40].The Region-II maintains I α V^2 relation and is dominated by space charge limited current (SCLC) (**Figure 3.14(b)**).At higher voltages, I α V^k represents Region III, where k is greater than 2. In our case, k is found to be 2.56. Therefore, Region III is governed by trap free SCLC theory[41,42]. The observation reminds the change in current conduction mechanism on the surface. The threshold voltage (V_{th}), 0.19 V (**Table 3.4**) refers to the switch over of electron transport

mechanism in the Schottky diode. In region II, the product of carrier mobility and dielectric constant ($\mu_{eff}.\varepsilon_r$) has been estimated from the slope of the J *vs.* V^2 graph of the SCLC region (**Figure 3.14(b)**) using the Mott–Gurney equation[43] which is found to be 3.7×10^{-6} $m^2V^{-1}s^{-1}$. This product represents the conduction ability of the sample and shows a moderate value. The reason behind this result may be explain considering the trap in the system.

Trap charges are said to play a major role in the SCLC region[44] during the current conduction process of the thin film-based devices.These traps introduce energy levels into the energy gap between the compound's highest occupied molecular orbital (HOMO) and lowest unoccupied molecular orbital (LUMO)[45-46]. Because of the presence of trap levels, a large number of the carriers injected from the electrode are trapped and crowded at the electrodes. When this process is dominant, it is referred to as trap charge limiting conduction (TCLC). The trap centres are assumed to be exponentially spread, according to **Equation 6**[47].

$$g(E) = \frac{N_T}{k_B T_T} \exp\left(\frac{-E}{kT_T}\right) \qquad (6)$$

Where N_T is the total trap concentration, E is the Fermi energy, k is the Boltzmann constant, and $T_T$is the characteristic temperature of the exponential trap distribution. The J-V characteristic was calculated from the Poisson of power law,$J \sim V^{m+1}$; whereV is the applied voltage and $m = T_T/T$. The linear fitting of lnJ vs lnV provided two threshold voltages and slopes for separate regions. The trap energy in SCLC region i.e., in Region-II has been calculated to be 0.041 eV. The trap energy value is pretty high. As a result, the charge carriers were unable to percolate to the electrode, resulting in moderate conductivity. However, trap energy can be lowered using various ways such as more homogenous film production and the introduction of guest elements, which may be the future scope of our work. The electrical analysis (**Tables 3.3** and **3.4**) of the Schottky device has concluded that **1** is promising and interesting material for the application of the thin film-based devices.

Table 3.4 Threshold voltages and different parameters related to estimation of trap energy.

Region I	Region II			Region III	
Value of slope (m_1)	Threshold voltage $V_{1\ th}$ (V)	Value of slope (m_2)	Trap energy, E_T(eV)	Threshold voltage V_{2th} (V)	Value of slope (k)
0.56	0.19	1.65	0.041	0.77	2.56

3.5 Electrochemical Study

Cyclic Voltammetry (CV, **Figure 3.15(a)**), Galvanostatic charge-discharge (GCD, **Figure 3.15(b)**) and Electrochemical impedance spectroscopic (EIS, **Figure 3.15(c)**) studies have been carried out withthe compound **1**. The CV measurement was taken at various scan rates (100, 80, 60, 40, 20, 10, 5, and 2 mV/s) in a potential range 0.2 to 0.4 (**Figure 3.15(a)**).The maximum specific capacitance was determined of 1F/g at 2mV/s scan rate. The energy storage property was further studied by the GCD cycles (**Figure 3.15(b)**)at different constant current densities (0.2, 0.16, 0.12, 0.08, 0.04 and 0.02 A/g). Specific capacitance value 1F/g was also obtained at 0.02 A/g. The impedance spectroscopy (**Figure 3.15(c)**) was taken in the frequency range 0.01-100000 Hz, with an AC perturbation voltage of 10 mV over a dc voltage of 0.1V. The results elucidate that the compound is redox stable in the electrochemical potential window and has moderate specific capacity.

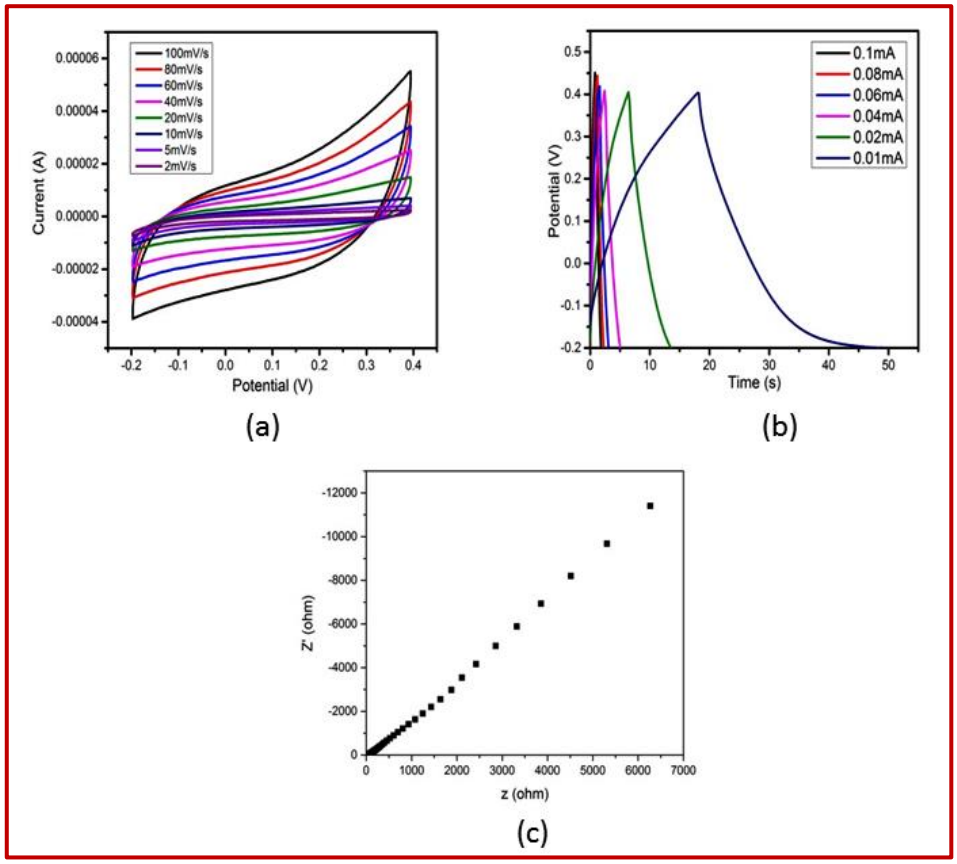

Figure 3.15 (**a**) The cyclic voltammograms; (**b**) The GCD profiles (**c**) The entire impedance spectra of compound **1**

Table 3.5 Comparison table for magnetism and electrical conductivity of compound **1** with different reported compounds.

SL. Number	Compound Name	Magnetism	Electrical conductivity	Refarance
1.	$\{[Mn_2(L)(tib)(H_2O)]\cdot 3DMA\cdot 4H_2O\}_n$ L= 5,5'-(1,4-xyly-lenediamino) diisophthalic acid, tib= 1,3,5-tris(1-imidazolyl)benzene	$\chi_M T$ = 8.21 cm^3 $kmol^{-1}$. Antiferromagnetic	-	48
2.	$[Mn_3(NDC)_3(DMA)_4]_n$ NDC = 2,6 napthalene dicarboxylic acid	$\chi_M T$ = 12.8186 cm^3 $kmol^{-1}$. Weak	-	49

	DMA= N,N-dimethylacetamide	antiferromagnetic		
3.	$[Mn(cmpc)(N_3)]\cdot H_2O$ cmpc = 1-carboxylatomethyl pyridinium-4-carboxylate	$\chi_M T$ = 4.38 emu-$mol^{-1}k$. Antiferromagnetic	-	50
4.	$[Mn_3(\mu\text{-}L)_6(H_2O)_6]$ L=4-(1,2,4-triazol-4-yl) ethanedisulfonate)	$\chi_M T$ = 12.95-cm^3kmol^{-1}. Antiferromagnetic	-	51
5.	$[Mn_2(tptc)(H_2O)(NMP)]\cdot NMP$ tptc= [1,1':4',1"-terphenyl]-2',4,4",5'-tetracarboxylic acid NMP = [N-methyl-2-pyrrolidone	$\chi_M T$ =4.058 cm^3kmol^{-1}. Antiferromagnetic	-	52
6.	$[Mn_2(L1)4/3(L2)_2]_n$ L1 = 4′-(4-pyridyl)-4,2′:6′,4″-terpyridine L2 = (4-phenyl)-2,6-bis(4-carboxyphenyl)pyridine)	$\chi_M T$ = 2.15 emu-$mol^{-1}k$. weak antiferromagnetic	-	53
7.	$[Mn_2(L)(N3)_2(H_2O)_2]\cdot 3H2O$ L= N,N′-bis(3,5-dicarboxylatobenzyl)-4,4′-bipyridinium	$\chi_M T$ = 4.09 emu k-mol^{-1}. Antiferromagnetic	-	54
8.	$\{[Mn_2L_2(CH_3OH)_{2.5}H_2O]\cdot 2.5CH_3OH\cdot 5.5H_2O\}_n$ L= 2,6-bis(6-carboxy-4- methyl-2-propyl-benzimidazol-1-ylmethy	$\chi_M T$ = 9.33-$cm^3kmol^{-1.}$ Antiferromagnetic	-	55
9.	$Mn_3(L)(DMA)_4\cdot 2DMA$ L= hexa[4-	$\chi_M T$ = 13.49-$cm^3kmol^{-1.}$	-	56

	(carboxyphenyl)oxamethyl]-3-oxapentane acid DMA= dimethylacetamide	Antiferromagnetic		
10.	$\{[Mn_5(L)_2(H_2O)_{12}]\cdot 6H_2O\}_n$ L = 2,4-di(3',5' dicarboxylphenyl)benzoic acid	$\chi_M T$ = 21.62- cm^3kmol^{-1}. Antiferromagnetic		57
11.	$\{[Mn_3(btcit)_2(bib)_2]\cdot 2DMF\}_\infty$ H_3btcit = 4,4',4''-[1,3,5-benzenetriyltris(carbonylimino)]trisbenzoic acid bib = 1,4-bis(imidazol-1-yl)benzene)	$\chi_M T$ = 13.18 emu- $kmol^{-1}$. Antiferromagnetic		58
12.	$[Mn_3L_2(H_2O)_3]\cdot 7.5DEF\cdot 3H_2O$ H3L = tris((4- carboxyl)phenyl)amine DEF = N,N-diethylformamide	$\chi_M T$ = 12.66- cm^3kmol^{-1}. Antiferromagnetic		59
13.	$\{[Mn_2(tdc)_2(pcih)_2(EtOH)]_n\}$ pcih= Pyridine-4-carboxaldehyde isonicotinoylhydrazone tdc= 2,5-thiophene dicarboxylic acid	$\chi_M T$ = 9.41 cm^3kmol^{-1}. Weak Antiferromagnetic	3.42×10^{-5} $S.m^{-1}$.	This work.

3.6 Conclusion

The development of functional hybrid materials has received tremendous impetus in recent years owing to their multi potential applications such as electronic device and magnetic properties. Interestingly, the 3D assembly of **1** exhibit electrical conductivity in the semiconducting region.An architecture of 3D mixed coordination polymer $\{[Mn_2(tdc)_2(pcih)_2(EtOH)]_n\}$ (**1**) bridged by 2,5-thiophene dicarboxylato-O (tdc^{2-}) and isonicotinoylhydrazidepyridyl-N (pcih = pyridine-4-carboxaldehyde isonicotinoyl hydrazine) is structurally characterized. Interestingly, the 3D assembly of **1** exhibits electrical conductivity in the semiconducting region (3.72 eV) and the experimental conductivity is 3.42×10^{-5} Sm^{-1}. The GCD measures specific capacity 3.42×10^{-5} Sm^{-1}. VTM study also shows two weakly interacting Mn(II) centres separated by 4.114 Å.

3.7 References

(1) Kitagawa, S.; Metal–organic frameworks (MOFs). *Chem. Soc. Rev.* **2014**,*43*, 5415-5418.

(2) Ahmed, F.; Roy, S.; Naskar, K.; Sinha, C.; Alam, S. M.; Kundu, S.; Vittal, J. J.; Mir, M. H. Halogen⋯ halogen interactions in the supramolecular assembly of 2D coordination polymers and the CO2 sorption behavior. *Cryst. Growth Des.* **2016**,*16*, 5514-5519.

(3) Hosono, N.; Terashima, A.; Kusaka, S.; Matsuda, R.; Kitagawa, S. Highly responsive nature of porous coordination polymer surfaces imaged by in situ atomic force microscopy. *Nat. Chem.* **2019**, *11*, 109−116.

(4) Kajiwara, T.; Higashimura, H.; Higuchi, M.; Kitagawa, S. Front Cover: Design and Synthesis of Porous Coordination Polymers with Expanded One-Dimensional Channels and Strongly Lewis-Acidic Sites. *ChemNanoMater.***2 018**, *4*, 103−105.

(5) Yadava, K.; Vittal, J. J. PhotosalientBehavior of PhotoreactiveZn(II) Complexes. *Cryst. Growth Des.* **2019**, *19*, 2542−2547.

(6) Dutta, B.; Jana, R.; Sinha, C.; Ray, P. P.; Mir, M. H. Synthesis of Cd(II) based 1D coordination polymer by in situ ligand generation and fabrication of photosensitive electronic device. *Inorg. Chem. Front.* **2018**, *5*, 1998−2005.

(7) Yang, Q.-Y.; Lama, P.; Sen, S.; Lusi, M.; Chen, K.-J.; Gao, W.-Y.; Shivanna, M.; Pham, T.; Hosono, N.; Kusaka, S.; Perry, J. J.; Ma, S.; Space, B.; Barbour, L. J.; Kitagawa, S.; Zaworotko, M. J. Reversible Switching between Highly Porous and Nonporous Phases of an Interpenetrated Diamondoid Coordination Network That Exhibits Gate-Opening at Methane Storage Pressures. *Angew. Chem., Int. Ed.* **2018**, *57*, 5684−5689.

(8) Farha, O. K.; OzgurYazaydın, A.; Eryazici, I.; Malliakas, C. D.; Hauser, B. G.; Kanatzidis, M. G.; Nguyen, S. T.; Snurr, R. Q.; Hupp, J. T. De novo synthesis of a metal−organic framework material featuring ultrahigh surface area and gas storage capacities. *Nat. Chem.* **2010**, *2*, 944−948.

(9) Farha, O. K.; Hupp, J. T. Rational design, synthesis, purification, and activation of metal− organic framework materials. *Acc. Chem. Res.***2010**, *43*, 1166−1175.

(10) Muthu, S.; Yip, J. H.; Vittal, J. J. Coordination networks of Ag(I) and N, N′-bis (3-pyridinecarboxamide)-1, 6-hexane: structures and anion exchange. *Dalton Trans.***2002**, *24*, 4561−4568.

(11) Toh, N. L.; Nagarathinam, M.; Vittal, J. J. Topochemical Photodimerization in the Coordination Polymer $[\{(CF_3CO_2)(\mu O_2CCH_3)Zn\}_2(\mu\text{-bpe})_2]_n$ through Single-Crystal to Single-Crystal Transformation. *Angew. Chem., Int. Ed.***2005**, *44*, 2237−2241.

(12) Chakraborty, A.; Roy, S.; Eswaramoorthy, M.; Maji, T. K. Flexible MOF-aminoclay nanocomposites showing tunable stepwise/ gated sorption for C_2H_2, CO_2 and separation for CO_2/N_2 and CO_2/CH_4. *J. Mater. Chem. A.* **2017**, *5*, 8423−8430.

(13) Xu, Z.; Han, L.-L.; Zhuang, G.-L.; Bai, J.; Sun, D. In Situ Construction of Three Anion-Dependent Cu(I) Coordination Networks as Promising Heterogeneous Catalysts for Azide-Alkyne "Click" Reactions. *Inorg. Chem.* **2015**, *54*, 4737−4743.

(14) Brozek, C. K.; Dinca, M. Cation exchange at the secondary building units of metal-organic frameworks. *Chem. Soc. Rev.* **2014**, *43*, 5456−5467.

(15) Chen, W.-M.; Meng, X.-L.; Zhuang, G.-L.; Wang, Z.; Kurmoo, M.; Zhao, Q.-Q.; Wang, X.-P.; Shan, B.; Tung, C.-H.; Sun, D. A superior fluorescent sensor for Al^{3+} and UO_2^{2+} based on a Co(II) metal−organic framework with exposed pyrimidyl Lewis base sites. *J. Mater. Chem.A.* **2017**, *5*, 13079−13085.

(16) Dong, K.; Peng, X.; Wang, Z. L. Fiber/fabric- based piezoelectric and triboelectric nano generators for flexible/stretchable and wearable electronics and artificial intelligence. *Adv. Mater.* **2020**, *32*, 1902549.

(17) Saparov, B.; Mitzi, D. B. Organic–inorganic perovskites: structural versatility for functional materials design. *Chem. Rev.* **2016**, *116*, 4558-4596.

(18) Sun, Y.; Gao, S.; Xie, Y. Atomically-thick two-dimensional crystals: electronic structure regulation and energy device construction. *Chem. Soc. Rev.* **2014**, *43*, 530-546.

(19) Wannapaiboon, S.; Schneemann, A.; Hante, I.; Tu, M.; Epp, K.; Semrau, A. L.; Fischer, R. A. (Control of structural flexibility of layered-pillared metal-organic frameworks anchored at surfaces. *Nat. Commun.* **2019**,*10*, 1-10.

(20) Roztocki, K.; Jędrzejowski, D.; Hodorowicz, M.; Senkovska, I.; Kaskel, S.; Matoga, D. Effect of linker substituent on layers arrangement, stability, and sorption of Zn-isophthalate/acylhydrazone frameworks. *Cryst. Growth Des.* **2018**,*18*, 488-497.

(21) Behera, N.; Duan, J.; Jin, W.; Kitagawa, S. The chemistry and applications of flexible porous coordination polymers. *Energy Chem.* **2021**,*3*, 100067.

(22) Urgel, J. I.; Mishra, S.; Hayashi, H.; Wilhelm, J.; Pignedoli, C. A.; Di Giovannantonio, M.; Fasel, R. On-surface light-induced generation of higher acenes and elucidation of their open-shell character. *Nat. Commun*. **2019**,*10*, 1-9.

(23) Choudhury, F. K.; Devireddy, A. R.; Azad, R. K.; Shulaev, V.; Mittler, R. Local and systemic metabolic responses during light-induced rapid systemic signaling. *Plant Physiol.* **2018**,*178*,1461-1472.

(24) Fathi, S.; Srinivasan, R.; Fenner, A.; Fathi, S. Machine learning applications in urban building energy performance forecasting: A systematic review. *Renew. Sustain. Energy Rev.* **2020**,*133*, 110287.

(25) Gandini, A.; Lacerda, T. M.; Carvalho, A. J.; Trovatti, E. Progress of polymers from renewable resources: furans, vegetable oils, and polysaccharides. *Chem. Rev.* **2016**,*116*, 1637-1669.

(26) Belviso, C. State-of-the-art applications of fly ash from coal and biomass: A focus on zeolite synthesis processes and issues. *Prog. Energy Combust. Sci.* **2018**,*65*, 109-135.

(27) Yuan, C.; Wu, H. B.; Xie, Y.; Lou, X. W. Mixed transition metal oxides: design, synthesis, and energy related applications. *Angew. Chem. Int. Ed.* **2014**,*53*, 1488-1504.

(28) Arshad, N.; Singh, A.; Chugh, B.; Akram, M.; Perveen, F.; Rasheed, I.; Altaf, F.; Channar, P. A.; Saeed, A.Experimental, theoretical, and surface study for corrosion inhibition of mild steel in 1 M HCl by using synthetic anti-biotic derivatives. *Ionics*. **2019**, *25*, 5057-5075.

(29) Sheldrick, G. M. A short history of SHELX. *ActaCrystallographica Section A: Foundations of Crystallography.* **2008**, *64*, 112-122.

(30) Spackman, M. A.; Jayatilaka, D. Hirshfeld surface analysis. *CrystEngComm.* **2009**,*11*,19-32.

(31) Clausen, H. F.; Chevallier, M. S.; Spackman, M. A.; Iversen, B. B. Solvothermal synthesis of new metal organic framework structures in the zinc-terephthalic acid-dimethylformamide system. *New J. Chem.***2010**,*34*,193-199.

(32) Rohl, A. L.; Moret, M.; Kaminsky, W.; Claborn, K.; McKinnon, J. J.; Kahr, B. Hirshfeld surfaces identify inadequacies in computations of intermolecular interactions in crystals: pentamorphic 1, 8-dihydroxyanthraquinone. *Cryst. Growth Des.* **2008**, *8*, 4517-4525.

(33) Parkin, A.; Barr, G.; Dong, W.; Gilmore, C. J.; Jayatilaka, D.; McKinnon, J. J.; Spackman M. A.; Wilson,C. C. Comparing entire crystal structures: structural genetic fingerprinting. *CrystEngComm.* **2007**, *9*, 648-652.

(34) Spackman, M. A.; McKinnon, J. J. Fingerprinting intermolecular interactions in molecular crystals. *CrystEngComm.* **2002**, *4*, 378-392.

(35) Klein, C. L.; O'Connor, C. J.; Majeste, R. J.; Trefonas. L. M. Magnetic properties and molecular structure of complexes of substituted pyrazine ligands co-ordinated to iron (II) and copper (II) low dimensional antiferromagnetic interactions in diaquabis (pyrazine carboxylato) iron (II). *J. Chem. Soc., Dalton Trans.***1982**,*12*, 2419-2423.

(36) Wood, D. L.; J. S. Tauc. Weak absorption tails in amorphous semiconductors. *Physical review B*, **1972**, *8*,3144.

(37) McCarthy, P. T., Reifenberger, R. G., Fisher, T. S. Thermionic and photo-excited electron emission for energy-conversion processes. *Front. Energy Res*. **2014**, *2*, 54.

(38) Cheung, S. K.; Cheung, N. W. Extraction of Schottky Diode Parameters from Forward Current-Voltage Characteristics. *Appl. Phys. Lett*. **1986**, *49*, 85–87.

(39) Gupta, R. K.; Yakuphanoglu, F. Photoconductive Schottky Diode Based on Al/p-Si/SnS 2/Ag for Optical Sensor Applications. *Sol Energy*. **2012**, *86*, 1539–1545.

(40) Roy, S.; Halder, S.; Drew, M. G. B.; Ray, P. P.; Chattopadhyay, S. Fabrication of an Active Electronic Device Using a Hetero-Bimetallic Coordination Polymer. *ACS omega*. **2018**,*3*, 12788–12796.

(41) Jain, A.; Kumar, P.; Jain, S. C.; Kumar, V.; Kaur, R.; Mehra, R. M. Trap Filled Limit Voltage (VTFL) and V2 Law in Space Charge Limited Currents. *J. Appl. Phys*. **2007**, *102*. 094505.

(42) Güllü, Ö.; Aydoğan, Ş.; Türüt, A. Fabrication and Electrical Characteristics of Schottky Diode Based on Organic Material. *Microelectron. Eng*. **2008**, *85*, 1647–1651.

(43) Ahmed, F.; Halder, S.; Dutta, B.; Islam, S.; Sen, C.; Kundu, S.; Sinha, C.; Ray, P. P.; Mir, M. H. Synthesis and Structural Characterization of a Cu(II)-Based 1D Coordination Polymer and Its Application in Schottky Devices. *New J. Chem*. **2017**, *41*, 11317–11323.

(44) Sen, S.; Manik, N. B. Effect of Different Sized Multi Walled Carbon Nanotubes on the Barrier Potential and Trap Concentration of Malachite Green Dye Based Organic Device. *Adv. Mater. Sci. Eng*. **2020**, *20*, 16–26.

(45) Sen, S.; Manik, N. B. Correlation between Barrier Potential and Charge Trapping under the Influence of Titanium Di Oxide Nanomaterials in Organic Devices. *Results in Materials*. **2020**, *8*, 100145.

(46) Sarkar, A. S.; Pal, S. K. Exponentially Distributed Trap-Controlled Space Charge Limited Conduction in Graphene Oxide Films. *J. Phys. D: Appl. Phys.***2015**, *48*, 445501.

(47) Xu, C.; Luo, R.; Zhang, D.; Zhang, X.; Zong, Z.; Fan, C.; Fan, Y. Mn (II)/Co (II)-based metal-organic frameworks assembled by 5, 5'-(1, 4-xylylenediamino) diisophthalic acid and various nitrogen-containing ligands for photocatalytic and magnetic properties. *J. Solid State Chem.* **2021**, *303*, 122535.

(48) Dhankhar, S. S.; Nagaraja, C. M. Green synthesis, optical and magnetic properties of a Mn II metal–organic framework (MOF) that exhibits high heat of H_2 adsorption. *RSC advances*. **2016**, *6*, 86468-86476.

(49) Wang, Y. Q.; Yue, Q.; Qi, Y.; Wang, K.; Sun, Q.; Gao, E. Q. Manganese (II), iron (II), and mixed-metal metal–organic frameworks based on chains with mixed carboxylate and azide bridges: magnetic coupling and slow relaxation. *Inorg. Chem.* **2013**, *52*, 4259-4268.

(50) Moneo-Corcuera, A.; Pato-Doldan, B.; Sánchez-Molina, I.; Nieto-Castro, D.; Galán-Mascarós, J. R. Crystal Structure and Magnetic Properties of Trinuclear Transition

Metal Complexes (MnII, CoII, NiII and CuII) with Bridging Sulfonate-Functionalized 1, 2, 4-Triazole Derivatives. *Molecules.* **2021**, *26***,** 6020.

(51) Zhou, X.; Liu, P.; Huang, W. H.; Kang, M.; Wang, Y. Y.; Shi, Q. Z. Solvents influence on sizes of channels in three fry topological Mn (II)-MOFs based on metal–carboxylate chains: syntheses, structures and magnetic properties. *CrystEngComm.* **2013** ,*15*, 8125-8132.

(52) Chen, Y.-Q.; Liu, S.-J.; Li, Y.-W.; Li, G.-R.; He, K.-H.; Qu, Y.-K.; Hu, T.-L.; Bu, X.-H. A two-fold interpenetrated coordination framework with a rare (3, 6)-connected loh1 topology: Magnetic properties and photocatalytic behavior. *Cryst. Growth Des.***2012**, *12*, 5426-5431.

(53) Gong, T.; Yang, X.; Fang, J. J.; Sui, Q.; Xi, F. G.; Gao, E. Q. Distinct chromic and magnetic properties of metal–organic frameworks with a redox ligand. *ACS Appl. Mater. Interfaces*. **2017**,*9*, 5503-5512.

(54) Qi, C.; Zhang, D.; Gao, S.; Ma, H.; He, Y.; Ma, S. Yang, X. Crystal structure and magnetic property of a metal-organic framework (MOF) containing double-stranded chain with metallomacrocycles and dinuclearMn (II) subunits. *J. Mol. Struct.* **2008**, *891*, 357-363.

(55) Yi, F. Y.; Sun, Z. M. Solvent-controlled syntheses, structure, and mJ. Solid State Chem. agnetic properties of trinuclear Mn (II)-Based metal–organic frameworks. *Cryst. Growth Des.***2012**, *12*, 5693-5700.

(56) Yan, Y. T.; Zhang, W. Y.; Zhang, F.; Cao, F.; Yang, R. F.; Wang, Y. Y.; Hou, L. Four new metal–organic frameworks based on diverse secondary building units: sensing and magnetic properties. *Dalton Trans.* **2018**, *47*, 1682-1692.

(57) Chen, Y. Q.; Liu, S. J.; Li, Y. W.; Li, G. R.; He, K. H.; Chang, Z.; Bu, X. H. Mn (ii) metal–organic frameworks based on Mn3 clusters: from 2D layer to 3D framework by the "pillaring" approach. *CrystEngComm.***2013,***15*, 1613-1617.

(58) Kim, H.; Eom, S.; Park, S.; Kang, D. W.; Wang, M.; Kim, Y.; Hong, C. S. Structure, photoluminescence, and magnetic properties of a Mn (ii)-based metal–organic framework. *New J. Chem.* **2020**,*44*, 18694-18702.

Chapter 4

Strategy for the improvement of electrical conductivity of a 3D Zn(II)-coordination polymer doubly bridging by mesaconato and pyridyl-isonicotinoyl hydrazide Schottky diode device

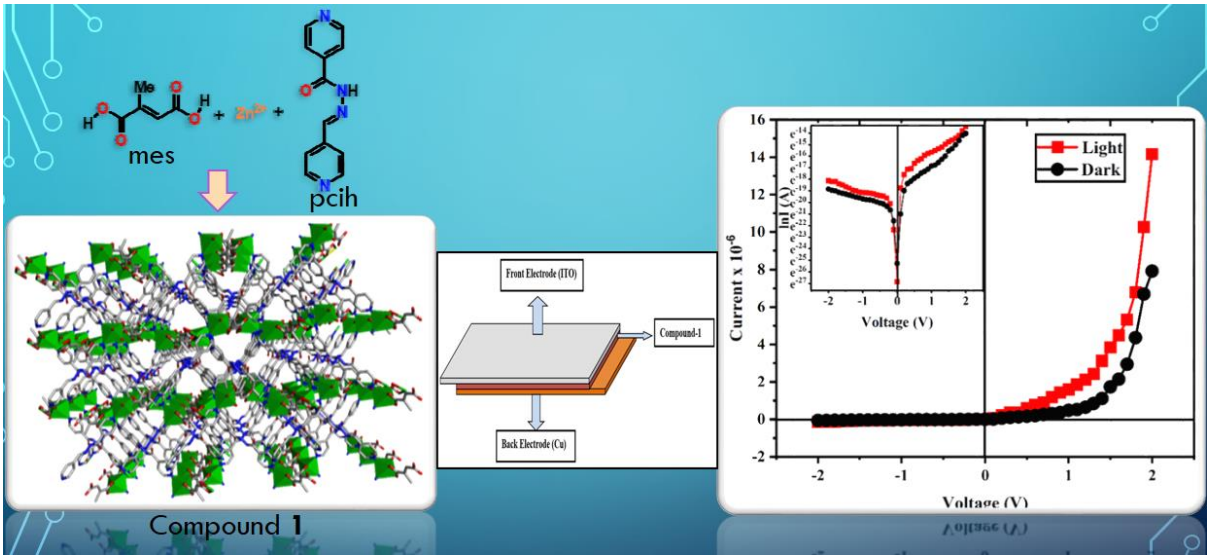

Abstract:

Out of many stimulating research fields, the search for energy materials is taking of highest priority in recent times due to issues related to sustainable development. Explicit investigation in energy is focused on the coordination polymers (CPs)/metal-organic frameworks (MOFs). Due to ordered orientation, impressive stability, and tuneable composition the MOFs have appropriatemultifunctional daises for electrochemical and photochemical energy conversion and storage. In this study, two bridging molecules, mesaconic acid (**H_2mes**) and pyridine-4-carboxaldehyde iso-nicotinoyl hydrazone(**pcih**) coordinate orthogonally to the Zn(II) metal node to construct a 3Dnetwork, **[Zn(mes)(pcih)(H_2O)$_2$]$_n$,** (**1**).The existence of non-covalent interactions make a robust 3D superstructure. The Tauc's plot calculates the band gap, 3.62 eVfrom UV-Vis spectroscopic data which maintains to design a Schottky device(diode area, 9×10^{-6} m^2 and the Richardson constant, 1.20×10^6 $AK^{-2}m^{-2}$) and measures the electrical conductivity $2.98\times10^{-4}Sm^{-1}$ (in dark);upon illumination, the conductivity is enhanced to $7.01\times10^{-4}Sm^{-1}$.However, the photosensitivity value of 1.72 can be revealed to consider the material as a next-generation technological aspect. It is expected that these material families may be the ornament for the researchers of energy material.

4.1 Introduction

In the history of scientific discovery, 1913 is a remarkable year because Alfred Warner (1866-1919) was awarded the Novel prize for their contribution tothe historic coordination theory of transition metal complexes. Coordination chemistry is now playing a central role in the development of chemistry and allied subjects for the intensive progress of human civilization. An interesting aspect of the coordination theory is the structure-function relation and application in diverse fields.[1-3]Multidentate ligands consisting of two or more donorcenterscan continuously extend in a special pattern to generate polymeric form, known as co-ordination polymers (CPs)[4-12]; the terminology introduced by J.C. Bailer in the year 1967.[13]Mainly, dicarboxylateand bipyridyl based organic compounds are employed to design CPs. The dimensionality of the CPs is largely dependent on the nature of the organic linker, metal node, and the reaction condition which may be extended from 1D, 2D to 3D. The

presence of appropriate porosity in 2D or 3D CPs has defined aninnovative class of material known as, Metal-Organic Frameworks (MOFs).[13-15] The CPs/MOFs, a class of hybrid multifunctional crystalline materials of fascinating structural architectures and topologies, have been widely used in gas storage and separation, catalysis,sensing, magnetism, drug delivery, biotechnology, electrical conductivity, proton conductivity, smart device fabrications, etc.[16-23]At present,themajor global challenge is to stop C-emission and exploration of green energy resources or to maintain zero energy loss. Materials with smart electrical conductivity and sustainability are highly advantageous to this vision. With this expectation, many research groups are dedicated to designing a number of such materials to achieve laboratory-to-land applications.[24-27] Recently, our group has strategically designed a series of Zn(II)-coordination polymers[28]for the generation of higher electrical conductivity both at dark and light phase. In this work,ararely used mesaconic acid (**H_2mes**)and pyridine-4-carboxaldehyde iso-nicotinoyl hydrazone (**pcih**) have been served as organic linkers to Zn(II) to synthesize a 3D CP, **[Zn(mes)(pcih)(H_2O)$_2$]$_n$,** (**1**).The Tauc's plot shows the band gap, 3.62 eV, and insists to measure the electrical conductivity from a Schottky diode both at dark (2.98×10^{-4} Sm^{-1}) and light (7.01×10^{-4} Sm^{-1}) phases. Nevertheless, the photosensitivity value is 1.72, and has asserted to consider the molecular system for next-generationenergysupport device.

4.2 Experimental Section

4.2.1 Materials and General Methods

All the chemicals used during this work were purchased in reagent grade and were used without further purification. Infrared (IR) spectrum was recorded using a Perkin Elmer SPECTRUM II LITA FT-IR spectrometer. On the compound **1**, a PerkinElmer 240C elemental analyzer was used to conduct an elemental analysis (carbon, hydrogen, and nitrogen).Thermogravimetric analysis (TGA) was carried out using a Perkin Elmer Pyris Diamond TG/DTA thermal analyzer in a nitrogen atmosphere (flow rate: 50 cm^3 min^{-1}) at a temperature range of 30-800 °C with a heating rate of 10 °C/min. Powder X-ray diffraction measurements were made using a Bruker D8 Discover instrument (Cu-Kα source).We recorded UV/vis spectra using a PerkinElmer Lambda 25 spectrophotometer.

4.2.2 Synthesis of $[Zn(mes)(pcih)(H_2O)_2]_n$, (1)

To methanol solution (2 mL) of **pcih** (0.045 g, 0.2 mmol) an aqueous solution (2 mL) of $Zn(NO_3)_2.6H_2O$ (0.060 g, 0.2 mmol) was slowly and carefully layered followed by the covering of buffer solution of DMF-MeOH (2 mL, 1:1 v/v) and of $\mathbf{mes^{2-}}$ (0.026 g, 0.2 mmol) neutralized with Et_3N (0.042 g, 0.4 mmol) in EtOH (2 mL). The yellow, needle-shaped crystals of {**[Zn(mes)(pcih)(H$_2$O)$_2$]$_n$},** (**1**)(**Scheme 4.1**)were obtained after a week(0.178 g, yield 65%). Microanalytical data for$C_{17}H_{14}N_4O_7Zn$(%): C, 45.20 ; H, 3.12 ; N, 12.40 ; found: C,45.59; H,3.39 ; N, 12.46. IR (cm^{-1}): 1560 $\nu_{as}(COO^-)$, 1361$\nu_{sys}(COO^-)$(**Figure 4. 1**)**.**

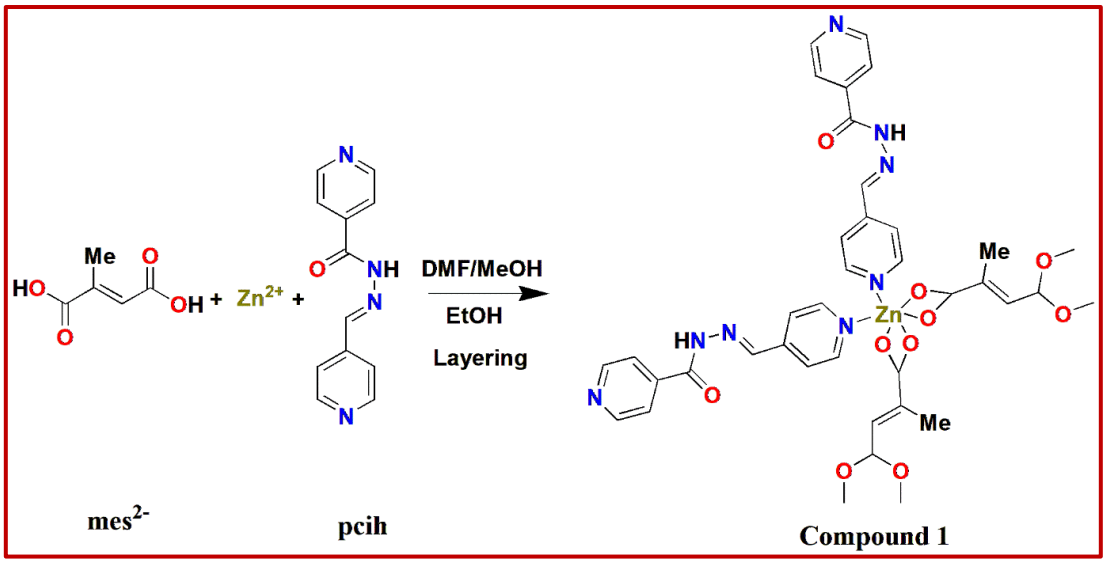

Scheme 4.1 Synthetic procedure of compound **1** through slow diffusion layering method.

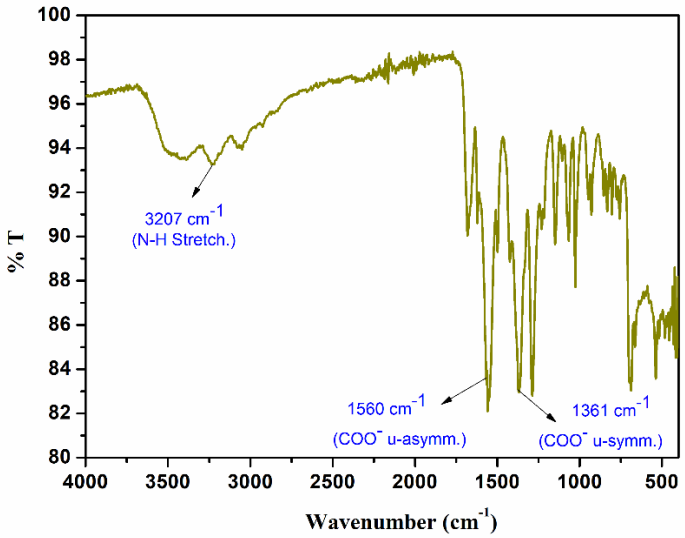

Figure 4.1 IR spectroscopy of Compound **1** .

4.2.3 Single Crystal X-Ray Diffraction Measurements

A rod-shaped yellow colored single crystal of the compound **1** was taken for Single X-Ray Diffraction data collection using a Bruker SMART APEX-III CCD diffractometer furnished with graphite-monochromatic Mo-Kα radiation (λ=0.71073 Å). The structure of the compound was solved with direct method and was refined by full-matrix least squares on F2 using the SHELXL-2016/6[29]program package. The non-hydrogen atoms present in the architecture were well-refined with an isotropic thermal parameter. The hydrogen atoms were positioned in their geometrically idealized positions and controlled to ride on their parent atoms. Least squares refinements of all reflections within the hkl range $-13 \leq h \leq 13$, $-18 \leq k \leq 18$, $-17 \leq l \leq 17$ were utilized to carry out the unit cell parameters and crystal-orientation matrices. Collected data ($I>2\sigma(I)$) of crystal was integrated by employing the SAINT program[30]and the absorption correction was performed through SADABS[31].

Table 4.1 Crystallographic results and refinement parameters for compound **1**

Compound	**1**
CCDC No.	2209342
Sum formula	C17 H14 N4 O7 Zn
Molecular weight	451.71
crystal system	Monoclinic
space group	P 21/c
a(Å)	11.6228(19)
b(Å)	15.296(3)
c(Å)	14.557(2)
β(°)	109.254(5)
V(Å^3)	2443.2(7)

T(K)	273(2)
Z	4
D_{calcd}(Mg/m^3)	1.228
μ(mm^{-1})	1.043
λ(Å)	0.71073
θ range (°)	24.997-2.366
R_1[a] [$I > 2\sigma(I)$]	0.0942 (2497)
wR_2[b]	0.2946 (4294)
Goodness-of-fit	1.000

[a]$R_1=\Sigma||F_o|-|Fc||/\Sigma|F_o|$, [b]$wR_2=[\Sigma w(F_o^2-Fc^2)^2/\Sigma wF_o^2)^2]/2$,w= 1/[σ2(Fo2)+(0.0350P)2 + 0.9811P], where P= $(F_o^2+2Fc^2)/3$

Table 4.2 Selected bond lengths and bond angles in **1.**

Zn(1) - O(3)	2.035(6)	O(4) - C(4)	1.228(11)
Zn(1) - O(4)	2.433(6)	O(5) - C(10)	1.232(15)
Zn(1) - N(4)	2.051(7)	N(1) - C(14)	1.323(13)
Zn(1) - N(1)a	2.067(7)	N(1) - C(16)	1.297(12)
Zn(1) - O(1)c	2.349(9)	N(2) - N(3)	1.358(12)
Zn(1) - O(2)c	2.039(9)	N(2) - C(11)	1.272(12)
O(1) - C(1)	1.215(17)	N(3) - C(10)	1.345(13)

O(2) - C(1)	1.208(16)	N(4) - Zn(1) - N(1)a	101.1(3)
O(3) - C(4)	1.273(11)	N(4) - Zn(1) - O(1)c	91.7(3)
O(3) - Zn(1) - O(4)	57.3(2)	O(3) - Zn(1) - N(1)a	106.8(3)
O(3) - Zn(1) - N(4)	96.8(3)	O(3) - Zn(1) - O(1)c	94.2(3)
N(1)a - Zn(1) - O(1)c	153.7(3)	O(3) - Zn(1) - O(2)c	143.1(3)
C(1) - O(1) - Zn(1)b	83.5(7)	O(3) - Zn(1) - C(1)c	119.6(3)
N(4) - Zn(1) - O(2)c	105.5(3)	O(4) - Zn(1) - N(4)	153.9(2)
O(1)c - Zn(1) - C(1)c	28.6(4)	O(4) - Zn(1) - N(1)a	90.5(2)
O(2)c - Zn(1) - C(1)c	28.3(4)	O(4) - Zn(1) - O(1)c	87.7(3)
N(4) - Zn(1) - C(1)c	100.4(3)	O(4) - Zn(1) - O(2)c	95.9(3)
N(1)a - Zn(1) - O(2)c	97.3(3)	O(4) - Zn(1) - C(1)c	91.5(3)
N(1)a - Zn(1) - C(1)c	125.4(4)	O(1)c - Zn(1) - O(2)c	56.9(4)

a = -1+x,1/2-y,-1/2+z, b = x,3/2-y,-1/2+z, c = x,3/2-y,1/2+z

4.2.4 DFT computation

Optimization of the gas phase geometry of the compound 1 was carried out using Density Functional Theory (DFT) calculation of Gaussian Program Package 09[32-34].All calculations were performed using SCXRD coordinates and B3LYP method. LanL2DZ basis set were employed for all elements including Zn. Different electronic transitions were theoretically determined using the time-dependent density functional theory (TDDFT) formalism calculation[35]. Vibrational frequency calculations were performed to ensure that the DFT-optimized geometries represent the local minima and only positive eigenvalues.

4.2.5 Hirshfeld surface (HS) analysis

Hirshfeld surface and 2D finger print plot[36-39] were calculated with the help of CRYSTAL EXPLORER 3.1[40] using Crystal structure (CIF) file. The Hirshfeld surface was plotted over normalized contact distance (d_{norm})[41]. Shape index and decomposed fingerprint plot were presented in term of d_e vs d_i. The d_{norm}, expressed as

$$d_{norm} = (d_i - r_i^{vdw}) / r_i^{vdw} + (d_e - r_e^{vdw}) / r_e^{vdw}$$

where r_i^{vdw} and r_e^{vdw} are the van der Waals radii of the atoms, indicates the regions have the ability to intermolecular interactions[42]. The extended form of three-dimensional close contact in a crystal structure gives supramolecular structure.

4.3 Results and Discussion

4.3.1 Description of Molecular Structure of $[Zn(mes)(pcih)(H_2O)_2]_n$, (1)

The compound X-Ray crystallographic dataanalysis has reported that the crystal is monoclinic crystal system with space group,P 21/cand Z=4; D_x = 1.228 $g.cm^{-3}$(**Table 4.1**). The structural architecture has exhibited distorted octahedral geometry having ZnO_4N_2unit where Pyridyl-N of pyridine-4-carboxaldehyde iso-nicotinoyl hydrazone (**pcih**) and carboxylate-O of mesaconate ion (**mes^{2-}**) coordinates/chelates to Zn (II) and four free oxyzen atom present in the co-ordination sphere (**Figure 4.2**) . Both the ligands act as linear bridging spacer and propagates approximately in orthogonal fashion; thus, a 3D coordination network is constituted (**Figure 4.4**).

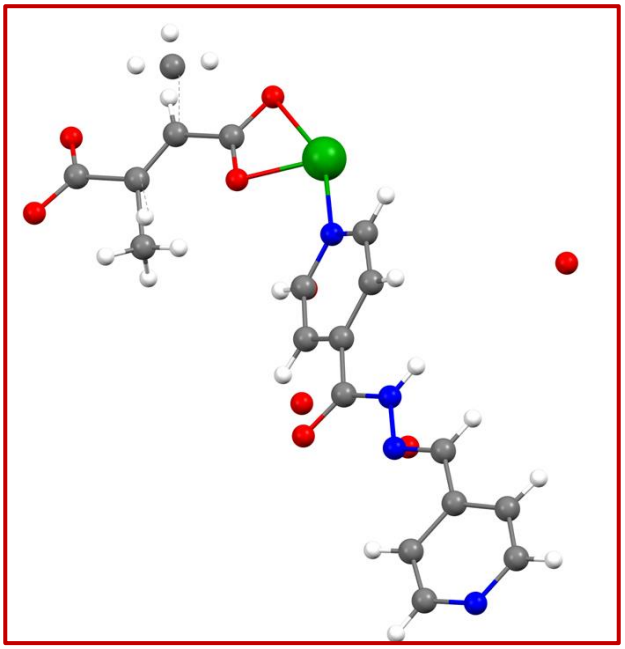

Figure 4.2 View of asymmetric unit along crystallographic axis b**.**

If the molecular structure has been considered along crystallographic cell axes, then it can be stated a rectilinear ligand which can help to extend the coordination in the infinite array to construct 3D structure(**Figure 4.3**).

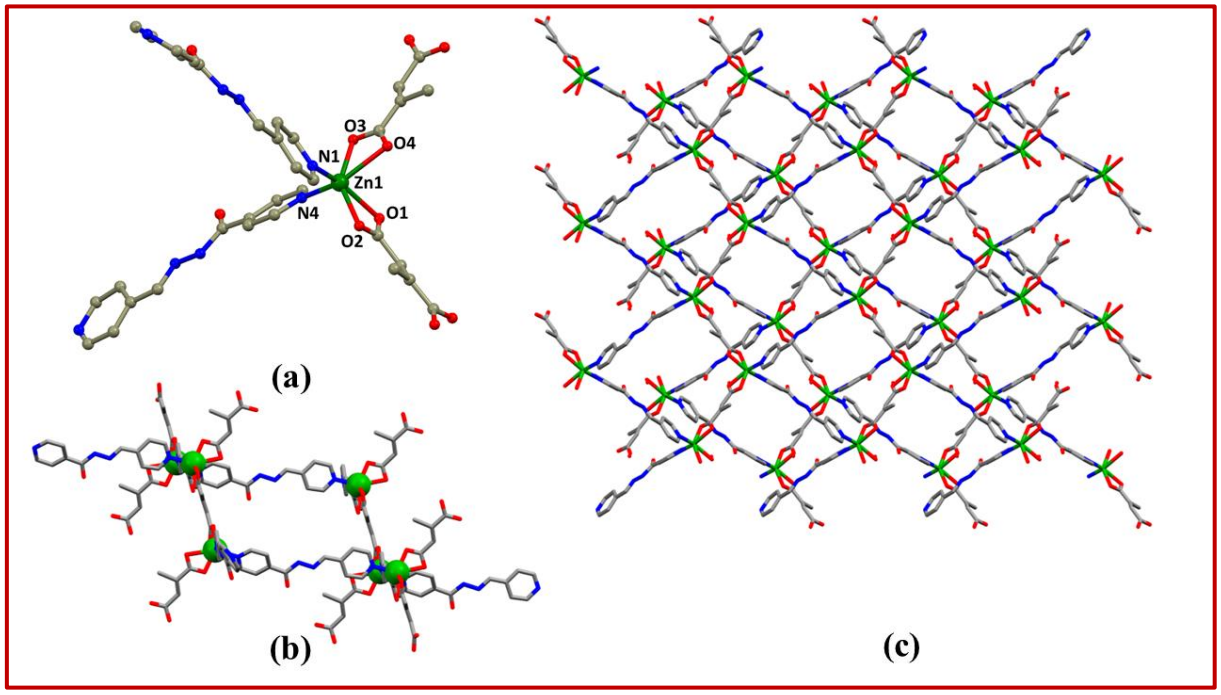

Figure 4.3 (**a**) Coordination environment around Zn(II)-meteal of **1**;(**b**) View of a portion of 3D network formed by continuous coordination of **pcih** and **mes**$^{2-}$; (**c**) Packing of 3Dstructure viewed along *a*- axis.(Hydrogen atoms are removed for clarity;C: gray; Cd: green; N: blue; O: red)

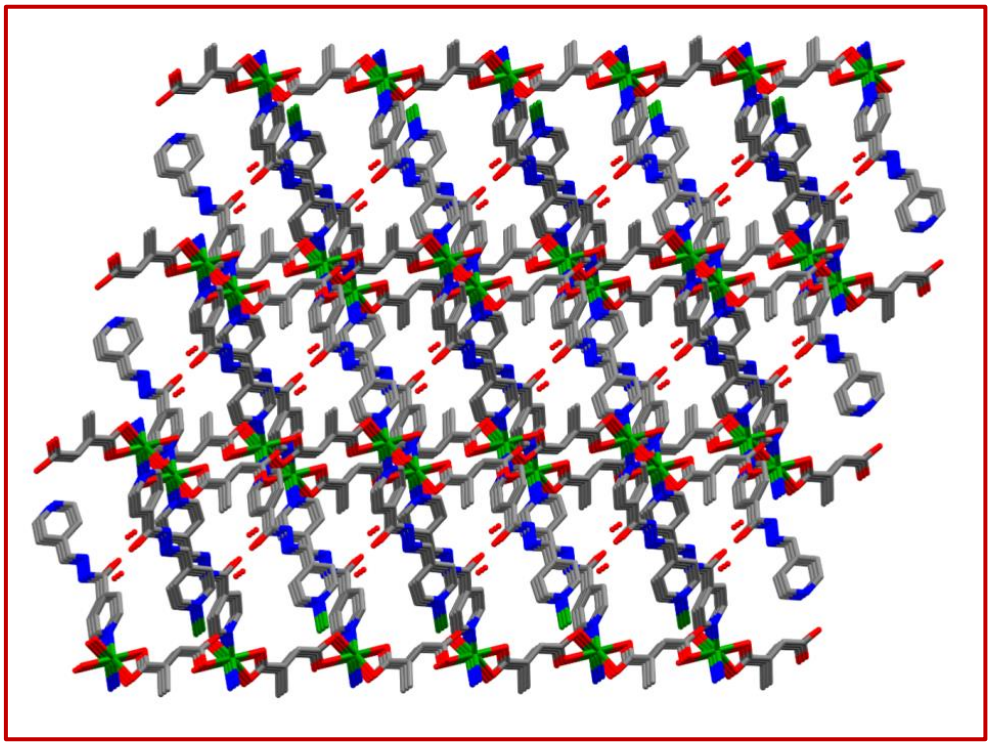

Figure 4.4 3D structure of **1.**

Interestingly, **mes**$^{2-}$ coordinated as chelating manner Zn(1)- O(1)c, 2.349(9); Zn(1)-O(2)c, 2.039(9); Zn(1)-O(3), 2.035(6); Zn(1)-O(4), 2.433(6) Å and O(3)- Zn(1) - O(4), 57.3 (2); O(1) - Zn(1) -O(2) , 56.9 (4) ; N(1)- Zn(1)- N(4), 101.1 (3) and **pcih** coordinated through pyridyl-N N(4)-Zn(1), 2.051; N(1)-Zn(1), 2.067 Å as mono-dentate fashion to fulfil the coordination environment.

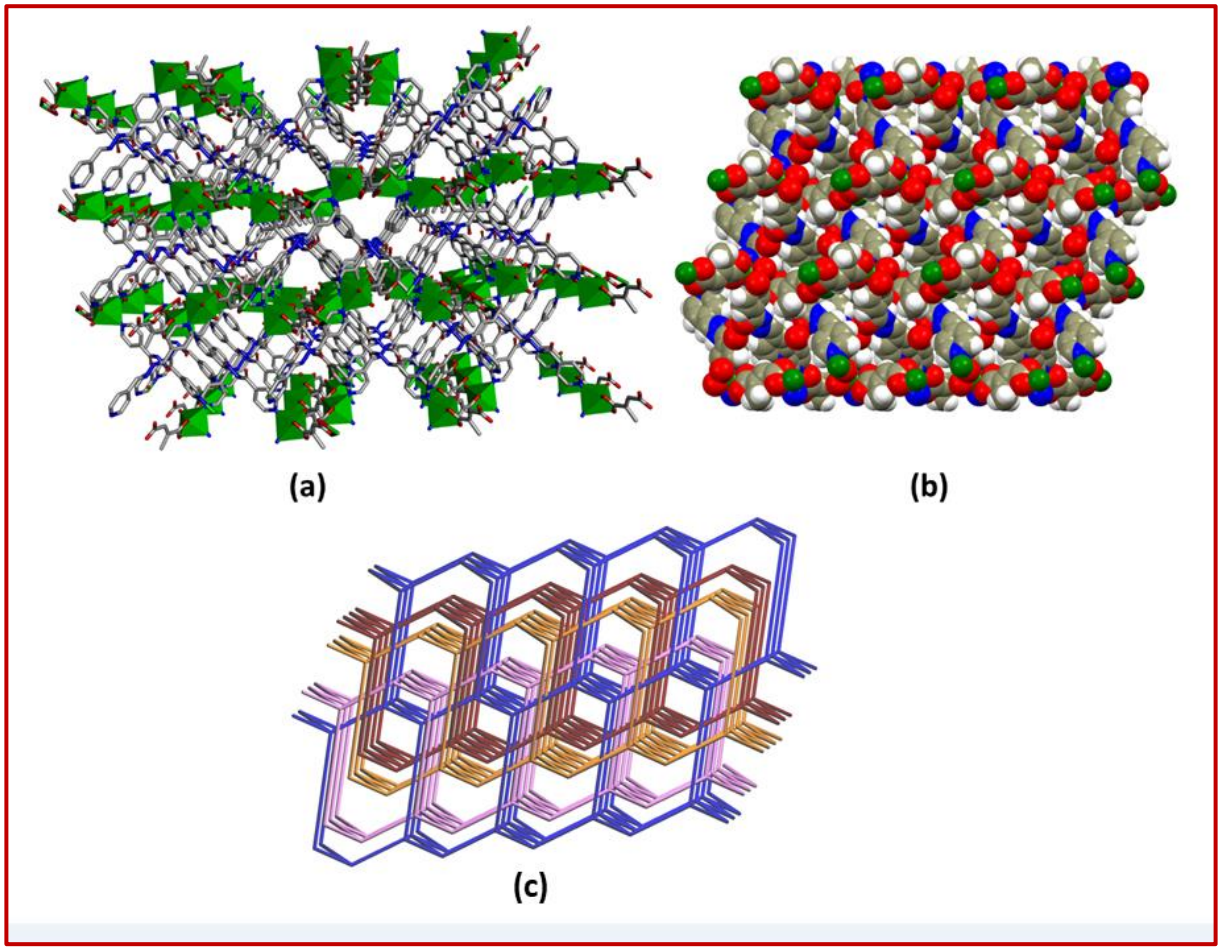

Figure 4.5 (a) 3D metal-organic framework structure of **1** in perspective view;(b) Space-fill view of network structure exhibited porosity. (c) Topological structure of **1**.

The pyridyl rings are oriented in a fashion to induce π···π stacking at a distance of 4.540 Å and propagates along the *a*-axis. The hydrogen bonding interactions (2.63 Å) exist in the di-carboxylate oxygen and -N-H hydrogen of **pcih** moiety to form a robust 3D geometry (**Figure 4.5(a,b)**). Non-classical hydrogen bonding is also there between O ('C=O') atom of isoniazide moiety and H ('CH_3') of meconate systemwith distance 2.776Å to improve the architecture stability.The Selected bond lengths and bond angles in **Table 4.2**.The topology of the as-synthesized Compound **1** is presented in (**Figure 4.5 (c)**) with the three digit point symbol dia ;4/6/c1 and It is a 3D -3D interpenetrated diamondoid network with four fold interpenetration.

4.3.2 Hirshfeld surface analysis

The Hirshfeld surfaces Theoretical manipulation of the intermolecular interaction of molecular crystals has been accounted by the Hirshfeld surface analysis. It is a powerful technique for determining the degree of atomic or residual contacts within a molecular crystal. We have inspected the asymmetric unit to examine the Hirshfeld surfaces, which comprise dnorm, shape index, and curvedness (**Figure 4.6**). In 1 the interactions between O···H atoms are the leading connections.

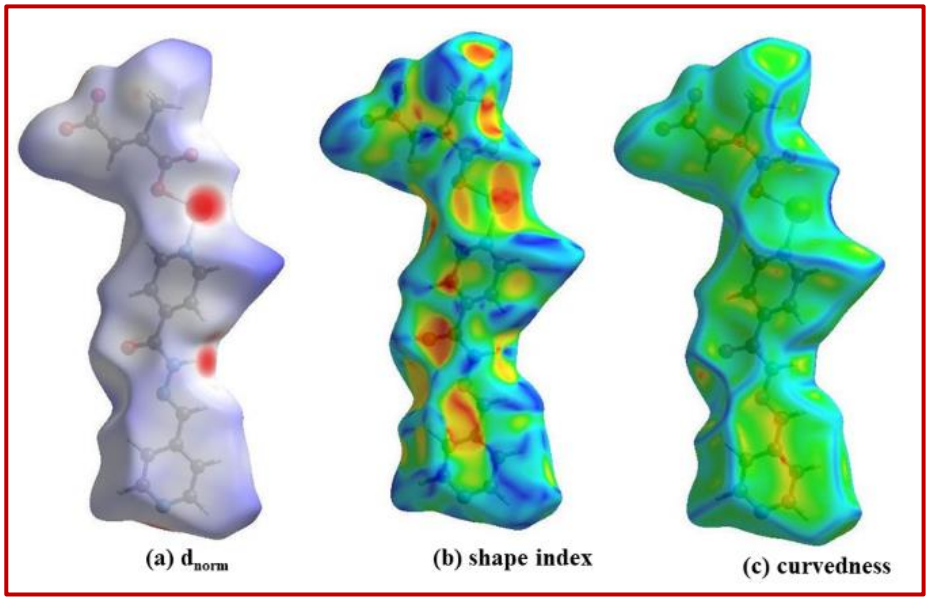

Figure 4.6 Hirshfeld surfaces mapped over (a) dnorm (b) shape index and (c) curvedness for **1**.

The de and di parameters, which explain the percentage dominance of a specific interaction in creating the supramolecular architecture, are used to construct the 2D fingerprint plots.Using the software Crystal Explorer, the HS is mapped with various attributes and 2D fingerprint plots are produced.

In the presentation of dnorm the colour codes - red, white, and blue patches are used to segregate between distances that are closer, equal, or farther away from van der Waals radii. As a distinctive representative of molecular surfaces, curvature is quantified using curvedness parameters and shape index to add further chemical context to crystal packing. The shape index displays the molecular surface contacts as corresponding hollows (red) and bumps

(blue), whereas the curvedness plot is predominantly made up of sizable green patches, with comparatively flat sections being separated by dark blue lines. Dark-blue edges in both the form index and the curvedness indicate a zone with a higher degree of curvature.

Theoretical manipulation of the intermolecular interaction of molecular crystals has been accounted by the Hirshfeld surface analysis (**Figure 4.6**)**.**In relation to the inside and outside of the molecule surfaces, two distinct yet appropriate distance parameters, di and de, are displayed between the 2D fingerprint graphs. First, a complete fingerprint plot is mapped to show all potential interactions inside the crystal structure. Nevertheless, specific elemental interactions, such as the atoms of C··H/H··C, account for 13.6% of the Hirschfeld total surface area. In the plot, the bottom spike (di = 1.6, de = 1.1) represents the C··H interaction, whereas the top spike (di = 1.1, de = 1.6) demonstrates the C··H interaction (**Figure 4.7**).TheHirshfeld surface comprises 30.2% of the O··H/H··O interaction. The bottom spike (di = 1.1, de= 0.8) embodies the O··H interaction, while the top spike (di = 0.8, de = 1.1) signifies the H··O interaction. The H···H interaction comprises 30.2% of the Hirshfeld surface. As a result, the extent of C··H/H··C and H···H interactions is higher and includes 30.2% of the entire surface, which is shown by a red point in the dnorm surface area.

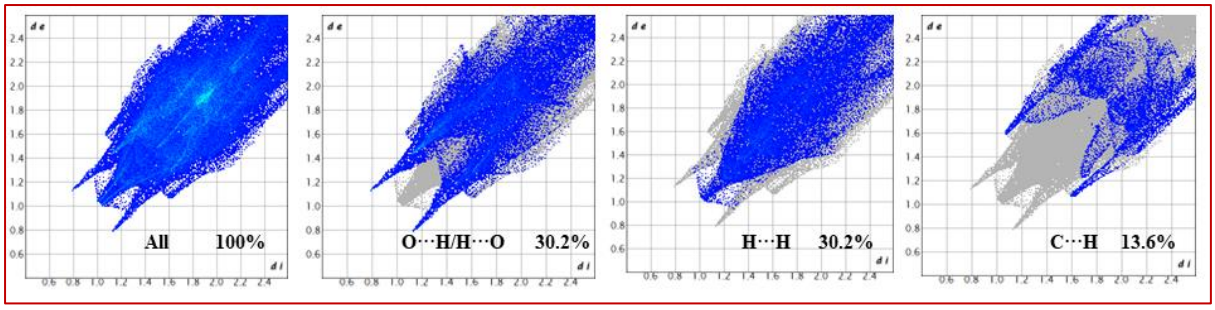

Figure 4.7 Areas of various intermolecular interactions are plainly visible in a 2D fingerprint plot.

Thus, Hirshfeld surface analysis is used to confirm the relevance of contacts in determining molecular crystal packing, followed by the assistance of various secondaryconnections.The overall Hirshfeld surface area for the compound **1**, along with all major and minor intermolecular interactions, are depicted in along with their percentage contributions (**Figure 4.8**).

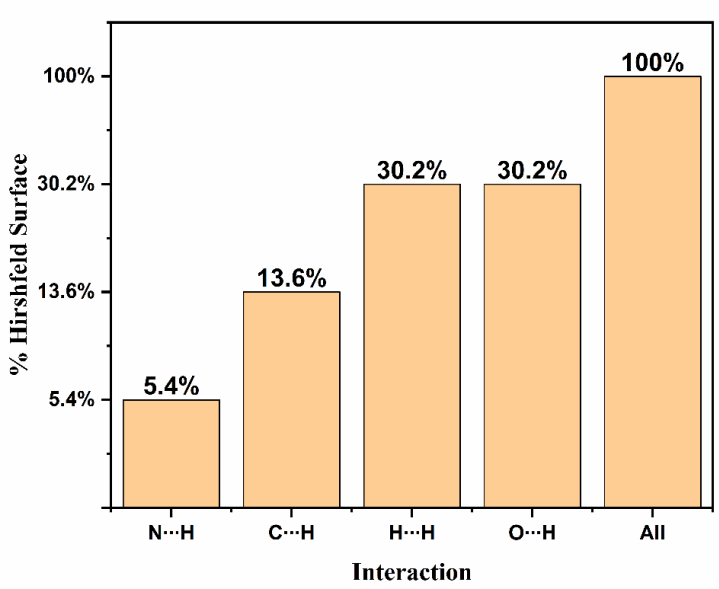

Figure 4.8 Hirshfeld surface area relative contributions from different intermolecular interactions (O, H, C and N) in **1**.

4.3.3. Crystallinity and Thermal stability

Powder X-ray diffraction The crystalline consistency of the substance is confirmed by Powder X-ray diffraction (PXRD) at room temperature.The majority of the peaks in the as-synthesized**1** pattern match those predicted from SCXRD rather well, indicating the bulk material system's phase purity (**Figure 4.9**).

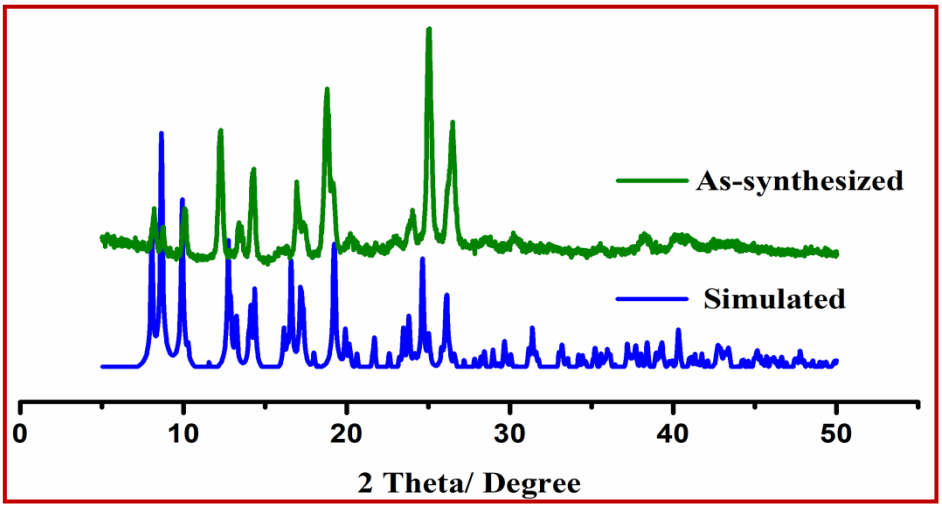

Figure 4.9 PXRD plot of compound **1.**

To authenticate the stability of material with respect to increasing temperature,the powdered sample has undergone thermogravimetric analysis (TGA) at temperatures between 30°C to 830°C while being in a N_2 environment.TGA curve showsweight loss has been happened 90°C, this weight loss corresponds to two molecules of aqua entities (experimental weightloss 8.74%, calculating 7.92%), followed by formation of residual ZnO(residue experimental 16.09% , calculating 16.97%)(**Figure S7**). The frameworks are essentially stable at 295 °C, proving good stability.

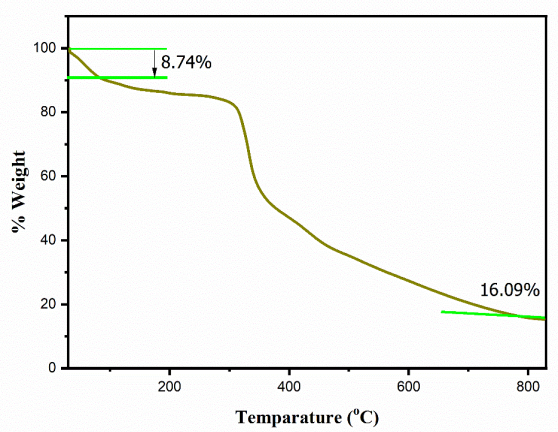

Figure 4.10 TGA plot of Compound **1.**

4.3.3 Electrical Conductivity

4.3.3.1 Device Fabrication

To conduct the electrical analysis of the sample, numerous MS (metal-semiconductor)junction devices were fabricated in a sandwich configuration. Indium-Tin-Oxide (ITO) coated glass was used as the front electrode, copperplate (Cu) as the back electrode, and compound **1**was sandwiched between them. In this case, the synthesized material**1** was well dispersed in DMFsolution by sonicating (35 mg/ml) in separate vials. Both electrodes (ITO-coated glass and Cu plates)were first washed with a diluted detergent. After 10 minutes of washing in the detergent at 60°C, rinsedwith de-ionized water. Electrodes were then sequentially sonicated inde-ionized water, acetone, and finally in2-propanol. At the final stage of the electrode cleaning process, electrodes were dried using the flow of N_2 and then kept in the oven at a temperature 70°C. Electrode substrates were exposed to UV light for ten minutes beforethe formation of the film on it.

UsingSCU 2700 spin coating unit, this newly prepared dispersed solution of compound **1** was spin-coated on the top of the ITO-coated glass substrate at 700 rpm for 1 min. The Cu plate was then placed over the sample and was dried for several minutes at 75°C in a vacuum oven to completely evaporate the solvent component. **Figure 4.11(a)** represents the FESEM image of the film's thickness of the sample spin-coated over a cover slide with the same procedure under the same condition. The sample was found to be spread consistently over the glass slide having a thickness of 2.525 µm. **Figure 4.11(b)** represents the schematic structure ofthe ITO/compound **1**/Cu device configuration. The current-voltage (*I-V*) characteristic of the devices was recorded using a Keithley 2400 sourcemeter unitwith a two-probe approach for electrical characterization. The measurements and preparation were carried out at room temperature.The circuit diagram of our experiment is depected in **Figure 4.11(c)**.

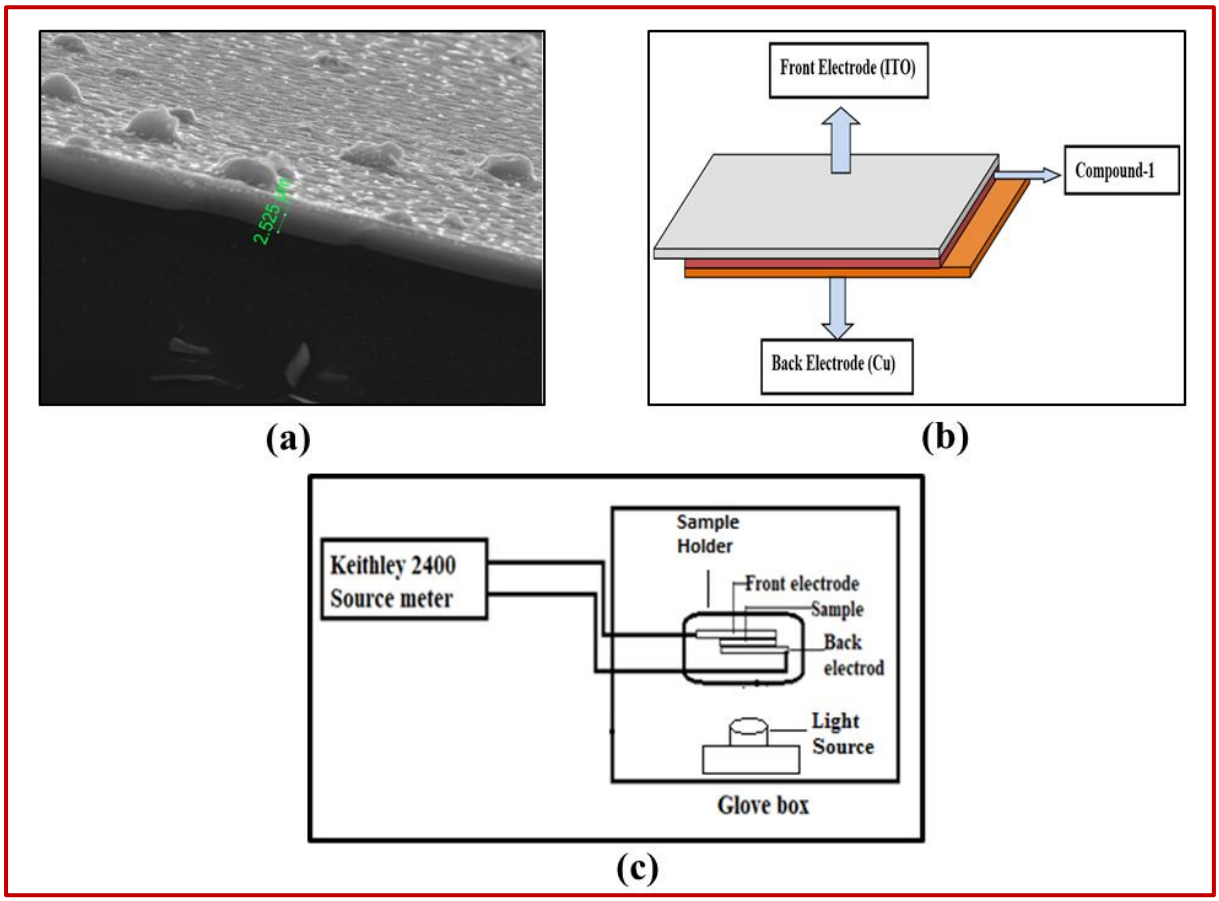

Figure 4.11 **(a)** SEM image showingthe thickness of compound **1** film **(b)** Schematic device structure.**(c)** Circuit Diagram for the Dark and photo I-V measurement.

4.3.3.2 Optical band gap

The optical spectrum (**Figure 4.12**) within the wavelength range 250 – 800 nm of a thin layer of **1** has been used to calculate the band gap by using Tauc's plot[43,44,45] and **Equation 1**. A sharp peak is found to be at 296.43 nm wavelength. This can be associated with the plausible electronic transition between n-π* states.

$$(\alpha h\nu)^{\frac{1}{n}} = A[h\nu - E_g] \quad (1)$$

(α, E_g, h and ν are absorption coefficient, band gap, Planck's constant, and frequency of light respectively; exponent n is a constant that depends on the electron transition process).

A is a constant that, in the best situation, is assumed to be **1**. The value of the exponent n in the equation above was taken into account as $n = {}^{1}/_{2}$ to compute the direct optical band gap[46]. By extrapolating the linear region of the plot $(\alpha h\nu)^2$ *vs.* $h\nu$ to α = 0 absorption, the values of direct optical band gap (E_g) of compound **1** were found to be 3.62 eV.

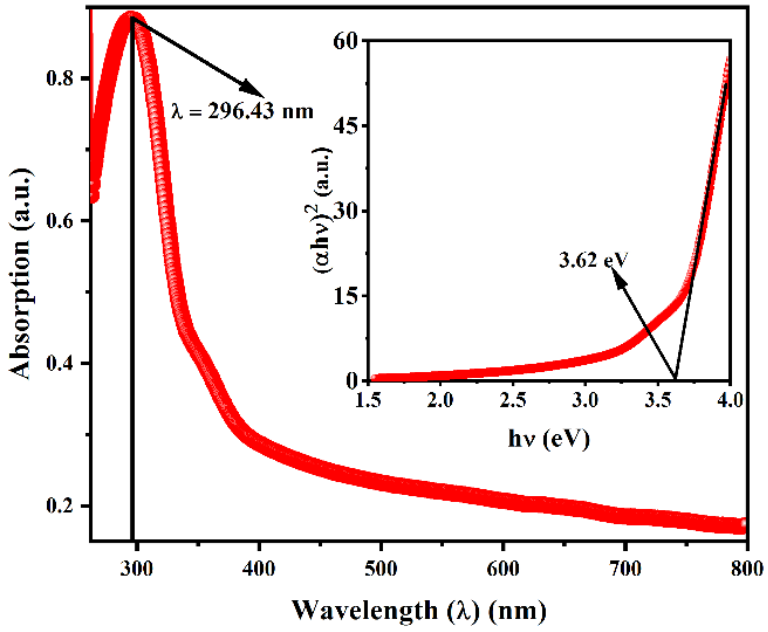

Figure 4.12 Absorption spectroscopy and Tauc's plot (Inset) of compound **1.**

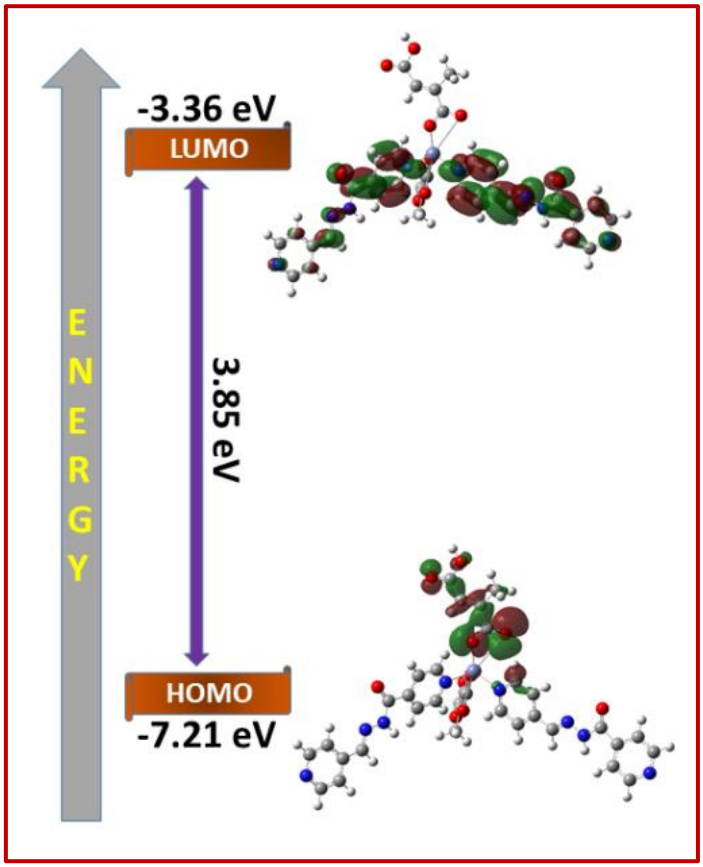

Figure 4.13 DFT calculated the HOMO-LUMO difference

Single crystal X-ray diffraction coordinates have been used to calculate the energy of frontier molecular orbitals. The HOMO-LUMO energy gap is 3.85 eV (**Figure 4.13**) which is quite similar to the direct band gap (3.62 eV) determined from Tauc's plot.

4.3.4 Electrical Characterization

The current-voltage (*I–V*) plot of the ITO/compound **1**/Cu Schottky device inthe voltage range -2V to +2V at ambient temperature under dark and light-irradiation conditions is shown in **Figure 4.14**. The current conduction mechanism changes after a particular transition voltage which is considered as threshold voltage (V_{th}, **Table 4.3**).

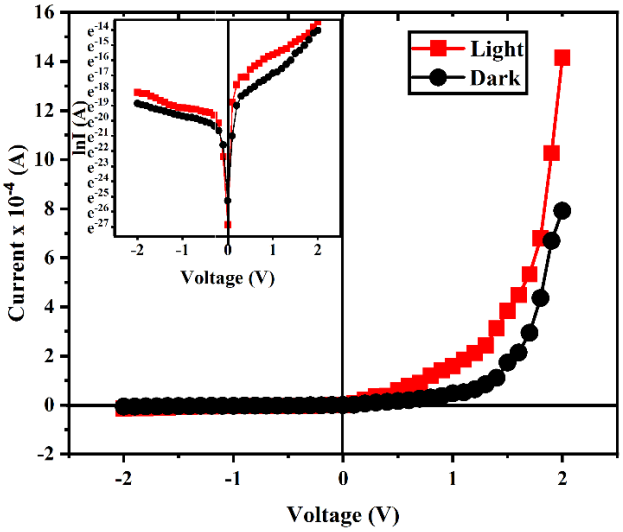

Figure 4.14 Current-Voltage (*I–V*) plotsof thin film device in dark and light conditions. The inset of the figure represents the lnI vs V plot.

According to thermionic emission (TE) theory, compound **1**'s rectification ratio was determined to be 6.09 at 1.84 V for illuminated conditions, and 9.30 in dark conditions at the same applied voltage. The photosensitivity of compound **1** was determined to be 1.72 at 1000 Wm^{-2}illumination. Using the TE theory[47,48,49]the current of a diode can be expressed as follows in **Equation 2**:

$$I = I_0 \exp\left(\frac{qV}{nkT}\right) \quad (2)$$

WhereI_0can be expressed as

$$I_0 = AA^{*}T^{2}\exp\left(\frac{-q\phi_b}{kT}\right) \quad (3)$$

where 'q' represents the charge of a carrier, 'k' is the Boltzmann constant, 'T' refers to the temperature in Kelvin, 'n' is the ideality factor which shows how closely a diode follows the ideal diode equation, area of the device is represented by'A', 'ϕ_b' is the barrier height of the junction, 'I_0' is the reverse saturation current, and 'A^{*}' stands for the effective Richardson constant. Taking 'log' in **Equation 3**, it can be obtained as in **Equation 4**:

$$\phi_b = \frac{kT}{q}\ln\left(\frac{AA^{*}T^{2}}{I_0}\right) \quad (4)$$

The effective diode area was considered as A = 9 × 10^{-6} m^2 and the Richardson constant was considered as A^*= 1.20 × 10^6 $AK^{-2}m^{-2}$. Cheung's equations (**Equations 5 and 6**) were used to calculate the series resistance, ideality factor, and barrier height.

$$\frac{dV}{d(\ln I)} = \frac{nkT}{q} + IR_s \quad (5)$$

$$H(I) = V - \left(\frac{nkT}{q}\right)\ln\left(\frac{I}{AA^*T^2}\right) \quad (6)$$

and H(I) is given as follows:

$$H(I) = n\phi_b + IR_s \quad (7)$$

Theslope ofthe linear portion of$\frac{dV}{d(lnI)}$*vs.* I plot (**Figure 4.15(a)**) gives the value of R_S and $\frac{nkT}{q}$ as the y-intercept. The *H(I)vs.* I plot (**Figure 4.15(b)**) has also a linear portion with a slope$R_S$and$n\phi_b$ as the y-intercept. Electrical parameters of low voltage regime values of σ, n, ϕ_b, R_s, and photosensitivity of the compound **1** based device have been given in **Table 4.4**.

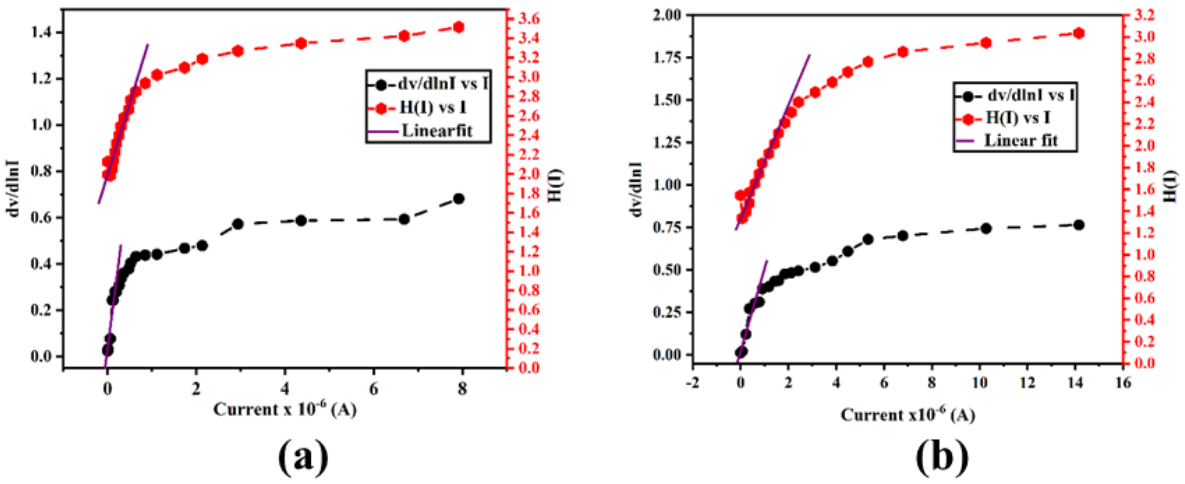

Figure 4.15 dV/dlnIvs. I and H(I) vs. I plot of compound **1** under **(a)** Dark condition and **(b)** Photo illuminated condition

Table 4.4 Schottky diode parameters of the compound **1**

Measured condition	Conductivity at 1.5 V (σ) × 10^{-4} (S m^{-1})	Photo sensitivity	Threshold Voltage (V_{th}) (V)	$\frac{dV}{d(lnI)}$ vs I Plot		H(I) vs I plot	
				Ideality Factor (η)	Series Resistance (R_S) (Ω)	Barrier Height (ϕ_b) (eV)	Series Resistance (R_S) (Ω)
Dark	2.98	1.72	0.316	2.141	405.638	0.411	360.250
Light	7.01		0.275	1.494	284.708	0.391	225.580

The ideality factor (η: 2.141 (dark), 1.494 (light)) greater than 1 indicates that the device behavioris not ideal due to the high electron and hole recombination in the depletion region, the presence of tunneling current, the presence of barrier height inhomogeneities presence at an interface[45,45]. However, η inthe dark phase is greater than in the light phase,and shows better electron transportation inthe light phase; which is supported by the lowering of series resistance (**Table 4.4**) and barrier height (ϕ_b) also at the light phase.This observation is an important finding about the sample's behavior. The barrier of Schottky junctions generally exhibits less interfacial charge carrier recombination and more homogeneity formation[46]. This shows that under illuminated conditions, the barrier uniformity of the fabricated device of compound **1** has been improved.

The barrier height (ϕ_b)was determined using the y-axis intercept of the *H(I)* vs. *I* curve and the slope of this plot providesecond determination of the series resistance. The decrease in barrier potential height of the present device under light may be due to the generation of photo-induced charge carriers and their accumulation near the conduction. The series resistance and barrier height estimated in separate techniques show good consistency in

value. When light is illuminated, the resultant series resistance was also decreased (**Table 4.4**), indicating its application in the field of optoelectronic devices.

We have further investigated the *lnI-lnV* plot of the I-V curve for better insight into the charge transport mechanism at the junction. The presence of two distinct zones, regions I and II, with varying slope values can be seen in **Figure 4.16(a)**. Here, the power law controls the current conduction mechanism ($I \propto V^m$), where m is the slope of the *I-V*curve[46].The sample displays ohmic behavior($I \propto V$) at low bias voltage (Region-I).The region-II corresponds to the higher ordered magnitude of slope at substantially higher voltage and displays current variation with a square of forward bias voltage ($I \propto V^2$). The slope (m=2) value in Region II suggests that the trap free space charge limited current (SCLC) conduction mechanism was dominant in the device[44]. If the injected carriers exceed the background carriers, a space charge field develops near the electrode until a particular applied voltage is reached. When the bias voltage reaches a certain level, the accumulated space charge begins to flow through the device.

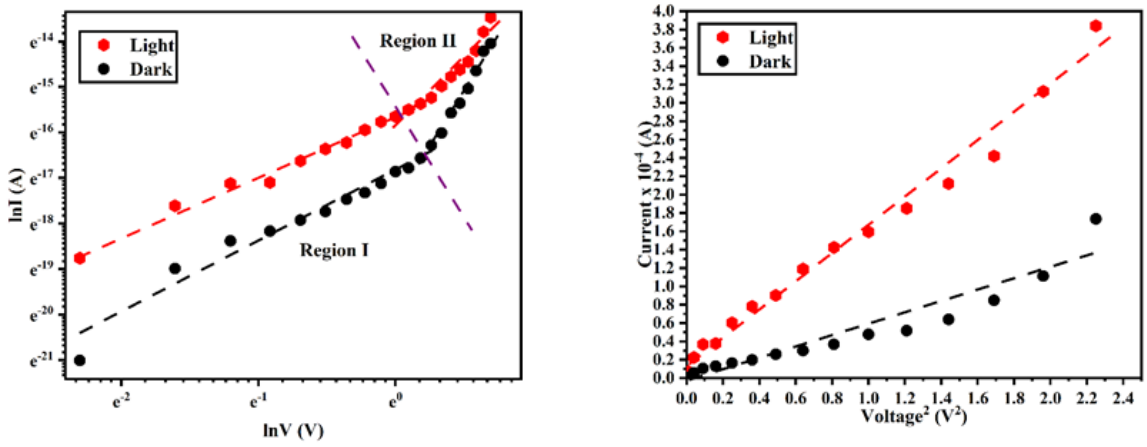

Figure 4.16 (a)ln I *vs.*ln V plot **(b)**I versus V^2 plotunder dark and light conditions

Using the Mott-Gurney equationand with the help ofabove explained SCLC model, the effective carrier mobility was calculated from the *I vs.* V^2 plot (**Figure 4.16(b)**).

$$I = \frac{9\mu_{eff}\varepsilon_0\varepsilon_r A}{8}\left(\frac{V^2}{D^3}\right) \qquad (8)$$

Where ε_0 is the permittivity of free space,is the relative dielectric constant of the synthesized material; μ_{eff} is the effective carrier mobility. To estimate the relative dielectric constant of compound **1**, the capacitance vs. frequency characteristic of the film was measured at a constant bias potential (1.5 V), as shown in **Figure 4.17**.

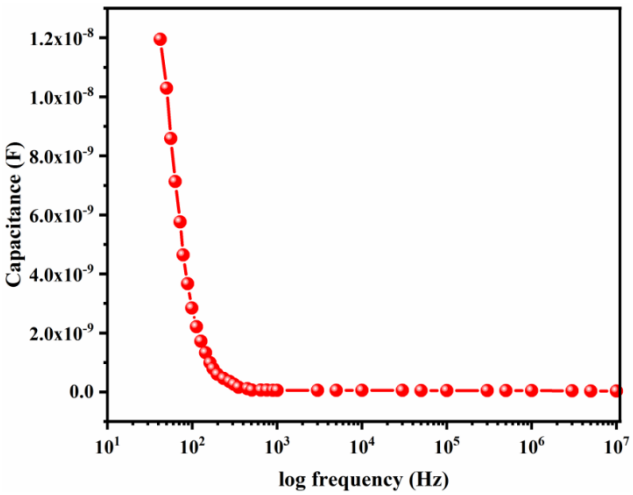

Figure 4.17 Capacitance vs. Frequency (*C–f*) plot

Employing **Equation 9**, the effective dielectric constant was determined as 5.06.

$$\varepsilon_r = \frac{1}{\varepsilon_0}\frac{CD}{A} \qquad (9)$$

Where C is the capacitance, which is obtained from the saturation value of **Figure 4.17**, D represents the thickness of the film. Now the transit time (τ) is the time, which is required by a carrier to transport from anode to cathode and is calculated with the help of following **Equation 10**. [48]

$$\tau = \frac{9\varepsilon_0\varepsilon_r A}{8D}\left(\frac{V}{I}\right) \qquad (10)$$

Equation 11 below shows the relationship between the diffusion length (L_d) and the transition time (τ).

$$L_d = \sqrt{2d\tau} \qquad (11)$$

Here, d is the diffusion coefficientestimated using Einstein–Smoluchowski **Equation 12**[50].

$$\mu_{eff} = \frac{qd}{kT} \quad (12)$$

Thediffusion length (L_d) of charge carriers is an important parameter of the device, which has been calculated from **Equation 11**. The values of all the parameters stated above have been demonstrated in **Table 4.5.** In the presence of light, carriers mobility has increased because of the generation carrier in light.The influence of charge trapping may be considered to explain the longer transit time of careers in dark conditions.The values of diffusion length show that the careers travel a larger path under illuminated conditions than in dark conditions. Since the compound **1** based device has an excellent charge conduction mechanism in the presence of light, it can be used as a potential material infuture electrical and optical device applications.

Table 4.5 Charge conducting parameters of the compound **1** based thin-film device

Measured Condition	Carrier mobility (μ_{eff}) × 10^{-4} ($m^2v^{-1}s^{-1}$)	Transit Time (τ) × 10^{-10} (Sec)	$\tau\mu_{eff}$ × 10^{-14} (m^2v^{-1})	Diffusion Coefficient (d) × 10^{-6}	Diffusion Length (L_d) × 10^{-8} (m)
Dark	1.68	4.30	7.22	4.35	6.11
Light	4.28	1.77	7.58	11.26	6.31

4.4 Conclusion

In summary, we have synthesized Zn(II)-coordinated 3D framework with rarely used mesaconic acid. The compound has been well characterized and structurally analysed to collaborate the structure-property relationship. The designed MOF reveals good electrical conductivity with a nearly identical ideality factor to the semiconductors. Current-voltage characteristics display the semiconducting behaviour of the molecule. This study also exhibits that this material is sensitive the light energy which can be a possible application of optoelectronic devices. The electrical conductivity (optical band gap, 3.62 eV; theoretical band gap 3.85 eV) with improved conductivity upon light irradiation (2.98 x 10^{-4} (dark), 7.01

x 10^{-4} (light) Sm^{-1}). The Schottky device of the compound shows a better ideality factor inthelight phase than the dark phase (2.141 (dark), 1.498(light)), and the series resistance is decreased on light irradiation. The increase in the conductivity by the influence of light can be abbreviated as the increase of the mobility of the charge carriers and for the increase in the charge career density by gaining the energy from the incident photon. Therefore, in this energy crisis civilization, the present study may be the paved way toward the laboratory-to-land application of such energy material in view of the technological aspect.

3.7 References

(1) Jurisson, S.;Berning, D.;Jia W. and Ma, D.Coordination compounds in nuclear medicine.*Chem. Rev.* **1993**, *93*, 1137-1156.

(2) Gütlich, P.;Garcia Y. and Woike, T. Photoswitchable coordination compounds.*Coord. Chem. Rev.* **2001**, *219*, 839-879.

(3) Kitagawa S. and Kawata, S. Coordination compounds of 1, 4-dihydroxybenzoquinone and its homologues. Structures and properties.*Coord. Chem. Rev.* **2002**, *224*,11-34.

(4) Bailar Jr., J. C. Coordination polymers. *Prep. Inorg. React*. **1964**, *1*, 1-27.

(5) Kitagawa, S.;Kitaura R. and Noro, S.I. Functional porous coordination polymers. *Angew. Chem. Int. Ed*. **2004**, *43*, 2334-2375.

(6) Batten, S. R.;Neville S. M. and D. R. Turner, Coordination polymers: design, analysis and application. *R. Soc. Chem.***2008**.

(7) Islam, S.; Datta, J.; Ahmed, F.; Dutta, B.; Naaz, S.; Ray P. P. and Mir, M. H. Effect on Schottky behaviour of 1D coordination polymers by altering para-substituents on benzoate ligands. *New. J. Chem.***2018**, *42*, 13971-13977.

(8) Yi, L.; Ding, B.; Zhao, B.; Cheng, P.; Liao, D. Z.; Yan, S. P.; Jiang, Z. H. Novel triazole-bridged cadmium coordination polymers varying from zero-to three-dimensionality. *Inorg. Chem.* **2004,** *43*, 33-43.

(9) Abazari, R.;Yazdani, E.;Nadafan, M.;Kirillov, A.M.;Gao, J.;Slawin A. M. and Carpenter-Warren, C.L.Third-order nonlinear optical behavior of an amide-tricarboxylate zinc (II) metal–organic framework with two-fold 3D+ 3D interpenetration. *Inorg. Chem.* **2021**, *60*, 9700-9708.

(10) Gu, J. Z.;Cai, Y.;Liang, X. X.;Wu, J.;Shi Z. F. and Kirillov, A. M.Bringing 5-(3, 4-dicarboxylphenyl) picolinic acid to crystal engineering research: hydrothermal assembly, structural features, and photocatalytic activity of Mn, Ni, Cu, and Zn coordination polymers. *CrystEngComm.* **2018**, *20*, 906-916.

(11) Abazari, R.;Sanati, S.;Morsaliand, A. andKirillov, M. Instantaneous sonophotocatalytic degradation of tetracycline over NU-1000@ ZnIn2S4 core–shell nanorods as a robust and eco-friendly catalyst. *Inorg. Chem.* **2021**, *60*, 9660-9672.

(12) Luo, X.;Abazari, R.;Tahir, M.;Fan, W. K.;Kumar, A.;Kalhorizadeh, T.;Kirillov, A. M. A.; Amani-Ghadim, R.;Chen J. and Zhou, Y. Trimetallic metal–organic frameworks and derived materials for environmental remediation and electrochemical energy storage and conversion. *Coord. Chem. Rev.* **2022**, *461*, 214505.

(13) A. E. Thorarinsdottir and T. D. Harris, Metal–organic framework magnets. *Chem. Rev.* **2020**, *120*, 8716-8789.

(14) Moosavi, S. M.; Nandy, A.; Jablonka, K. M.; Ongari, D.; Janet, J. P.; Boyd, P. G.; Lee, Y.; Smit, B. and Kulik. H. J. Understanding the diversity of the metal-organic framework ecosystem.*Nat. Commun.* **2020**, *11*, 1-10.

(15) Yang, X. G.; Lu, X. M.; Zhai, Z. M.; Qin, J. H.; Chang, X. H.; Han, M. L.; Li,F. F. and Ma, L. F. π-Type halogen bonding enhanced the long-lasting room temperature phosphorescence of Zn (ii) coordination polymers for photoelectron response applications. *Inorg. Chem. Front.* **2020**, *7*, 2224-2230.

(16) Shi, W.; Wu, G.; Yong, X.; Deng, T.; Wang, J. S.; Zheng, J. C.; Xu, J.; Sullivan M. B. and Yang, S. W. Orbital-engineering-based screening of π-conjugated d^8 transition-metal coordination polymers for high-performance n-type thermoelectric applications.*ACS Appl. Mater. Interface.* **2018**, *10*, 35306-35315.

(17) Li, R.;Chen T. and Pan, X.Metal–organic-framework-based materials for antimicrobial applications. *ACS nano*. **2021**,*15*, 3808-3848.

(18) Dutta, B.;Maity, S.;Ghosh, S.;Sinha C. and Mir, M. HAn acetylenedicarboxylato-bridged Mn (ii)-based 1D coordination polymer: electrochemical CO_2 reduction and magnetic properties.. *New J. Chem.* **2019**, *43*, 5167-5172.

(19) Xian, G.;Wang, L.; Wan, X.; Yan, H.; Cheng, J.; Chen, Y.; Lu, J.;Li, Y.; Li, D.; Dou J. and Wang, S. Two multiresponsive luminescent Zn-MOFs for the detection of different chemicals in simulated urine and antibiotics/cations/anions in aqueous media. *Inorg. Chem.* **2022**, *61*,7238–7250.

(20) Bennett,T. D. and Horike, S. Liquid, glass and amorphous solid states of coordination polymers and metal–organic frameworks. *Nat. Rev. Mater.* **2018**, *3*, 431-440.

(21) Liu, Y.; Lv, S.; Liu, D. and Song, F. Recent development of amorphous metal coordination polymers for cancer therapy. *Acta Biomater.* **2020**, *116*, 16-31.

(22) Shit, M.; Paul, S.; Chatterjee, T.; Dutta, B. and Sinha, C. Towards design of energy efficient semiconducting material: an example of 1D Cd (II)-2, 5-thiophene dicarboxylato Co-ordination Polymer.*ES Energy Environ.*, **2022**, *16*, 40-46.

(23) Paul, S.;Choi, S.J. and Kim, H.J. Enhanced proton conductivity of a Zn (II)-based MOF/aquivion composite membrane for PEMFC applications. *Energy Fuels.* **2020**, *34*, 10067-10077.

(24) Ghorai, P.; Dey, A.; Hazra, A.; Dutta, B.; Brandão, P.; Ray P. P. and Saha, A. Cd (II) based coordination polymer series: fascinating structures, efficient semiconductors, and promising nitro aromatic sensing.*Cryst. Growth Des.***2019**, *19*, 6431-6447.

(25) Naaz, S.;Das, P.;Frontera, A.;Dutta, B.;Khan, S.;Ray,P. P. and Mir, M. H.Halogen⋯ Halogen and π–Hole Interactions in Supramolecular Aggregates and Electrical Conductivity Properties of Cu (II)-Based 1D Coordination Polymers.*Cryst. Growth Des.* **2022**, *22*, 5189-5197.

(26) Dutta, B.; Pal, B.; Dey, S.; Maity, S.; Ray P. P. and Mir, M. H. Exploitation of Structure-Property Relationships towards Multi-Dimensional Applications of a Paddle-Wheel Cu (II) Compound. *Eur. J. Inorg. Chem.* **2022**, *2022*, e202100904.

(27) Dutta, B.; Jana, R.; Sinha, C.; Ray P. P. and Mir, M. H.Synthesis of a Cd (II) based 1D coordination polymer by in situ ligand generation and fabrication of a photosensitive electronic device.*Inorg. Chem. Front.***2018**, *5*, 1998-2005.

(28) Bairy, G.; Dey, A.; Dutta, B.; Maity S. and Sinha, C.Rational synthesis of a pyridyl-imidazoquinazoline based multifunctional 3D Zn (II)-MOF: structure, luminescence, selective and sensitive detection of Al^{3+} and TNP, and its semiconducting device application. *Dalton Trans.*, 2022, **51**, 13749-13761.

(29) G. M. Sheldrick, SHELXL 2014, SHELXL-2016/6 and SHELXL-2017/1, Program for Crystal Structure Solution, University of Göttingen, 2014, 2016, 2017.

(30) SMART and SAINT; Bruker AXS Inc.: Madison, WI, 1998.

(31) Bruker (2001). SADABS. Bruker AXS Inc., Madison, Wisconsin, USA.

(32) Frisch, M. J.;Trucks, G. W.;Schlegel, H. B.;Scuseria, G. E.;Robb, M. A.;Cheeseman, J. R.; Scalmani, G.;Barone, V.;Mennucci, B.; G. Petersson, A.;Nakatsuji, H.;Caricato, M.;Li, X.;Hratchian, H. P.;Izmaylov, A. F.;Bloino, J.;Zheng, G.;Sonnenberg, J. L.; Hada, M.;Ehara, M.;Toyota, K.;Fukuda, R.;Hasegawa, J.;Ishida, M.;Nakajima, T.;Honda, Y.;Kitao, O.;Nakai, H.;Vreven, T.;Montgomery Jr., J. A.;Peralta, J. E.;Ogliaro, F.;Bearpark, M.;Heyd, Brothers, J. J.;Kudin, E. K. N.;Staroverov, V. N.;Kobayashi, R.;Normand, J.;Raghavachari, K.;Rendell, A.;Burant, J. C.; Iyengar, S. S.; Tomasi, J.;Cossi, M.;Rega, N.;Millam, J. M.;Klene, M.;Knox, J. E.; Cross, J. B.; Bakken, V.; Adamo, C.; Jaramillo, J.; Gomperts, R.; Stratmann, R. E.; Yazyev, O.; Austin, A. J.; Cammi, R.; Pomelli, C.; Ochterski, J. W.; Martin, R. L.; Morokuma, K.; Zakrzewski, V. G.; Voth, G. A.; Salvador, P.;Dannenberg, J. J. S. ; Dapprich, A. D.; Daniels, Farkas, O.; Foresman, J. B.; Ortiz, J. V.;Cioslowski J. and Fox, D. J. Gaussian 09, Revision D.01, Gaussian Inc., Wallingford, CT, 2009.

(33) Becke, A. D. Density-functional thermochemistry. III. The role of exact exchange, *J. Chem. Phys*. **1993**, *98*, 5648–5652.

(34) Wadt W.R. and Hay, P.J.Ab initio effective core potentials for molecular calculations. Potentials for K to Au including the outermost core orbitals. *J. Chem. Phys*. **1985**, *82*, 299-310.

(35) O'Boyle, N.; Tenderholt, M. A.; Langner, L. K. M.; Cclib: a library for package-independent computational chemistry algorithms. *J. Comput. Chem*. **2008**, *29*, 839–845.

(36) Hirshfeld, F.L.; Bonded-atom fragments for describing molecular charge densities.*Theor. Chim. Acta*. **1977**, *44*, 129-138.

(37) Rohl, A. L.; Moret, M.; Kaminsky, W.; Claborn, K.; McKinnon J. J. and Kahr, B. Hirshfeld surfaces identify inadequacies in computations of intermolecular interactions in crystals: pentamorphic 1, 8-dihydroxyanthraquinone. *Cryst. Growth Des*. **2008**, *8*, 4517-4525.

(38) Parkin, A.; Barr, G.; Dong, W.; Gilmore, C. J.; Jayatilaka, D.; McKinnon, J. J.; Spackman M. A. and Wilson, C. C. Comparing entire crystal structures: structural genetic fingerprinting.*CrystEngComm*. **2007**, *9*, 648-652.

(39) S. K. Wolff, D. J. Grimwood, J. J. McKinnon, D. Jayatilaka and M. A. Spackman, Crystal Explorer, 2007,**2**.

(40) Stavila,V.; Talin, A.A. and Allendorf, M.D. Highly efficient fullerene/perovskite planar heterojunction solar cells via cathode modification with an amino-functionalized polymer interlayer.*Chem. Soc. Rev*. **2014**, *43*, 5994-6011.

(41) Zhang, J.; Huang, Y.; Yue, D.; Cui, Y.; Yang Y. and Qian, G. A luminescent turn-up metal–organic framework sensor for tryptophan based on singlet–singlet Förster energy transfer.*J. Mater. Chem*. **2018**, *6*, 5174-5180.

(42) Spackman, P. R.; Turner, M. J.; McKinnon, J. J.; Wolff, S. K.; Grimwood, D. J. ; Jayatilaka D. and Spackman, M. A.CrystalExplorer: A program for Hirshfeld surface analysis, visualization and quantitative analysis of molecular crystals. *J. Appl. Cryst*. **2021**, *54*, 1006-1011.

(43) E. H. Rhoderick, R. H. Williams, *Metal–Semiconductor Contacts*; Clarendon Press,Oxford, 2nd edn., **1988**.

(44) Samanta, A.; Pal S. K. and Jana,S. Exploring flowery MnO_2/Ag nanocomposite as an efficient solar-light-driven photocatalyst. *New J. Chem.***2022**, *46*, 4189-4197.

(45) Karan, A. K.; Bhunia S. and Manik, N. B. Study on the Conductivity of a Sunset Yellow Dye-Based Natural Organic Device. *J. of Electr. Mater.* **2022**, *51*, 7156–7163.

(46) Gupta, R. K. and F. Yakuphanoglu.Photoconductive Schottky diode based on Al/p-Si/SnS_2/Ag for optical sensor applications. *Sol. Energy.* **2012**, *86*, 1539-1545.

(47) Blom, P. W. M.; de Jong, M. J. M. and van Munster, M. G. Electric-field and temperature dependence of the hole mobility in poly (p-phenylene vinylene). *Phys. Rev. B.* **1997**, *55*, 656-659.

(48) Jain, A.; Kumar, P.; Jain, S. C.; Kumar, V.; Kaur R. and Mehra, R. M. Trap filled limit voltage (VTFL) and V_2 law in space charge limited currents. *J. Appl. Phys*. **2007**, *102*, 94505-94509.

(49) Gullu, O. and Turut, A. Electrical analysis of organic dye-based MIS Schottky contacts.*Microelec. Eng*. **2010**, *87*, 2482–2487.

(50) K. C. Kao, Dielectric Phenomena in Solids, Elsevier Inc., San Diego, California, **2004**.

Chapter 5

Mn (II) 3D coordination framework with mixed 5-aminoisophthalatoand Pyridyl-isonicotinoylHydrazone Bridges: Structure, Electrical Conductivity, Anti-cancer Activity and Drug delivery

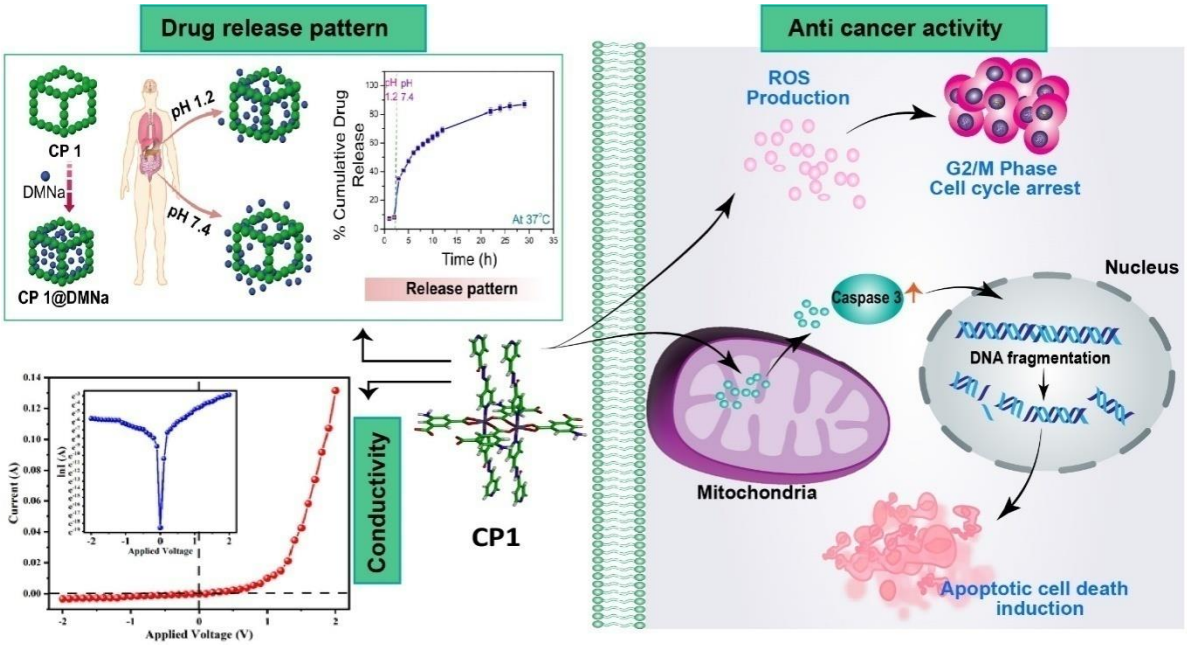

Abstract:

A 3D-Coordination Polymer of Mn(II), **[Mn_2(aisp)$_3$(pcih)$_2$(solvent)]$_n$(CP1)** (**pcih** = Pyridine-4-carboxaldehyde isonicotinoyl hydrazine and **H_2aisp** = 5-aminoisophthalic acid)is constructed by doubly hetero-bridging ligandsand has been characterized by Single Crystal X-Ray diffractipon measurements. The non-covalent forces (H-bonding, π···π interactions) bring robustness and stability (thermal and chemical) to the framework. The optical band gap of **CP1**obtained from Tauc's plot (2.98 eV) has been comparable with DFT computation value (HOMO and LUMO energy difference =2.80 eV) and insists for the fabrication of semiconducting device. A thin film device is fabricated (ITO/**CP1**/Cu) and measures the electrical conductivity,1.57×10^{-6} $m^2V^{-1}s^{-1}$and the series resistance (Rs), 331Ω at dark phase. Isoniazid, an antibiotic,used to prepare a Schiff base, **pcih,**andthe present compound, **CP1**,has motivated us to examinethe anticancer efficiency against as many as four cancer cell lines (HeLa, PC3, MDA-MB 231, A549) and has been compared with NKE (human normal kidney epithelial)cell line. The **CP1**shows better impact in inhibiting the proliferation of HeLacells (IC_{50}: 17.58 ± 1.56 µM) than other cancer cells ($IC_{50:}$ 21.52 ± 2.44 µM (PC3), 36.41 ± 1.72 µM (MDA-MB 231), 50.29 ± 3.81 µM (A549)). Loading and delivery of drug, Diclofenac Sodium (DMNa), has been tested in two different pH = 1.2 (simulated stomach environment) and at pH = 7.4 (simulated intestinal environment) which shows ~8% release at pH, 1.2 and ~87% release at pH 7.4within 30 h. The **CP1**, a magic material and stable insolution at different pH (1-10), shows multifaceted applications such as energy saving, anticancer activityand drug delivery. The design is certainly an important footstep towards the Sustainable Development Goals (SDGs).

5.1 Introduction

Polymers and hybrid materials have established their multifaceted deliverable outcome-based properties to meet many challenges of the environment and the society[1-5]such asclean energy,ensuring health, zero-waste management, supply of hygienic water, pollution free air etc.A number of such materials are employed to fabricate energy saving electronic devices.[6-11] Some of the external factors affect the stability and efficiency of such devices made up of organic polymers.[12-14]However, after the historic recognition of the co-ordination chemistry

(Alfred Warner, Nobel prize in 1913), it extends the exploration in different branches of science.[15-20]Organic-inorganic hybrid compounds are such materials those show promising applications in diverse fields following SDGs protocol.[21-26]The co-ordination polymers(CPs)/Metal-Organic Frameworks (MOFs) are such hybrid materials and establish their importance for well-being of the civilization.[25]

The rising prominence of coordination polymers in anticancer research stems from their versatile design, allowing customization of size, shape, and porosity. Their porous structures are well-suited for drug delivery, facilitating targeted and controlled release of therapeutic agents with excellent biocompatibility, and thereby these materials are supporting theragnostic applications. Certain coordination polymers, incorporating cytotoxic metal ions/ligands, are contributing to intrinsic anticancer activity. Furthermore, their pH-responsive behaviour enhances drug release specifically in the acidic tumour environment. Motivated by these properties, our research endeavour includes the synthesis of a Mn(II) 3D isoniazid-Schiff base coordination polymer, denoted as **CP1**, to explore its anticancer application.[27]

In the construction of organic-inorganic hybrid system like CPs/MOFs,carboxylato, amine/imine-N etc. bridging ligands act central role to link metal centres (M^{n+}) and create diverse structural platform of different dimensionalities (1D/2D/3D).[2,3] Presence of additional non-covalent interactions (hydrogen bonding, $\pi\cdots\pi$) make them durable and strong. Their architectural design is so meticulous that makes the materialstable but sensitive to external stimuli (mechanical, optical, thermal, magnetic, field induction) and have ensured the applications in stimuli responsive activities.[2-15]These materials are serving as gas storage and separation system, catalysts, charge transporting and capacitor, drug delivery, light harvesting etc. Normally, carboxylate bridging ligands would not conduct electricity due to presence of insulating C-centres. While the presence of metal (even diamagnetic) knots controls the energy difference between valence and conduction bands and make them helpful for electrical communicators and/or semiconductors.[5-13]In the last few years, it is explored that CPs are working as better electrical conductors and storage systemthan conventional electrical devices. Some excellent porous conducting polymer (PCP) of Zn(II), Cd(II) and few other transition metal ions are reported recently.[28-38] From the best of our knowledge Mn(II) based co-ordination polymers are still rare in literature for serving as electrical conductor. It is assumed that d^5 high-spin electronic configuration of Mn(II) having highest

magnetic field may accelerate the electronic properties of the materials. Keeping in mind all these information, we have deigned a Mn(II) 3D co-ordination polymer(**CP1**) of5-Aminoisophthalic acid(**H_2aisp**) and Pyridine-4-carboxaldehyde isonicotinoyl hydrazine (**pcih,** an isoniazid condensed pyridyl Schiff base) and has characterized by Single Crystal Diffraction measurements. The**CP1** shows band gap,2.98 eV (Tauc's plot) where DFT computed energy gap ($E_{LUMO} - E_{HOMO}$) of the synthon of the **CP1** is2.80 eV. The electrical conductivity value of **CP1** is $1.57 \times 10^{-6}\ m^2V^{-1}s^{-1}$at dark phase along with series resistance (R_s) 331 Ωwhich insist for the fabrication of energy saving electrical devices competent to the Sustainable Development Goals (SDGs).

Because of antimicrobial and anti-tuberculotic activity of isoniazid[39-41] and biological importance of Mn (II), the anticancer activity of the **CP1** is examined which shows considerable cytotoxicity against HeLa, PC3, MDA-MB 231, A549 cell lines (cancer cells), and has been compared with NKE (human normal kidney epithelial) cell line. Anti-proliferative activity of the **CP1**is correlated with standard drug cisplatin. Highest anticancer efficiency is observed against HeLa (IC_{50}:17.58 ±1.56 µM) cell line. Along with drug activity, the framework of **CP1**is tested for drug loading (Diclofenac Sodium) and its release in different pH. Theoretical calculation of **CP1**has also taken care of to establish the non-covalent bonding interactions in the superstructure (Hirshfeld Surface Analysis) and to explain the electrical conductivity and drug delivery activities (DFT computation).

5.2 Experimental Section

5.2.1 Materialsand General Methods

Isoniazid (INZ), 4-Pyridine Carboxaldehyde and 5 aminoisopthalic acid (**H_2asa**) was purchased from TCI Chemicals (India) Pvt. Ltd. High purity $MnCl_2$. $4H_2O$ was purchased from Sigma Aldrich Co. DCFDA (# D6883) was purchased from Sigma-Aldrich (India). Fetal bovine serum (#16000044) was obtained from Gibco, USA and MEM sodium pyruvate, MEM non-essential amino acids L-glutamine and Gentamicin, were procured from Hi-Media, India. All other chemicals including solvents were of AR grade. All the above chemicals were used without further purification.

Infrared (IR) spectrum (cm^{-1}) was recorded using a Perkin Elmer SPECTRUM II LITA FT-IR spectrometer **(Figure 5.1)**. Elemental analysis (carbon, hydrogen, and nitrogen) of the compound was performed using a PerkinElmer 240C elemental analyser. Thermogravimetric analysis (TGA) was carried out on a PerkinElmer Pyris Diamond TG/DTA thermal analyser

under nitrogen atmosphere (flow rate: 50 cm^3 min^{-1}) at the temperature range of 30−800 °C with a heating rate of 2 °C/min. Powder X-ray diffraction (PXRD) measurements were performed at room temperature with a PANalytical diffractometer equipped with a Cu micro focal tube (λ = 1.54178 Å) at 40 kV and 40 mA. UV−vis spectra were collected using a PerkinElmer Lambda 25 spectrophotometer.

5.2.2 Synthesis of {[Mn_2(aisp)$_3$(pcih)$_2$(solvent)]$_n$}(CP1)

A solution of Pyridine-4-carboxaldehyde isonicotinoyl(**pcih**) (0.045 g, 0.2 mmol) in MeOH (2 mL) was slowly and carefully layered onto a solution of $MnCl_2 \cdot 4H_2O$ (0.040 g, 0.2 mmol), in H_2O (2 mL) using buffer solution of DMF and MeOH (2 mL, 1:1 (v/v)) followed by layering of **H_2aisp** (0.037 g, 0.2 mmol) neutralized with Et_3N (0.042 g, 0.4 mmol) in ethanol (2 mL). The yellow, prism-shaped crystals of **{[Mn_2(aisp)$_3$(pcih)$_2$(solvent))]$_n$}(CP1)(Scheme 5.1)** were obtained after a week(0.320 g, yield 70%). Elemental analysis (%) calcd for $C_{20}H_{15}MnN_5O_5$: C, 52.19; H, 3.28; N, 15.21; found: C, 52.09; H, 3.34; N, 15.38. FTIR (cm^{-1}): 1540ν_{as}(COO$^-$), 1275ν_{sys}(COO$^-$) (**Figure 5.1**).

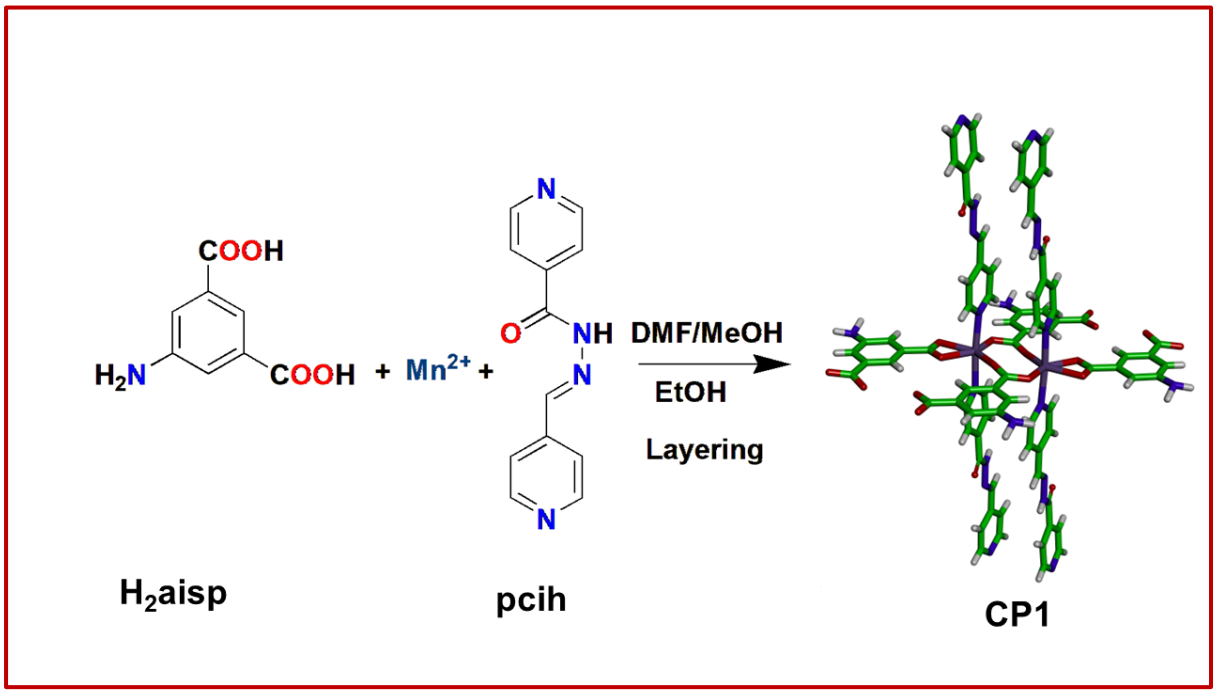

Scheme 5.1 Synthesis of **CP1**from **pcih** and **H_2aisp^{2-}**.

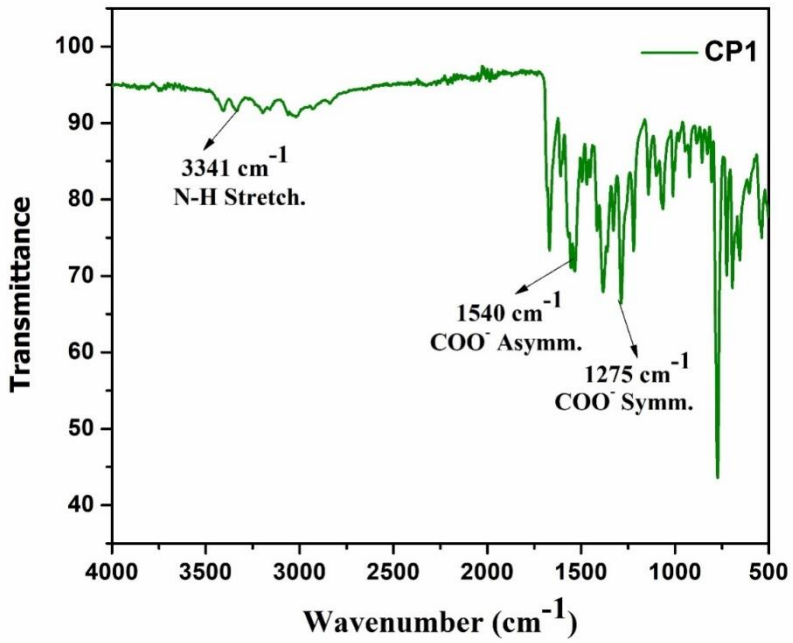

Figure 5.1 FTIR spectrum of **CP1**.

5.2.2 Single Crystal X-ray Crystallography

An X-ray diffractometer made by Bruker and model SMART APEX III outfitted with graphite-monochromatic MoKα radiation (λ = 0.71073 Å) was utilised to collect data on a single crystal of **1** (0.03 x 0.05 x 0.10 mm^3). The SHELX-97 package was used to solve the structure.[42]Non-hydrogen atoms were refined using anisotropic thermal parameters. The composition of unit cell parameters and crystal-orientation matrices of $C_{20}H_{15}MnN_5O_5$, were estimated by least-squares refinement of all hkl-range reflections $-11 < h < 11$, $-12 < k < 12$, $-14 < l < 14$. All of the hydrogen atoms were constrained to ride on their parent atoms in their geometrically perfect positions. During the formation of crystalline frameworks sometimes accessible voids can be generated because of the presence of solvent molecule with in it. In the present case the highly disorder nature of atoms in the solvent can't properly be able to assign in their atomic fractional occupancy. Therefore, these solvents were described in crystallographic information file and detected only through TGA analysis. However, it can be stated that there is no such contribution of such solvents in the stability of frameworks.

Table 5.1 Crystallographic results and refinement parameters for **CP1.**

Compound	**CP1**
CCDC No.	2238249
Sum formula	C20 H15 Mn N5 O5 [+ solvent]
Molecular weight	460.31
crystal system	Triclinic
space group	P -1
a(Å)	9.549(7)
b(Å)	10.241(8)
c(Å)	12.309(9)
α (°)	104.744(11)
β (°)	93.883(7)
λ (°)	102.165(5)
V(Å^3)	1128.5(15)
T(K)	93 K
Z	2
D_{calcd}(Mg/m^3)	1.355
μ(mm^{-1})	0.624
λ(Å)	0.71075
θ range (°)	25.400-2.200
R_1[a] [$I > 2\sigma(I)$]	0.0407(3499)
wR_2[b]	0.1422(4125)
Goodness-of-fit	0.990

[a]$R_1=\Sigma||F_o|-|Fc||/\Sigma|F_o|$, [b]$wR_2=[\Sigma w(F_o^2-Fc^2)^2/\Sigma wF_o^2)^2]/2$,w= 1/[σ2(Fo2)+(0.0350P)2 + 0.9811P], where P= $(F_o^2+2Fc^2)/3$

Table 5.2 Selected bond lengths and bond angles in **CP1.**

Mn(1) - O(17)	2.107(3)	O(17) - Mn(1) - N(1)	91.68(8)
Mn(1) - N(1)	2.303(3)	O(17) - Mn(1) - N(14)b	88.61(8)
Mn(1) - N(14)b	2.298(3)	O(24)c - Mn(1) - O(25)c	57.51(7)
Mn(1) - O(24)c	2.228(3)	O(24)c - Mn(1) - O(18)d	147.72(7)
Mn(1) - O(25)c	2.344(3)	O(25)c - Mn(1) - O(18)d	90.23(7)
Mn(1) - O(18)d	2.133(3)	Mn(1) - O(17) - C(17)	165.96(19)
O(10) - C(10)	1.225(3)	O(17) - Mn(1) - O(24)c	88.08(8)
O(17) - C(17)	1.255(3)	O(17) - Mn(1) - O(25)c	145.56(8)
O(18) - C(17)	1.270(4)	O(17) - Mn(1) - O(18)d	124.20(8)
O(24) - C(24)	1.254(3)	N(1) - Mn(1) - N(14)b	174.62(10)
O(25) - C(24)	1.282(4)	N(1) - Mn(1) - O(24)c	93.69(9)
N(1) - C(2)	1.346(5)	N(1) - Mn(1) - O(25)c	89.52(7)
N(1) - C(6)	1.336(4)	N(1) - Mn(1) - O(18)d	86.33(9)
N(8) - N(9)	1.386(3)	N(14)b - Mn(1) - O(24)c	91.69(7)
N(9) - C(10)	1.367(4)	N(14)b - Mn(1) - O(25)c	93.28(7)
N(8) - C(7)	1.281(4)	N(14)b - Mn(1) - O(18)d	89.07(8)

a = -1+x,1/2-y,-1/2+z, b = x,3/2-y,-1/2+z, c = x,3/2-y,1/2+z, d= 1+x,1/2-y,1/2+z

5.2.3 Thermal Analysis and PXRD

The crystallinity of the finely grounded sample was checked by using powder X-ray diffraction (PXRD) at room temperature and compared to a simulated spectrum. Almost all of the major peaks in the PXRD pattern of the as-synthesized **CP1(Figure 5.2)** matched with

that of simulated from single crystal data, indicating phase clarity and bulk material uniformity.

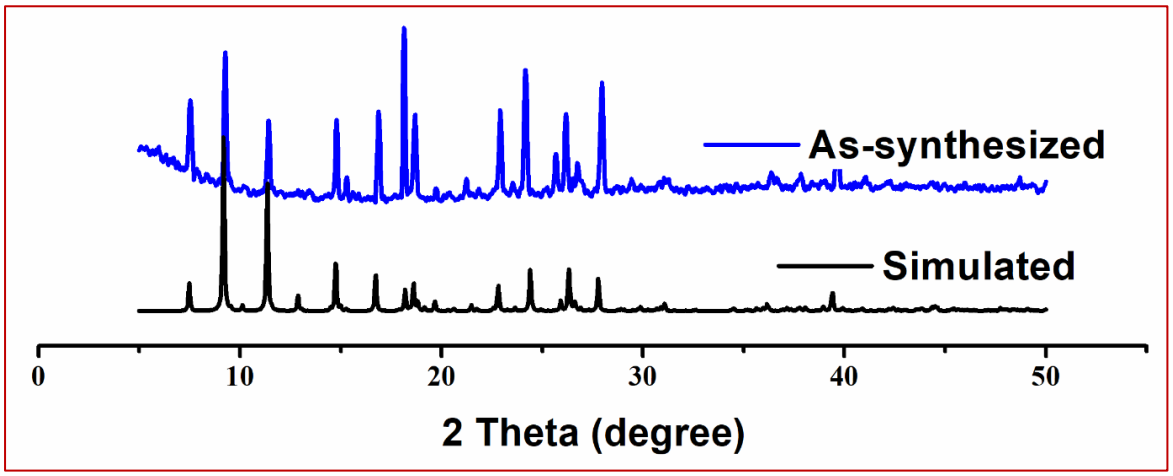

Figure 5.2 PXRD plot of **CP1.**

Thermogravimetric analysis (TGA) of **CP1** in the range of 30-800 °C at a rate of 10°C min^{-1} in a N_2 atmosphere shows good stability up to 200° C (**Figure 5.3**), after which the compound undergoes thermal decomposition. The final residue is MnO (Cal. 15.51 %; Exptl. 16.37 %).

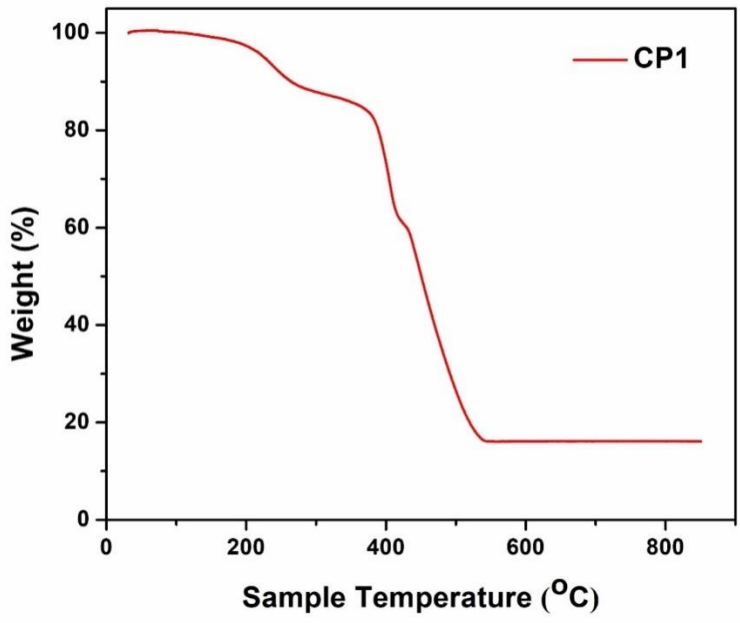

Figure 5.3 TGA plot of **CP1**.

5.2.4 DFT computation

Optimization of the gas phase geometry of the **CP1** was carried out using Density Functional Theory (DFT) calculation of Gaussian Program Package 09.[43-45]All calculations were performed using SCXRD coordinates and B3LYP method. LanL2DZ basis set were employed for all elements including Mn. Different electronic transitions were theoretically determined using the time-dependent density functional theory (TDDFT) formalism calculation.[45]Vibrational frequency calculations were performed to ensure that the DFT-optimized geometries represent the local minima and only positive eigenvalues.

5.2.5 Device fabrication and characterization

The device fabrication process follows three consecutive steps as per our previously published papers[46-48]. First step is the sample preparation process; 30 mg/ml solution was prepared by sonication of **CP1** with N,N-dimethylformamide (DMF) for 4h at room temperature. Alongside two electrodes (Indium-tin-oxide coated glass (ITO) and copper plate (Cu)) are washed with detergent and then sonicated with DI water and 2-propanol subsequently for 2 h each and then dried in a nitrogen environment. By an APEX 2700 spin coater unit we spin coat the samples in between the two electrodes with 1000 r.p.m for 20 seconds and dried them in an oven with 800C for 3 hours. The structure of the prepared device is depicted in **Scheme 5.2** below.

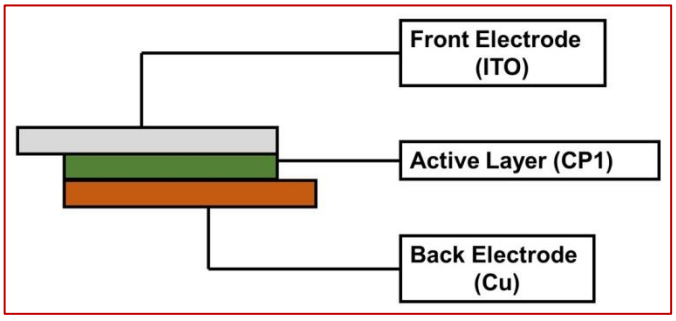

Scheme 5.2 Prepared device structure of **CP1** in sandwiched form.

5.2.6 Electrical Measurements

The synthesized material, **CP1**was used to fabricate thin film semiconducting device. Metal-Semiconductor (MS) junction was prepared by employing **CP1** as the semiconductor component and Al as the connecting metal in the device. To investigate the electrical characteristics of the synthesized material, a thorough analysis of the device's characteristics

was conducted. Keithley 2635B source meter equipment was used to record Current -Voltage (I-V) data for the device for electrical characterization (using two probe method) at ambient temperature (303K). The device, Al/compound/ITO, was subjected to a bias voltage range of -1V to +1V, and corresponding current values were recorded.

5.3 Results and Discussion

5.3.1 Structural description of CP1

The compound The **CP1** belongs to Triclinic crystal system with space group, P-1 and Z=2; D_x = 1.355 g.cm^{-3} (**Table 5.1; CCDC Number: 2238249**). The structure shows that the core unit is distorted octahedral with MnO_4N_2 coordination sphere where Pyridyl-N from two **pcih**coordinates in transoid configuration and three 5-aminoisophthalate ions (**aisp^{2-}**) coordinate aboutMn (II)centrewhere two **aisp^{2-}** act as monodentate O-donor and third one is carboxylate chelator (**Figure 5.4 (a)**) which satisfy charge of metal ion, Mn^{2+}.The coordination of three**aisp^{2-}** about Mn(II) makes a 2D rectangular framework that is coordinated through bridging and chelating carboxylate groups (**Figure 5.4(b)**). Both the ligands areserving as bridging group to the adjacent Mn(II) centresand propagate approximately in orthogonal fashion whicharchitect a 3D coordination network (**Figure 5.5**).

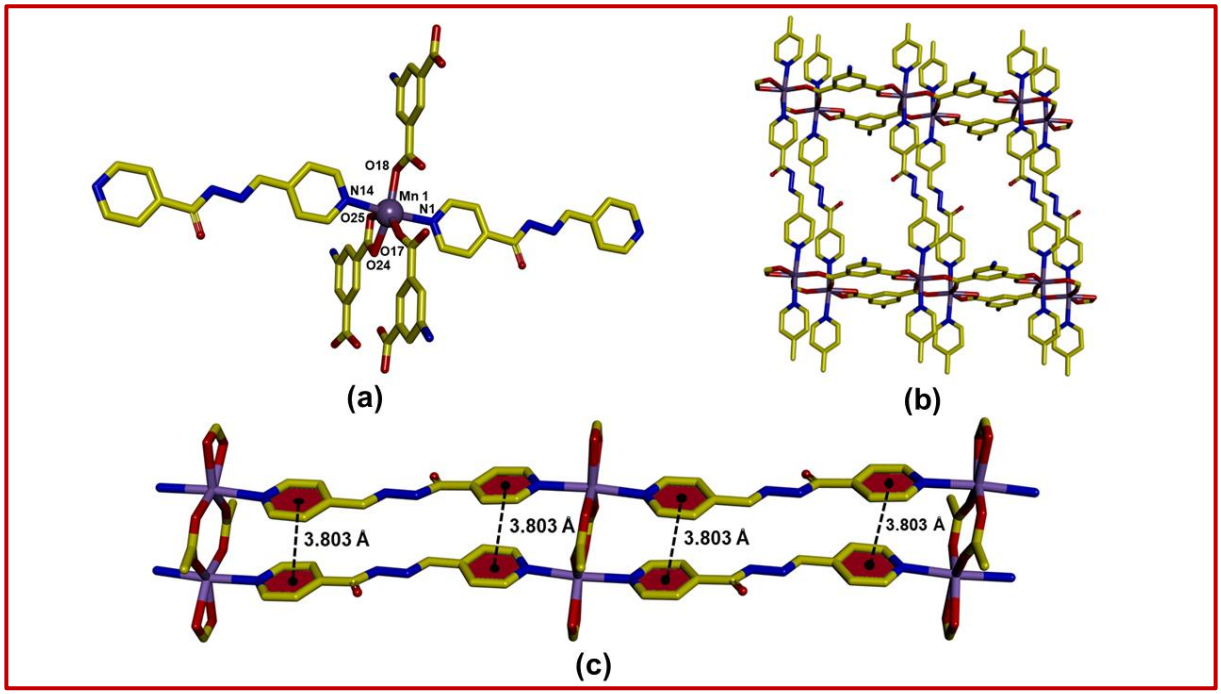

Figure 5.4 (a) Monomeric unit of **CP1**;**(b)** 2D supramolecular assembly of **CP1** through the coordination bonding (of **pcih** and **aisp^{2-}**); **(c)** π···π interactions of pyridyl rings in **CP1**.

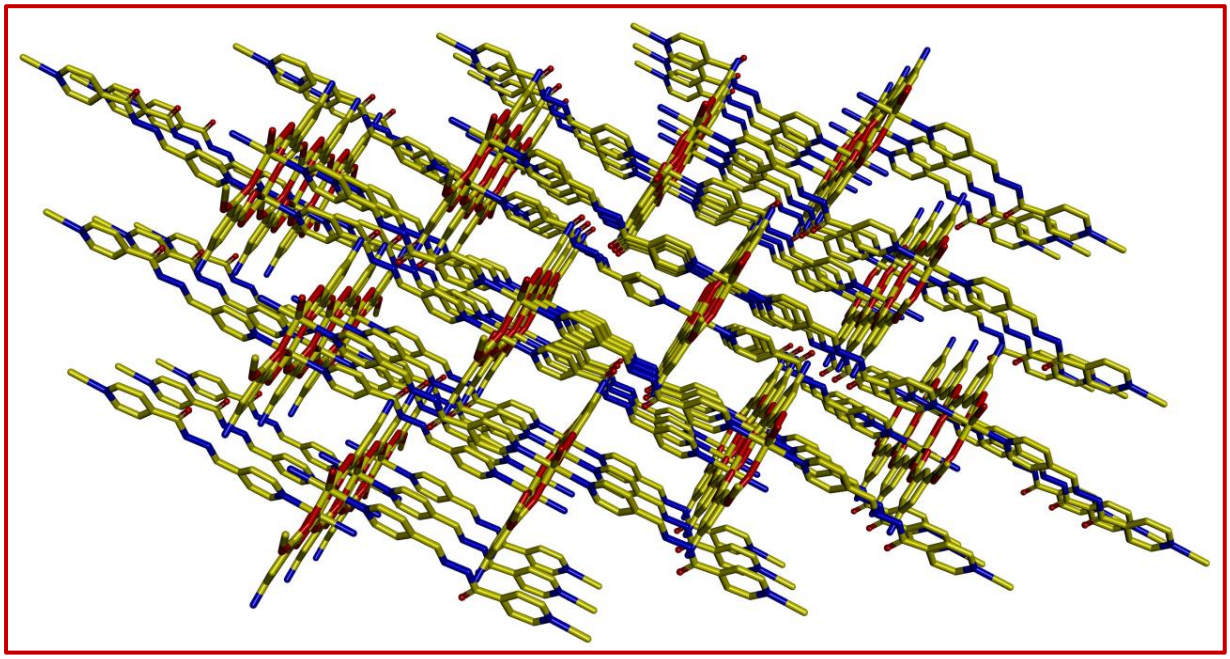

Figure 5.5 3D pattern of **CP1.**

The metric parameters (**Table 5.2**) of chelating **aisp**$^{2-}$are Mn(1) – O(17), 2.108(2); Mn(1) - O(24)c, 2.228(3); Mn(1) - O(25)c, 2.344(2); Mn(1) - O(18)d, 2.133(2) Å. The chelate angle is 57.51°(O(24) – Mn(1) – O(25)).Two monodentate bridging **aisp**$^{2-}$ are co-ordinately distorted which is reflected from the bond angle extended by carboxylate-O about Mn(II), O(17) – Mn(1) – O(18), 124.22(7)°. The **pcih** is coordinated to adjacent Mncentres in rod fashion through pyridyl-N and the bond distances are Mn(1) - N(1), 2.303(3); Mn(1) - N(14)b, 2.298(3)Å.Two bridging ligands propagate almost perpendicularly that is evident from angular disposition around Mn(II) in the coordination sphere: N(14) – Mn(1) – O(18), 89.07(8)°; O(18) – Mn(1) – N(1), 86.34(9)°. The pyridyl rings are so positioned to persuade π···π stacking at a distance of 3.803 Å and propagates along the *a*-axis **(Figure 5.4(c))**. The hydrogen bonding interactions (asip-O---H-N(**pcih**)) exist between di-carboxylate-O and -N-H hydrogen of **pcih** moiety to form a robust 3D geometry.The H-bonding of free -NH_2 of **asip**$^{2-}$(2.275Å) enhances the strength of the geometry to make the geometry strong and robust.The topology of the as-synthesized **CP1** is presented in (**Figure 5.6(a, b, c)**) with the three-digit point symbol dia;4/6/c1 and it is a 3D -3D interpenetrated diamonded network with four-fold interpenetration.

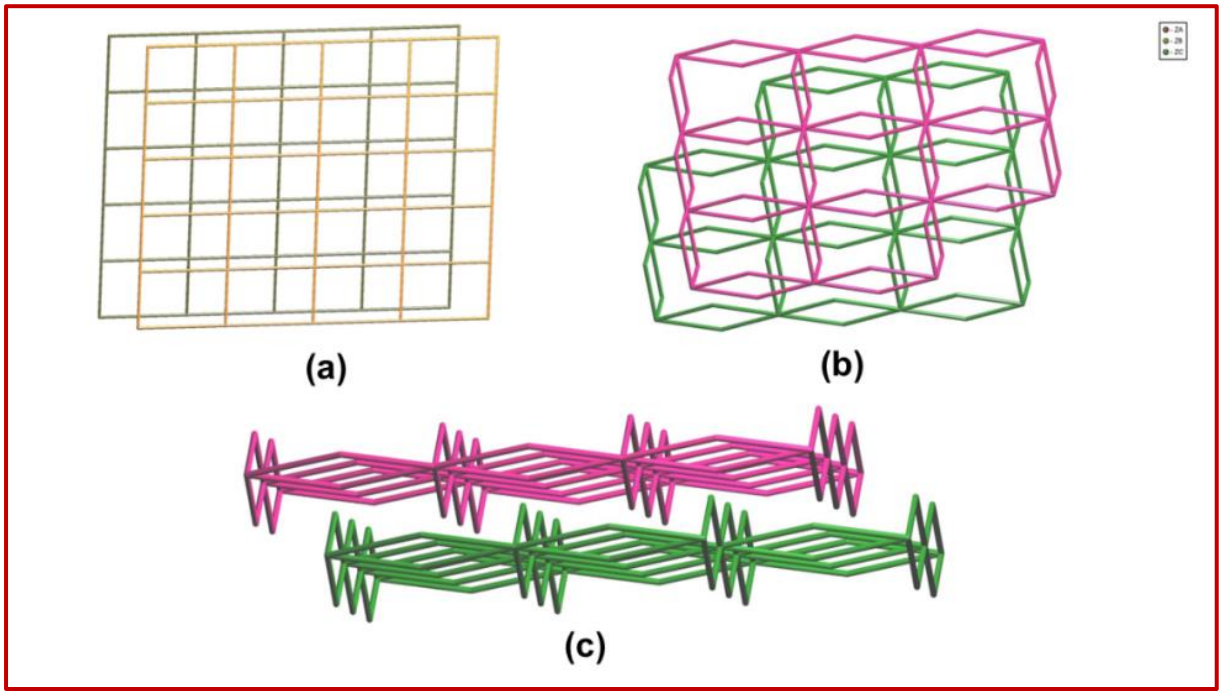

Figure 5.6 Topological structure of compound **CP 1** (a, b, c).

Hydrogen bonding in **CP1** has been accounted by the Hirshfeld surface analysis (**Figure 5.7**)where the contribution comes from C··H/H··C (19.3%), O··H/H··O (23%) and N··H/H··N(7%) interactions (**Figure 5.8**).

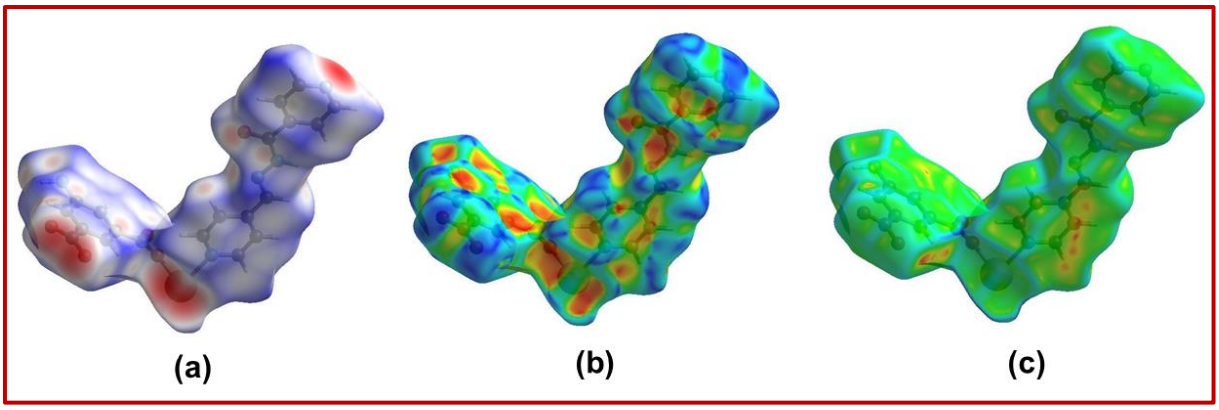

Figure 5.7 The Hirshfeld surface analysis of **CP1** (obtained using SXRD Parameters), **(a)**d_{norm},**(b)** Shape index **(c)** Curvedness.

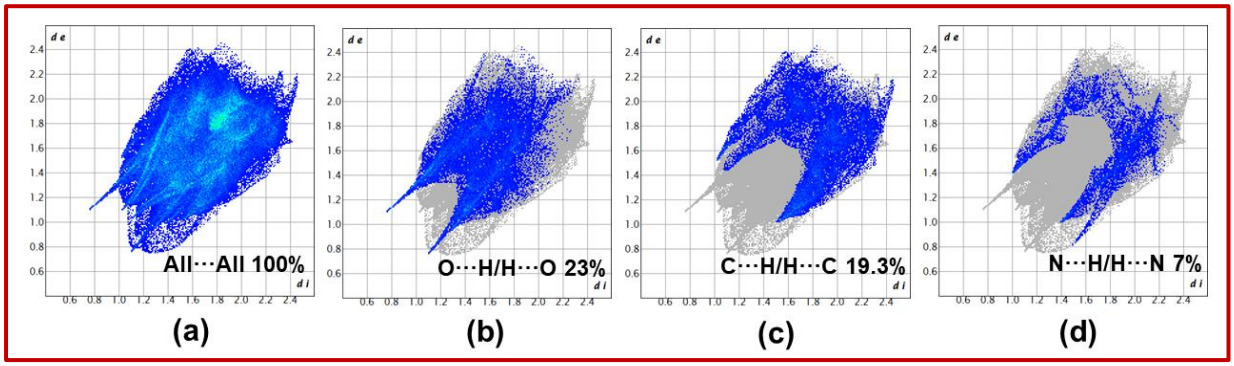

Figure 5.8 Various intermolecular interactions visible in a 2D fingerprint plot of **CP 1, (a)** All**, (b)** O···H/H···O **(c)** C···H/H···C and **(d)** N···H/H···N

The powder X-ray diffraction pattern (PXRD) of the bulk material is matched well with simulated data collected from SCXRD (**Figure 5.2**)which reportsthe high purity of the material. From thermogravimetric analysis (TGA) it is clear that the accessible solvent molecule has been released at 240 °C (Calculated solvent = 9.60%; Experimental 9.50%) (**Figure 5.3**). However, from SCXRD data, we are not being able to define exactly the solvent. However, after the removal of solvent by thermal treatment, the structural architecture remains consistent which is proved by PXRD data. The phase purity and thermal stability of **CP1** makes it suitable for potential material for making of devicesfor different applications.

Use of scanning electron microscopy (SEM) is helpful to examine for any fouling, either dissociation/association or impurity, of any sample during prolong period of suspension in solution of different pH (1-10).The SEManalyses of **CP1**(**Figure 5.9**,**pH 1, 5, 10**) shows that gross morphology of the material remains intact both in acidic (pH, 1 and 5) and basic (pH, 10) medium.

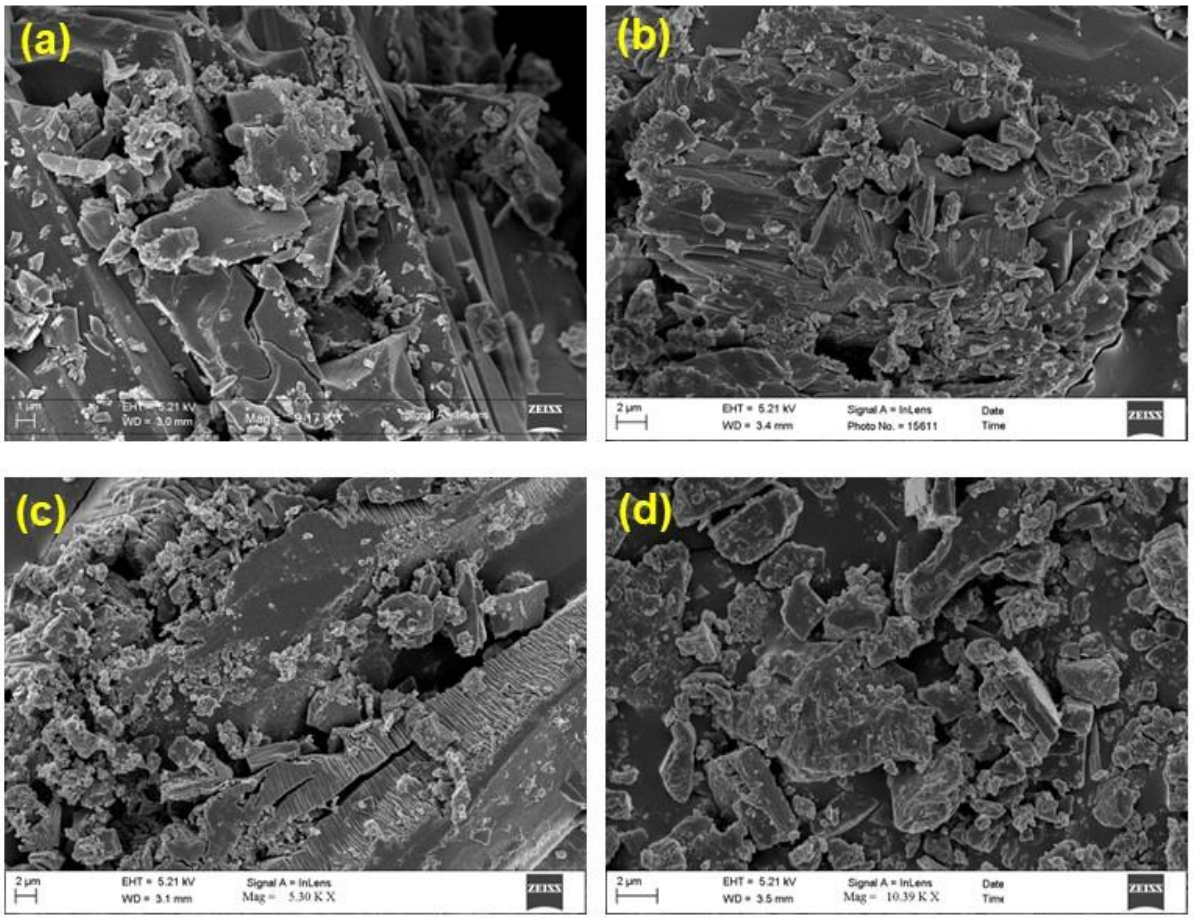

Figure 5.9 (a-d). The SEM images of (**a**) original **CP1; (b-d) CP1** collected from the solution of **pH 1 (b), 5 (c)& 10**(d)

The significant peak positions in PXRD (**Figure 5.10, pH 1, 5, 10**) remain unchanged; which have confirmed that the bulk phase consistency and pH stability of material during device fabrication.

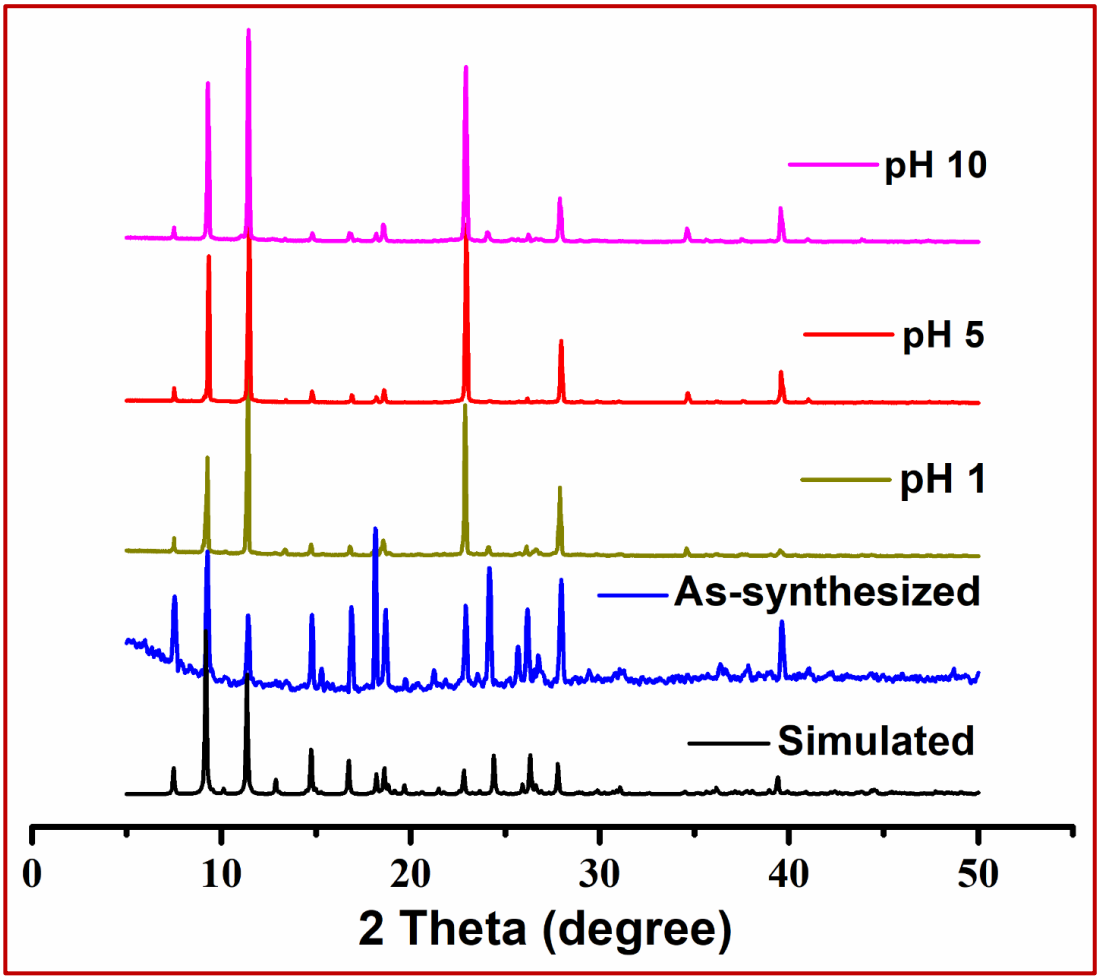

Figure 5.10 Powder X-ray Diffraction spectra of original **CP1** and collected from the solution at pH 1, 5, 10.

5.3.2 Optical Characterization

The DMF suspension of **CP1** has been coated on ITO plate and sandwiched with Cu-plate to fabricate Schottky device (**Scheme 5.2**) for electrical characterization. The UV-Vis spectroscopy of the prepared device has been measured (inset of **Figure 5.11**) in between 290 to 800 nm wavelength and the optical bandgap (2.98 eV) is calculated using Tauc's equation (**Equation 1**) from Tauc's plot (**Figure 5.11**)[49].

$$(\alpha h\nu)^{\frac{1}{n}} = A[h\nu - E_g] \qquad \textbf{(1)}$$

where, $\alpha$is the absorption coefficient;E_g is the optical band gap; h is the Plank's constant; ν stands for frequency of irradiated light and exponent n is the characteristic value of electron transition process and n=1/2 for direct allowed transition.

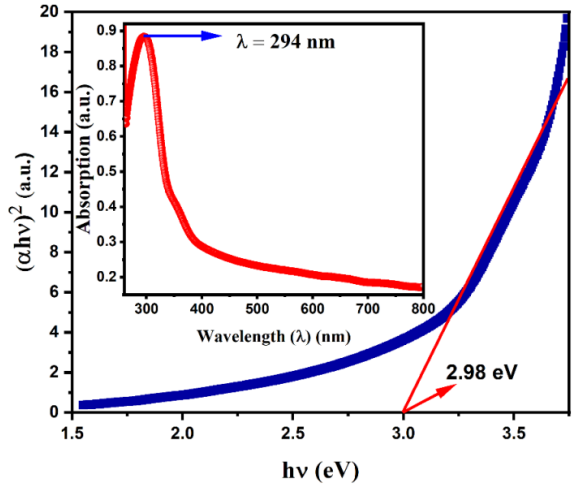

Figure 5.11 Tauc's plot of **CP1**in thin film state. (Inset) Absorption spectrum of **CP1**.

The geometry of **CP1** is optimized using the coordinates of the Single Crystal X-Ray Diffraction measurements following DFT computation technique and the energy of MOs are calculated. The energy gap, (E_{LUMO} (-3.29 eV) – E_{HOMO} (-6.09 eV)) is 2.80 eV (**Figure 5.12**)and it is lower than the band gap evaluated from Tauc's plot (2.98 eV, **Figure 5.11**).

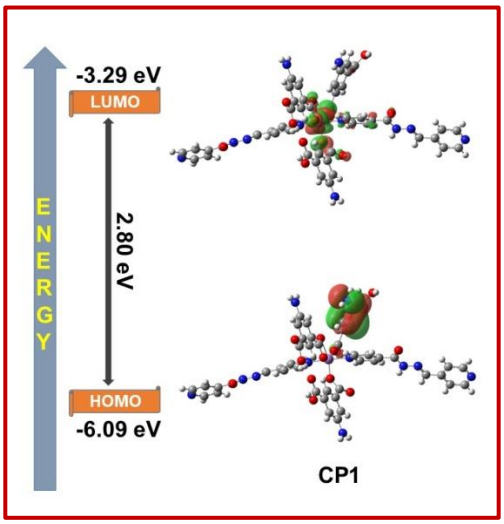

Figure 5.12. HOMO-LUMO gap of **CP1** from DFT computation using crystallographic parameters.

The experimental result is obtained from the polymer(**CP1**) while in DFT computation, a discrete molecular synthon is considered.For coordination polymer with d^5 system, the band edges depend on the electronic state of the geometrical framework. Some selected FMOs along with their respective energies are listed in the Supporting Information file (**Table 5.3**).

Table 5.3 Some selected orbital of the **CP1** along with their energy.

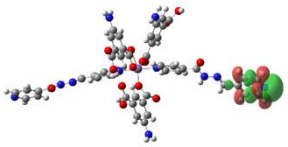 **HOMO – 5** **(-7.10 eV)**	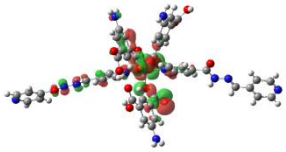 **HOMO - 4** **(-6.93 eV)**	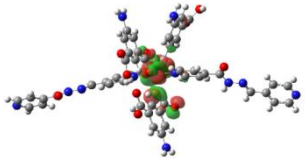 **HOMO - 3** **(-6.67 eV)**
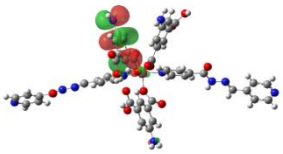 **HOMO - 2** **(-6.20 eV)**	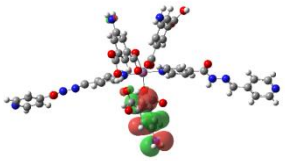 **HOMO - 1** **(-6.19 eV)**	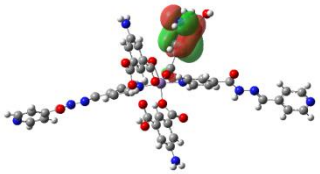 **HOMO** **(-6.09 eV)**
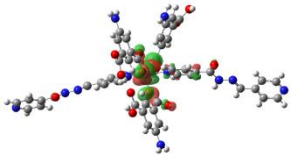 **LUMO** **(-3.29 eV)**	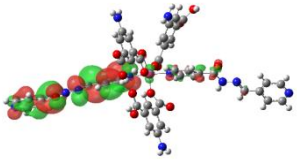 **LUMO + 1** **(-2.96 eV**	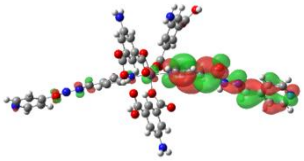 **LUMO + 2** **(-2.87 eV)**
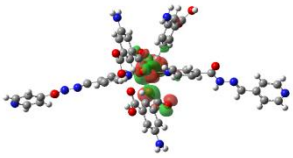 **LUMO + 3** **(-2.45 eV)**	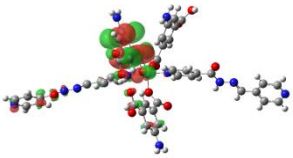 **LUMO + 4** **(-2.25 eV)**	 **LUMO + 5** **(-2.20 eV)**

5.3.3 Electrical Characterization

Powder The electrical data have been collected using the device in the dark phase with Keithly 2400 source meter (**Scheme 5.2**).

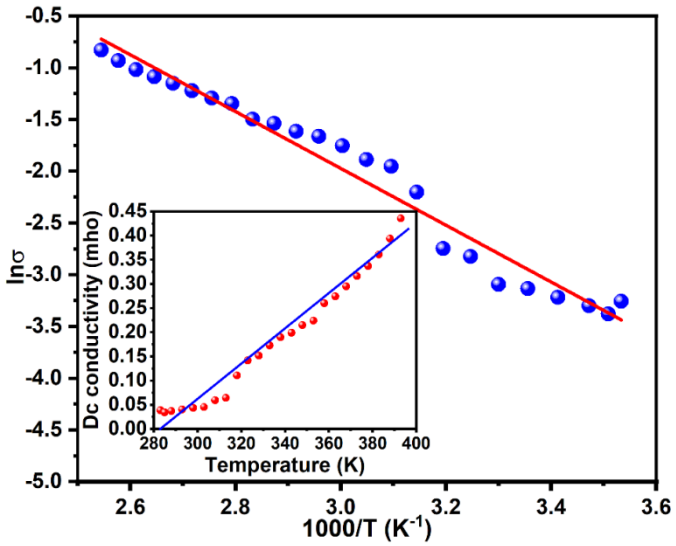

Figure 5.13 Arrhenius plot of **CP1** based device. (Inset) Temperature dependent conductivity of prepared device at 2 volt applied voltage between the temperature range 283K to 393K measured using Agilent 4294 A spectrometer.

The temperature dependent conductivity plot (**Figure 5.13**) has been examined following the Arrhenius equation (**Equations 2** and **3**)[50,51]within 283-393 K and the σ_0, a pre-exponential factor for high temperature conductivity limit (5.23 Ω^{-1} m^{-1}) and ΔE, the activation energy (1.03×10^{-20}eV) are obtained from the device.

$$\sigma = \sigma_0 e^{-(\frac{\Delta E}{k_B T})} \quad \textbf{(2)}$$

Taking 'ln' on both side we can write

$$\ln\sigma = \ln\sigma_0 - \frac{\Delta E}{k_B T} \quad \textbf{(3)}$$

The mechanism of the charge conduction process in the device may be explained by the thermionic emission theory and the current flow can be explained by the Richardson-Schottky equation (**Equation 4**).[52,53]

$$I = I_0 \exp[\frac{qV}{nkT}] \quad \textbf{(4)}$$

Where I_0 is the reverse saturation current (**Equation 5**) and is given below.

$$I_0 = \left[AA^* T^2 \exp\left(\frac{-q\phi_{bo}}{kT}\right)\right] \quad \textbf{(5)}$$

(A^* represents the Richardson constant and rest of the symbols have own usual meanings [52].)The **Equations 6**&**7**determine $A^*$and barrier height (ϕ_{b0}) (**Figure 5.14**).

$$\ln\left(\frac{I_0}{AT^2}\right) = \ln(A^*) - q\frac{\phi_{b0}}{kT} \qquad \textbf{(6)}$$

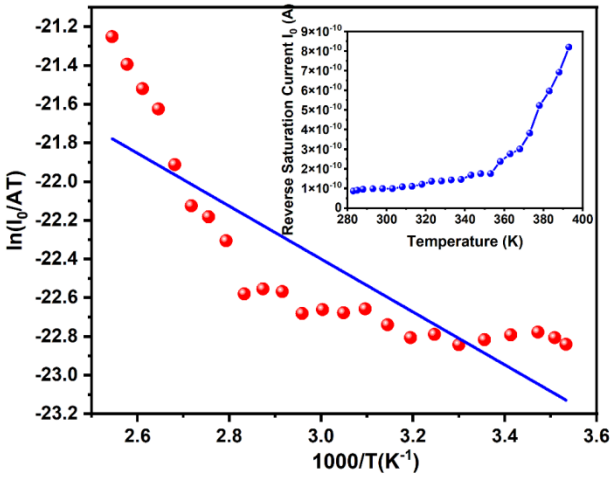

Figure 5.14 Richardson plot of **CP1** based device. (Inset) Temperature dependent Reverse saturation current of prepared device.

It is seen that the variation of reverse saturation current is not a straight line. This explains the inhomogeneous barrier height at the interface. From linear fitting of the plot the calculated value of Richardson constant for the device is$1.13 \times 10^{-8}Am^{-2}K^{-2}$.

The **Equation 7** is derived from the **Equations 4** and **5** and the barrier height, ϕ_{b0}, of the prepared devicehas been calculated (0.11 eV).

$$\phi_{b0} = \frac{kT}{q}\ln\left(\frac{AA^*T^2}{I_0}\right) \qquad \textbf{(7)}$$

The room temperature current-voltage (I-V) is non-linear (**Figure 5.15**) which represents a good rectifying behavior of the device and the observed non-linear variation of rectification ratio with the applied voltage is given in the **Figure 5.15**.

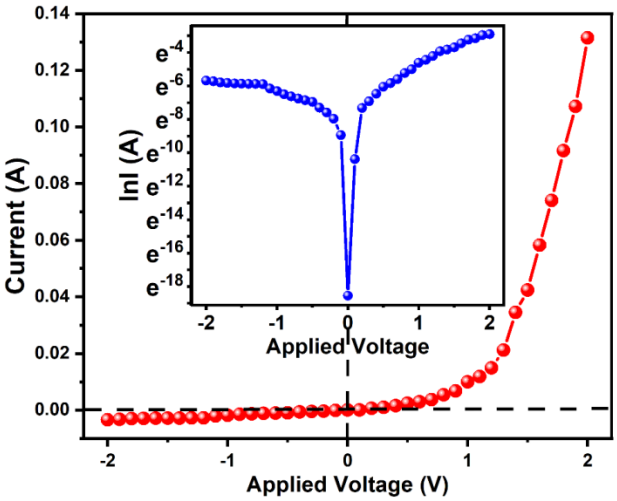

Figure 5.15 Current-Voltage characteristics of ITO/**CP1**/Cu. (Inset) Semi log current-voltage characteristics of the prepared device.

The ideality factor (n), 1.68 is calculated (**Equation 8**) from the lnI-V plot (**Figure 5.16(a)**) and H(I) vs I plot (**Figure 5.16(b)**) of the prepared **CP1**based device at room temperature.

$$n = \frac{q}{kT}\left(\frac{V}{\ln I}\right) \qquad \textbf{(8)}$$

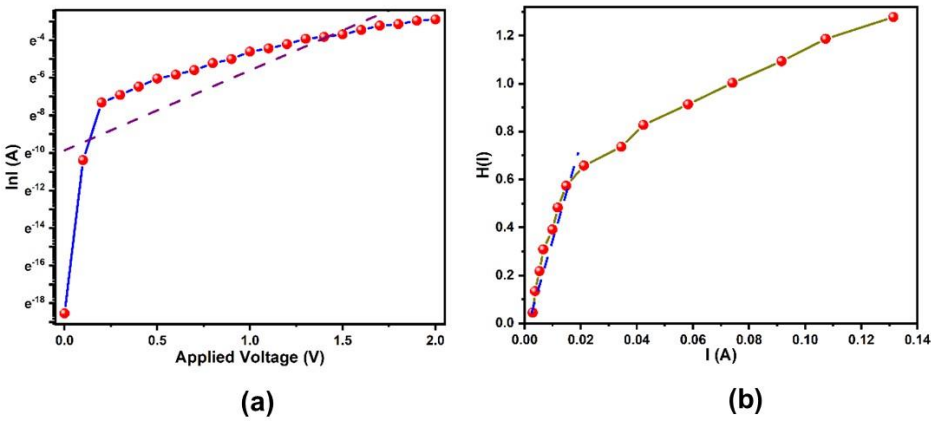

Figure 5.16 (**a**) lnI vs V plot of ITO/ **CP1**/Cu. Dashed line represents the best linear fit to the plot. (**b**) H(I) vs I plot of the prepared device.

The deviation of ideality factor from the $n \approx 1$(ideal value) may be due to the presence of interfacial inhomogeneous barrier height and also for the large amount of carrier recombination around the depletion region.[54,55] According to Cheung's equation (**Equations**

9, 10)[54] the value of series resistance (R_S) and barrier height (ϕ_b) are 331 Ω and 0.19 eV respectively.

$$H(I) = n\phi_b + IR_s \quad \textbf{(9)}$$

Where the function H(I) is calculated as

$$H(I) = V - \left(\frac{nkT}{q}\right)\ln\left(\frac{I}{AA^*T^2}\right) \quad \textbf{(10)}$$

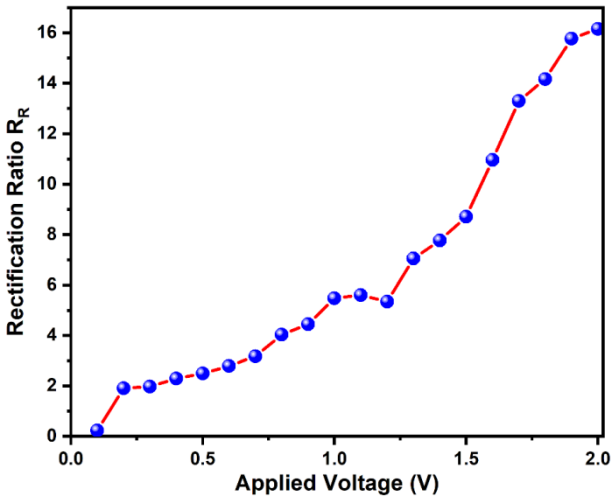

Figure 5.17 Current-Voltage characteristics of ITO/**CP1**/Cu. (Inset) Semi log current-voltage characteristics of the prepared device.

Further the rectification ratio of the device varies with voltage (**Figure 5.17**) and suggests deviation from ideality at higher voltage which may interpret the difference in mechanism of electron transportation in the electrode phase. Similarly, the lnI vs V (**Figure 5.18(a)**) plots are used to examine the characteristics of the device and carrier transport mechanism to extract the value of dielectric constant-mobility product, threshold voltage and trapping information for the device. There are three distinct regions (**Figure 5.18(a)**) representing different charge transport mechanisms. Region, I represent the ohmic (I α V) conduction mechanism. Here current through the device is only controlled by the field generated charge carriers and the slope is 1.79 along with threshold voltage 0.69 V (**Table 5.4**).[56]In Region II, the conduction mechanism obeys the I α V^2pattern (**Figure 5.18(b)**) where threshold voltage is decreased to 0.035 V and the slope is 2.04. Here conduction mechanism is dominated by the Space Charge Limited Current (SCLC). In Region III the conduction current obeys I α V^k

law (k = 2.61 in this work) and threshold voltage becomes 1.03 V. The conduction mechanism in region III may be due to the circulation of trapped charge of SCLC model.[57,58]The parameters from I-V plots in different regions (**Table 5.4**) account the suitability of the electronic device towards development of energy saving instruments.

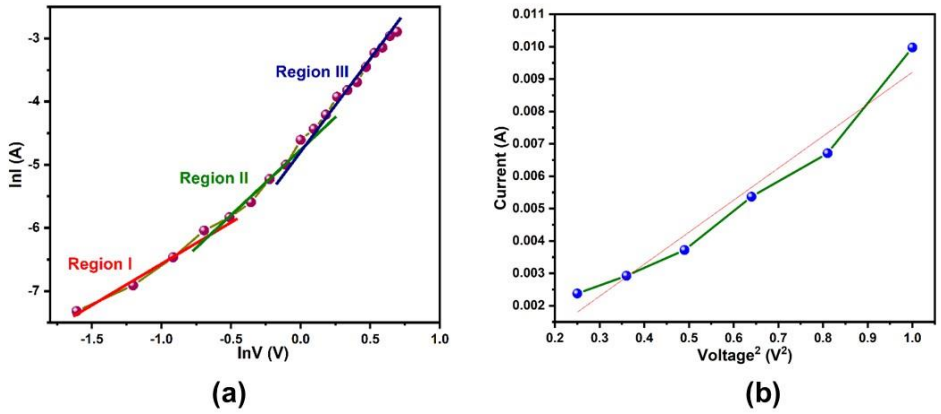

Figure 5.18 (**a**) lnI vs lnV plot; and (**b**) I vs V^2 plot of the device for the region II.

The Mott-Gurney equation **(Equation 11)**[59]is used to calculate carrier mobility and dielectric constant product ($\mu_{eff}\varepsilon_r, 1.57 \times 10^{-6}\ m^2V^{-1}s^{-1}$) from I vs V^2(Region II in **Figure 5.18(a)** plotwhich brings the conclusion for the moderate conductivity of the device.

$$I = \frac{9\mu_{eff}\varepsilon_0\varepsilon_r A}{8}\left(\frac{V^2}{d^3}\right) \quad \textbf{(11)}$$

The unusual enhancement of current upsurge in Region III of lnI-lnV plot **Figure 5.18(a)** is explained by trap assisted mechanism (**Equation 12**).[60] Presence of closely spaced large number of energy levelsenhance the lifetime of trapped charge and plays a major contribution to the current conduction process in the SCLC region.Thus, a large number of carriers are trapped and forms a cloud near the electrodes.

$$g(E) = \frac{N_T}{kT_T}\exp\left[\frac{-E}{kT_T}\right] \quad \textbf{(12)}$$

where,N_T is the trap concentration;E represents the Fermi energy; k is the Boltzmann constant;T_T is the characteristics temperature.

Table 5.4 I-V plots related parameter of **CP1** based device

Region I	**Region II**			**Region III**	
Slope (m_1)	Threshold Voltage V_{th1} (V)	Slope (m_2)	Trap energy E_T (eV)	Slope (m_3)	Threshold Voltage V_{th2} (V)
1.79	0.69	2.04	0.035	2.56	1.03

Considering the Poisons power law, $I \approx V^{m+1}$ $\left(m = \frac{T_T}{T}\right)$on the I-V characteristics threshold voltage and slope for the separate regions are calculated and the details are depicted in the **Table 5.4**. This observation makes a conclusion that **CP1** is a promising and potential material in the electrical and opto-electrical appliances.

5.3.4 Biological Study

5.3.4.1 Cell culture and maintenance

In the present study four cancerous cancer cell line PC-3, HeLa, MDA-MB-231, A549 and human normal kidney epithelialcell line NKE were obtained from Bose Institute, Kolkata. All the above cell lines were cultured using DMEM or RPMI medium, supplemented with 10% FBS, non-essential amino acids, 1mM sodium pyruvate, 2mM L-glutamine, 100 mg/L streptomycin, 100 units/L penicillin, and 50 mg/L gentamycin in a 37°C humidified incubator containing 5% CO_2.

5.3.4.2 Cell survivability assay

Cell survivability of the compound was studied on four cancer cell line PC-3, HeLa, MDA-MB-231, A549 as well as human normal kidney epithelialcell line NKE, using MTT assay [13,14]and cisplatin was used as a standard control. Briefly cells were seeded in 96-well plates at 1×10^4 cells per well and exposed to compound **CP1** at concentrations of 0-100 µM for 24 h. Then the cells were washed with 1XPBS by twice and incubated with MTT solution (450 µg/mL) for 3-4 h at 37ºC. The resulting formazan crystals were dissolved in an MTT

solubilization buffer and at 570 nm wavelength, the absorbance was measured and the value was compared with control cells.

5.3.4.3 Trypan blue exclusion assay

Trypan blue exclusion assay was performed and the number of viable cells present in the cell suspension was determined. One such experiment was briefly described. HeLa cells were exposed to required concentration of Compound **CP1** and after treatment, the cells were resuspended within 1 x PBS buffer and mixed with trypan blue solution (0.4%) in 1:1 dilution for the duration of 10 min and counted with hemo-cytometer.

5.3.4.4 Annexin V-FITC/PI staining for apoptosis assay

Induction of apoptosis was quantified via flow cytometric analysis using the Annexin V-FITC apoptosis detection kit (BD Bioscience)[15]. Briefly HeLa cells were seeded in a 6 well plate at a density of 1×10^6 cells /ml. Post incubation cells were treated with compound **CP1** (9 µM, 18 µM and 36 µM), **CP1** (36 µM) + NAC and **CP1** (36 µM) + Caspase 3 inhibitor treated cells were trypsinized and re-suspended in 100µL of 1X binding buffer solution supplied within the kit and incubated with 5 µL of annexin V-FITC and 5 µL of PI for 15 min at room temperature in dark before acquiring data using BD FACS Verse flow cytometer (BD Biosciences, San Jose, CA). Annexin V/FITC positive cells were regarded as apoptotic cells analyzed using Cell Quest Software (BD Biosciences).

5.3.4.5 Measurement of cellular ROS using DCFDA

To estimate the intercellular reactive oxygen species (ROS) production due to **CP1** treatment, DCFDA method was used[16]. Briefly HeLa cells were seeded in a 6 well plate and treated with test compound **CP1** (9 µM, 18 µM and 36 µM) for 24h time period and H202 was used as a standard control and NAC as a negative control. Post incubated with 10µMH_2DCFDA for 30 min at 37^0 C. For fluorescent imaging, H_2DCFDA incubated cells were washed and suspended in 1XPBS and directly imaged under fluorescent microscope (Leica).

5.3.4.6 Cell cycle profiling assay by propidium iodide staining

The HeLa cells were seeded in each petri dish for 24 h and then were treated with different concentration of the compound **CP1** (9µM, 18 µM, and 36 µM) for the time period of 24 h. Post treatment, cells were fixed by 75% ethanol for 24 hrs at −20 °C.After centrifugation, the cells pellets were re-suspended in 1XPBS buffer and RNaseA (20 µM) was treated for 2 h at

37°C. Finally, propidium iodide (PI) was added and incubated at room temperature for 20 min and were analyzed using BD FACS Verse flow cytometer and analyzed using BD FACS DIVA software[17].

5.3.4.7 Caspase 3/7 activation assay

Post treatment To estimate the changes in caspase 3 protease activity of HeLa cells treated with the compound **CP1**, a colorimetric assay using caspase 3/7 assay kit (abcam) was used [5]. After treating with the desired concentration of compound **CP1** (9µM, 18 µM, and 36 µM) cell lysates were prepared from HeLa cells, with RIPA buffer method. An aliquot of 150 µg of protein was used for each condition. DTT (10mM) and DEVD-p-NA substrate (200µM) were added according to manufacturer's protocol and incubated at 37 °C for 2h. Finally, OD was measured at 400 nm in ThermoMultiskan GO microplate reader and the graph was plotted.

5.3.4.8 Apoptotic Nuclear Morphology Study by DAPI Staining

To identify any morphological changes within the nucleus of HeLa cells upon treatment with synthesized compounds **CP1**, DAPI (4′, 6-diamidino-2-phenylindole) staining was used[18]. The MDA-MB 231 cells were seeded in 6-well plates containing coverslips and treated with respective doses of **CP1** for 48 h. Post treatment cells were washed with 1x PBS and DAPI staining was done and under fluorescence microscope (Leica).

5.3.4.9 Cytotoxicity studies of CP1

Isoniazid, an antibiotic to treat tuberculosis, is used for functionalization to prepare new molecules and also the metal complexes of some of the eligible derivatives. These have been used to explore drug related activities. The bridging ligand, **pcih** is obtained by the condensation of Isoniazid with pyridine-4-carboxaldehde and we apprehend biomedical activity of the metal complexes therefrom. Upon complexation the polarity of the ligand is normally diminished and the transportation through the cell membrane may be enhanced which causes increase in bioavailability of the drug along with biologically important metal ion in cell. To assess the ability of **CP1** to block the proliferation of four cancer cell linesPC-3, HeLa, MDA-MB-231, A549 and NKE (human normal kidney epithelial)cell line, MTT assay has been performed and has been compared with Cisplatin, a versatile broad spectrum anticancer drug, as a standard.The IC_{50}dataof the experiments (**Figure 5.19 (a** and **b)**) show that **CP1** possesses cytotoxicity against most cancer cell lines, relative to the normal cell line,

NKE and its efficacy in inhibiting proliferation of HeLa (IC_{50}, 17.58 ± 1.56 µM) is highest compared to other cancer cells (PC3: IC_{50},21.52 ± 2.44 µM; A549: IC_{50},50.29 ± 3.81 µM; MDA-MB 231: IC_{50},36.41 ± 1.72 µM). Thus, based on this study HeLa has been selected for further studies.

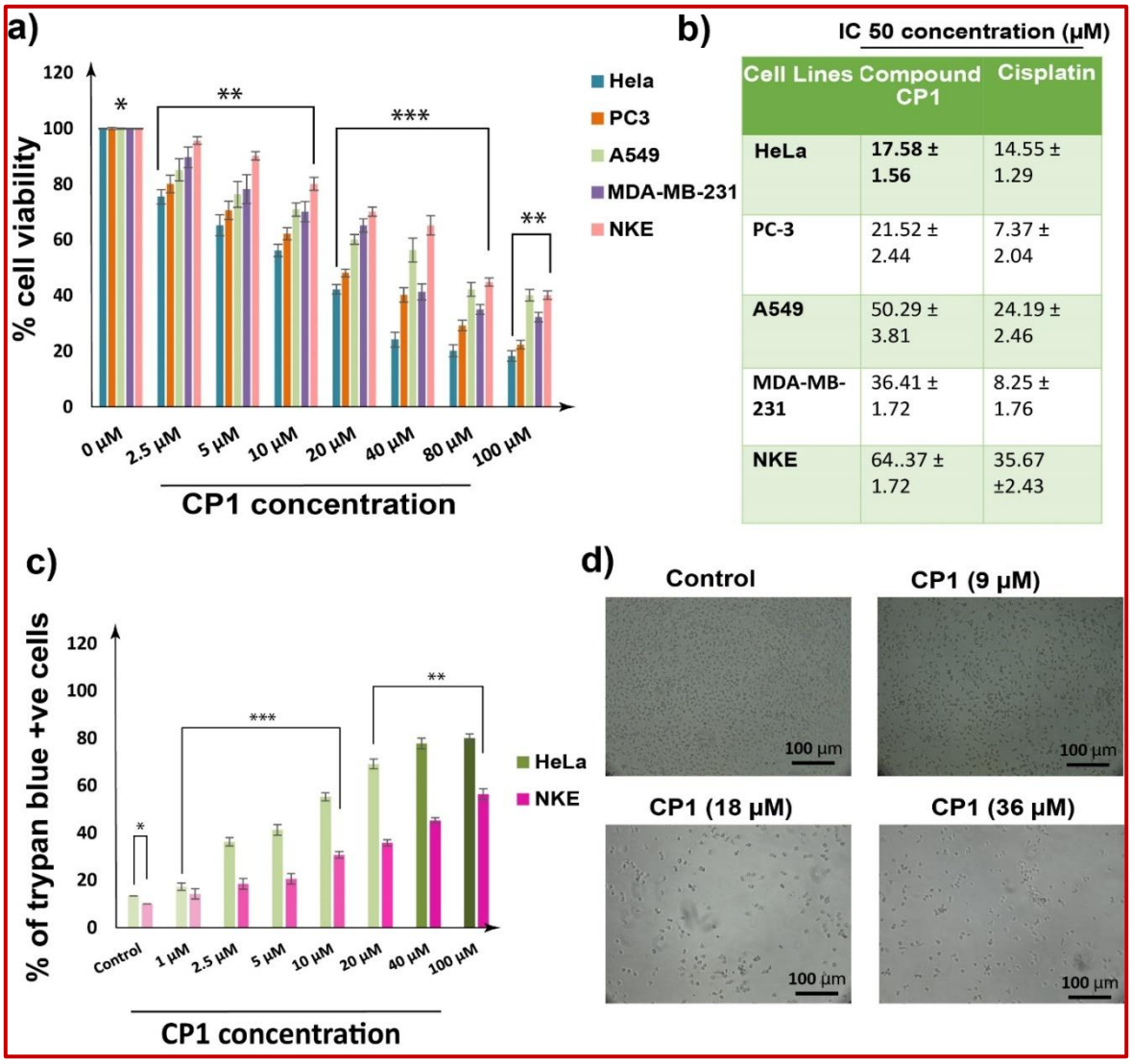

Figure 5.19 In vitro cytotoxicity was measured by MTT assay: (**a)** Bar graph;**(b)** IC_{50} values of **CP1** in PC-3, HeLa, MDA-MB 231, A549 cancer cells, and NKE (human normal kidney epithelialcell line;**(c)** Trypan blue assay and**(d)** Phase contrast microscopic imaging of **CP1**. All the experiments have been repeated thrice and the results were expressed as mean ± SEM. The level of significance was set at ***(P<0.001); **(P ≤0.01-0.001); *(P ≤0.01-0.05) in respect to the control.

To re-establish the findings of MTT assay, Trypan blue assay has also been performed in NKE and HeLa cell line and treated with different concentration of **CP1**. The result (**Figure 5.19c**) clearly shows the dose dependent increase in Trypan blue positive HeLa cell in comparison to NKE cell line which obviously supports the result from MTT assay that the drug **CP1** is selectively more effective in HeLa cell line than normal cell line.To support this observation,phase contrast microscopicimaging of **CP1** has been performed (**Figure 5.19d**) which has revealed that as compared to control setup, treated setup showed concentration-dependent increase in the level of morphological change to induce death in HeLa cells (**Figure 5.19d**).

5.3.4.10 CP1 inhibits cell cycle progression by inducing G2/M arrest

FACS (Fluorescence Activated Cell Sorting)analysis using PI (propidium iodide) was performed to measure the effects of **CP1** on cell cycle distribution profile of HeLa cells and their anti-proliferative mechanism. Flow cytometric data (**Figure 5.20**) clearly showed a significant level of increase in the G2/M phase cell proportion upon addition of **CP1** which is accompanied by a significant decrement in G1 phase cell population. A dose dependent increase in induction of G2/M arrest at a concentration of (9 µM, 18 µM and 36 µM) of **CP1** showed arrest of G2/M by 22.92%, 29.77% and 52.13 % of cell population respectively (**Figure 5.20(a, b)**). Further DAPI ((4′,6-diamidino-2-phenylindole), a blue-fluorescent DNAstaining also showed dose dependent increase in polynuclear fragmentation and nucleus shrinking was noted to HeLa cells in response to **CP1** treatment. In comparison, no polynuclear fragmentation or nucleus shrinking was observed in control set (**Figure 5.20c**). Altogether these results clearly indicate the intracellular **CP1** mediated DNA fragmentation and G2/M phase cell cycle arrest is involved in **CP1** mediated cell death.

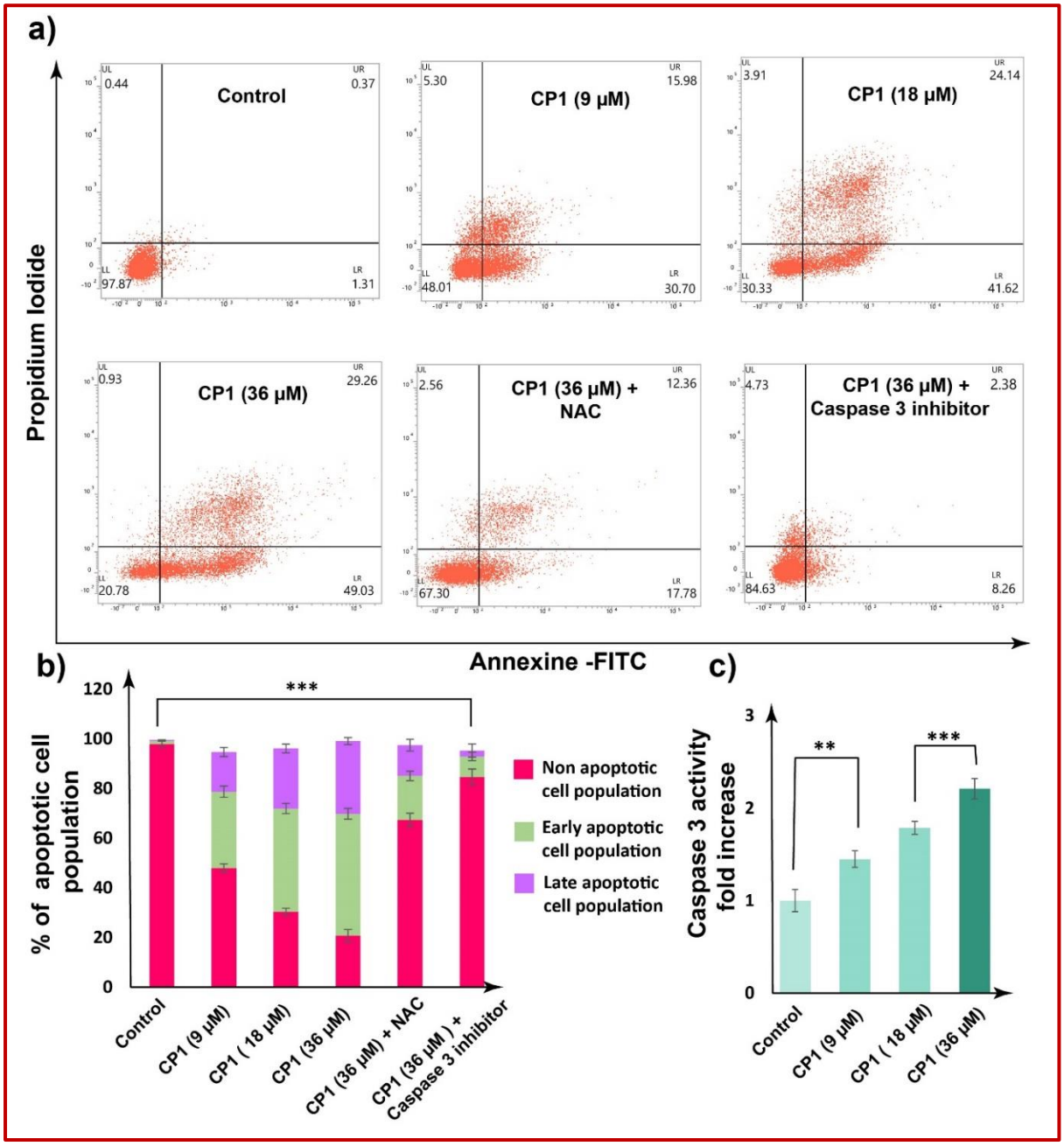

Figure 5.20. (**a**) FACS analysis, and (**b**) Histogram showingconcentration-dependent increase in HeLa cell G2/M cell population, in response to treatment with different concentrations of **CP1**(9 µM, 18 µM and 36 µM)**.** (**c**) Apoptotic Nuclear Morphology Study by DAPI Staining for the detection of **CP1** mediated DNA damage. All the experiments have been repeated thrice and the results were expressed as mean ± SEM. The level of significance was set at ***(P<0.001); **(P ≤0.01-0.001); *(P ≤0.01-0.05) in respect to the control.

5.3.4.11 Caspase 3 mediated apoptotic cell death:CP1 treatment promotes

Results from Annexin V conjugated with fluorescein isothiocyanate/propidium iodide (V-FITC^{+}/PI^{-})flow cytometric assay showed an increased number of apoptotic cell population with the increase in concentration of **CP1**(9µM, 18 µM, and 36 µM). The sample was treated for 24h.

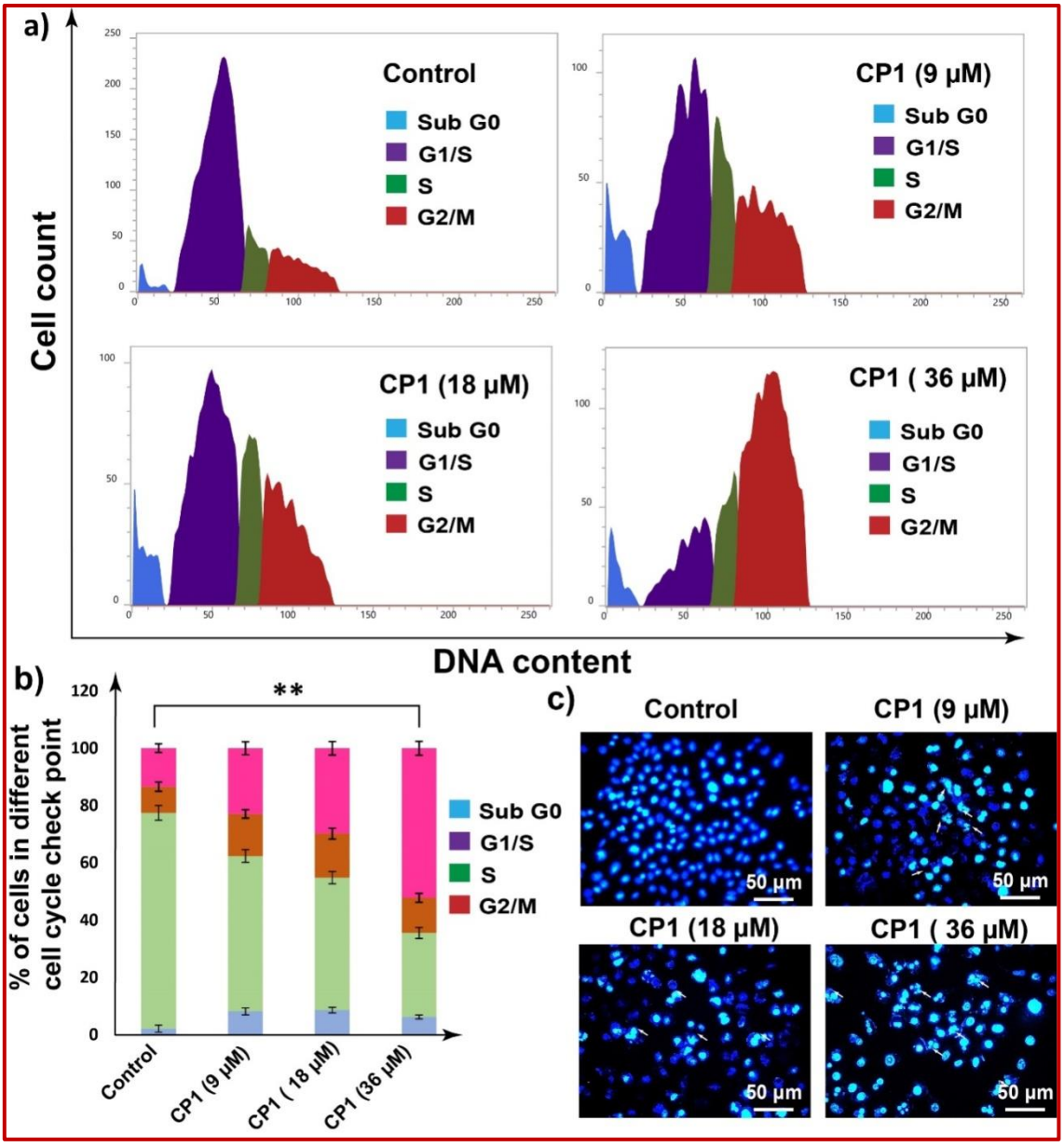

Figure 5.21 FACS analysis: (**a**) concentration-dependent increase in annexin V-FITC/PI-positive population of HeLa cells, in response to treatment with **CP1** (9 µM, 18 µM, and 36 µM), **CP1** (36 µM) + NAC, **CP1** (36 µM) + Caspase 3 inhibitor; (**b**) Histograms representing dose-dependent increase in the apoptotic cell population percentage in response to **CP1;** (**c**)

Histograms representing dose-dependent increase in caspase 3 activity in response to **CP1**. All the experiments have been repeated thrice and the results were expressed as mean ± SEM. The level of significance was set at ***(P<0.001); **(P ≤0.01-0.001); *(P ≤0.01-0.05) in respect to the controlpresented 1.45-, 1.78- and 2.21-fold increase in caspase 3 activity respectively when compared with control set up, suggesting that **CP1** mediated cell death of HeLa cells was due to apoptosis induction, induced by increase caspase 3.

with the media and the cell population was followed by the increased annexin V-FITC^{+}/PI^{-} (early apoptotic and late apoptoticaltogether) to 46.68%, 65.67% and 78.29%, respectively in comparison to 1.68 % in control setup (**Figure 5.21a**). Further in another experimental setup where HeLa cells were pretreated with ROS scavengerN-Acetyl-Cysteine (NAC) and Caspase 3 inhibitor seperately, a decrease in apoptotic cell poulation upon **CP1** (36 µM) treatment had been observed which indicated that Caspase 3 and ROS both could be involved in **CP1** mediated apoptotic cell death process (**Figure 5.21(a** and **b)**).

To further reinstate of Annexin V-FITC/PI assay, caspase-3/7 activity assay was performed, to find whether caspase 3 protease activity increased after **CP1** treatment. The results from caspase 3/7 assay **(Figure 5.21c)** clearly displayed dose dependent increase in caspase 3 activity and at a concentration of 9 µM, 18 µM, and 36 µM of **CP1**.

5.3.4.12 Intracellular ROS accumulation: Induction by CP1

To further determine whether **CP1** apoptotic cell death was due to intracellular Reactive Oxygen Species (ROS) accumulation, H_2DCFDA (2',7'-dichlorodihydrofluorescein diacetate) fluorescence assay was performed and ROS generation was measured using FACS and fluorescence microscopic analysis. Images of **CP1** treated cells disclosed a dose dependent increase in the level of green colour fluorescent intensity as compared to control untreated cells which is indicating the intracellular ROS accumulation. Further in comparison to control at a concentration of 36 µM of **CP1**, 2.69 ± 0.09-fold increase in fluorescence intensity was noted, which was close to H_2O_2 induced increment in green fluorescence intensity, 3.09 ± 0.21. Nonetheless, HeLa cells pre-treated with 10 mM NAC, a potent and widely accepted inhibitor of ROS, decreased **CP1** induced ROS generation in comparison to **CP1** treatment alone, at a concentration of 36 µM (**Figures 5.22a** and **5.22b**).

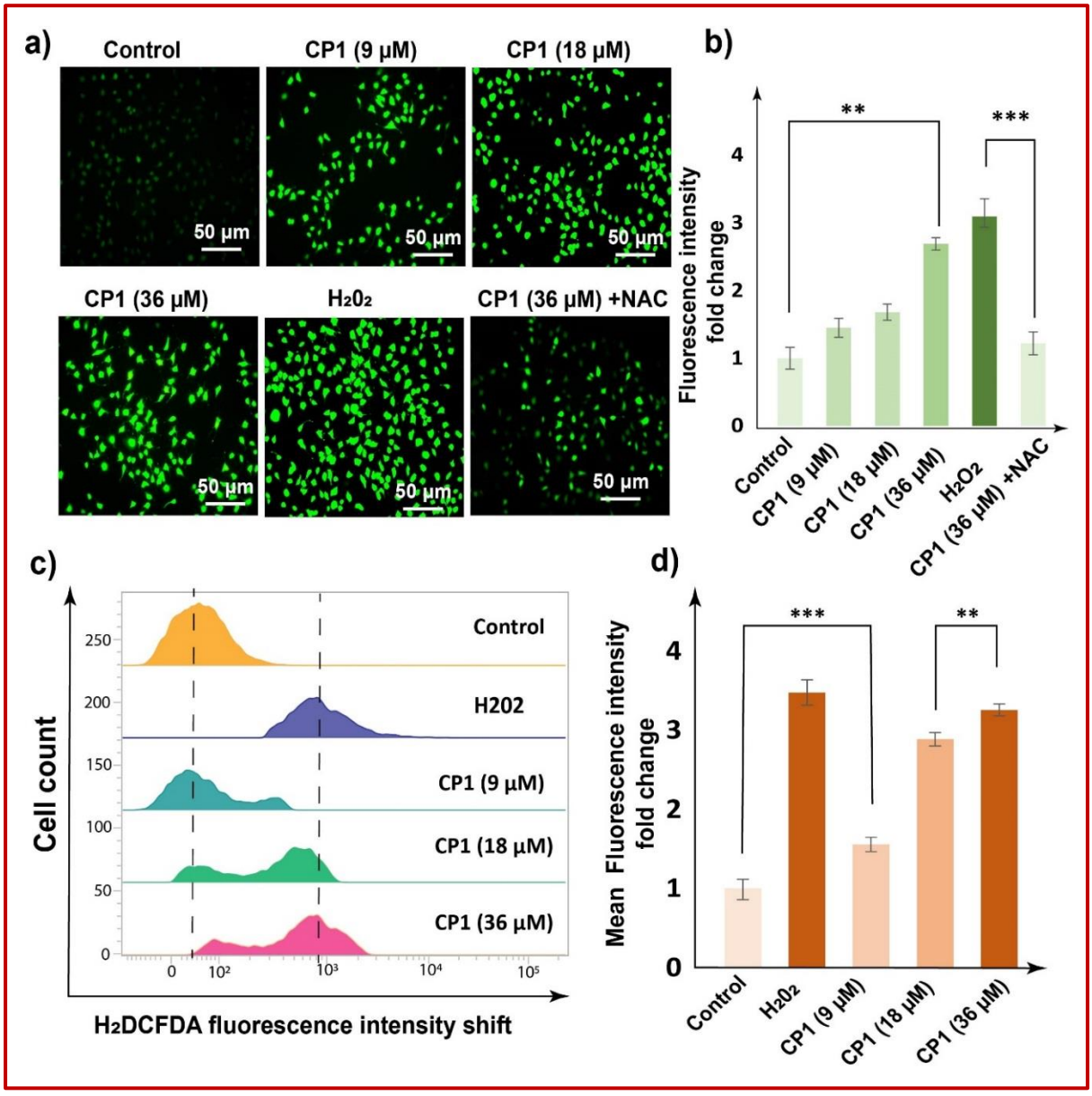

Figure 5.22 **(a)** Concentration-dependent increase in intercellular ROS accumulation of HeLa cells, in response to treatment with **CP1** and H_2O_2 Post treatment with **CP1** (9 µM, 18 µM and 36 µM) for 24 h, cells were stained with H_2DCFDA and fluorescence microscopic photos; **(b)** variation in fluorescence intensity; **(c)** displayed stacked presentation of FACS analysis and **(d)** exhibited fold change in mean fluorescence intensity. The level of significance was set at ***(P<0.001); **(P ≤0.01-0.001); *(P ≤0.01-0.05) in respect to the control.

Additionally, flow cytometric data also confirmed the dose-dependent increase in the level of Mean Fluorescence Intensity (MFI) in cells treated with **CP1**. Treatment of H_2O_2 (1 µM)and **CP1** treatment at a concentration of 9 µM, 18 µM and 36 µM for 24 h increased the MFI to

3.48 ± 0.16 (H_2O_2 only), 1.56 ± 0.08 (9 µM,**CP1**), 2.89 ± 0.13 (18 µM, **CP1**), and 3.26 ± 0.076 (36 µM, **CP1**) in comparison to control setup ((**Figures 5.22c** and **5.22d**). Altogether, the result clearly indicates that intracellular ROS accumulation is involved in apoptotic cell death mediated by **CP1.**

5.3.4.13 Loading of Diclofenac Sodium (DMNa) to CP1 and *In-Vitro* Release

An exciting property of the CPs/MOFs is the encapsulation of live-saving drugs and their targeted delivery in living cells. The features of the good transporter are environment dependent (pH, polarity, stimulation by light, magnetic, mechanical, thermal etc.) easy and fast uploading and no-loss, as-required release in the cells. Doxorubicin encapsulation in CPs nanoclusters and its delivery is focused research for high-end cancer treatment protocol.[61]Drug arresting and target distribution of the **CP1** is examined for Diclofenac Sodium (DMNa) at two different pH.The % of loading and encapsulation ratio is~ 52.2% in both cases. The study has investigated that the release behavior of **CP1@DMNa** in a PBS solution at two distinct pH levels (pH 1.2 and pH 7.4) **(Figure 5.24(a))**, while maintaining a normal human body temperature of 37°C. The pH selection is considered on the basis of simulated stomach environment at pH = 1.2 and simulated intestinal environment at pH = 7.4. The UV-vis spectroscopic experimentshave been employed to quantify the concentration of the released drug, and the resulting release profiles (**Figure 5.23**).

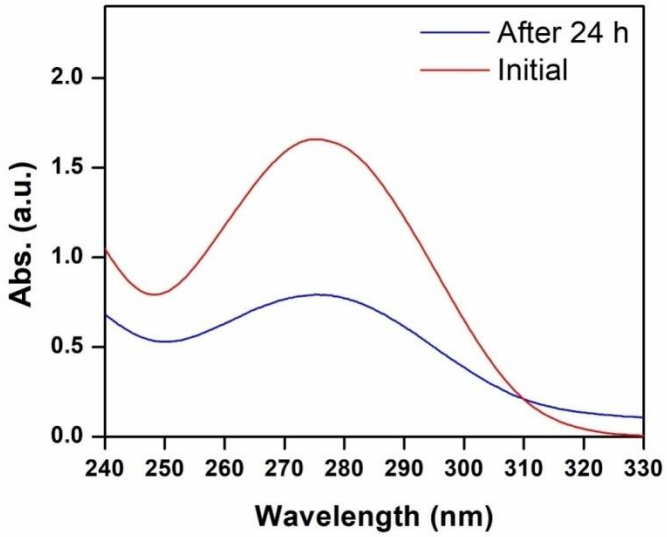

Figure 5.23 UV-visible absorption spectra of Diclofenac Sodium (DMNa) (blank) and after shocking by **CP1** for 24 h at 37˚C

Within a simulated stomach environment (pH 1.2), only approximately ~ 8% of the drug was released, primarily comprising molecules situated at the center of the pores. This restrained release can be attributed to the limited guest-guest interaction among the molecules. Conversely, a significant enhancement in drug release was observed within a simulated intestinal environment (pH 7.4) and % of maximum drug molecules were released in the first 13h. Then, the delivered rate of drug slowed down and approximately ~ 87% release over a span of 30 h.

By comparing the drug release behavior across distinct pH values, the pH-responsive release mechanism of **CP1@DMNa** were elucidated **(Figure 5.24(b))**. It is well-established in the literature that pyridine-based heterocycles undergo protonation and deprotonation in acidic and neutral environments, respectively.[62] Consequently, the framework of **CP1** became positively charged under acidic condition due to protonation, leading to the establishment of an electrostatic force between the material and the anionic drug, Diclofenac sodium (DMNa). This electrostatic interaction effectively hindered the release of DMNa.

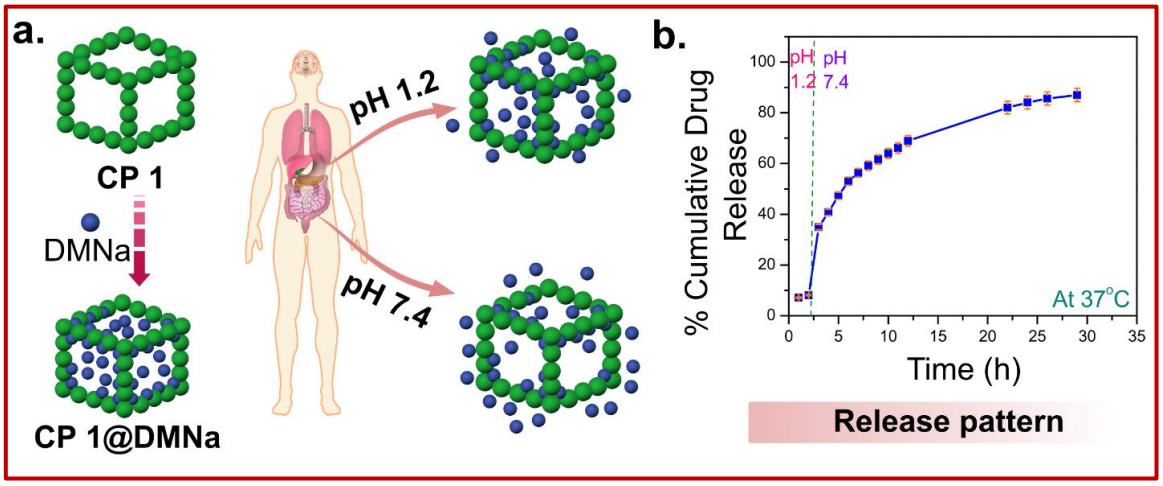

Figure 5.24 **(a)** The study investigated the release behavior of **CP1@DMNa**in a PBS solution at two distinct pH levels (pH 1.2 and pH 7.4),**(b)**The pH-responsive release mechanism of**CP1@DMNa**.

Conversely, a deprotonation effect occurred within the pH 7.4 medium, resulting in the neutralization and easy release. As a result, a substantial release of drug molecules was observed.This distinctive release mechanism highlights the remarkable pH-responsive behavior of **CP1** within the digestive system, underscoring its promising potential as an oral drug carrier.

When the results are combined, it can be concluded that the **CP1** demonstrates dual-functional activity from a single framework through enhanced conductivity and better biological activity, which are compared to published CP-based materials (**Table 5.5**). According to the table, the current **CP1** is a better functional material than the others in terms of applications.

Table 5.5 Comparison of dual-action **CP1** coordination polymers with previously reported coordination polymers.

SL. No.	Compound Name	Electrical Conductivity ($S.m^{-1}$)	Biological & Drug delivery activity	References
1.	$[Cd(HL_2)_2(N(CN)_2)_2]_n$	2.44×10−7	-	21
2.	$[Pb_2(bdc)_{1.5}(aiz)(MeOH)_2]_n$	3.66×10−7	-	22
3.	$[CdL_3(l\text{-}1,3\text{-}SCN)_2]_n$	2.16×10−8	-	23
4.	$[Co(3\text{-}clpy)_2(fum)_2(H_2O)_2]_n$	4.84□10−6	-	24
5.	$[Cu(fum)(4\text{-}phpy)_2(H_2O)]$	6.13×10−6	-	25
6.	$[Cd(adc)(4\text{-}phpy)_2(H_2O)_2]_n$	3.04×10−7	-	26
7.	$C_{20}H_{18}CuN_2O_{10}$(Cu-MOF2)	7.60×10−6	-	27
8.	$[Zn(adc)(4\text{-}phpy)_2(H_2O)_2]_n$	7.78×10−8	-	26
9.	$[Cd_2(L_1)_2(NCS)_2(CH_3OH)]_n$	6.72×10−5	-	21
10.	$C_{40}H_{34}Cu_2N_6O_{18}$(Cu-MOF1)	4.34×10−6	-	27
11.	$\{[Cd(HL_1)_2(N(CN)_2)_2]\cdot H_2O\}_n$	6.15×10−7	-	21
12.	$[Pb_2(bdc)_{1.5}(aiz)]_n$	6.12×10−6	-	22
13	$[Mn_2(aisp)_3(pcih)_2(solvent)]_n$	1.57×10^{-6}	Yes	This Work

Where, HL_2 = 2-Methoxy-6-((quinolin-5-ylimino)methyl)phenol], H_2bdc = 1,4-benzene dicarboxylic acid, aiz = (E)-N′-(thiophen-2- ylmethylene)isonicotino hydrazide), HL_3 = 2-(2-(ethylamino)ethyliminomethyl)-6-ethoxyphenol, 3-clpy = 3-Chloropyridine, H_2fum = fumaric acid, 4-phpy= 4-phenylpyridine, H_2adc= acetylenedicarboxylic acid, HL1 = 2-

Methoxy-6- ((quinolin-3-ylimino)methyl)phenol, pcih = Pyridine-4-carboxaldehyde isonicotinoyl hydrazine, H_2aisp = 5-aminoisophthalic acid.

5.4 Conclusion

In summary, the Mn(II)-3D coordination framework, **[Mn_2(aisp)$_3$(pcih)$_2$(solvent)]$_n$(CP1**)is structurally established as well as thermal, chemical stability (different pH),phase purity have been verified. The electrical conducting propertyshows non-ohmic feature of trapped charge and plays a major contribution to the current conduction process in the SCLC region. On considering medicinal character of isoniazid and its Schiff base complexes, the anticancer activity of **CP1** is examinedand shows highest efficiency onHeLa cells out of four different cancer cell lines. The dose-dependent morphological change of cells including condensed and fragmented chromatin and diminished cell viability approves the resistance to cell progression along with enhancement of intracellular ROS production which develops oxidative stress leading to apoptotic cell death. Besides, the **CP1** has loaded the drug, Diclofenac Sodium (DMNa) (**CP1@DMNa**) substantially and shows pH induced reversible releasing. Thus, the material executes multifaceted activities – energy material, drug activity and drug delivery system.

5.5 References

(1) Roy, A.; Guha Ray, P.; Bose, A.; Dhara, S.; Pal, S. pH-Responsive Copolymeric Network Gel Using Methacrylated β-Cyclodextrin for Controlled Codelivery of Hydrophilic and Hydrophobic Drugs, *ACS Appl. Bio Mater.* **2022**, *5*, 3530–3543.

(2) Kitagawa, S. Metal–organic frameworks (MOFs). *Chem. Soc. Rev*. **2014**, *43*, 5415-5418.

(3) Maji, T.K.; and Kitagawa, S. Chemistry of porous coordination polymers. *Pure Appl. Chem.* **2007**, *79*, 2155-2177.

(4) Liu, X.J.; Fang, Q.R.; Zhu, G.S.; Xue, M.; Shi, X.; Wu, G.; Tian, G.; Qiu, S.L. and Fang, L. Crystal structure and fluorescence of a novel 3D inorganic–organic hybrid polymer with mixed ligands. *Inorg. Chem. Comm*.**2004**,*7*, 31-34.

(5) Shit, M.; Paul, S.; Chatterjee, T.; Dutta, B. and Sinha, C. Towards Design of Energy Efficient Semiconducting Material: An Example of 1D Cd (II)-2, 5-thiophene dicarboxylato Co-ordination Polymer. *ES energy environ.***2022**,*16*, 40-46.

(6) Xu, M.M.; Xie, L.H. and Li, J.R. Metal–Organic Framework/Polymer Hybrid Materials. *Hybrid Metal-Organic Framework and Covalent Organic Framework Polymers*.**2021**, *39*, 72.

(7) Stavila, V.; Talin, A.; A. and Allendorf, M.D. MOF-based electronic and opto-electronic devices. *Chem. Soc. Rev*. **2014**, *43*, 5994-6010.

(8) Naskar, K.; Dey, A.; Dutta, B.; Ahmed, F.; Sen, C.; Mir, M.H.; Roy, P.P. and Sinha, C. Intercatenated coordination polymers (ICPs) of carboxylato bridged Zn (II)-isoniazid and their electrical conductivity. *Cryst. Growth Des*.**2017**, *17*, 3267-3276.

(9) Naaz, S.; Das, P.; Khan, S.; Dutta, B.; Roy, S.; Frontera, A.; Ray, P.P. and Mir, M.H. Cu (II)-Based Molecular Hexagons Forming Honeycomb-like Networks Exhibit High Electrical Conductivity. *Inorg. Chem*.**2022**,*61*,19828-19837.

(10) Allendorf, M.D.; Schwartzberg, A.; Stavila, V. and Talin, A.A roadmap to implementing metal–organic frameworks in electronic devices: challenges and critical directions. *Chem. Eur. J*.**2011**, *17*, 11372-11388.

(11) Dou, J.H.;Arguilla, M.Q.; Luo, Y.; Li, J.; Zhang, W.; Sun, L.; Mancuso, J.L.; Yang, L.; Chen, T.; Parent, L.R. and Skorupskii, G. Atomically precise single-crystal structures of electrically conducting 2D metal–organic frameworks. *Nat. Mater*.**2021**, *20*, 222-228.

(12) Dutta, B.; Jana, R.; Bhanja, A.K.; Ray, P.P.; Sinha, C. and Mir, M.H. Supramolecular aggregate of Cadmium (II)-based one-dimensional coordination polymer for device fabrication and sensor application. *Inorg. Chem*.**2019**, *58*,2686-2694.

(13) Horike, S.;Umeyama, D. and Kitagawa, S. Ion conductivity and transport by porous coordination polymers and metal–organic frameworks. *Acc. Chem. Res*. **2013**, *46*, 2376-2384.

(14) Halder, S.; Dey, A.; Bhattacharjee, A.; Ortega-Castro, J.; Frontera, A.; Ray, P.P. and Roy, P. A Cd (II)-based MOF as a photosensitive Schottky diode: experimental and theoretical studies. *Dalton Trans*.**2017**, *46*, 11239-11249.

(15) Kim, J.H.; Park, H.W.; Koo, S.J.; Lee, D.; Cho, E.; Kim, Y.K.; Shin, M.; Choi, J.W.; Lee, H.J. and Song, M. High efficiency and stable solid-state fiber dye-sensitized solar cells obtained using TiO_2 photoanodes enhanced with metal organic frameworks. *J. Energy Chem*.**2022**,*67*, 458-466.

(16) Beg, S.; Rahman, M.; Jain, A.; Saini, S., Midoux, P., Pichon, C., Ahmad, F.J. and Akhter, S., Nanoporous metal organic frameworks as hybrid polymer–metal composites for drug delivery and biomedical applications. *Drug Discov. Today*. **2017**, *22*,625-637.

(17) Sanchez, C.; Shea, K.J. and Kitagawa, S. Recent progress in hybrid materials science. *Chem. Soc. Rev*.**2011**, *40*, 471-472.

(18) Chongdar, S.; Bhattacharjee, S.; Bhanja, P. and Bhaumik, A. Porous organic–inorganic hybrid materials for catalysis, energy and environmental applications. *Chem. Comm*.**2022**,*58*, 3429-3460.

(19) Cui, Y.; Li, B.; He, H.; Zhou, W.; Chen, B. and Qian, G. Metal–organic frameworks as platforms for functional materials. *Acc. Chem. Res*.**2016**, *49*, 483-493.

(20) Wang, X.; Zhu, G.; Wang, C. and Niu, Y. Effective degradation of tetracycline by organic-inorganic hybrid materials induced by triethylenediamine. *Environ. Res.***2021**,*198*, 111253.

(21) Li, N. Y.; Liu, D.; Abrahams, B. F. and Lang, J. P. Covalent switching, involving divinylbenzene ligands within 3D coordination polymers, indicated by changes in fluorescence. *Chem Comm.* **2018**, *54*, 5831-5834.

(22) Shi, Y. X.; Li, W. X.; Zhang, W. H. and Lang, J. P. Guest-induced switchable breathing behavior in a flexible metal–organic framework with pronounced negative gas pressure. *Inorg. Chem.* **2018**, *57*, 8627-8633.

(23) Shit, M.; Sahoo, D.; Dutta, B.; El Fallah, S.; Kundu, A.; Manik, N.B. and Sinha, C. Exploration of Variable Temperature Magnetism and Electrical Properties of a Pyridyl-isonicotinoylHydrazone Bridged Three-Dimensional Mn-Metal–Organic Framework with a ThiopheneDicarboxylato Link. *Cryst. Growth Des*.**2022**,*22*, 7143-7152.

(24) Shit, M.; Das, P.; Paul, S.; Samanta, A.; Aziz, S.M.; Ray, P.P. and Sinha, C. In quest of New Energy Material: 3D Mn (II)-coordination Polymer, the Schottky Device and Theoretical Interpretation. *ES Mater. Manuf.***2022**, *19*, 804.

(25) Zhang, X.; Wang, W.; Hu, Z.; Wang, G.; Uvdal, K. Coordination polymers for energy transfer: Preparations, properties, sensing applications, and perspectives, *Coord. Chem. Rev.***2015**, *284*, 206-235.

(26) Mallakpour, S.; Nikkhoo, E. and Hussain, C. M. Application of MOF materials as drug delivery systems for cancer therapy and dermal treatment, *Coord. Chem. Rev.* **2022**, *451*, 214262.

(27) McKinlay, A. C.; Morris, R.E.; Horcajada, P.;Férey, G.;Gref, R.; Couvreur, P. and Serre, C. BioMOFs: metal–organic frameworks for biological and medical applications. *Angew. Chem., Int. Ed. Engl.***2010**, *49*, 6260-6266.

(28) Chandra, A.; Das, M.; Pal, K.; Jana, S.; Dutta, B.; Ray, P. P. and Sinha, C. Three-dimensional-coordination polymer of Zn (II)-carboxylate: Structural elucidation, photoelectrical conductivity, and biological activity. *ACS Omega***2019**, *4*, 17649-17661.

(29) Dutta, B.; Pal, B.; Dey, S.; Maity, S.; Ray, P.P. and Mir, M.H. Exploitation of Structure- Property Relationships towards Multi- Dimensional Applications of a Paddle- Wheel Cu (II) Compound. *Eur. J. Inorg. Chem*.**2022**,*2022*, e202100904.

(30) Khan, S.; Halder, S.; Dey, A.; Dutta, B.; Ray, P.P. and Chattopadhyay, S. Synthesis of an electrically conductive square planar copper (II) complex and its utilization in the fabrication of a photosensitive Schottky diode device and DFT study. *New J. Chem*.**2020**, *44*, 11622-11630.

(31) Kondo, M.; Yoshitomi, T.; Matsuzaka, H.; Kitagawa, S. and Seki, K. Three- Dimensional Framework with Channeling Cavities for Small Molecules: $\{[M_2(4, 4'\text{- bpy})_3(NO_3)_4]\cdot xH2O\}_n$ (M Co, Ni, Zn). *Angew. Chem., Int. Ed. Engl.***1997**, *36*,1725-1727.

(32) Kanoo, P.; Matsuda, R.;Kitaura, R.; Kitagawa, S. and Maji, T.K. Topological difference in 2D layers steers the formation of rigid and flexible 3D supramolecular isomers: Impact on the adsorption properties. *Inorg. Chem*.**2012**, *51*, 9141-9143.

(33) Khan, S.; Halder, S.; Dey, A.; Dutta, B.; Ray, P.P. and Chattopadhyay, S. Synthesis of an electrically conductive square planar copper (II) complex and its utilization in the fabrication of a photosensitive Schottky diode device and DFT study. *New J. Chem*.**2020,** *44*, 11622-11630.

(34) Sun, L.; Campbell, M.G. and Dincă, M. Electrically conductive porous metal–organic frameworks. *Angew. Chem., Int. Ed. Engl*.**2016**, *55*, 566-3579.

(35) Khan, S.; Halder, S.; Ray, P.P.; Herrero, S.;González-Prieto, R.; Drew, M.G. and Chattopadhyay, S. A semiconducting copper (II) coordination polymer with (4, 4) square grid topology: Synthesis, characterization, and application in the formation of a photoswitch. *Cryst. Growth Des*.**2018**, *18*, 651-659.

(36) Khan, S.; Das, P.; Naaz, S.; Brandão, P.; Choudhury, A.;Medishetty, R.; Ray, P.P. and Mir, M.H. A dual-functional 2D coordination polymer exhibiting photomechanical and electrically conductive behaviors. *Dalton Trans*.**2023**, *52*, 17934-17941.

(37) Khan, S.; Halder, S.; Dey, A.; Dutta, B.; Ray, P.P. and Chattopadhyay, S. Synthesis of an electrically conductive square planar copper (II) complex and its utilization in the

fabrication of a photosensitive Schottky diode device and DFT study. *New J. Chem.***2020**, *44*, 11622-11630.

(38) Shit, M.; Halder, S.; Dey, A.; Dutta, B.; Chanthapally, A.; Jana, K. and Sinha, C. Pyridyl-IsonicotinoylHydrazone-Bridged Zn (II) Coordination Framework with Thiophenedicarboxylato Link: Structure, Biological Activity, and Electrical Conductivity. *Inorg. Chem.***2023**,*62*, 19937-19947

(39) Cai, H.; Huang, Y.L. and Li, D. Biological metal–organic frameworks: Structures, host–guest chemistry and bio-applications. *Coord. Chem. Rev.***2019,***378*,207-221.

(40) Wang, H.S.; Wang, Y.H. and Ding, Y. Development of biological metal–organic frameworks designed for biomedical applications: from bio-sensing/bio-imaging to disease treatment. *Nanoscale Adv.***2020**, *2*,3788-3797.

(41) Duman, F.D. and Forgan, R.S.Applications of nanoscale metal–organic frameworks as imaging agents in biology and medicine. *J. Mater. Chem. B.* **2021,** *9*, 3423-3449.

(42) Sheldrick, G.M., Gilmore, C.J., Hauptman, H.A., Weeks, C.M., Miller, R. and Usón, I., 2012. Shelx.

(43) Frisch,M. J.; Trucks, G. W.; Schlegel, H. B.;Scuseria, G. E.; Robb, M. A.; Cheeseman, J. R.;Scalmani, G.; Barone, V.;Mennucci, B.; Petersson, G. A.;Nakatsuji, H.; Caricato, M.; Li, X.;Hratchian, H. P.; Izmaylov, A. F.;Bloino, J.; Zheng, G.; Sonnenberg, J. L.; Hada, M.; Ehara, M.; Toyota, K.; Fukuda, R.; Hasegawa, J.; Ishida, M.; Nakajima, T.; Honda, Y.; Kitao, O.; Nakai, H.; Vreven, T.; Montgomery Jr., J. A.; Peralta, J. E.; Ogliaro, F.; Bearpark, M.; Heyd, J. J.; Brothers, E.; Kudin, K. N.; Staroverov, V. N.; Kobayashi, R.; Normand, J.;Raghavachari, K.; Rendell, A.; Burant, J. C.; Iyengar, S. S.; Tomasi, J.; Cossi, M.; Rega, N.; Millam, J. M.; Klene, M.; Knox, J. E.; Cross, J. B.;Bakken, V.; Adamo, C.; Jaramillo, J.; Gomperts, R.; Stratmann, R. E.; Yazyev, O.; Austin, A. J.; Cammi, R.; Pomelli, C.; Ochterski, J. W.; Martin, R. L.; Morokuma, K.; Zakrzewski, V. G.; Voth, G. A.; Salvador, P.; Dannenberg, J. J.; Dapprich, S.; Daniels, A. D.; Farkas, O.; Foresman, J. B.; Ortiz, J. V.; Cioslowski, J. ; Fox, D. J.; Gaussian 09, Revision D.01, Gaussian Inc., Wallingford, CT, 2009.

(44) Hay, P.J.; Wadt, W.R. Ab initio effective core potentials for molecular calculations. Potentials for K to Au including the outermost core orbitals. *J. Chem. Phys*.**1985**,*82*, 299-310.

(45) O'Boyle, N. M.; Tenderholt, A. L.; Langner, K. M.Cclib: a library for package- independent computational chemistry algorithms. *J. Comput. Chem*.**2008**, *29*, 839-845.

(46) Karan, A.K. and Manik, N.B. Estimation of Richardson constant for natural organic dye based cells using orange-lemon and apple-green. International Journal of Innovative Research in Physics, **2021**, *2*, 62-67.

(47) Karan, A.K.; Bhunia, S. and Manik, N.B. Study on the Conductivity of a Sunset Yellow Dye-Based Natural Organic Device. *J. Electron. Mater.***2022** ,*51* ,7156-7163.

(48) Karan, A.K.; Sahoo, D.; Sen, S. and Manik, N.B. Evaluation of Richardson constant of fruit dyes using carmoisine and tartrazine. *Int. j. innov. res. technol. sci. eng.***2022** ,*3* ,25-31.

(49) Tauc, J.; Optical properties and electronic structure of amorphous Ge and Si. *Mater. Res. Bull.***1968**, *3*, 37-46.

(50) Pazhanimuthu, C.; Investigation of dielectric and thermal properties of nano-dielectric materials in electrical applications. *Int. J. Eng. Innov. Technol.***2012**, *2* ,62-67.

(51) Elliott, S. R.; Philos. Mag. B Phys. Condens. Matter. Stat. Mech. Electron. *Opt. Magn. Prop.***1978**, *37*, 553.

(52) Karan, A.K. and Manik, N. B. Estimation of Richardson constant for natural organic dye based cells using orange-lemon and apple-green. *Int. J. Innov. Res. Technol. Sci. Eng.***2021**, *2* , 62-67.

(53) Tung, R.T. Electron transport at metal-semiconductor interfaces: General theory. *Physical Review B.***1992**,*45*,13509.

(54) Cheung, S.K. and Cheung, N.W. Extraction of Schottky diode parameters from forward current- voltage characteristics. *Appl. Phys. Lett.***1986**, *49*, 85-87.

(55) Nouchi,R.; ApNouchi,J. R. and Tanimoto, T. Substituent-Controlled Reversible Switching of Charge Injection Barrier Heights at Metal/Organic Semiconductor

Contacts Modified with Disordered Molecular Monolayers. *ACS Nano*.**2015**,*9*, 7429-7439

(56) Gupta, R. K. and Yakuphanoglu, F. Photoconductive Schottky diode based on Al/p-Si/SnS2/Ag for optical sensor applications. *Sol. Energy.***2012**, *86*, 1539-1545.

(57) Roy, S.; Halder, S.; Drew, M.G.; Ray, P.P. and Chattopadhyay, S. Fabrication of an active electronic device using a hetero-bimetallic coordination polymer. *ACS Omega***2018**, *3* , 12788-12796.

(58) Jain, A.; Kumar, P.; Jain, S. C.; Kumar, V.; Kaur, R. and Mehra, R. M. Trap filled limit voltage (VTFL) and V2 law in space charge limited currents. *J. Appl. Phys.***2007**, *9*, 102.

(59) Güllü, Ö.; Aydoğan, Ş. and Türüt, A.B.D.U.L.M.E.C.İ.T., Fabrication and electrical characteristics of Schottky diode based on organic material. *Microelectron. Eng.* **2008**, *85*, 1647-1651.

(60) Ahmed, F.; Halder, S.; Dutta, B.; Islam, S.; Sen, C.; Kundu, S.; Sinha, C.; Ray, P. P. and M. H. Mir,Synthesis and structural characterization of a Cu(ii)-based 1D coordination polymer and its application in Schottky devices, *New J. Chem.***2017**, *41*, 11317.

(61) Imaz, I; Rubio-Martínez, M.; García-Fernández, L.; García, F.; Ruiz-Molina, D.; Hernando, J.; Puntes, V.; and Maspoch, D., Coordination polymer particles as potential drug delivery systems, *Chem. Commun.***,2010**,*46*, 4737-4739.

(62) Roy, A.; Manna, K.; Ray, P. G.; Dhara, S. and Pal, S. β-Cyclodextrin-based ultrahigh stretchable, flexible, electro-and pressure-responsive, adhesive, transparent hydrogel as motion sensor. *ACS Appl. Mater. Interfaces.***2022**, *14*, 17065-17080.

Chapter 6

Highly efficient detection of Pd^{2+} in aqueous medium by a newly designed elusive Mn (II) coordination polymer

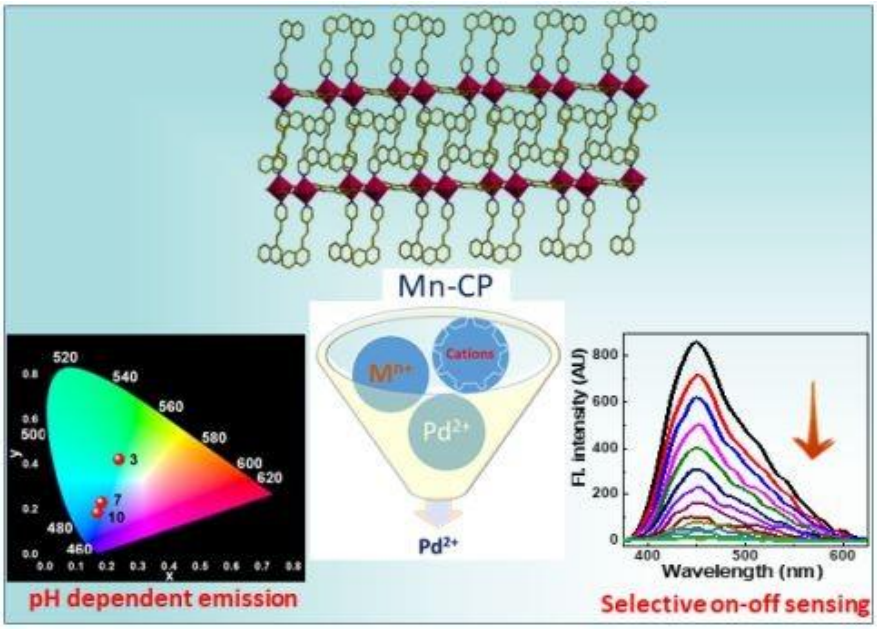

Abstract:

The first example of paramgnetic Mn(II)-based coordination polymer acts as pH-dependent emitting material [λ_{em}= 525 nm (pH = 2.0-4.0) and 450 nm (pH = 5.0-12.0)]. Its emission is quenched by Pd^{2+} in aqueous medium in presence of other thirteen cations with reasonably low pH-dependent limits of detection [21.178 ppb (pH= 3), 15.005 ppb (pH = 7.0) and 59.940 ppb (pH = 10.0)] as described by well-established mechanism. Therefore, urgency of such stable sensor remains high in regard to the environmental pollution.

6.1 Introduction

Palladium (Pd) and its compounds in various redox states (Pd(0/II/IV))[1] are employed as catalysts in the large number of organic syntheses; namely a few, Stille coupling,[2] Heck coupling,[3]Buchwald-Hartwig coupling,[4] and Suzuki coupling.[5,6] After the catalytic circle, Pd metal becomes abundant to the nature. Moreover, many electronic and electrical devices composed of this metal are unnerved into the open environment which causes the pollution.[7,8]Thus, Pd used in different fields spread in the environment and enters into the human body.[9,10] Pd at very low dose causes allergic action on live cells and the highest toxicity is shown by Pd^{2+} because of its very strong affinity to DNA-bases, and S-proteins/biomolecules.[11,12] Ingestion of Pd(II) to living being is immensely toxic and carcinogenic. The recommended dietary intake of Pd by WHO is <1.5 μg per day per person with the threshold value of 5 ppm.[13]Leaching of Pd(0/II/IV) to the pharmaceutical product during the catalytic synthesis may enter into the living body during therapeutical application, which may cause numerous side effects and abnormalities. The deposition of Pd^{2+} in cells also causes alopecia, asthma and even abortion.[14,15] Therefore, it is important to detect Pd^{2+} in an urgency manner for sustainable human health. In recent time, out of various techniques, the luminescent procedure of detection is very much popular because of its simple instrumentation, fast action, selective, specific and sensitive recognition, cost effective, direct use from laboratory to land and for real sample analysis.[16-20] In this context, coordination polymers (CPs)[21-24] are more efficient than that of molecular sensors for the identification of trace amount of Pd at any redox state because of their higher stability, better sensitivity and recyclicability.

Mn(II) (d^5) complexes are normally silent to luminescence because of extensive paramagnetic quenching.[25] Therefore, it remains challenge to fabricate Mn(II) based complexes that exhibit luminiscence properties. However, there are few examples of Mn(II) coordination complexes that show bright emission and have been utilized for diverse applications.[26] In this regard, we report the synthesis of a one-dimensional (1D) CP $[Mn(tdc)(nvp)_2(H_2O)]\cdot(DMF)$ (**Mn-CP**) synthesized using 2,5-thiophenedicarboxlic acid (H_2tdc) and 4-(1-naphthylvinyl)pyridine (nvp)(**Scheme 6.1**). The bright luminescene of **Mn-CP** is selectively quenched by the Pd^{2+} in aqueous solution even in presence of other thirteen cations with pH-dependent limits of detection (LODs). As per the literature survey, this is perhaps the first example of Mn(II)-based 1D CP that detects toxic Pd^{2+} in aqueous solution. The interaction between **Mn-CP** and Pd^{2+} has been inferred from FTIR, XPS, SEM and TGA data along with theoretical calculations. Interestingly, in the aqueous medium of wide range of pH values, **Mn-CP** selectively binds with Pd^{2+} even in presence of competitive analytes via 'on-off' sensing technique.

6.2 Experimental Section

6.2.1 Materials and General Methods

$MnCl_2\cdot4H_2O$, 2,5-thiophenedicarboxlic acid (H_2tdc) and 4-(1-naphthylvinyl)-pyridine (nvp) were purchased from different commercial resources and were used without further purification. The elemental analyses (C, H and N) were executed by PerkinElmer elemental analyser at 240° C. PerkinElmer spectrometer was used to determine the FTIR spectra.The powder X-ray diffraction data was collected at room temperature using the Bruker D8 advance X-ray diffractometer using CuKα radiation source (λ = 1.548 Å). PerkinElmer TGA 4000 system were used in thermogravimetric analysis within 30−800 °C with heating rate of 10 °C min^{-1} under nitrogen atmosphere. Fluorescence and UV-Vis spectra were examined by PerkinElmer LS55 spectrofluorimeter and PerkinElmer Lambda-25 spectrophotometer, respectively. Fluorescence lifetimes were measured using the Horiba JobinYvon fluorescence spectrophotometer. Optical characterization of the synthesized material was performed by SHIMADZU UV-1900 UV-Vis spectrophotometer.

6.2.2 Synthesis of Mn-CP

The Mn-CP was synthesized by slow diffusion method. A methanolic solution (2 mL) of nvp (0.046 g, 0.2 mmol) was carefully added to an aqueous solution (2 mL) of $MnCl_2 \cdot 4H_2O$ (0.040 g, 0.2 mmol), using 2 mL of a 1:1 (v/v) buffer solution of DMF and H_2O. After that, an ethanolic solution (2 mL) of H_2tdc (0.035 g, 0.2 mmol) neutralized with Et_3N (0.010 g, 0.1 mmol) was layered upon it. After three days, yellow color needle shaped crystals of $[Mn(tdc)(nvp)_2(H_2O)] \cdot DMF$ (Mn-CP) appeared with 65% yield (0.284 g) (**Scheme 6.1**). Elemental analysis (%) Calculated for $C_{43}H_{37}MnN_3O_6S$: C, 66.32; H, 4.79; N, 5.40. Found: C, 66.12; H, 4.25; and N, 4.95.

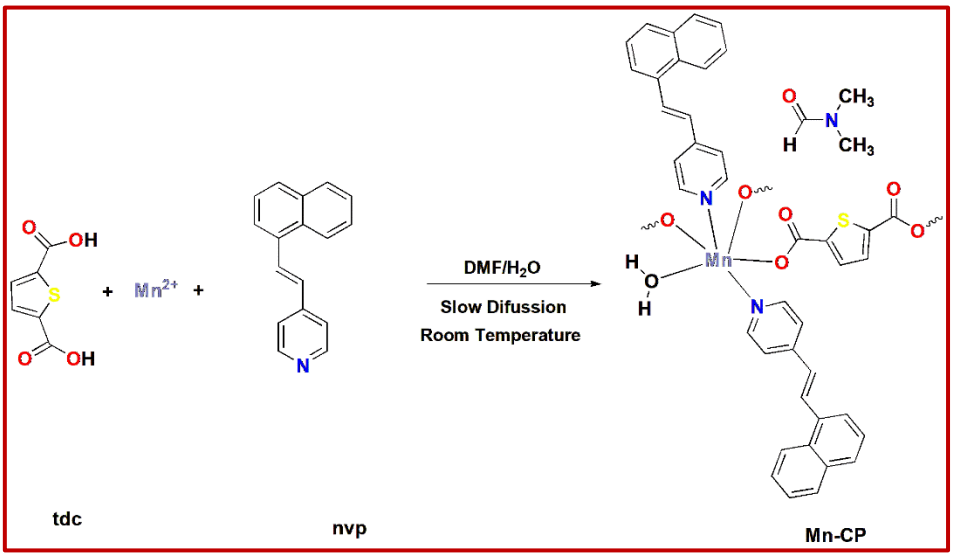

Scheme 6.1 Synthesis of **Mn-CP** using $MnCl_2 \cdot 4H_2O$, 4-(1-naphthylvinyl) pyridine (nvp) and 2,5-thiophene dicarboxylic acid (H_2tdc).

6.2.3 X-ray crystal structure determination

Yellow crystals of Mn-CP were taken for single crystal X-ray diffraction with the help of Bruker APEX-III CCD diffractometer equipped with graphite-mono chromated MoKα radiation (λ = 0.71073 Å) at 273 ± 2 K. Elucidation of single crystal structure was performed with the help of SHELX-97 package.[27] Non-hydrogen atoms were refined with anisotropic thermal parameters. Hydrogen atoms are situated in their geometrically idealised position and constrained to ride over their parent atoms. Crystallographic data and selected bond-angles/ bond-lengths of Mn-CP were tabulated in **Table 6.1** and **Table 6.2** , respectively.

Table 6.1 Crystal data and refinement parameters for **Mn-CP.**

CCDC NO.	**2223201**
formula	$C_{43}H_{37}MnN_3O_6S$
fw	778.76
crystal system	Triclinic
space group	$P\bar{1}$
a (Å)	10.9746(9)
b (Å)	12.1606(10)
c (Å)	15.9129(13)
α (deg)	97.410(3)
β (deg)	104.870(2)
γ (deg)	109.955(2)
V (Å^3)	1873.7(3)
Z	2
d_{calcd} (g/cm^3)	1.380
u (mm^{-1})	0.461
λ (Å)	0.71073
GOF on F^2	0.994
final *R* indices [$I > 2\sigma(I)$][a,b]	*R*1 = 0.0609(6076) *wR*2 = 0.1504(8421)

[a]$R_1 = \Sigma||F_o|-|Fc||/\Sigma|F_o|$, [b]$wR_2 = [\Sigma w(F_o^2-Fc^2)^2/\Sigma wF_o^2)^2]/2$, $w = 1/[\sigma^2(F_o^2) + (0.0350P)^2 + 0.9811P]$, where $P = (F_o^2+2Fc^2)/3$

Table 6.2 Selected bond lengths and bond angles in **Mn-CP.**

Mn1 - O1	2.126(2)	O1 - Mn1 - O3_b	90.73(9)
Mn1 - O9S	2.258(2)	O9S - Mn1 - N1	88.31(12)
Mn1 - N1	2.279(3)	O9S - Mn1 - N2	94.37(12)
Mn1 - N2	2.266(3)	O9S - Mn1 - O2_a	84.39(11)
Mn1 - O2_a	2.121(3)	O9S - Mn1 - O3_b	83.12(11)

Mn1 - O3_b	2.191(2)	N1 - Mn1 - N2	175.49(13)
S002 - C36	1.722(4)	N1 - Mn1 - O2_a	89.98(12)
S002 - C39	1.720(4)	N1 - Mn1 - O3_b	88.18(11)
O1 - C35	1.242(4)	N2 - Mn1 - O2_a	93.89(12)
O2 - C35	1.247(4)	N2 - Mn1 - O3_b	88.54(11)
O3 - C40	1.253(4)	O2_a - Mn1 - O3_b	167.42(9)
O4 - C40	1.250(4)	C36 - S002 - C39	91.58(17)
O1 - Mn1 - O9S	171.20(11)	Mn1 - O1 - C35	154.7(2)
O1 - Mn1 - N1	85.21(11)	C35 - O2 - Mn1_a	150.6(2)
O1 - Mn1 - N2	91.74(11)	C36 - S002 - C39	91.58(17)
O1 - Mn1 - O2_a	101.52(9)	Mn1 - O1 - C35	154.7(2)
C35 - O2- Mn1_a	150.6(2)	C40 - O3 - Mn1_b	136.0(2)
Mn1 - N1 - C1	121.9(3)	Mn1 - N1 - C5	121.9(3)

Symmetry-Code: a = 1-x, 1-y, 1-z; b = 2-x, 1-y, 1-z

6.2.4 UV-Visible and fluorescence experiments

A stock solution of **Mn-CP** (10^{-3} M) was prepared using 7.78 mg of **Mn-CP** to 10 mL 3:2 (v/v) acetonitrile and methanol solution. Moreover, NaCl, $MgCl_2$, $BaCl_2$, $ZnCl_2$, $CdCl_2$, $HgCl_2$, $CuCl_2$, $NiCl_2$, $CoCl_2$, $PbCl_2$, $PdCl_2$, $FeCl_3$, $CrCl_3$ and $AlCl_3$metal salts of fixed mass were dissolved to prepare 10^{-3} M solution. UV-Vis and fluorescence experiments were performed at 25 °C at different pH values taking 50 mM **Mn-CP** in water followed by addition of equivalent amount of solution of metal salts. The wavelengths evaluated in the UV-Vis experiment were used as the excitation wavelength for fluorescence study. The LOD value of **Mn-CP** was determined using the $3\sigma/M$ method, where σ and M are standard deviation and slope of calibration curve, respectively. Binding constant (K_{SV}) values were examined using Stern-Volmer equation: $I_0/I = K_{SV}[Q] + 1$, where [Q] and I_0/I are concentration of Pd^{2+} and emission intensities of **Mn-CP** in absence/ presence of Pd^{2+}, respectively.

6.2.5 Computational details

Physical and chemical properties of a coordination polymer depend on their structural (interaction ability, pores and pore size) and electronic features.[28,29] Band structure and band

gap are the most important parameters for understanding of electronics of the coordination polymer.[30,31] Here, the split between the valence band and the conduction band energy is the band gap where electron may not exist. Band structure is the range of energy levels where electrons may present and based on this, it can be divided into major two classes (i) direct band gap and (ii) indirect band gap.[32] In the case of materials having direct band gap, the momentum of the highest energy state of the valence band and the lowest energy state in the conduction band are equal. As a results, the vertical transition of electrons can be possible in such materials. The band properties of the coordinate polymer have been calculated with the help of CASTEP program with Linux codes.[33] In the case of Mn-CP, the Perdew-Burke- Ernzerh of (PBE) functional with generalized gradient approximation (GGA) was used for the calculations.[34] The structure of the complex in the unit cell was optimized using the Broyden-Fletcher-Goldfarb-Shannon (BFGS) algorithm. It was converged to > 0.001 eV A−1 through the Hellmann-Feynman force. The Koelling-Harmon method was used relativistic treatment. The additional convergence criteria for inter ionic displacement and the total energy were set to be 0.001 Å per atom and 1×10^{-5} eV per atom respectively. The ultrafine plane-wave cut off energy with the ultra-soft pseudo-potential scheme was utilized for the basis set.

5.3 Results and Discussion

The synthesized The synthesized Single crystal X-ray diffraction (SCXRD) measurements reveal that **Mn-CP** crystallizes in the triclinic space group *P*-1 with *Z* = 2. The asymmetric unit contains one Mn(II) ion, one tdc dianion, two nvp ligands, and one water. It further contains a DMF molecule in the crystal lattice. Two Mn(II) centres are joined by two tdc ligands to genereate 8-membered chelate ring composed of dimeric $[Mn_2(O_2CC)_2]$ unit. Each Mn(II) centre acquires distorted octahedral geometry and is appended with two nvp in axial position, while three carboxylate anions and aqua molecule design the equatorial plane. Here, the dimeric $[Mn_2(O_2CC)_2]$ units are connected via tdc ligands to generate a one-dimensional (1D) coordination network (**Figure 6.4a**). Interestingly, these 1D chains fabricate a three-dimensional (3D) supramolecular self-assembly through extensive hydrogen bonding and π···π interactions (**Figure 6.1**).

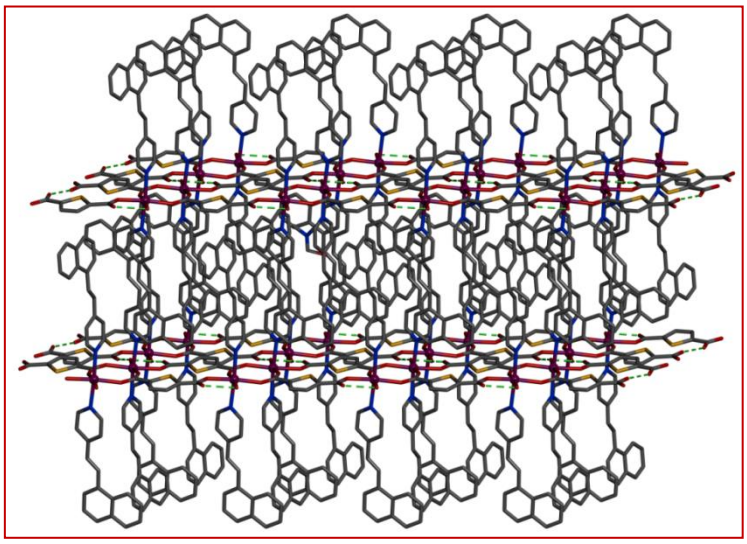

Figure 6.1 3D supramolecular architecture of **Mn-CP**.

In view of structural aspects, the construction of 3D aggregate directly regulates the material applications of this system.

The purity of the bulk material is confirmed by comparing its powder X-ray diffraction pattern (PXRD) with simulated data obtained from SCXRD (**Figure 6.2**).

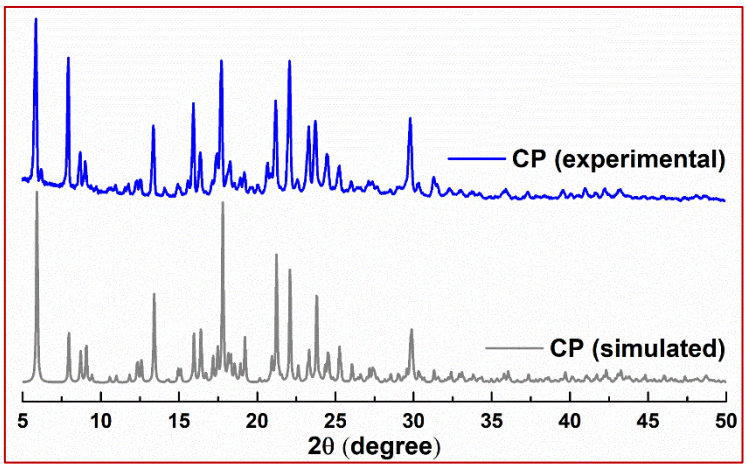

Figure 6.2 Powder XRD of simulated**Mn-CP** (grey)and experimental **Mn-CP** (blue).

The thermal stability is determined by thermogravimetric analysis (TGA), which shows that **Mn-CP** is fairly stable upto 140 ^{o}C (**Figure 6.3**).

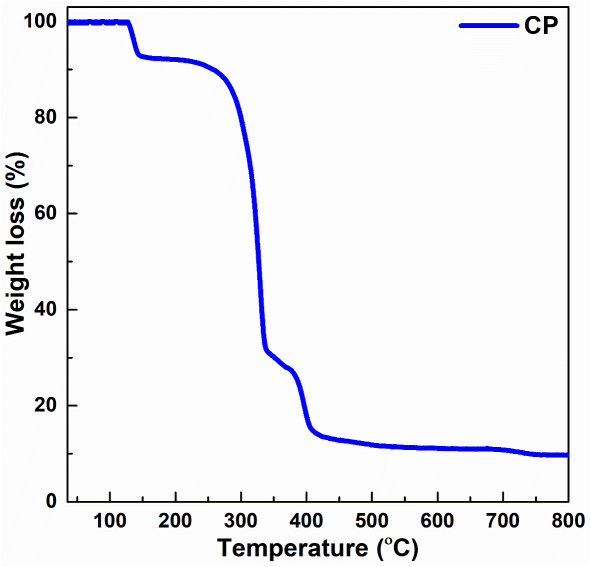

Figure 6.3 TGA plot of **Mn-CP**.

The initial weight loss at 140 °C is due to loss of lattice DMF molecule (experimental 9.5% and calculated 9.3%). The desolvated **Mn-CP** becomes stable upto250 °C and then ultimately decomposes to produce the residue MnO_2 (experimental 11.5% and calculated 11.3%). In addition, existence of magnetically active unpaired electron is supported by the EPR spectra of **Mn-CP** (**Figure 6.4b**).

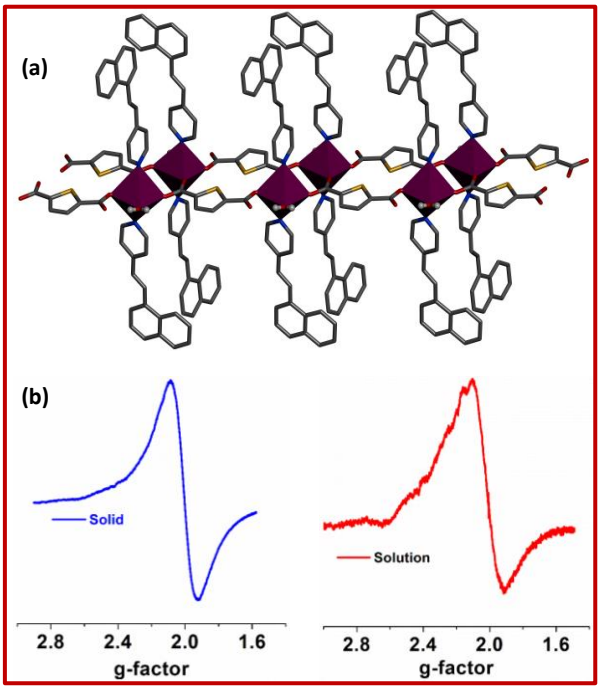

Figure 6.4 (**a**) Crystal structure of 1D chain ofMn-CP and (**b**) EPR spectra of Mn-CP

The structure of **Mn-CP** shows that both fused aromatic rings and >C=C< bonds of nvp ligands undergo $\pi\cdots\pi$ stacking, which offers a congenial environment to create π-cavity for selective sensing of soft metal ions via metal$\cdots\pi$ interactions (**Figure 6.5**).

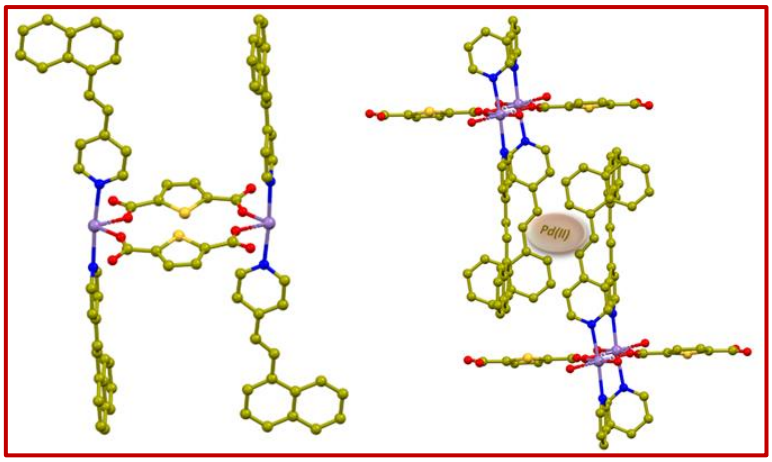

Figure 6.5 A view of 16-membered metallo-macrocycle and orientation 4-nvp ligands in a fashion to make a π-cavity.

Here, the absorption and emission behaviour of **Mn-CP** are found to be pH dependent (**Figure 6.6**).

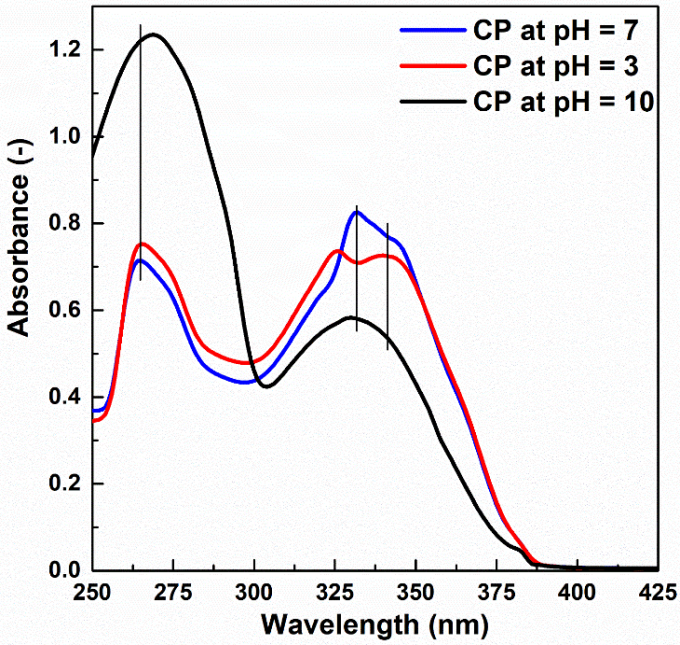

Figure 6.6 UV-vis spectra of **Mn-CP**at pH = 3, pH = 7 and pH = 10.

With increasing pH, the absorption maximum (λ_{abs}) of **Mn-CP** in acetonitrile-methanol (1:1, v/v) suspension is shifted to longer wavelength (λ_{abs}= 331 nm at pH = 3.0, and 342 nm at pH = 7.0, 10.0) (**Figure 6.6**), whereas the emission maximum is blue shifted (λ_{em}= 525 nm at pH = 2.0-4.0 to 450 nm at pH = 6.0-12.0) (**Figure 6.7**).

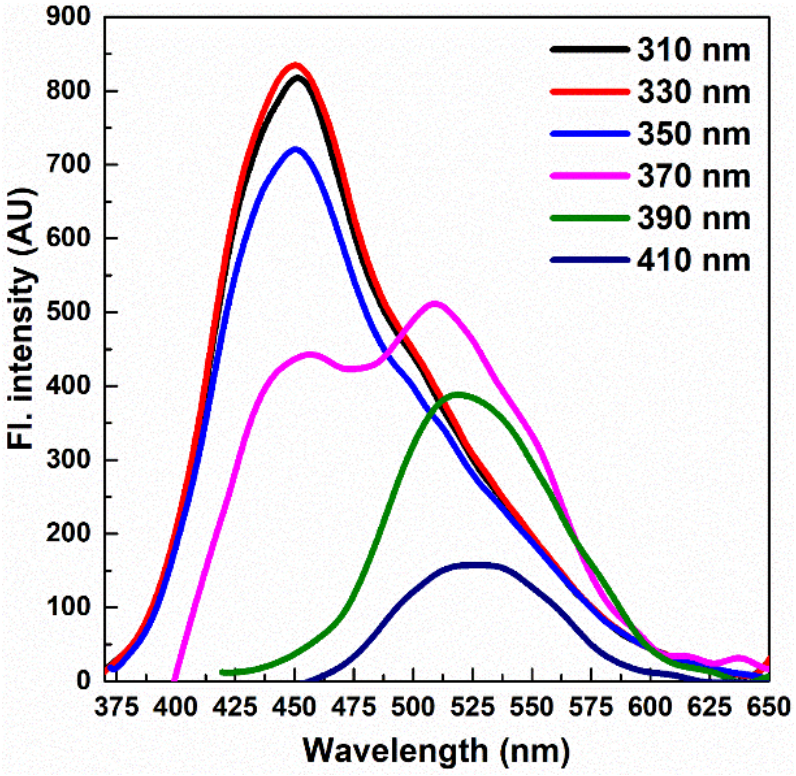

Figure 6.7 Excitation-dependent emission of **Mn-CP** at λ_{ex} = 310, 330, 350, 370, 390 and 410 nm;concentration of **Mn-CP** = 1×10^{-3}M in acetonitrile-methanol (1:1, v/v), excitation slit = 10 and emission slit = 10.

The **Mn-CP** shows excitation dependent emission (**Figure 6.7**), in which the CIE color coordinates are recorded at (x, y) = (0.17341, 0.18058), (0.1732, 0.1798), (0.17463, 0.18834), (0.19369, 0.31622), (0.24624, 0.55964) and (0.23745, 0.63511) at λ_{ex} = 310, 330, 350, 370, 390 and 410 nm, respectively, at pH = 7 (**Figure 6.9b**). Injection of emission energy from a luminophore into analyte may either enhance or cause quenching of the emission and has been used as convenient sensing process for the trace quantity detection of toxic heavy metal ions or hazardous substances in water.[35]

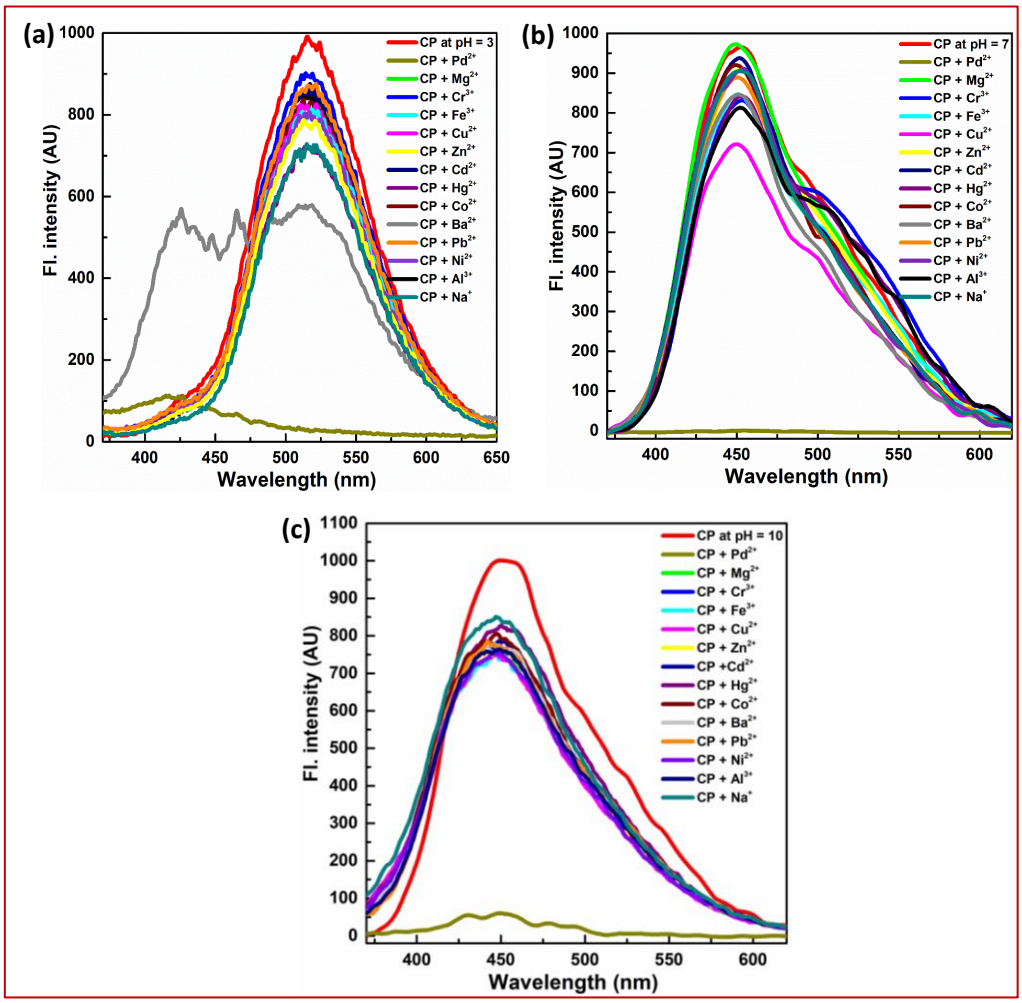

Figure 6.8 Pd^{2+} binding abilities of **Mn-CP** in presence of metal ions at (a) pH = 3, (b) pH = 7 and (c) pH = 10; concentration of **Mn-CP** = 1×10^{-3}M in acetonitrile-methanol (1:1, v/v), excitation slit = 10 and emission slit = 10.

Thus, the spectroscopic detection studies are performed using **Mn-CP** in acetonitrile-methanol (v/v, 1:1) suspension using different metal ions in aqueous medium in different pH (**Figure 6.8**).

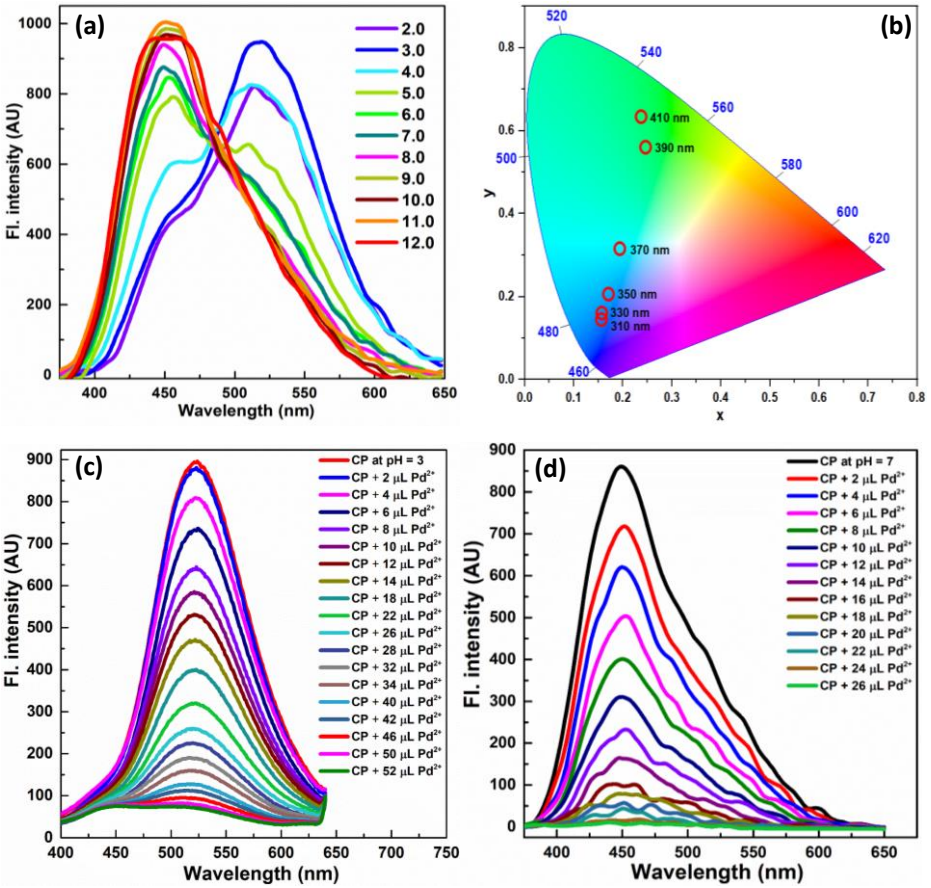

Figure 6.9 (**a**) Fluorescence spectra of Mn-CP at pH = 7.0 and pH = 3.0, (**b**) CIE plot of Mn-CP showing excitation wavelength-dependent emission at pH = 7; and fluorescence titration plots of Mn-CP using 2 μL of Pd^{2+} in every step at (**c**) pH = 3 and (d) pH = 7; concentration of Mn-CP = 1×10^{-3}Min acetonitrile-methanol (1:1, v/v), excitation slit = 10 and emission slit = 10.

It is observed that the emission intensities of **Mn-CP** are quenched drastically by adding aqueous solution of Pd^{2+}(**Figure 6.9c and 6.9d**). In contrast, the emission intensity remains unaltered in presence of other metal ions, such as Fe^{3+}, Al^{3+}, Cr^{3+}, Cd^{2+}, Zn^{2+}, Ni^{2+}, Co^{2+}, Cu^{2+}, Pb^{2+}, Hg^{2+}, Ba^{2+}, $Mg^{2+}$and Na^{+} in aqueous solution (**Figure 6.8 and 6.10**).

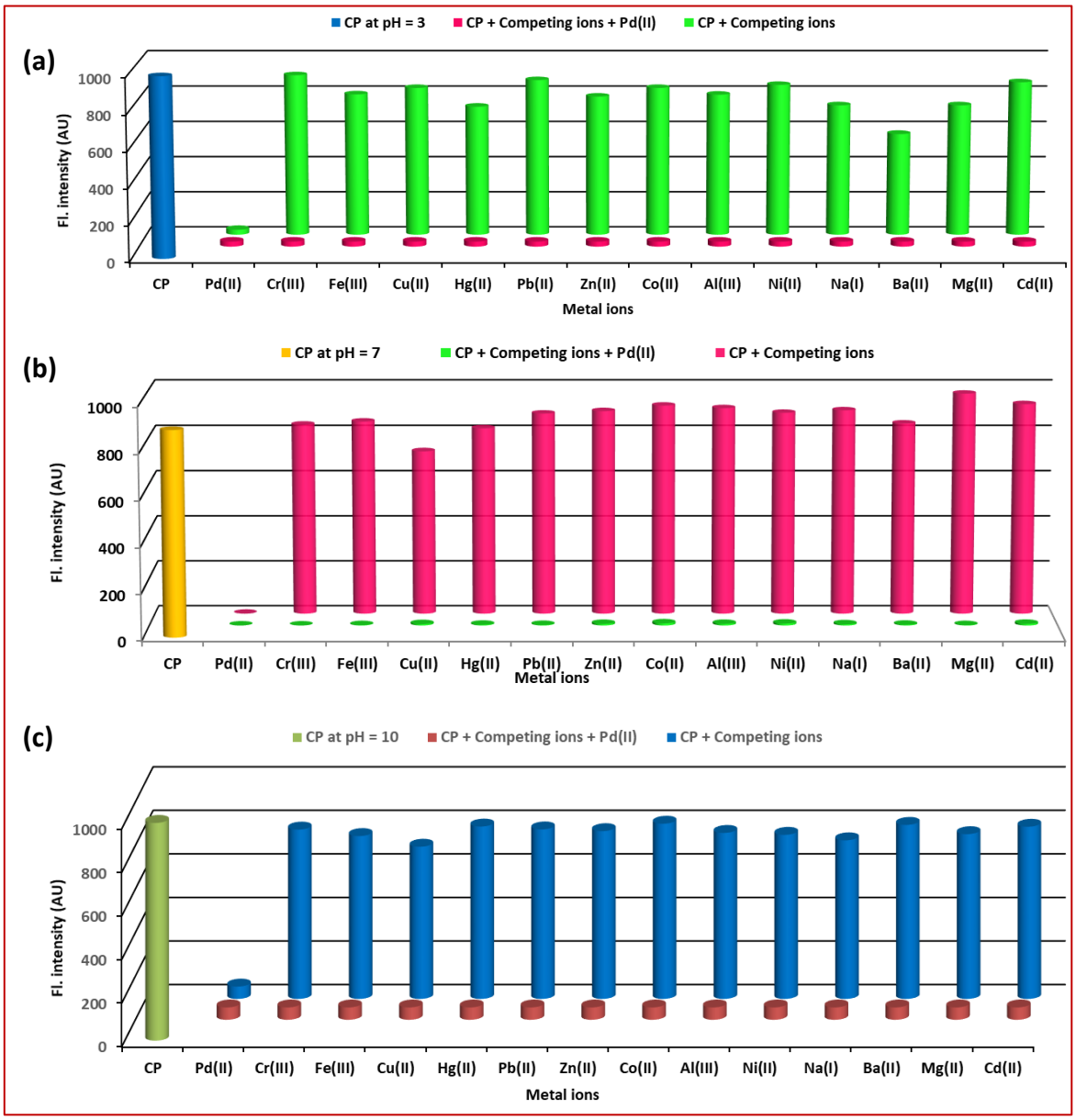

Figure 6.10 Pd^{2+}binding abilities of **Mn-CP** in mere/ simultaneous presence of metal ions at (a) pH = 3, (b) pH = 7and (c) pH = 10;concentration of **Mn-CP** = 1×10^{-3}M inacetonitrile-methanol (1:1, v/v), excitation slit = 10 and emission slit = 10.

In the fluorometric titration, the emission intensities of **Mn-CP** are decreasing gradually by the addition of 2 μL of Pd^{2+} in every step in aqueous medium (**Figure 6.9c** and **6.9d**).

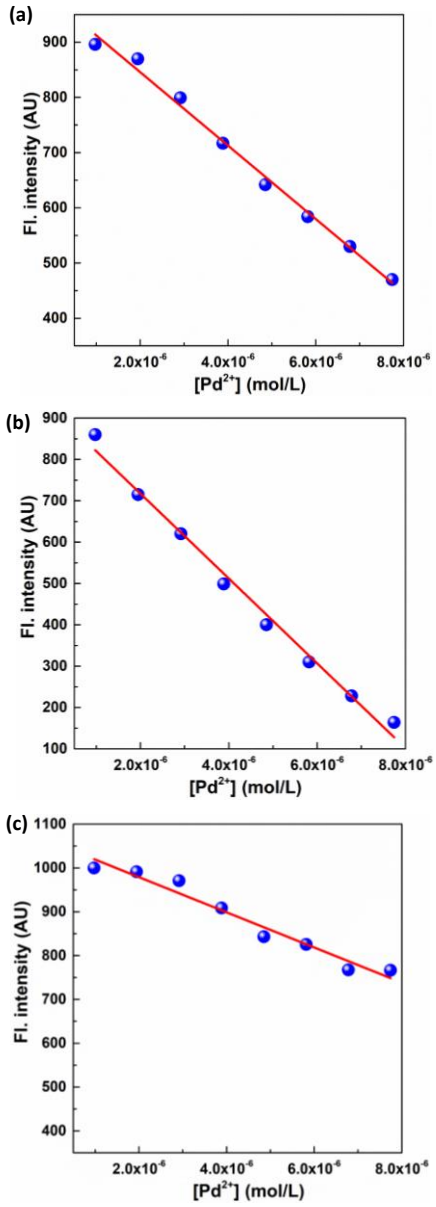

Figure 6.11 LODplots of **Mn-CP** at (**a**) pH = 3, (**b**) pH = 7and (**c**) pH = 10

The LODs of **Mn-CP** are calculated by using $3\sigma/M^{\ddagger}$ method and these are pH-dependent; 1.99 × 10^{-7} M (21.178 ppb) at pH = 3.0; 1.41 × 10^{-7} M (15.005 ppb) at pH = 7.0 and 3.38 × 10^{-7} M (59.940 ppb) at pH = 10.0(**Figure 6.11a-c**). The binding constants (calculated using Stern-Volmer (SV) equation)are also pH-dependent and the highest value (K_{SV} = 265533.02) is obtained at pH = 7.0 (**Figure 6.12a-c**) where σ= 4.45 (pH = 3.0); 4.80 (pH = 7.0); 4.50 (pH = 10.0) and M = 0.67 × 10^{8} (pH = 3.0); 1.02 × 10^{8} (pH = 7.0) and 4.00 × 10^{7} (pH = 10.0) respectively, (**Figure 6.11a-c**); K_{sv} = 89252.23 M^{-1} (pH = 3.0); 265533.02 M^{-1} (pH = 7.0) and 47753.91 M^{-1} (pH = 10.0).

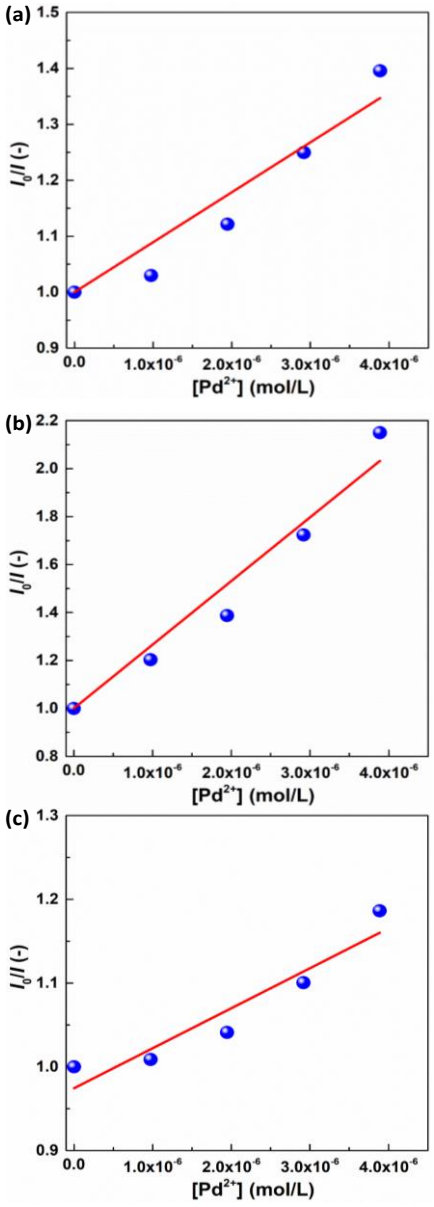

Figure 6.12 K_{sv} plots of **Mn-CP** at (**a**) pH = 3, (**b**) pH = 7 and (**c**) pH = 10

The decay profile of excited state of **Mn-CP** follows static and dynamic quenching process in presence of Pd^{2+} (**Figure 6.13a-c**).

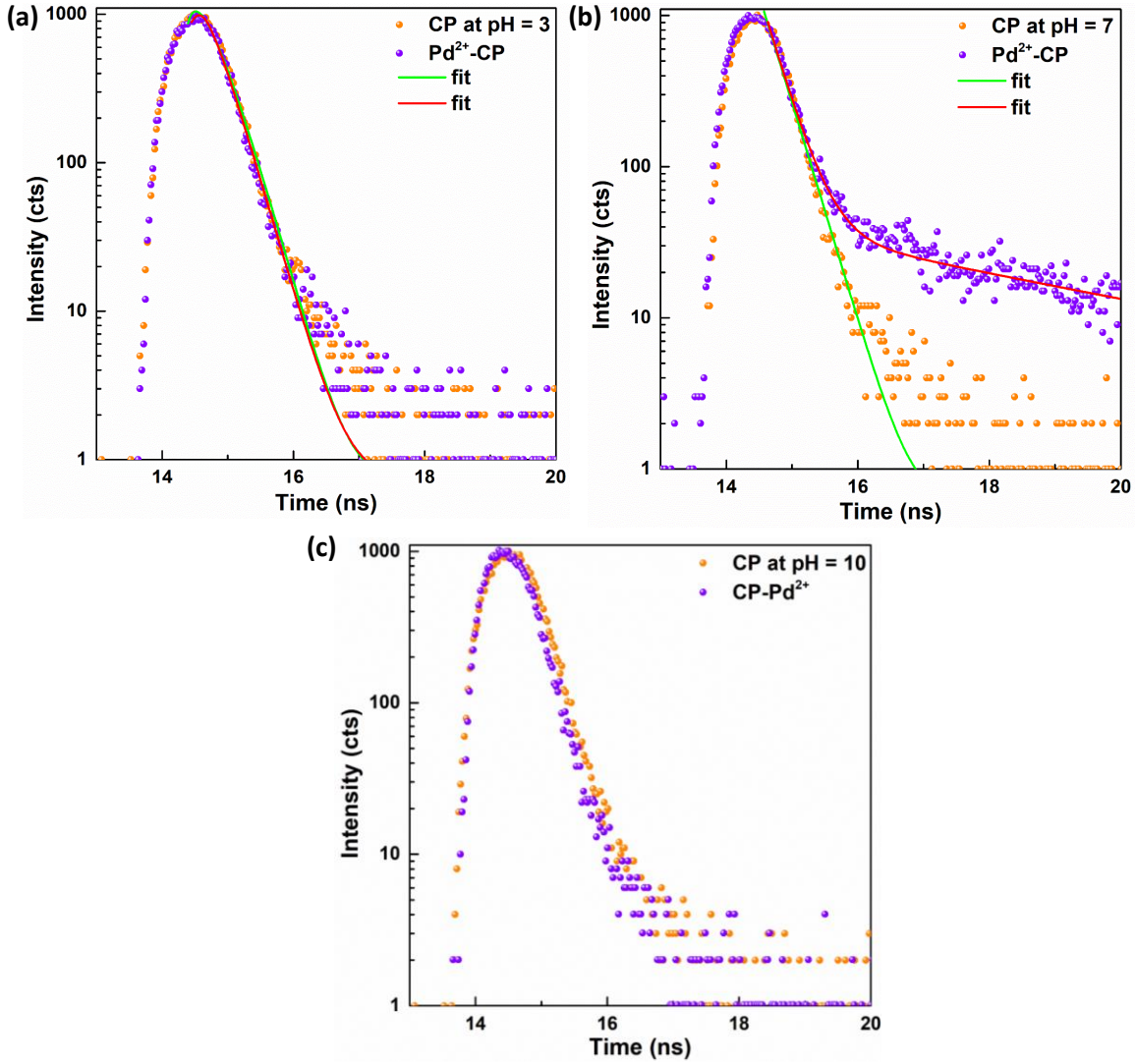

Figure 6.13 Fluorescence lifetimes of **Mn-CP**and Pd^{2+}-**Mn-CP** at (**a**) pH = 3, (**b**) pH = 7 and (**c**) pH = 10; concentration of **Mn-CP** = 1 × 10^{-3}M in acetonitrile-methanol (1:1, v/v), excitation slit = 10 and emission slit = 10.

The changes are also noted in UV-Vis studies (**Figure 6.14a-c**). The lifetime of excited **Mn-CP** is independent of pH (0.24 ns at pH= 3.0; 0.25 ns at pH = 7.0 and 0.24 ns at pH = 10.0); while it varies upon addition of Pd^{2+} (Pd^{2+}-**Mn-CP**) and the values are obtained as 0.21 ns at pH = 3.0; 0.42 ns at pH = 7.0 and 0.20 ns at pH = 10.0 (**Figure 6.14a-c**).

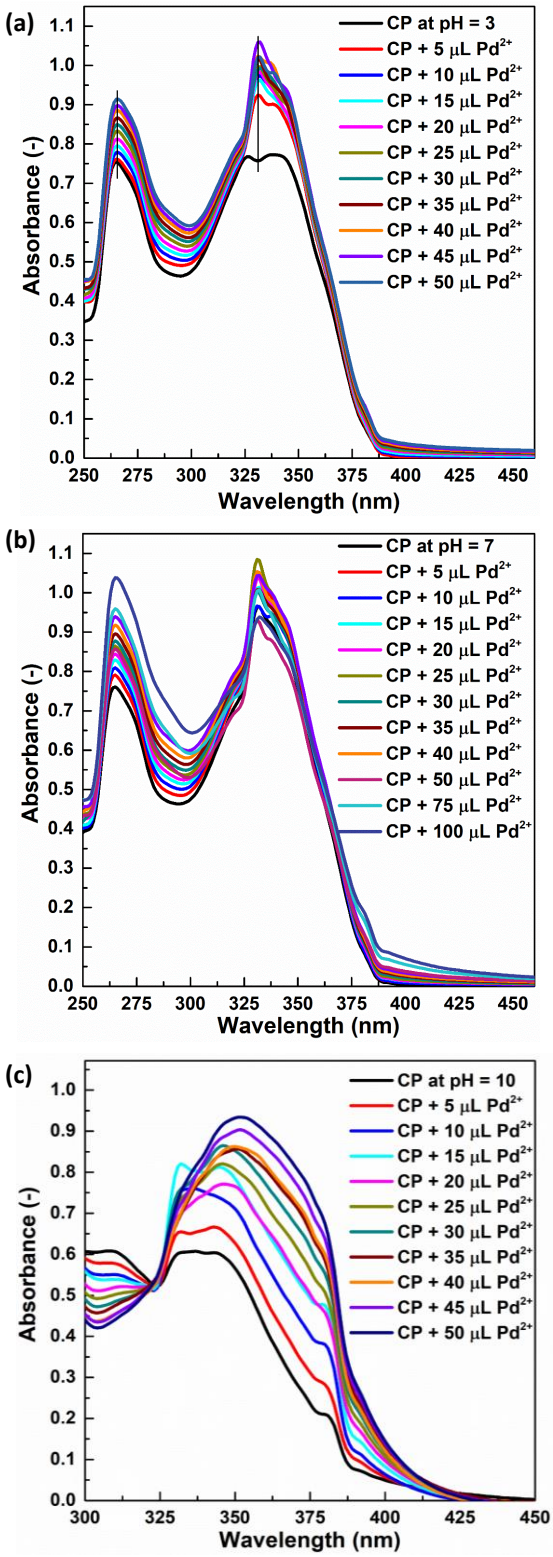

Figure 6.14 UV-vis spectra using variable concentrations of $Pd^{2+}$of **Mn-CP**at(**a**) pH = 3, (**b**) pH = 7 and (**c**) pH = 10; concentration of **Mn-CP** = 1×10^{-3}M in acetonitrile-methanol (1:1, v/v).

To get insight into the mechanism of Pd^{2+} binding of **Mn-CP**, FTIR studies have been performed in parent **Mn-CP** and Pd^{2+}-**Mn-CP**. *In situ* experiment reveals the complete obsolesce of strong peak at 1673 cm^{-1} in Pd^{2+}-**Mn-CP**, which confirms the strong interaction between >C=C< bond of nvp (**Mn-CP**) and Pd^{2+} ions *via* the formation of partial C-Cbonds (**Figure 6.15** and **Table 6.1**).[36]

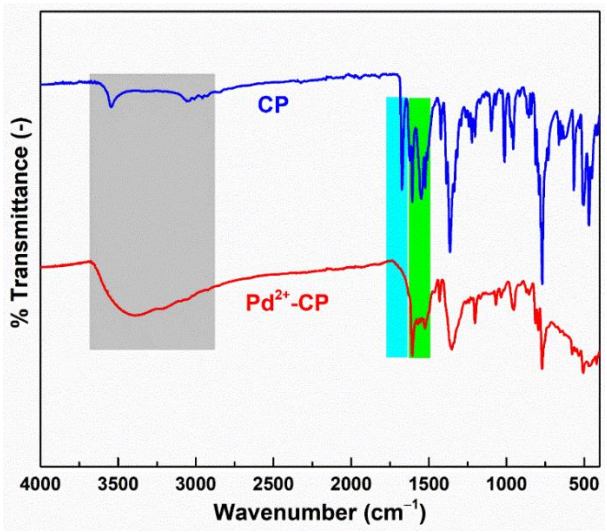

Figure 6.15 FTIR spectra of **Mn-CP**andPd^{2+}-**Mn-CP**

Table 6.3 FTIR analyses of **Mn-CP** and Pd^{2+}-**Mn-CP**.

Mn-CP	**Assignment**	**Pd^{2+}-Mn-CP**	**Assignment**
3544	O–H *str.* of H_2O	3391 (broadand intense peak)	The peaks become broad because of absorption of moisture. In addition, C–H *str.* of all types are present within the region.
3058	C–H *str.*		
1673	C=C *str.*of conjugated with aryls	Absent	The complete obsolesce of peaks for C=C *str.* (trans and conjugated) confirms the strong interaction of C=C with $Pd^{2+}$and conversion of C=C to C–C.

1622 and 1606	C=C *str.* of pyridine	1630 (shoulder) and 1607	The intensity of peak at 1622 cm^{-1} is reduced and shifted towards higher wavenumber because of reduction of extended conjugation via stronger interaction between C=C and Pd^{2+}.
1548	C=N *str.* of pyridine	1566	The peak shifted towards higher wavelength because of reduction of extended conjugation via interaction between C=C and Pd^{2+}.
1365 (sharp)	C–H *deformation*	1356 (broad)	C–H *deformation*
1222 (strong) and 1202	C–H deformation	1220 (weak) and 1202	C–H *deformation*
1098	C–H *deformation*	Absent	C–H *deformation*
957	C–H *deformation* vibration of *trans* substituted alkene	954	C–H *deformation* vibration of *trans* substituted alkene

Because of this interaction and partly disruption of extended conjugation, the peak at 1622 cm^{-1} related to the C=C *str.* of pyridine unit of **Mn-CP** shift to 1630 cm^{-1} in Pd^{2+}-**Mn-CP** (**Figure 6.15**). In this context, peak at 1548 cm^{-1} for C=N *str.* of pyridine unit of **Mn-CP** shift to 1560 cm^{-1} in Pd^{2+}-**Mn-CP**. In addition, the interaction between **Mn-CP** and Pd^{2+} affected *stretching* and *bending* vibrations of C-H. Accordingly, peaks at 3544 (O-H *str.*) and 3058 (C-H *str.*) cm^{-1} in **Mn-CP** appear as single broad peak at 3391 cm^{-1} (**Figure 6.15**). Additionally, the C-H deformation bands at 1365, 1222, 1202, 1098, and 957 cm^{-1} in **Mn-CP** alter in Pd^{2+}-

Mn-CP (**Table 1**). The TGA of Pd^{2+}-**Mn-CP** shows different pattern with respect to that of **Mn-CP** within 35-800 °C (**Figure 6.16**).

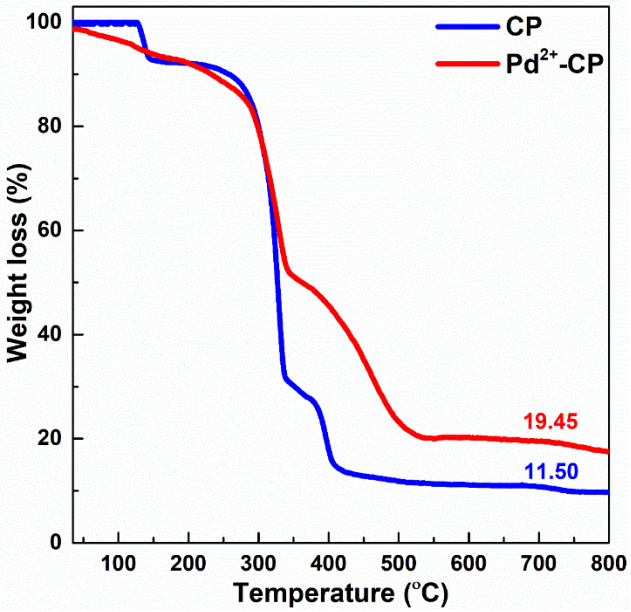

Figure 6.16 TGA plots of **Mn-CP** and Pd^{2+}-**Mn-CP**.

The interaction of Pd^{2+} ion with **Mn-CP** results restricted weight loss in the second stage. The weight loss decreases from 62.36% in **Mn-CP** to 42.36% in Pd^{2+}-**Mn-CP**. Importantly, in presence of Pd^{2+}, the degradation of main backbone of Pd^{2+}-**Mn-CP** continues up to 550 °C. Finally, within 550-800 °C, Pd^{2+}-**Mn-CP** associates with higher amount of non-degradable inorganic residue of 19.45% compared to **Mn-CP** (11.50%) (**Figure 6.16**).

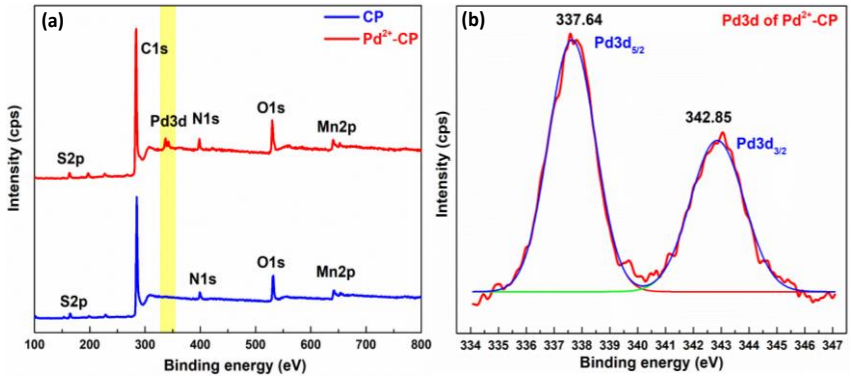

Figure 6.17 (a) XPS survey spectra of **Mn-CP** and Pd^{2+}-**Mn-CP** and Pd3d XPS spectrum of Pd^{2+}-**Mn-CP**.

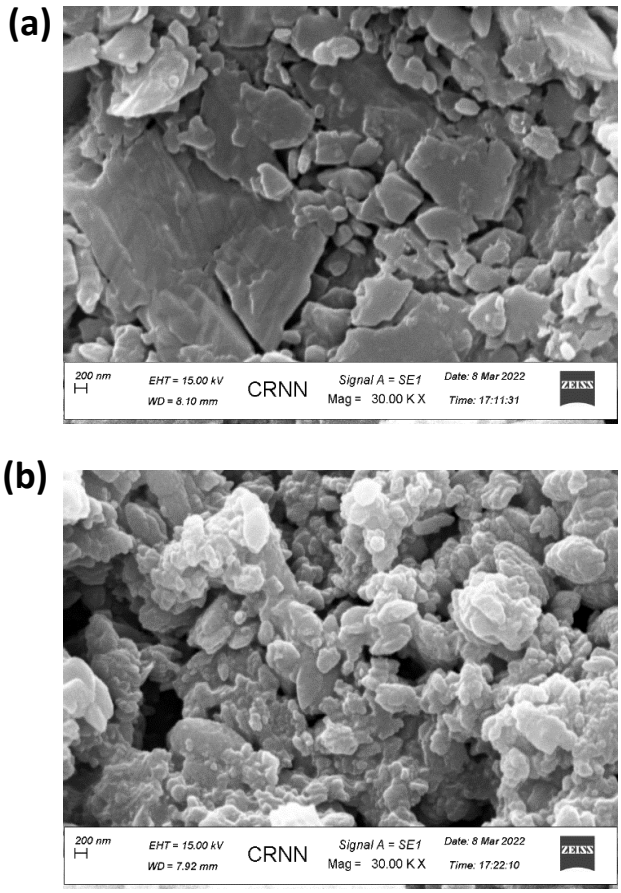

Figure 6.18 SEM photomicrographs of (**a**) **Mn-CP** and (**b**) Pd^{2+}-**Mn-CP** at magnification of 30 kx and electron high tension 15.00 kV.

The SEM images of **Mn-CP** and Pd^{2+}-**Mn-CP** (**Figure 6.18a** and **6.18b**) show that the surface microstructure of Pd^{2+}-**Mn-CP** is relatively rough and size is smaller than **Mn-CP** itself. It suggests the disruption of the surface upon intrusion of Pd^{2+} which indirectly supports the Pd-binding (**Figure 6.18b**). In XPS, the strong interaction between **Mn-CP** and Pd^{2+} infers from shifting of C1s, O1s and S2p binding energies from 284.56, 531.22 and 163.88 eV in **Mn-CP** to 284.38, 530.95 and 163.58 eV in Pd^{2+}-**Mn-CP**, respectively (**Figure 6.17a**; **Figure 6.19** and **Table 6.4**).

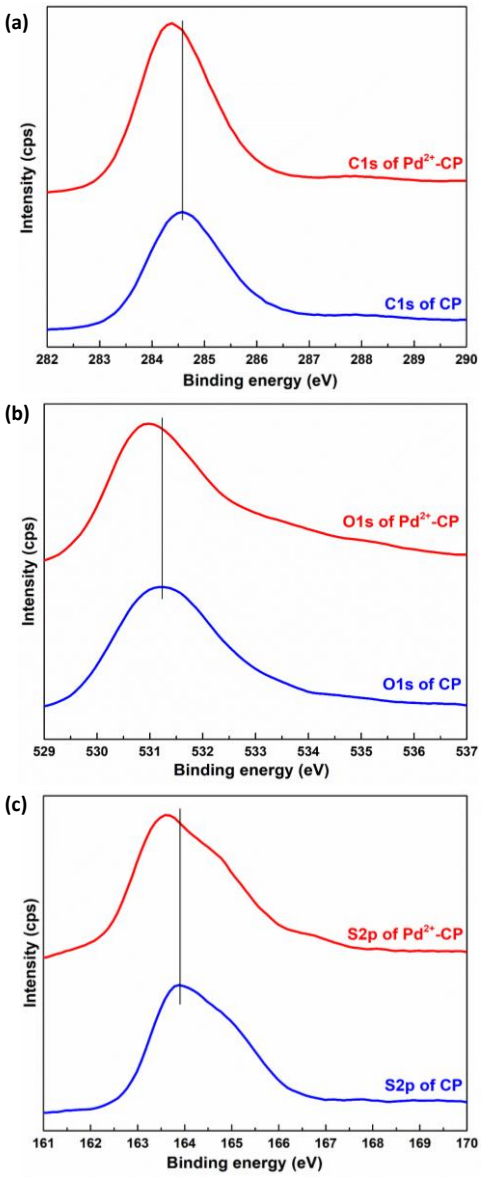

Figure 6.19 (a) C1s, (b) O1s and (c) S2p XPS spectra of **Mn-CP**andPd^{2+}-**Mn-CP**.

In this context, binding energies of Pd^{2+} in pure $PdCl_2$ appear at 338.40 ($3d_{5/2}$) and 343.70 ($3d_{3/2}$) eV shift[37] to lower values to 337.64 ($3d_{5/2}$) and 342.85 ($3d_{3/2}$) eV in Pd^{2+}-**Mn-CP**, respectively (**Figure 6.17b**).[38] However, nonparticipation of N1s and Mn2p in any kind of bonding is confirmed from unaltered binding energies (**Figure 6.20a** and **6.20b** and **Table 6.2**).

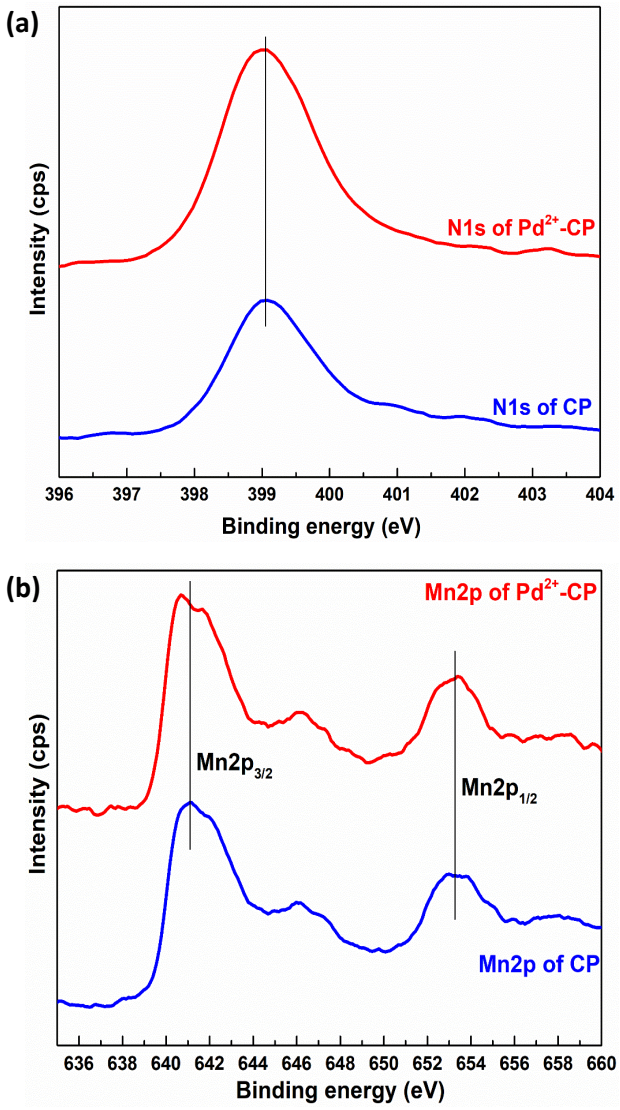

Figure 6.20 (**a**) N1s and (**b**) Mn2p XPS spectra of **Mn-CP** and Pd^{2+}-**Mn-CP**.

Table 6.4 XPS analyses of **Mn-CP** and Pd^{2+}-**Mn-CP**.

Element	**Orbital**	**Binding energy (eV) in Mn-CP**	**Binding energy (eV) in Pd^{2+}-Mn-CP**	**Assignment**
C	1s	284.56	284.38	The binding energy of C1s in Pd^{2+}-**Mn-CP** decreased by 0.18 eV after binding with Pd^{2+}

N	1s	399.04	399.03	Unaltered binding energy
O	1s	531.22	530.95	The binding energy of O1s in Pd^{2+}-**Mn-CP** decreased by 0.27 eV after binding with Pd^{2+}
S	2p	163.88	163.58	The binding energy of S2p in Pd^{2+}-**Mn-CP** decreased by 0.30 eV after binding with Pd^{2+}
Mn	$Mn2p_{3/2}$	641.10	641.00	Unaltered binding energy confirmed non-involvement of Mn in interaction.
	$Mn2p_{1/2}$	653.28	653.38	
Pd	$Pd3d_{5/2}$	338.40 (pure)	337.64	The increase in electron density in Pdwas confirmed from the significant lowering of $Pd3d_{5/2}$ binding energy in Pd^{2+}-**Mn-CP**.
	$Pd3d_{3/2}$	343.70 (pure)	342.85	The increase in electron density in Pdwas confirmed from the significant lowering of $Pd3d_{3/2}$ binding energy in Pd^{2+}-**CP**.

Together with the increased in electron density of metal centre as confirmed by XPS and complete obsolesce of peak at 1673 cm^{-1} in FTIR establish the strong interactions of **Mn-CP** with Pd^{2+} ions.

To get additional insights into the interaction between **Mn-CP** and Pd^{2+}, **Mn-CP** and Pd^{2+}-**Mn-CP** were computed theoretically to calculate band structures, band gaps and density of state (DOS).

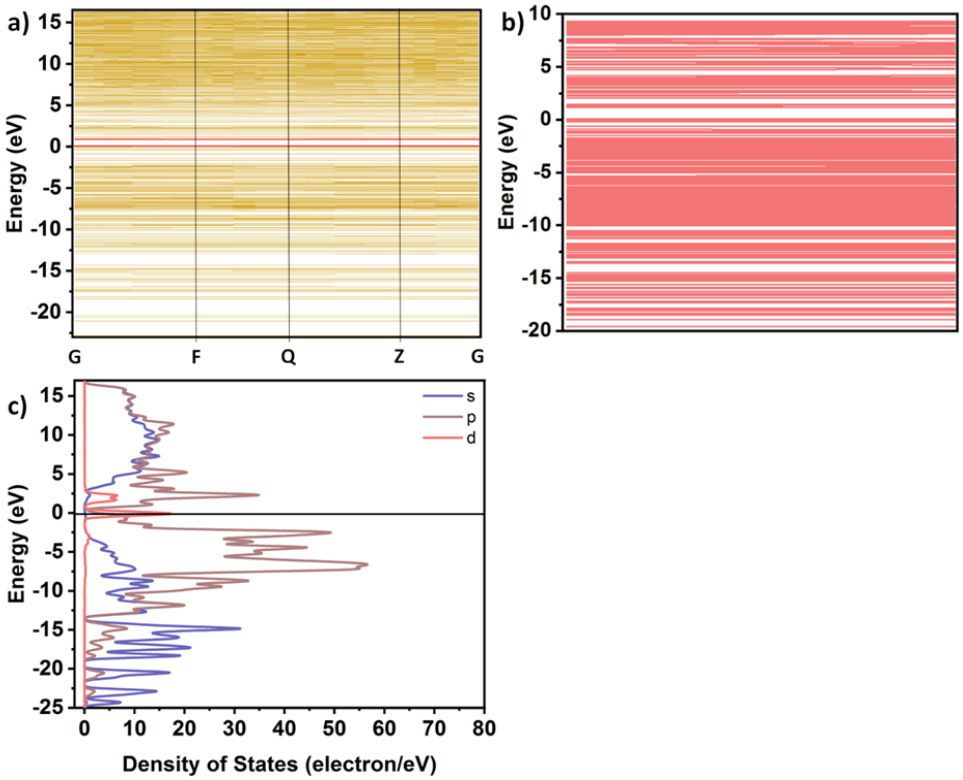

Figure 6.21 Energy levels distribution of (a) Mn-CP; (b) Pd2+-Mn-CPand (c) partial density of state of Mn-CP.

In **Mn-CP**, the band structure is spread over the energy spectrum from −25 to 17 eV. Such distribution of energy levels (**Figure 6.22a**) creates a narrow band gap of 0.81 eV, with maxima and minima of valence bands at 0.93 and 0.12 eV, respectively, which are lower with respect to silicon. Inaddition, both energy levels are located at the *Z* point. On contrary, the Pd^{2+}-**Mn-CP** is composed of large conduction band and small valence band (**Figure 6.21**).

Binding of Pd^{2+} with **Mn-CP** (via formation of π-complex) results band gap enhancement of 1.098 eV, because of stability of valence band maxima (0.072 eV) and instability of the valence

band minima (1.170 eV) (**Figure 6.22b**). Accordingly, the energy levels shift from *Z*-point in **Mn-CP** to F-point in Pd^{2+}-**Mn-CP**.

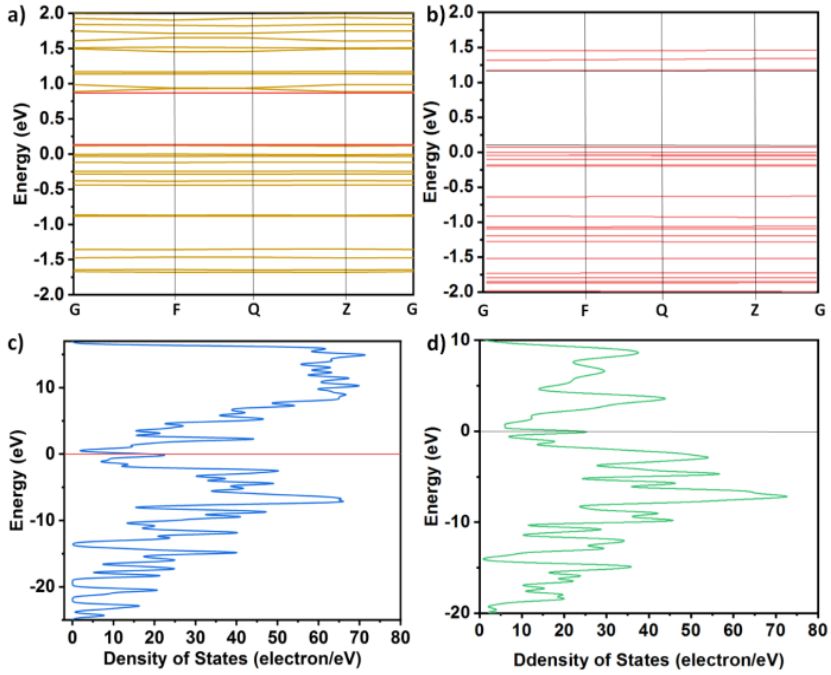

Figure 6.22 Zoomed form of energy levels distribution of band structure of (a) **Mn-CP** and (b) Pd^{2+}-**Mn-CP**; andDOS of (c) **Mn-CP**and (d) Pd^{2+}-**Mn-CP** system.

It is confirmed that the **Mn-CP** comprises of direct band gap and allows distribution of vertical electron transition (**Figure 6.22**). Accordingly, the higher energy of valence band maxima helps to interact with guests through electron donation, whereas lower energy of valence band minima helps to interact with guests by electron acceptance. Because of the low band gap, the **Mn-CP** becomes soft in nature (σ = 2.47 eV^{-1}) and interacts with soft acid Pd^{2+} through electron donation. The conduction band minima of **Mn-CP** is associated with significant contributions from 2s and 2p states of ligands and minor contribution from 3d states of metal as confirmed from the measurements of total DOS and partial DOS (**Figure 6.22c** and **6.22d**). The valence band maxima of **Mn-CP** are located mostly on the 3d state of metal and subordinately on the 2p state. The photo-physical properties of **Mn-CP** and the interaction between **Mn-CP** and Pd^{2+} metal ions are governed mainly by the 3d state of Mn(II) of **Mn-CP**. Thus, after binding with Pd^{2+} via formation of π-complex, DOS of **Mn-CP** is decreased drastically and has resulted damage of extended conjugation. This is one of the most important reasons for the quenching of fluorescence of **Mn-CP** in presence of Pd^{2+}.

5.4 Conclusion

In summary, an elusive nvp appended 1D Mn(II) CP has been prepared which shows pH and excitation dependent emission. The **Mn-CP** exhibits selective 'on-off' sensing of Pd^{2+} in aqueous medium even in the presence of thirteen competitive metal ions within wide ranges of pH. The lower LODs of 21.178, 15.005 and 59.940 ppb at pH = 3.0, pH = 7.0 and pH = 10.0, respectively, confirm the sensitivity of the material. The strong binding affinity between **Mn-CP** and Pd^{2+} has been confirmed by XPS and other characterization techniques, such as the highest K_{SV} value (265533.02 M^{-1}) at pH = 7.0 and DOS measurements by computational studies. To the best of our knowledge, this is the first example of Mn(II)-based CP that shows Pd^{2+} sensing in water with exceptionally low LOD values.

5.5 References

(1) Kielhorn, J.; Melber, C.; Keller D. and Mangelsdorf, I. Palladium–a review of exposure and effects to human health. *Int. J. Hyg. Environ. Health.* **2002**, *205*, 417-432.

(2) Kim, Y. M. and Yu, S. Palladium (0)-catalyzed amination, Stille coupling, and Suzuki coupling of electron-deficient aryl fluorides. *J. Am. Chem. Soc.* **2003**, *125*, 1696-1697.

(3) Beletskaya, I. P. and Cheprakov, A. V. The Heck reaction as a sharpening stone of palladium catalysis. *Chem. Rev.* **2000**, *100*, 3009-3066.

(4) Audisio, D.; Messaoudi, S.; Peyrat, J. F.; Brion, J. D. and Alami, M. A convenient and expeditious synthesis of 3-(N-substituted) aminocoumarins via palladium-catalyzed Buchwald–Hartwig coupling reaction. *Tetrahedron Lett.* **2007**, *48*, 6928-6932.

(5) Yusop, R. M., Unciti-Broceta, A., Johansson, E. M. V., Sanchez-Martin R. M. and Bradley, M. Palladium-mediated intracellular chemistry. *Nat. Chem.* **2011**, *3*, 239-243.

(6) Weiss, J. T.; Dawson, J. C.; Macleod, K. G.; Rybski, W.; Fraser, C.; Torres-Sanchez, C.; Patton, E. E.; Bradley, M.; Carragher N. O. and Unciti-Broceta, A. Extracellular palladium-catalysed dealkylation of 5-fluoro-1-propargyl-uracil as a bioorthogonally activated prodrug approach. *Nat. Commun*. **2014**, *5*, 3277.

(7) Bedford, R. B.; Cazin C. S. J. and Holder, D. The development of palladium catalysts for CC and Cheteroatom bond forming reactions of aryl chloride substrates. *Coord. Chem. Rev.* **2004**, *248*, 2283-2321.

(8) Mandal, R.; Garai, A.; Peli, S.; Datta P. K. and Biradha, K. Photoinduced Bending of Single Crystals of a Linear Bis- Olefin via Water- Templated Solid- State [2+ 2] Photopolymerization Reaction. *Chem. Eur. J.* **2020**, *26*, 396-400.

(9) Van Vaerenbergh, B.; Lauwaert, J.; Thybaut, J. W.; Vermeir P. and Clercq, J. D. Pd nanoparticle and molecular Pd^{2+} leaching pathways for a strongly acid versus strongly basic resin supported Pd nanoparticle catalyst in Suzuki coupling. *J. Chem. Eng.* **2019**, *374*, 576-588.

(10) Zhe, W.; Zhang, B.; Yang, S.; Yang, X.; Meng, F.; Zhai, L.; Li, Z.; Zhao, S.; Zhang G. and Qin, Y. Dual Pd^{2+} and Pd^{0} sites on CeO_2 for benzyl alcohol selective oxidation. *J. Catal.* **2022**, *414*, 385-393.

(11) Zhou, W.; Saran R. and Liu, J. Metal sensing by DNA. *Chem. Rev.* **2017**, *117*, 8272-8325.

(12) Melber, C.; Keller, D.; Mangelsdorf, I. Environmental Health Criteria 226; Palladium, World Health Organization: Geneva, 2002, 1−222.

(13) Cho D. G. and Sessler, J. L. Modern reaction-based indicator systems. *Chem. Soc. Rev.* **2009**, *38*, 1647-1662.

(14) Aljohani, E. T.; Shehata, M. R.; Alkhatib, F.; Alzahrani S. O. and Abu- Dief, A. M. Development and structure elucidation of new VO^{2+}, Mn^{2+}, Zn^{2+}, and Pd^{2+} complexes based on azomethine ferrocenyl ligand: DNA interaction, antimicrobial, antioxidant, anticancer activities, and molecular docking. *Appl. Organomet. Chem.* **2021**, *35*, e6154.

(15) Shengyi, G.; Zhou, E.; Liu, Y.; Gui, Z. and Feng, G. A Pd^{2+}-free near-infrared fluorescent probe based on allyl ether isomerization for tracking CORM-3 with high contrast imaging in living systems. *Anal. Chem.* **2022**, *94*, 2042-2047.

(16) Bhanja, A. K.; Mishra, S.; Saha K. D. and Sinha, C. A fluorescence 'turn-on' chemodosimeter for the specific detection of Pd^{2+} by a rhodamine appended Schiff base and its application in live cell imaging. *Dalton. Trans.*, **2017**, *46*, 9245-9252.

(17) Chakraborty, P.; Rana, A.; Mukherjee, S. and Biswas, S. Metal–organic-framework-based chemosensor for ultrafast and ultrasensitive detection of Pd^{2+} ions in water, real specimens, and test strips. *Inorg. Chem.* **2023**, *62*, 802-809.

(18) Bhunia, S.; Sahoo, D.; Maity, S.; Dutta, B.; Bera, S.; Manik, N. B. and Sinha. C. Aminoisophthalate Bridged Cd (II)-2D Coordination Polymer: Structure Description, Selective Detection of Pd^{2+} in Aqueous Medium, and Fabrication of Schottky Diode. *Inorg. Chem.* **2023**, *62*, 11976-11989.

(19) Keum, D.; Kim, S. and Kim, Y. A robust luminescent Ba (II) metal–organic framework based on pyridine carboxylate ligand for sensing of small molecules. *Chem. Comm.* **2014**, *50*, 1268-1270.

(20) Liu, Q.; Liu, C.; Cai, S.; He, S.; Zhao, L.; Zeng X. and Gong, J. A highly sensitive sensor for colorimetric detection of palladium (II) in lysosomes and its applications. *Dalton Trans.* **2022**, *51*, 3116–3121.

(21) Bera, S.; Dutta, B.; Mandal, D.; Sinha C. and Mir, M. H. A Dual Functional 2D MOF Exhibiting Rare Photosalient Effect as well as Selective Pd (II) Sensing in Aqueous Medium. *Inorg. Chem.* **2022**, *61*, 13244-13249.

(22) Dutta, B.; Bera, S.; Bairy, G.; Shit, M.; Khanra, S.; Sinha C. and Mir, M. H. Exploitation of a series of Zn (II)-coordination polymers for Pd (II)-detection in aqueous medium. *ES Energy. Environ.* **2022**, *16*, 74-81.

(23) Mir, M. H.; Bera, S.; Khan, S.; Maity, S.; Sinha C. and Dutta, B. Sunlight assisted SCSC dimerization of a 1D coordination polymer impacts the selectivity of Pd (II) sensing in water. *Chem. Comm.* **2021**, *57*, 6197-6200.

(24) Dutta, B.; Debsharma, K.; Dey. S.; Naaz, S.; Sinha C. and Mir, M. H. Designing of Interdigitated Coordination Polymer for Fluorogenic Sensing of Pd (II) in Water with Reversible Nonphase Mechanochromism. *Adv. Mater. Interfaces*, **2022**, *9*, 2201120.

(25) Lakowicz, J. R. "Principles of Fluorescence Spectroscopy", 3rd Edition, 2006, Springer.

(26) Qin, Y.; She, P.; Huang, X.; Huangand, W. and Zhao, Q. Luminescent manganese (II) complexes: Synthesis, properties and optoelectronic applications. *Coord. Chem. Rev.* **2020**, *416*, 213331.

(27) Sheldrick, G. M. SHELXT–Integrated space-group and crystal-structure determination. *Acta Crystallogr. A: Found. Adv.* **2015**, *71*, 3-8.

(28) Materazzi, S. Coordination Compounds and Inorganics. In Handbook of Thermal Analysis and Calorimetry . *Elsevier Science BV.* **2008**, *5*, 439-502.

(29) Batten, S. R.; Champness, N. R.; Chen, X. M.; Garcia-Martinez, J.; Kitagawa, S.; Öhrström, L.; O'keeffe, M.; Paik Suh, M. and Reedijk, J. Terminology of metal–organic frameworks and coordination polymers (IUPAC Recommendations 2013). *Pure Appl. Chem.* **2013**, *85*, 1715-1724.

(30) Okubo, T.; Himoto, K.; Tanishima, K.; Fukuda, S.; Noda, Y.; Nakayama, M.; Sugimoto, K.; Maekawa, M. and Kuroda-Sowa, T. Crystal structure and band-gap engineering of a semiconducting coordination polymer consisting of copper (I) bromide and a bridging acceptor ligand. *Inorg. Chem.* **2018**, *57*, 2373-2376.

(31) Prabu, M.; Asha, K. S.; Sinha, M.; Poduval, A. and Mandal, S. The structural diversity, band gap energy and photoluminescence properties of thiophenedicarboxylate based coordination polymers. *CrystEngComm.* **2016**, 18, 536-543.

(32) Cox, P. A. Transition metal oxides: an introduction to their electronic structure and properties. Oxford university press. **2010**, 27.

(33) Clark, S.; Segall, M.; Pickard, C. and Hasnip, P. MI ARTICLE Journal Name Probert, K. Refson and MC Payne. *Z. Kristallogr.–Cryst. Mater*. **2005**, *220*, 567-570.

(34) Perdew, J. P. and Wang, Y. Accurate and simple analytic representation of the electron-gas correlation energy. *Phys. Rev. B*. **1992**, *45*, 13244.

(35) Chonamada, T. D.; Sharma, B.; Nagesh, J.; Shibu, A.; Das, S.; Bramhaiah, K.; Rajendar, N.; Johnand; N. S. and Santra, P. K. *ChemistrySelect*. **2019**, *46*, 13551-13557.

(36) Ghosh, S.; Steinke, F.; Rana, A.; Alam, M. and Biswas, S. A Metal- Organic Framework with Allyloxy Functionalization for Aqueous- Phase Fluorescence Recognition of Pd (II) Ion. *Eur. J. Inorg. Chem.* **2021**, *2021*, 3846-3851.

(37) Militello M. C. and Simko, S. J. Palladium chloride ($PdCl_2$) by XPS. *Surf. Sci. Spectra*. **1994**, *3*, 402-409.

(38) Lu, Y.; Liang, Y.; Zhao, Y.; Xia, M.; Liu, X.; Shen, T.; Feng, L.; Yuan N. and Chen, Q. Fluorescent test paper via the in-situ growth of COFs for rapid and convenient detection of Pd (II) ions. *ACS Appl. Mater. Interfaces*. **2021**, *13*, 1644-1650.

Chapter 7

Summary of the Research Work

The research in chemical science is encompassing all the issues related to life, society and civilization such as – power crisis, job opportunities, health and medicine, environmental remediation etc. Keeping these issues in mind materials are developed to manifest civilization and to maintain sustainable development goals (SDGs). Despite of numerous materials appear till date, coordination polymeric (CP) compounds are at the front line for addressing almost all the issues related to SDGs. Therefore, design and structural characterization of CPs or related material and exploration of their activity are of prime importance (**Chapter-1**). The confirmation of the structure of molecules are carried out by Single Crystal X-ray Diffraction (SCXRD) measurements along with other spectroscopic studies (UV-Vis, FTIR, Mass, NMR, PXRD, Fluorescence). Thermal stability has been assessed by DTA/TGA. Electrochemical studies determine the redox state of the matter. Current dissertation describes a review on CPs and their characterization, exploration of properties and defines the research gap. In this research work the CPs of Mn(II) (d^5) and Zn(II) (d^{10}) have been studied using N and O donor bridging ligands. The coordination polymers (CPs) will be explored for their use in the fabrication of the electronic devices having photo-responsibility, biological applications with respect to different cell lines and anticancer efficiency, optical sensors in presence of different competitive analysis. Metal salt and organic linkers are used for the synthesis of CPs as **Table 7.1**.

In Chapter 2, Zn(II) based CP of tdc^{2-} (2,5-thiophene dicarboxylate) and pich (Pyridine-4-carboxaldehyde isonicotinoyl hydrazine), $\{[Zn_2(tdc)_2(pcih)_2]_n\}$(**1**) has been used to design Schottky Diode barrier (band gap 3.74 eV) and shows high electrical conductivity (2.21×10^{-5} S cm^{-1}) which has been improved upon light irradiation (6.36×10^{-5} S cm^{-1}). The material shows promising anticancer activity against MDA-MB-231 cancer cells.

In Chapter 3, the structure determination of $\{[Mn_2(tdc)_2(pcih)_2(EtOH)]_n\}$ (**2**) approves a 3D supramolecular architecture. Magnetic measurement shows week anti-ferromagnetism ($\chi_M T$, 9.41cm^3Kmol^{-1} at 300 K). The band gap of **2**, 3.72 eV, lies in semiconducting region and determines the conductivity 3.42×10^{-5} Sm^{-1}.

A 3D network, $[Zn(mes)(pcih)(H_2O)_2]_n$, (**3**) (**Chapter 4) (**mes^{2-} = mesaconate), has been structurally established and the Tauc's plot determines the band gap 3.62 eV in the semiconducting region, The electrical conductivity is 2.98×10^{-4} Sm^{-1} in the dark and 7.01×10^{-4} Sm^{-1} in the light.

Crystal structure of $[Mn_2(aisp)_3(pcih)_2(solvent)]_n$ (**4**) ($aisp^{2-}$ = 5-aminoisophthalate) (**Chapter**

5) is 3D CP and the electrical conductivity is $1.57 \times 10^{-6}\ m^2V^{-1}s^{-1}$. The material shows anticancer activity against four cancer cell lines (HeLa, PC3, MDA-MB 231, and A549). The loading and delivery of Diclofenac Sodium (DMNa) shows that at pH, 1.2 only 8% drug release while 87% delivery is noted at pH 7.4 within a 30-hour period.

The paramagnetic Mn(II)-based coordination polymer (**Chapter 6**) acts as pH-dependent emitting material [λ_{em}= 525 nm (pH = 2.0-4.0) and 450 nm (pH = 5.0-12.0)]. The emission is quenched by Pd^{2+} in aqueous medium in presence of other thirteen cations with reasonably low pH-dependent limits of detection [21.178 ppb (pH= 3), 15.005 ppb (pH = 7.0) and 59.940 ppb (pH = 10.0)]. The material may be useful for regulating heavy metals in the environment.

Table 7.1 Metal salt and organic linkers are used for the synthesis of CPs.

Chapter	Metal Salt	Organic Linker	Single Unit of CPs
2.	$Zn(NO_3)_2$, $6H_2O$	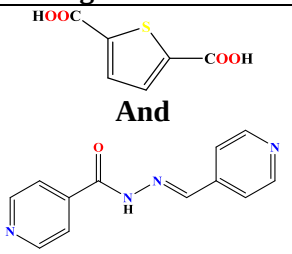	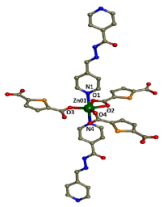
3.	$Mn(NO_3)_2$, $6H_2O$	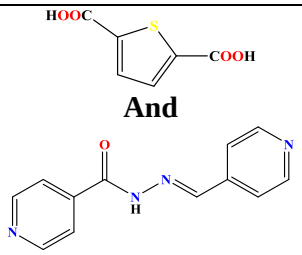	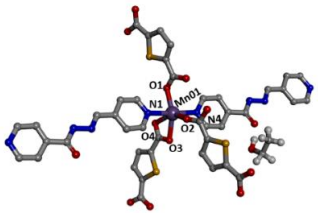
4.	$Zn(NO_3)_2$, $6H_2O$	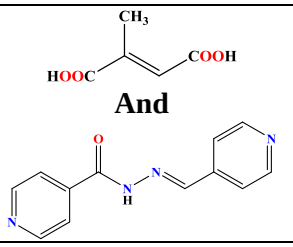	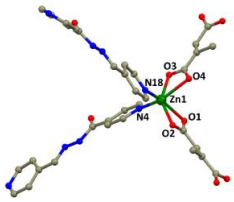
5.	$Mn(NO_3)_2$, $6H_2O$	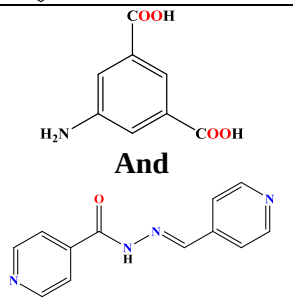	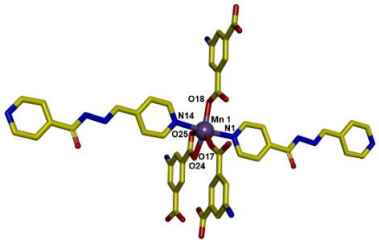
6.	$Mn(NO_3)_2$, $6H_2O$	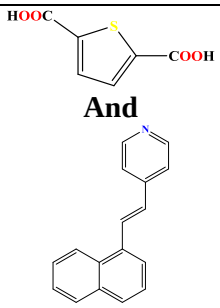	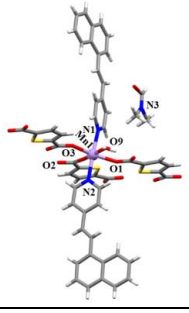

List of Publications

1. **Shit, M.**; Paul, S.; Chatterjee, T.; Dutta, B. and Sinha, C. Towards Design of Energy Efficient Semiconducting Material: An Example of 1D Cd (II)-2, 5-thiophene dicarboxylato Co-ordination Polymer. ***ES energy environ.*** **2022**, *16*, 40-46.

2. **Shit, M**.; Dey, A.; Das Mahapatra, A.; Dutta, B.; Naskar, K.; Ray, P.P. and Sinha, C. Supramolecular assembly of an Au (III) complex of 2- (3- phenyl- 1H- 1, 2, 4- triazol- 5- yl) pyridine: Structure, biological studies and charge transportation. ***Appl. Organomet. Chem.*** **2022**, *36*, p.e6754.

3. **Shit, M.**; Sahoo, D.; Dutta, B.; El Fallah, S.; Kundu, A.; Manik, N. B. and Sinha, C. Exploration of Variable Temperature Magnetism and Electrical Properties of a Pyridyl-isonicotinoyl Hydrazone Bridged Three-Dimensional Mn-Metal–Organic Framework with a Thiophene Dicarboxylato Link. ***Cryst. Growth Des.*** **2022**, *22*, 7143-7152.

4. **Shit, M.**; Das, P.; Paul, S.; Samanta, A.; Aziz, S.M.; Ray, P. P. and Sinha, C. In quest of New Energy Material: 3D Mn(II)-coordination Polymer, the Schottky Device and Theoretical Interpretation. ***ES Mater. Manuf.*** **2022**, *19*, 804.

5. **Shit, M.**; Karan, A. K.; Sahoo, D.; Manik, N. B.; Dutta, B. and Sinha, C. Strategy for the improvement of electrical conductivity of a 3D Zn (ii)-coordination polymer doubly bridged by mesaconato and pyridyl-isonicotinoyl hydrazide based Schottky diode device. ***New J. Chem.*** **2023**, *47*, 5922-5929. Dutta, B.; Bera, S.;Bairy, G.;

6. **Shit, M.**; Halder, S.; Dey, A.; Dutta, B.; Chanthapally, A.; Jana, K. and Sinha, C. Pyridyl-Isonicotinoyl Hydrazone-Bridged Zn (II) Coordination Framework with Thiophenedicarboxylato Link: Structure, Biological Activity, and Electrical Conductivity. ***Inorg. Chem.*** **2023**, *62*, 19937-19947.

7. **Shit, M**.; Karan, A.K.; Maity, S.; Slawin, A.M.; Manik, N.B.; Dutta, B. and Sinha, C. Succinato-bridged Cd (II)-nicotinylhydrazone 3D coordination polymer: structure, photoconductivity and computational studies. ***J. Coord. Chem.*** **2024**, 1-13.

8. **Shit, M**.; Halder, S.; Manna, K.; Karan, A.K.; Samanta, A.; Manik, N.B.; Pal, S.; Jana, K. and Sinha, C. Mn (II) 3D Coordination Framework with Mixed 5-

Aminoisophthalato and Pyridyl-isonicotinoyl Hydrazone Bridges: Structure, Electrical Conductivity, Anticancer Activity, and Drug Delivery. ***ACS Appl. Polym. Mater.*** **2024**.

9. Dutta, B.; Bera, S.; Bairy, G.; **Shit, M.**; Sinha, C.; Khanra, S. and Mir, M. H. Exploitation of a series of Zn (II)-coordination polymers for Pd (II)-detection in aqueous medium. ***ES energy environ.*** **2022**, *16*, 74-81.

10. Ghosh, S.; Paul, S.; Halder, S.; **Shit, M.**; Karmakar, A.; Nandi, J.B.; Jana, K. and Sinha, C. Trace level CN− measurement by 'turn-on'emission using Coumarinyl-Benzothiazolyl Schiff base probe in living and non-living environment. ***J. Indian Chem. Soc.*****2023**,*100*, 100957.

11. Paul, S.; Dutta, B.; Das, P.; Halder, S.; **Shit, M.**; Ray, P.P.; Jana, K. and Sinha, C. Double advantages of 2D coordination polymer of coumarinyl- pyridyl Schiff base decorated Zn (II): The fabrication of Schottky device and Anti- carcinogenic activity. ***Appl. Organomet. Chem.*****2023,***37*, e7160.

Right and Permission:

Chapter 1:

Figure reprinted with permission from *Angew. Chem. Int. Ed.* **2020**, *59*, 2-15. Copyright 2020: Wiley. (**Figure 1.4 and Ref. No-33**)

Figure reprinted with permission from *Angew. Chem. Int. Ed.* **2020**, *59*, 6652-6664. Copyright 2020: Wiley. (**Figure 1.6 and 1.7 and Ref. No-57**)

Figure reprinted with permission from *CrystEngComm.* **1999**, *20*, 6082-6087, Copyright 1999: Royel Chemical Society. (**Figure 1.8 and Ref. No-64**)

Figure reprinted with permission from *Nature.* **2021**, *13*, 191–199. Copyright 2021: Springer nature. (**Figure 1.12 and Ref. No-87**)

Chapter 2:

Reprinted (adapted) with permission from *Inorg. Chem.* **2023**, *62*, 19937-19947. Copyright 2023: American Chemical Society.

Chapter 3:

Reprinted (adapted) with permission from *Cryst. Growth Des.* **2022**, *22*, 7143-7152. Copyright 2022: American Chemical Society.

Chapter 4:

Reprinted (adapted) with permission from *New J. Chem.* **2023**, *47*, 5922-5929. Copyright 2023: Royal Society of Chemistry.

Chapter 5:

Reprinted (adapted) with permission from *ACS Appl. Polym. Mater.* **2024**, *6*, 2637-2648. Copyright 2024: American Chemical Society.

List of Conferences Attended:

1. **Poster Presentation:** International Conference on Recent Trends in Chemical Sciences – 2022 (RTCS 2022), December 16-18, 2022, IIT(ISM) Dhanbad, India.
2. **Poster Presentation:** 31st CRSI National Symposium & CRSI-ACS Symposium Series in Chemistry (CRSI NSC-31), July 6-8, 2023, NIT Rourkela, India.
3. **Oral Presentation:** Diamond Jubilee Celebration and International Conference ESMAC-2023, November 18-20, 2023, KIIT University, Odisha & CSIR-IMMT, India.
4. **Oral Presentation:** 6th Regional Science and Technology Congress, 2023-24, December 12-13, 2023, Sidho-Kanho-Birsha University, Purulia, West Bengal, India.

Awards and Recognition:

1. CSIR-NET JRF in Chemical Sciences, December 2017.
2. Indian Photobiology Society Research Excellent Award for Best Oral Presentation in Diamond Jubilee Celebration and International Conference ESMAC-2023.
3. Award for "Outstanding Paper" in Chemical Sciences of 6th Regional Science and Technology Congress, 2023-24.
4. RSC-IPS Young Scientist Award – 2024 recognized by Indian Photobiology Society.

Inorganic Chemistry

pubs.acs.org/IC

Article

Pyridyl-Isonicotinoyl Hydrazone-Bridged Zn(II) Coordination Framework with Thiophenedicarboxylato Link: Structure, Biological Activity, and Electrical Conductivity

Manik Shit, Satyajit Halder,[¶] Arka Dey,[¶] Basudeb Dutta, Anjana Chanthapally, Kuladip Jana,* and Chittaranjan Sinha*

Cite This: https://doi.org/10.1021/acs.inorgchem.3c02593

Read Online

ACCESS | Metrics & More | Article Recommendations | Supporting Information

ABSTRACT: Multidimensional applicability of functional materials is one of the focal attractions in today's scientific research. Highly stable and crystalline coordination polymers served as one of the active members in the club of multifunctional materials. Toward this concept, a 3-dimensional (3D) coordination framework, $\{[Zn_2(\mathbf{tdc})_2(\mathbf{pcih})_2]_n\}$ (**1**) ($\mathbf{tdc}^{2-}$, 2,5-thiophene dicarboxylate; **pcih**, pyridine-4-carboxaldehyde isonicotinoyl hydrazine), is designed and has been structurally well characterized by single crystal X-ray crystallography. One of the carboxylate groups of $\mathbf{tdc}^{2-}$ chelates to Zn(II), while the other carboxylato group (−COO) acts as bridging-O to neighboring Zn(II); the **pcih** serves as pyridyl-N bridging motif to two Zn(II) centers. The optical band gap, 3.83 eV (Tauc's plot), implies probable semiconducting ability of the material. Interestingly, the device fabricated using compound **1** measures the electrical conductivity, 2.21×10^{-5} S cm^{-1}, and series resistance (R_s), 807 Ω, at the dark phase, which are improved significantly to 6.36×10^{-5} S cm^{-1} and 460 Ω, respectively, under illumination conditions. Isoniazid, used to synthesize **pcih** and hence the Zn(II) compound **1**, is a medicine; so, the medicinal efficiency of **1** is checked by measuring the anticancer activity against MDA-MB-231, HeLa, HCT-116, and HepG2 cells. It is observed that drug efficacy is highest on MDA-MB-231 cells (IC_{50}: 19.43 ± 1.36 μM) than other cancer cells [IC_{50}: 24.43 ± 2.02 μM (HeLa), 26.06 ± 3.48 μM (HCT-116), and 44.28 ± 3.04 μM (HepG2)]. Therefore, the material has significant contribution in the area of energy and health toward the sustainable development goals.

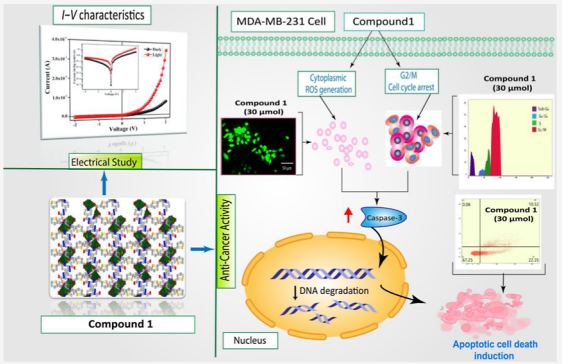

INTRODUCTION

Considerable success has been achieved in the field of coordination polymers/metal organic frameworks (CPs/MOFs) toward the application in various fields of science, engineering, technology, health, and so forth in the last three decades[1−] toward the sustainable development goals (SDGs). The CPs/MOFs are promising because of their high porosity, large surface area, flexible surface chemistry, adorable surface activity, and so forth. These materials have been used in separation, storage, catalysis, drug transport, sensing of ions/small molecules, and so forth.[4−12] A recent strategy has focused on the challenging program of integrating different functions in one system of CPs/MOFs toward the design of the multifunctional materials for achieving SDG commitment, especially for the designing of energy saving materials[13,14] and biologically efficient drugs.[15]

Zinc-based coordination polymers or metal organic frameworks (Zn-CPs/Zn-MOFs) have attracted much attention due to their versatile application in the field of high electrical conductivity,[16] CO_2 capture-and-reduction to value added chemicals and activation for the chemical transformation to useful organics,[17] heterogeneous catalyzes,[18] sensing for toxic ions and explosives at ultratrace level,[19] gas sorption and separation,[20] drug delivery,[21,22] and so forth. Metallo-organic polymers are designed by exploiting appropriate organic spacers with functional groups, which are made by bridging metals or metal clusters for architecting the crystalline materials useful in material science. Conducting metal−organic frameworks (c-MOFs) are of high priority. Although Zn-CPs/Zn-MOFs have received considerable attention in the chemical science and material engineering, their application to the conducting and energy saving fields has been given attention only recently.[13,23]

The device fabricated by using CPs/MOFs shows, in many cases, stimulation by light irradiation and enhancement of electrical conductivity, which will be truly helpful to utilize the

Received: July 27, 2023
Revised: November 10, 2023
Accepted: November 10, 2023

ACS Publications © XXXX American Chemical Society

CRYSTAL GROWTH & DESIGN

pubs.acs.org/crystal

Article

Exploration of Variable Temperature Magnetism and Electrical Properties of a Pyridyl-isonicotinoyl Hydrazone Bridged Three-Dimensional Mn-Metal–Organic Framework with a Thiophene Dicarboxylato Link

Published as part of a Crystal Growth and Design virtual special issue on Molecular Magnets and Switchable Magnetic Materials

Manik Shit, Dipankar Sahoo, Basudeb Dutta, Salah El Fallah, Adwaita Kundu, Nabin Baran Manik, and Chittaranjan Sinha*

Cite This: *Cryst. Growth Des.* 2022, 22, 7143–7152

Read Online

ACCESS | Metrics & More | Article Recommendations | Supporting Information

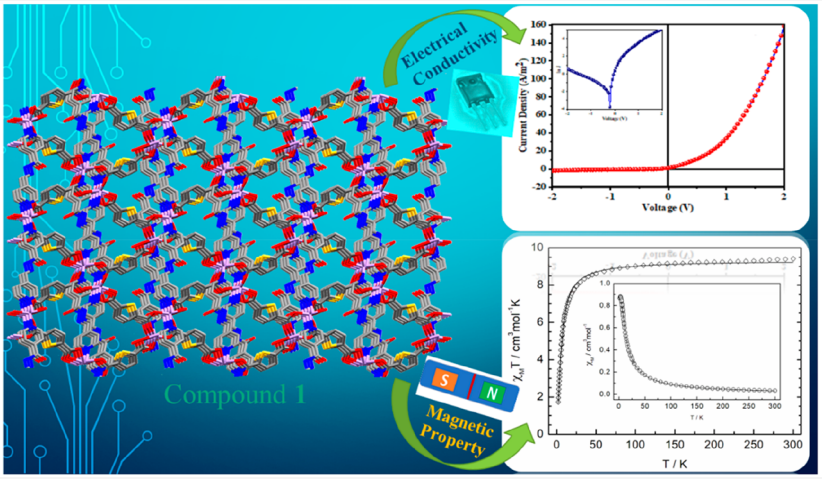

ABSTRACT: In emerging trends in our technology-dependent society, the applicability of multifunctional coordination polymers (CPs) and metal–organic frameworks is highly stimulating. In search of such chemical compounds, a Mn(II), d^5, based metal–organic framework (MOF), $\{[Mn_2(\mathbf{tdc})_2(\mathbf{pcih})_2(EtOH)]_n\}$ (**1**), has been designed with the coordination of multidentate ligands $\mathbf{tdc}^{2-}$ (2,5-thiophene dicarboxylato) and **pcih** (pyridine-4-carboxaldehyde isonicotinoylhydrazone). The structure determination by single crystal X-ray diffraction has revealed the formation of three-dimensional (3D) supramolecular architecture via the combined nearly perpendicular bridging of **pcih** and $\mathbf{tdc}^{2-}$ ligands. A variable temperature magnetic measurement of **1** shows weak antiferromagnetism (χ_{MT}, 9.41 cm^3 K mol^{-1} at 300 K) with two as good as "isolated" Mn(II) centers ($S = 5/2$ with $g \approx 2.07$). Magnetic exchange is considered through 9/10 carboxylato bridged atoms inclusively spanning two Mn(II) centers at a distance of 4.114 Å. Interestingly, the 3D assembly of **1** exhibits electrical conductivity in the semiconducting region (band gap, 3.72 eV; barrier height, 0.65 eV; series resistance, 0.03 Ω). A Schottky barrier diode feature is recorded at a threshold potential of 0.19 V and follows a non-ohmic relation ($I \alpha V^2$), and the conductivity is 3.42×10^{-5} S m^{-1}. A galvanostatic charge–discharge (GCD) experiment measures the moderate specific capacitance of 1 F/g at a 2 mV/s scan rate.

INTRODUCTION

Magnetic properties are unique characteristics of transition metal containing compounds. Transition metal ions contain unpaired electrons in any of their redox states, and individual electrons have both spin and orbital components of magnetic moment. Ions of multielectrons (d^n, f^n; $n > 1$) show interelectronic interactions and constitute different states of

Received: July 19, 2022
Revised: October 24, 2022
Published: November 4, 2022

ACS Publications

© 2022 American Chemical Society

NJC

ROYAL SOCIETY OF CHEMISTRY

PAPER

View Article Online
View Journal | View Issue

Check for updates

Cite this: *New J. Chem.*, 2023, **47**, 5922

Strategy for the improvement of electrical conductivity of a 3D Zn(II)-coordination polymer doubly bridged by mesaconato and pyridyl-isonicotinoyl hydrazide based Schottky diode device†

Manik Shit,‡[a] Arnab Kanti Karan,[b] Dipankar Sahoo,[b] Nabin Baran Manik,[b] Basudeb Dutta *[ac] and Chittaranjan Sinha *[a]

Received 6th November 2022,
Accepted 21st February 2023

DOI: 10.1039/d2nj05455h

rsc.li/njc

Out of many stimulating research fields, the search for energy materials has become of highest priority in recent times due to issues related to sustainable development. Specific investigation in energy has focused on the coordination polymers (CPs)/metal–organic frameworks (MOFs). Due to their ordered orientation, impressive stability, and tuneable composition, MOFs are an appropriate multifunctional platform for electrochemical and photochemical energy conversion and storage. In this study, two bridging molecules, mesaconic acid (**H_2mes**) and pyridine-4-carboxaldehyde iso-nicotinoyl hydrazone (**pcih**) coordinate orthogonally to the Zn(II) metal node to construct a 3D network, **$[Zn(mes)(pcih)(H_2O)_2]_n$** (**1**). The formation of non-covalent interactions leads to a robust 3D super structure. A Tauc plot was used to calculate the band gap, 3.62 eV, from UV-Vis spectroscopic data, which enabled us to design a Schottky device (diode area: 9×10^{-6} m^2 and Richardson constant: 1.20×10^6 A K^{-2} m^{-2}) and measure the electrical conductivity, 2.98×10^{-4} S m^{-1} (in the dark); upon illumination, the conductivity is enhanced to 7.01×10^{-4} S m^{-1}. Furthermore, a photosensitivity value of 1.72 was observed, giving the material next-generation technological potential. It is expected that this material may provide inspiration for researchers of energy materials.

Introduction

In the history of scientific discovery, 1913 is a remarkable year because Alfred Warner (1866–1919) was awarded the Nobel prize for their contribution to the historic coordination theory of transition metal complexes. Coordination chemistry now plays a central role in the development of chemistry and allied subjects for the intensive progress of human civilization. An interesting aspect of coordination theory is the structure-function relation and application in diverse fields.[1–3] Multidentate ligands consisting of two or more donor centers can continuously extend in a special pattern to generate a polymeric form, known as coordination polymers (CPs);[4–12] this terminology was introduced by J. C. Bailer in the year 1967.[13] Mainly, dicarboxylate and bipyridyl based organic compounds are employed to design CPs. The dimensionality of the CPs is largely dependent on the nature of the organic linker, metal node, and the reaction conditions, and may be extended from 1D to 2D and 3D. The presence of appropriate porosity in 2D or 3D CPs has defined an innovative class of materials known as Metal–Organic Frameworks (MOFs).[13–15] The CPs/MOFs, a class of hybrid multifunctional crystalline materials with fascinating structural architectures and topologies, have been widely used in gas storage and separation, catalysis, sensing, magnetism, drug delivery, biotechnology, electrical conductivity, proton conductivity, smart device fabrication, *etc.*[16–23] At present, the major global challenge is to stop C-emission, explore green energy resources and maintain zero energy loss. Materials with smart electrical conductivity and sustainability are highly advantageous to this vision. With this expectation, many research groups have been dedicated to designing a number of such materials to

[a] *Department of Chemistry, Jadavpur University, Jadavpur, Kolkata, 700 032, India. E-mail: crsjuchem@gmail.com*
[b] *Department of Physics, Condensed Matter Physics Research Centre, Jadavpur University, Kolkata, 700032, India*
[c] *Department of Chemical Sciences, Indian Institute of Science Education and Research Kolkata, Mohanpur, West Bengal, 741246, India. E-mail: dutta.basu11@gmail.com*

† Electronic supplementary information (ESI) available. CCDC 2209342. For ESI and crystallographic data in CIF or other electronic format see DOI: https://doi.org/10.1039/d2nj05455h

‡ Present Address: Narajole Raj College, Paschim Medinipur, Narajole, 721211, India.

 This journal is © The Royal Society of Chemistry and the Centre National de la Recherche Scientifique 2023

ACS APPLIED POLYMER MATERIALS

pubs.acs.org/acsapm Article

Mn(II) 3D Coordination Framework with Mixed 5-Aminoisophthalato and Pyridyl-isonicotinoyl Hydrazone Bridges: Structure, Electrical Conductivity, Anticancer Activity, and Drug Delivery

Manik Shit, Satyajit Halder,[#] Kalipada Manna,[#] Arnab Kanti Karan,[#] Arnab Samanta,[#] Nabin Baran Manik, Sagar Pal, Kuladip Jana,[*] and Chittaranjan Sinha[*]

Cite This: https://doi.org/10.1021/acsapm.3c02805 Read Online

ACCESS | Metrics & More | Article Recommendations | Supporting Information

ABSTRACT: A 3D coordination polymer of Mn(II), $[\mathbf{Mn_2(aisp)_3(pcih)_2(solvent)}]_n$(**CP1**) (**pcih** = pyridine-4-carboxaldehyde isonicotinoyl hydrazine and $\mathbf{H_2aisp}$ = 5-aminoisophthalic acid), was constructed by doubly heterobridging ligands and was characterized by single-crystal X-ray diffraction measurements. The noncovalent forces (H-bonding, $\pi\cdots\pi$ interactions) bring robustness and stability (thermal and chemical) to the framework. The optical band gap of **CP1** obtained from Tauc's plot (2.98 eV) is comparable with the DFT computation value (HOMO and LUMO energy difference = 2.80 eV) and is crucial for the fabrication of a semiconducting device. A thin-film device ITO/**CP1**/Cu was constructed at the measured electrical conductivity of 1.57×10^{-6} m^2 V^{-1} s^{-1} and the series resistance (R_s) of 331 Ω, at a dark phase. Isoniazid, an antibiotic, used to prepare a Schiff base, **pcih**, and the present compound, **CP1**, motivated us to examine the anticancer efficiency against as many as four cancer cell lines (HeLa, PC3, MDA-MB 231, A549) and was compared with the NKE (human normal kidney epithelial) cell line. **CP1** showed a better impact in inhibiting the proliferation of HeLa cells (IC_{50}: 17.58 ± 1.56 μM) than other cancer cells (IC_{50}: 21.52 ± 2.44 μM (PC3), 36.41 ± 1.72 μM (MDA-MB 231), 50.29 ± 3.81 μM (A549)). Loading and delivery of drug diclofenac sodium (DMNa) were tested in two different pH = 1.2 (simulated stomach environment) and pH = 7.4 (simulated intestinal environment), which showed ∼8% release at pH 1.2 and ∼87% release at pH 7.4 within 30 h. **CP1**, a magic material and stable in solution at different pH (1−10), showed multifaceted applications such as being energy saving, anticancer activity, and drug delivery. The design is certainly an important footstep toward the sustainable development goals (SDGs).

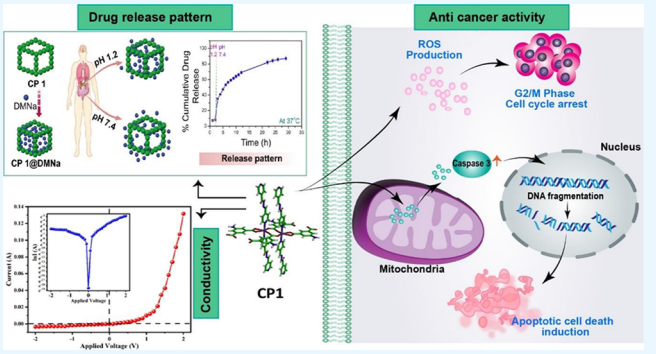

KEYWORDS: *3D-Mn(II) coordination polymer, 5-aminoisophthalato, pyridyl-isonicotinoyl hydrazide bridging, electrical conductivity, anticancer activity, drug delivery*

INTRODUCTION

Polymers and hybrid materials have established their multifaceted deliverable outcome-based properties to meet many challenges of the environment and the society[1−5] such as clean energy, ensuring health, zero-waste management, supply of hygienic water, and pollution-free air. A number of such materials are employed to fabricate energy-saving electronic devices.[6−11] Some of the external factors affect the stability and efficiency of such devices made up of organic polymers.[12−14] However, after the historic recognition of the coordination chemistry (Alfred Warner, Nobel prize in 1913), it extends the exploration in different branches of science.[15−20] Organic−inorganic hybrid compounds are such materials that show promising applications in diverse fields following SDG protocol.[21−26] The coordination polymers (CPs)/metal−organic frameworks (MOFs) are such hybrid materials, and their importance is established for the well-being of civilization.[25]

The rising prominence of CPs in anticancer research stems from their versatile design, allowing customization of the size, shape, and porosity. Their porous structures are well suited for drug delivery, facilitating targeted and controlled release of therapeutic agents with excellent biocompatibility, and thereby, these materials are supporting theragnostic applications. Certain CPs, incorporating cytotoxic metal ions/ligands,

Received: November 19, 2023
Revised: February 6, 2024
Accepted: February 7, 2024

ACS Publications © XXXX American Chemical Society